
NLTE in iron-group elements. Analysis of Mn and Co in metal-poor stars

Maria Bergemann



München 2008

NLTE in iron-group elements. Analysis of Mn and Co in metal-poor stars

Maria Bergemann

Dissertation
an der Fakultät für Physik
der Ludwig-Maximilians-Universität
München

vorgelegt von
Maria Bergemann
aus Kazan, Russland

München, den 31. Oktober 2008

Erstgutachter: Prof. Dr. Thomas Gehren

Zweitgutachter: Dr. Achim Weiss

Tag der mündlichen Prüfung: 11. Dezember 2008

Contents

Zusammenfassung	ix
Summary	x
1 Introduction	1
2 Theory of stellar atmospheres and line formation	5
2.1 Physical principles	5
2.1.1 Model of a stellar atmosphere	5
2.1.2 How to determine the number densities of absorbing atoms.	7
2.1.3 Line formation	9
2.1.4 Hyperfine structure	10
2.2 Physics translated to computer language	12
2.2.1 Calculation of level populations	12
2.2.2 Calculation of spectral lines	13
3 Methods developed for Mn and Co	15
3.1 Stars and observations	15
3.2 Stellar parameters	15
3.3 Model atmospheres	18
3.3.1 Reference models	18
3.3.2 Solar models	19
3.4 NLTE calculations	20
3.4.1 Atomic structure and energy levels	21
3.4.2 Radiative rates	22
3.4.3 Collisional rates	27
3.4.4 Comparison of rates	28
3.5 Spectrum synthesis and abundance analysis	30
3.5.1 Oscillator strengths	31
3.5.2 Hyperfine structure	34
4 Statistical equilibrium of Mn and Co	37
4.1 NLTE effects on Mn levels	37
4.2 Influence of uncertain parameters	41
4.2.1 Completeness of the atomic model	41
4.2.2 Photoionization	44
4.2.3 Inelastic collisions with H I atoms	47
4.3 NLTE effects on Co levels	47
4.4 Statistical equilibrium of Co in metal-poor stars	51

5	NLTE effects on spectral lines and abundances	53
5.1	NLTE and HFS effects on solar Mn line formation	54
5.2	NLTE effects on Mn lines in a wide range of stellar parameters	57
5.2.1	Collisions with H I atoms	59
5.3	NLTE and HFS effects on the formation of Co lines	61
5.3.1	Lines of Co II in NLTE	63
6	Abundances in the Sun	67
6.1	Solar abundance of Mn	67
6.1.1	Ionization equilibrium of Mn in the Sun	71
6.2	Solar abundance of Co and related uncertainties	72
6.2.1	Ionization equilibrium of Co in the Sun	75
7	Abundances in metal-poor stars	77
7.1	Manganese	77
7.1.1	Some aspects of a differential stellar analysis	77
7.1.2	Mn in metal-poor stars	79
7.1.3	Constraints on the accuracy of NLTE abundances	83
7.2	Cobalt	85
7.3	The trend of $[\text{Mn}/\text{Fe}]$ with $[\text{Fe}/\text{H}]$	88
7.4	The trend of $[\text{Co}/\text{Fe}]$ with $[\text{Fe}/\text{H}]$	91
8	Fe-peak elements and the Galactic evolution	95
8.1	Observational constraints	95
8.2	Explosive nucleosynthesis	98
8.3	Chemical evolution of Mn and Co in the Galaxy	100
9	Conclusions	107
	Glossary	111
	Nomenclature	117
A	Tables	121
	Bibliography	133
	Acknowledgements	140
	Curriculum Vitae	143

Zusammenfassung

Das statistische Gleichgewicht von Mn und Co in den Atmosphären kühler Sterne wird in dieser Arbeit erstmalig untersucht. Für die *neutralen Ionen* dieser beiden Elemente werden signifikante Abweichungen vom lokalen thermodynamischen Gleichgewicht (LTE) gefunden. Diese ergeben sich für Co I aus der Überionization. Im Mn I sind die Abweichungen vom LTE das Resultat starker Strahlungsprozesse in gebundenen Übergängen, solange sonnenähnliche Metallhäufigkeiten und Temperaturen vorherrschen. In Sternatmosphären, in denen das Strahlungsfeld verstärkt wird, also in metallarmen Sternen mit solaren oder supersolaren Temperaturen, wird die Überionisation auch in Mn I zum dominanten Prozess. Die Grundzustände der einfach ionisierten Spezies bleiben weitgehend unabhängig vom nicht-lokalen thermodynamischen Gleichgewicht (NLTE). Die Besetzung der *angeregten* Zustände in Mn II und Co II wird allerdings durch Absorptionsprozesse in Linienübergängen modifiziert. Dadurch sind Abweichungen vom LTE auch in den Linien ionisierter Spezies zu finden. Die NLTE-Besetzungsdichten werden zur Bestimmung von Elementhäufigkeiten von Mn und Co benutzt. Die solaren Häufigkeiten dieser Elemente befinden sich in Übereinstimmung mit denen in chondritischen Meteoriten. Für 17 Zwergsterne und Unterriesensterne mit Metallhäufigkeiten $-2.5 < [\text{Fe}/\text{H}] < 0$ werden *differentielle Häufigkeitsanalysen* relativ zur Sonne durchgeführt. Die Häufigkeiten werden mit Methoden der Spektrumsynthese bestimmt, wobei die Hyperfeinstruktur-Aufspaltung berücksichtigt wird. Generell sind alle NLTE-Häufigkeiten in metallarmen Sternen größer als LTE-Häufigkeiten. Die Differenz $[\text{El}/\text{Fe}]_{\text{NLTE}} - [\text{El}/\text{Fe}]_{\text{LTE}}$ nimmt mit abnehmender Metallhäufigkeit $[\text{Fe}/\text{H}]$ zu und erreicht Werte von 0.4 dex für Mn und 0.6 dex für Co in den metallärmsten Sternen. Der $[\text{Mn}/\text{Fe}]$ -Trend bleibt bei solaren Werten im gesamten Bereich der Metallhäufigkeiten, die hier untersucht werden; die $[\text{Co}/\text{Fe}]$ -Verhältnisse nehmen mit abnehmenden Eisenhäufigkeiten in Sternen der Dicken Scheibe und des Halo zu. Die NLTE-Häufigkeiten für alle Sterne können durch das Netzwerk explosiver Nukleosynthese in Supernova-Ereignissen (SN) erklärt werden. Verschiedene Modelle werden vorgeschlagen. Die Produktion von Mn kann mit primären (metallizitäts-unabhängigen) Ereignissen in SNe II großer Massen zusammenhängen, möglicherweise in Kombination mit einem sekundären Ereignis in SNe II mit geringerer Masse, welches bereits eine Anreicherung mit Metallen voraussetzt. Ein zweiter Prozess setzt voraus, daß die Mn-Produktion in allen SNe II unabhängig von der vorangehenden Metalleanreicherung ist, und daß eine Überproduktion von Mn relativ zu Co in SNe Ia geschieht. Dabei ergibt sich die Möglichkeit, daß ein größerer Anteil von Fe und Mn in SNe Ia produziert wird, und nur ein kleinerer Anteil in SNe II. Für Co wird ein *sekundärer* Ursprung vorgeschlagen. Der größte Anteil muß hier von kurzlebigen, massereichen Sternen kommen, die als SNe II explodieren; Beiträge von SNe Ia zur Co-Produktion sind als geringfügig anzusehen. All diese Folgerungen gründen auf Mn- und Co-Häufigkeiten in metallarmen Sternen, die aus den Linien der *neutralen* Elemente abgeleitet werden. Die differentiellen Häufigkeiten, die aus den UV-Linien der *ionisierten* Elemente bestimmt werden, sind systematisch geringer um 0.3 – 0.6 dex. Diese Diskrepanz könnte das Ergebnis unerkannter Blends im Sonnenspektrum sein. Eine ganz andere Schlußfolgerung wäre, daß das Modell für die NLTE-Analyse in seinem gegenwärtigen Zustand nicht ausreicht, um eine hinreichend genaue Beschreibung des Ionisationsgleichgewichts für Mn und Co zu geben.

Summary

The statistical equilibrium of Mn and Co in the atmospheres of cool stars of different Galactic populations is analyzed for the first time. Significant departures from local thermodynamic equilibrium (LTE) level populations are found for the neutral ions. They are related to the overionization in Co I. Deviations from LTE in Mn I are due to the strong radiative processes in discrete transitions as long as the solar metallicities and temperatures are considered. In the environments where the radiation field is amplified, such as metal-poor stars with solar or super-solar effective temperatures, the overionization in Mn I is a dominant process. The ground states of singly ionized species are almost unaffected by non-local thermodynamic equilibrium (NLTE). However, the photon pumping modifies the number densities of excited states in Mn II and Co II. Hence, deviations from LTE also occur in the lines of ionized species. The NLTE level populations are used to determine the abundances of Mn and Co in the solar photosphere. The proposed solar abundances of these elements are in agreement with that in chondritic meteorites. The differential abundance analysis of Mn and Co is carried out for 17 subdwarfs and subgiants in the metallicity range $-2.5 < [\text{Fe}/\text{H}] < 0$. The abundances are derived by method of spectrum synthesis and hyperfine splitting of spectral lines is accurately taken into account. The NLTE abundances of Mn and Co in metal-poor stars are higher than the LTE abundances. The difference $[\text{El}/\text{Fe}]_{\text{NLTE}} - [\text{El}/\text{Fe}]_{\text{LTE}}$ increases with decreasing $[\text{Fe}/\text{H}]$ and reaches 0.4 dex for Mn and 0.6 dex for Co in the most metal-poor objects. The $[\text{Mn}/\text{Fe}]$ trend is solar all over the metallicity range studied here; $[\text{Co}/\text{Fe}]$ ratios steadily increase with decreasing Fe abundances in the halo and thick disk stars. The NLTE abundances for the stars of the halo, thick and thin disks can be explained within the framework of explosive nucleosynthesis in supernova (SN) events. Several scenarios are suggested. The production of Mn can be associated with the primary (metallicity-independent) event in SNe II of high masses, possibly combined with a secondary event in lower-mass SNe II, which requires pre-existing metals. A second scenario assumes metallicity-independent Mn yields from all SNe II, and an overproduction of Mn relative to Co in SNe Ia. This scenario allows for the possibility that a larger fraction of Fe and Mn is produced in SNe Ia compared to the SNe II. For Co, a secondary origin is proposed. The largest yield has to come from short-lived massive stars, exploding as SNe II; contribution of SNe Ia to Co production must be relatively small. These conclusions are based on Mn and Co abundances in metal-poor stars derived from the lines of neutral elements. The differential NLTE abundances determined from the UV lines of ionized elements are systematically lower by 0.3 – 0.6 dex. The discrepancy could be due to the unaccounted blends in the lines of the solar spectrum. Otherwise, the conclusion is that the NLTE analysis in its present state fails to provide a correct description of the *ionization equilibrium* for Mn and Co in stellar atmospheres.

Chapter 1

Introduction

The chemical composition of low-mass metal-poor stars in the Milky Way is a subject of an increased interest. The interest is mainly stipulated by the correlation of surface element abundances with the age of such stars. This correlation is not a coincidence: *old low-mass stars* were born soon after the initial formation of the Galaxy, which was at that times poor in chemical elements heavier than He, so-called metals. As the time passed, more and more massive stars exploded as supernovae, and enriched the interstellar medium (ISM) in the Galaxy with elements from C to U. The star formation in the Galaxy went on, and next generations of stars of different masses have been born in the continually changing ISM. The low-mass stars are evolving very slowly, and even after several Gyr their atmospheres are still untouched by the processes of nuclear fusion that takes place in stellar cores. Thus, such stars carry the same chemical composition as the ISM at that epoch of their formation. Knowing the mechanisms, which produce the chemical elements in the Milky Way, carry them to the ISM and recycle them, one can reconstruct the *Galactic chemical evolution* (GCE). The GCE is a paramount part of the galaxy formation and evolution in general because it gives valuable constraints on the formation of stars and stellar populations, the dynamics of gas, and stellar lifetimes.

There are two types of objects, which contribute to the enrichment of the Galaxy with *heavy elements*: SNe II and SNe Ia. SNe II are linked to the gravitational collapse of massive stars with $M > 8M_{\odot}$ at the end of their hydrostatic evolution. SNe Ia are explained by exploding white dwarfs in binary systems. Their progenitors are intermediate to low mass stars that started to contribute elements to the interstellar medium ~ 1 Gyr later. For metallicities $[\text{Fe}/\text{H}] \leq -1$, only SNe II contributed to the ISM enrichment (Thielemann et al. 1996). Hence, surface abundances of old low-mass stars with these metallicities are a good constraint to the yields of SNe II. Extending the sample of stars to higher metallicities, $[\text{Fe}/\text{H}] \geq -1$, allows us to trace the additional contribution from SNe Ia. On the one side, stellar evolution calculations provide yields of sufficient accuracy for a majority of abundant elements, Ca ... Si. These can be incorporated into the theoretical GCE models to predict the evolution of *element abundances* in the ISM in time.

For the heavier elements, in particular the Fe-group (V, Ti, Cr, Mn, Fe, Co, Ni) created in explosive burning conditions, the stellar yields are still highly uncertain. The production of these elements is very sensitive to the mechanism of supernova explosion and progenitor structure which are not well understood. In massive stars, large uncertainties are related to the explosion energy, and position of the mass cut between the central neutron star (or black hole) and the ejected envelope (Woosley & Weaver 1995). The abundances of elements with odd number of neutrons and protons (Mn, Co) also depend on a neutron-to-proton ratio of a star, which is determined not only by the initial composition of a star but also by hydrostatic stages of stellar evolution prior to explosion. The treatment of convection, semi-convection, and overshooting determine the structure of the progenitor, and may significantly change the element yields. For SNe Ia, there is even no agreement on what *is* a type Ia supernova. Different mechanisms for the explosion were proposed; the most widely-used is the “delayed detonation” scenario, in which a C-O white dwarf

experiences an initial central deflagration which develops into a detonation. In the latter case, it was found that the abundances of the Fe-group depend on the density in deflagration-detonation transitions (Iwamoto et al. 1999).

So, at present there is no clear scenario even for the iron production. As emphasized by Timmes et al. (1995), it is likely that one third of solar iron is produced in SNe Ia, and two thirds in SNe II, but the inverse scenario is also possible considering *uncertainties in yields*. A situation is even more uncertain for the other iron-peak elements. The only solution is to derive additional constraints on average Fe-peak abundances of SNe II and SN Ia from the observations of low-metallicity stars. This became a standard practice: *to calibrate stellar yields and GCE models by fitting observed abundances*. However, in this process one often forgets that the spectroscopically determined abundances in low-mass stars are not really “observed”. Any parameter determined from stellar spectra is strongly model-dependent because it implies *fitting* the available physical models to the observations. One of the most important issues in the modeling is the description of an excitation-ionization equilibrium of an element in a stellar atmosphere. The choice of local thermodynamic equilibrium (LTE), or non-local thermodynamic equilibrium (NLTE) depends on the aims of the research. Under the simple LTE assumption, the thermodynamic state of the atmospheric plasma is a function of a local temperature and density alone and it is described by Boltzmann-Saha distributions. Under NLTE, the radiative transfer problem becomes much more complicated because the interaction of gas particles with the radiation field must be taken into account explicitly. When one studies the formation of spectral lines and wants to derive an *atmospheric abundance of an element*, the assumption of NLTE is absolutely necessary.

The majority of Fe-group elements, mainly due to their complex atomic structure, were not studied in NLTE. Among others, these are Mn and Co, which are the objects of the present work. Many researchers encountered problems with excitation and ionization balance of Mn in metal-poor stars. The discrepancy of a factor of 3 between abundances in metal-poor giants derived from strong and weak spectral lines of neutral Mn¹ was noted by Cayrel et al. (2004). Later, Lai et al. (2008) confirmed it for metal-poor subdwarfs. According to Johnson (2002), the manganese abundances derived from Mn II lines are systematically higher than abundances derived from Mn I lines. Actually, *the failure to satisfy excitation and ionization equilibria of the elements is the most common problem of LTE*. Neither of the problems mentioned for Mn has ever been reported for Co. But this is simply due to a very limited number of studies focused on Co abundance determinations in the Sun and metal-poor stars. In all of them, researchers used only a few Co I lines, persistently ignoring the spectral lines of Co II for some unknown reasons.

There is another complication, associated with the abundance calculations for Mn and Co: their lines have a very specific broad shape, which is due to the hyperfine splitting of fine structure of energy levels. This splitting arises because the atoms have *odd* number of protons in the nucleus, and thus non-zero nuclear spins. The importance of HFS on profile shapes was recognized long ago. Abt (1952) noted that if the solar Mn I line at 5420 Å were modeled without HFS, one would need a temperature of 96 000 K or a turbulent velocity of 5.5 km s⁻¹ to fit it. However, only few authors take into account HFS of Mn and Co in the analyses (McWilliam et al. 2003, del Peloso et al. 2005), the others neglect it and provide numerous reasons to justify their choice. There are only two studies in the literature dedicated to the analysis of the influence of HFS on the Mn and Co abundances, Prochaska & McWilliam (2000) and del Peloso et al. (2005). Both demonstrated that neglect of HFS leads to a systematic overestimation of abundances that is particularly important when the *abundance trends* in metal-poor stars are investigated.

However, the importance of the early studies, even if performed under LTE and without HFS, must not be underestimated. They all agree that there is a clear correlation between individual abundances of Mn and Co of a star and its metallicity²: Mn is strongly depleted relative to iron in metal-poor stars (Gratton 1989, Nissen et al. 2000, Sobeck et al. 2006), whereas Co/Fe ratios are nearly solar (Gratton & Sneden 1991) and even supersolar (Ryan et al. 1991, McWilliam et al. 1995, Reddy et al. 2006). Different assumptions are invoked to explain the trends, but

¹Hereafter, we adopt the standard notation to designate neutral and ionized element as El I and El II, respectively.

²The terms “relative iron abundance” and “metallicity” are usually used interchangeably, and both refer to [Fe/H] (see glossary).

they can not reconcile all observational facts simultaneously, especially when other elements of the iron group (Cr, Ni) are considered. A critical issue is the *main astrophysical production site* of manganese and cobalt. In particular, some researchers favor the theory of Mn overproduction with respect to Fe in SNe Ia (Nissen et al. 2000, Prochaska & McWilliam 2000, Sobek et al. 2006), the others (McWilliam et al. 2003, Feltzing et al. 2007) suggest that metallicity-dependent yields from SNe II explain the observed trends. Even worse, there exists no explanation for the increasing abundance of Co relative to Fe in metal-poor stars. This trend is inconsistent with a famous *odd-even effect* among the iron-peak nuclei (Burbidge et al. 1957), characterized by a general suppression of the stable odd-Z nuclei relative to their stable even-Z neighbors in metal-poor environments. Actually, the same problem exists for Cr and Ni in low-metallicity stars.

In the view of the uncertainties related to stellar evolution calculations, it is understandable that researchers try to overcome these problems from the side of stellar nucleosynthesis. With the help of an automated fitting procedure (e.g. Heger & Woosley 2008), one can find a set of SN II model parameters to obtain a best fit to observed abundance patterns in very metal-poor stars. Indeed, Heger & Woosley succeeded to reproduce Mn and Co abundances in a few very metal-poor stars, but *not simultaneously*. In general, such procedures are based on the assumption that the abundances of very metal-poor stars are determined by a *first generation* SNe or even by a single supernova. Whereas, it is hard to assume that for metallicities $[\text{Fe}/\text{H}] \sim -3$, characteristic of the most studied stars in the literature, some enrichment by second generations of SNe have not yet occurred. Also, Heger & Woosley note that any combination of the model parameters, like mass cut and explosion energy, does not reproduce Cr abundances in metal-poor stars, which is produced in the same conditions as Mn.

It is important to note that precisely these “strange” trends of Fe-peak elements (and Zn) with metallicity stipulated a number of astrophysical theories, some of which are considered today standard. For example, the above-mentioned idea that very low-metallicity stars reflect the chemical composition of a single supernova developed into the whole theory of the *supernova-induced star formation* (Tsujiimoto et al. 1999). In this theory of the Galactic evolution, stars in the halo are thought to be born from each supernova remnant, and when star formation terminates the remaining gas falls in the still-forming Galactic disk. The original idea is partly based on the McWilliam et al. (1995) discovery that Mn becomes dramatically deficient relative to Fe below $[\text{Fe}/\text{H}] \approx -2.5$, whereas the Co/Fe trend changes slope and increases. The “observed” scatter of Mn/Fe and Co/Fe ratios in metal-poor stars, as reported by Ryan et al. (1996), is viewed as a justification to this theory. The *hypernova* scenario (Umeda & Nomoto 2005, and references therein) is also a product of attempts to resolve the *discrepancies between the yields from conventional supernova models and the Fe-peak abundance trends in the Galactic halo*.

It is not only abundances in metal-poor stars, which are important for understanding the GCE. In fact, any model of the Galactic evolution should be able to reproduce the *chemical composition of the Sun*, i.e. the abundance pattern in the ISM at solar birth. Curiously, this test also fails for Fe-peak elements: the predicted solar abundances of Sc, V, Cr, Co, Mn, Ti are either too high or too low, depending on the GCE model (Goswami & Prantzos 2000, François et al. 2004). There exists an independent tool to determine whether discord with observations is due to the chemical evolution model parameters (including SN yields) or in solar abundances themselves. It implies comparison of the abundances determined from lines in the Sun’s photospheric spectrum to those in C I type carbonaceous meteorites, which are the thought to be chemically unfractionated. The spectroscopic abundance of Co in the solar atmosphere is in agreement with that in CI chondrites. However, for Mn there appears to be $\sim 30\%$ difference between the solar photospheric and the meteoritic C I abundance. It is not yet clear whether to attribute this to an incorrect allowance for HFS and neglect of NLTE effects in the calculation of the solar Mn abundance. The uncertainty assigned to the Mn (and Cr) abundance in meteorites is also larger than that of the other elements because some mineralogical process, e.g. aqueous alteration (Lodders 2003), is thought to have changed the distribution of elements in the chondrite parent body. The fit of photospheric and meteoritic abundances of the reference element Si is also very important in this context. Thus, our understanding of the solar abundances for particular elements is still far from complete.

In the current project, we want to touch upon all of the above-mentioned problems related

to the composition of the Sun and meteorites, stellar nucleosynthesis, and the Galactic chemical evolution concentrating on two Fe-peak odd- Z elements, Mn and Co. In chapter 2, we summarize basic concepts of model atmosphere analysis and line formation. The methods adopted in the analysis are described in chapter 3. We investigate the *excitation-ionization equilibrium* of Co and Mn in stellar atmospheres (chapter 4) and predict what errors in abundance calculations occur when NLTE effects and hyperfine splitting of lines is neglected (chapter 5). Next, we analyze the abundances of these elements in the Sun, and compare them with that of meteorites to ascertain the reason for the discrepancies (chapter 6). Furthermore, we compute the NLTE abundances for a sample of 18 stars, which belong to three Galactic populations, thin and thick disk, and the halo (chapter 7). The results are compared with the previous abundance estimates from the literature. The evolution of abundance ratios in the Galaxy and implications for the Fe-peak element nucleosynthesis are discussed in chapter 8. Finally, the main results are summarized in chapter 9.

Note that many physical notations and terms used in the context of this dissertation are listed in the *Nomenclature* section and are additionally explained in the *Glossary* section.

Parts of this dissertation were published in Bergemann & Gehren (2007), Blackwell-Whitehead & Bergemann (2007), Bergemann & Gehren (2008).

Chapter 2

Theory of stellar atmospheres and line formation

2.1 Physical principles

2.1.1 Model of a stellar atmosphere

A stellar atmosphere consists of ionized and neutral atoms of *almost* all chemical elements, electrons, molecules, and those are freely “swimming” in the radiation field. It is a very complex system in a sense that many processes, both macroscopic and microscopic determine its state.

The macroscopic phenomena include dynamics, like stellar pulsations, convection, expanding envelopes, etc. The microscopic processes are those that take place on (sub)atomic scales, like interaction between ions, electrons, and photons.

Trying to model all these phenomena simultaneously and accurately is *at present* an Utopian idea. One has to restrict himself to a certain range of fundamental¹ stellar parameters, for which some simplifications can be made. In the current analysis, the focus will be set on stars with effective temperatures T_{eff} from 5000 to 6500 K, surface gravities $\log g$ from 3 to 5, and metallicities $[\text{Fe}/\text{H}]$ from 0 to -3 . This range of physical parameters describes solar-type stars, metal-poor subdwarfs and subgiants and it allows to make several assumptions:

1. the atmosphere consists of homogeneous plane-parallel layers (due to a very small thickness less than 0.1% of a stellar radius)
2. the atmosphere is static (no time-dependent dynamical phenomena)
3. the energy is transferred by radiation and convection (no heat conduction)

A mathematical model of an atmosphere is usually represented as a table containing the values of local electron temperature T_e and electron pressure P_e at each depth point. All other parameters can be calculated from these values, in particular we can describe how *a state of a gas changes with depth*. The models do not include the characteristics of the radiation field. Instead, these values are derived as a result of calculations with a specified model atmosphere.

To calculate a model, we have to solve several equations:

1. equation of radiative transfer for a plane-parallel atmosphere

$$\cos \theta \frac{dI_\nu}{dz} = \kappa_\nu I_\nu - \eta_\nu \quad (2.1)$$

¹called fundamental, because they define the physical conditions in the stellar atmosphere and are directly related to the physical properties of a star: mass (M), radius (R), and luminosity (L)

The equation describes a change of specific intensity I_ν , as radiation passes through a slab of a thickness dz . In a stellar atmosphere, the gradients of temperature and specific intensity are much greater in the radial direction than in horizontal direction, hence we can assume that I_ν depends only on the depth coordinate z and on the direction. For the plane-parallel approximation, the latter is represented by an angle θ between the direction of the light beam and the z axis. The parameters κ_ν and η_ν with dimensions cm^{-1} are extinction and emission coefficients per unit volume; their ratio gives a source function:

$$S_\nu = \frac{\eta_\nu}{\kappa_\nu} \quad (2.2)$$

As S_ν has the same units as I_ν , the source function can be viewed as a specific intensity emitted at some point in a gas.

2. equation of hydrostatic equilibrium:

$$\frac{dP_g}{dz} = g\rho \quad (2.3)$$

Gas pressure is balanced by the gravitational attraction, which does not change with depth.

3. equation of flux constancy, or energy conservation:

$$\frac{dF}{dz} = 0 \quad (2.4)$$

The total energy flux transported to the surface is constant and can be equated to the integral flux from the surface of a black body. Assuming that energy is carried out by radiation only, we get the *radiative equilibrium* equation:

$$\int_0^\infty J_\nu(z)\kappa_\nu(z)d\nu = \int_0^\infty \eta_\nu(z)d\nu \quad (2.5)$$

The coefficients κ_ν are derived from the continuous (*bound-free*) and discrete (*bound-bound*) atomic transitions². They are linked to the atomic cross-sections σ_ν by the relation:

$$\kappa_\nu = \sigma_\nu N \quad (2.6)$$

with N the number of absorbing particles per cm^{-3} , i.e. particle number density. The latter values are established by all (or *dominant*) processes of absorption and emission, which redistribute the atoms among different energy levels and ionization states. The number density of atoms at a certain excitation state N_i is called a *level population*. This term will be frequently used in the current work.

Determination of κ_ν , and η_ν requires accurate description of all opacity sources in the atmosphere. For the atmosphere modeling, one takes into account continuous and line opacity (a so-called line blanketing) due to different atoms and molecules. The sources of continuous and line opacity are standard in most of atmospheric models and will be described in Sect. 3.3.

Usually, the number of absorption lines exceeds millions. Hence, one needs an efficient method to treat them in the modeling. There are methods of opacity distribution functions (ODF) and opacity sampling (OS). In the ODF method, the spectrum is splitted into frequency intervals. For each interval, absorption coefficients are regrouped and their distribution as a function of frequency is tabulated for a range of temperatures, pressures, and abundances. As a result, we have an ODF table that is used in calculations. In the OS method, line blanketing is treated using the opacities chosen at randomly selected frequencies.

²Sometimes in the text, we will use the abridgement *b-b* for the bound-bound transitions, and *b-f* for the bound-free transitions

2.1.2 How to determine the number densities of absorbing atoms.

Solution I: The LTE assumption

For the purposes of model atmosphere calculations, one often uses *the assumption of local thermodynamic equilibrium (LTE)*. Here, ions, atoms and electrons are assumed to be in equilibrium with each other, and the influence of the radiation field on the level populations is negligible. This equilibrium is established by collisions between particles. Hence, distributions of particles over velocity, degrees of excitation and ionization are fixed by a local kinetic temperature T_e only. The local rate of energy generation η_ν depends only on the local thermodynamic properties of the gas. Still, the radiative energy distribution is physically allowed to depart from the local values, but it is not allowed to influence the energy distributions of matter. A non-local nature of radiation field is a result of *scattering processes*, namely photons moving through the gas are not absorbed by particles but only change their direction and often also experience a small shift in frequency. Due to scattering, the mean free path of a photon in the matter increases, so a photon can even escape from a star.

The main idea of LTE is to neglect the processes of scattering, or to assume them to be so weak that they do not take part in the establishing the excitation-ionization equilibrium of the elements. This is mathematically expressed with the following equations:

- Maxwell distribution of particles among velocities:

$$\frac{N(v)}{N} dv = \left(\frac{m}{2\pi kT} \right)^{\frac{1}{2}} e^{-\frac{1}{2}mv^2/kT} dv \quad (2.7)$$

with $N(v)$ the number density of atoms with velocities in the range $[v, v + dv]$, N the total number density of atoms, m the mass of a particle, k the Boltzmann's constant.

- Boltzmann distribution of particles among excitation energies E_i :

$$\frac{N_i}{N} = \frac{g_i}{U} e^{-\frac{E_i}{kT}} \quad \text{with} \quad U = \sum_k g_k e^{-\frac{E_k}{kT}} \quad (2.8)$$

The statistical weight g_i of the level i is defined as the number of degenerate sub-levels k of a level i . U is the partition function, which ensures that the populations N_i of all levels add up to the total population N of the species concerned.

- Saha distribution of particles among ionization states c :

$$\frac{N_{c+1}}{N_c} N_e = \frac{2\pi m_e kT}{h^3} \frac{2U_{c+1}}{U_c} e^{-\frac{E_{ion,c}}{kT}} \quad (2.9)$$

with N_e the number density of free electrons, m_e mass of the electron, h the Planck's constant. $E_{ion,c}$ is the ionization potential, or the minimum energy needed to remove an electron from the ground state of a lower stage of ionization c .

- The source function:

$$S_\nu \equiv \frac{2h\nu^3}{c^2} \frac{1}{e^{h\nu/kT} - 1} = B_\nu \quad (2.10)$$

There is just one value of temperature T , which enters the equations 2.7, 2.8, 2.9, 2.10 used to calculate the atomic number densities. This is a local kinetic temperature of the gas T_e at a particular depth point. It is the essence of LTE approach and simultaneously its weakest chain. Despite numerous analytical methods used by many authors to prove the validity of LTE, it is only an extreme case, which rarely applies in stellar atmospheres.

Solution II: Introduction to NLTE

To account for scattering in the processes of radiative transfer and, correspondingly, establishment of excitation-ionization equilibrium of an element, the concepts of NLTE, *non-local thermodynamic equilibrium* were introduced. First, the Saha - Boltzmann equations are replaced by statistical equilibrium equations. For example, an equation for a level i can be written like:

$$N_i \sum_{j \neq i} P_{ij} = \sum_{j \neq i} N_j P_{ji} \quad \text{for } i = 1, \dots, NL \quad (2.11)$$

Here, $P_{ij} = C_{ij} + R_{ij}$ is the total of collisional and radiative rates (per particle) which establish the equilibrium number of ions excited to the level i . A subscript ij means that a transition from the level i to the level j occurs. This equation must be written for each level i of every ion c in every volume of a stellar photosphere, and it describes the microscopic interaction between atoms, electrons and photons.

To close the system of statistical equilibrium equations, the equation of number conservation can be used:

$$\sum_{i,c} N_{i,c} = \frac{\alpha_{\text{el}}}{\alpha_{\text{H}}} \left(\sum_i N_{i,\text{H}} + n_p \right) \quad (2.12)$$

where $\alpha_{\text{el}}/\alpha_{\text{H}}$ is a fraction of all atoms and ions of a certain element relative to that of hydrogen.

For collisional rates, a number of theoretical formulae exists and they will be discussed later in Sect. 3.4.3. We note that these rates depend only on the local value of electron temperature and density, and transitions from a lower to an upper level are related to the inverse transitions from the upper to the lower level by the Saha-Boltzmann factor $\exp(-E_i/kT)$. The rates of transitions due to inelastic collisions are calculated according to:

$$C_{ij} = N_e \int_{v_0}^{\infty} \sigma_{ij}(v) v f(v) dv \quad (2.13)$$

where $\sigma_{ij}(v)$ is the electron collision cross-section, $f(v)$ is the Maxwellian velocity distribution, v_0 is the threshold velocity with $mv_0^2/2 = h\nu_0$.

Radiation field enters the equations 2.11 through the radiative rates R_{ij} :

$$R_{ij} = \int_0^{\infty} \frac{4\pi}{h\nu} \sigma_{ij}(\nu) J_\nu d\nu \quad R_{ji} = \int_0^{\infty} \frac{4\pi}{h\nu} \sigma_{ij}(\nu) \left(\frac{2h\nu^3}{c^2} + J_\nu \right) d\nu \quad (2.14)$$

where $\sigma_{ij}(\nu)$ is the cross-section of a transition from i to j , or *monochromatic* line extinction coefficient per particle in a state i (next section). The mean intensities J_ν at all frequencies relevant to the transition $i \rightarrow j$ are derived from the radiative transport equation 2.1, which can be rewritten in terms of the optical depth:

$$d\tau_\nu(z) = -\kappa_\nu dz \quad (2.15)$$

$$\mu \frac{dI_\nu(\tau_\nu, \mu)}{d\tau_\nu} = I_\nu(\tau_\nu, \mu) - S_\nu(\tau_\nu) \quad (2.16)$$

For true absorption and emission processes, the source function is defined by the Planck function. In NLTE, the part of local energy emission is due to scattering processes. So the source function also depends on the radiation field, which is at some frequencies non-local. As a result, we have a coupled system of statistical equilibrium (2.11) and radiative transfer (2.16) equations that must be solved simultaneously to get the distribution of elements among excitation states and ionization stages.

2.1.3 Line formation

A spectral line is not infinitely narrow. Different processes like natural, pressure and Doppler broadening give the line its specific bell-curved shape *profile* seen in a spectrum. In addition to the intrinsic broadening of the local line extinction coefficient there are broadening mechanisms, which act on the emergent intensity (or flux) profile. These are stellar rotation, and macroturbulence. Finally, the instrumental broadening is due to the finite resolution of a spectrograph.

Natural line broadening results from the Heisenberg uncertainty principle applied to the energy of the level and its lifetime. Pressure broadening is due to elastic collisions with nearby particles. The emission probability distribution around the line center ν_0 is described by a Lorentz profile with the damping constant γ :

$$\psi(\nu - \nu_0) = \frac{\gamma/4\pi^2}{(\nu - \nu_0)^2 + (\gamma/4\pi)^2} \quad (2.17)$$

with γ_R for natural damping and γ_n for pressure broadening. For interactions with different particles, n takes different values: $n = 3$ for resonance broadening (between hydrogen atoms), $n = 4$ for the quadratic Stark effect (with charged particles), and $n = 6$ for van der Waals broadening (with neutral hydrogen atoms). The general expression for the damping constant is:

$$\gamma_n = N \int_{-\infty}^{\infty} v f(v) \sigma_n(v) dv \quad (2.18)$$

where N and $f(v)$ are the number density and velocity distribution of perturbing particles, σ_n is the broadening cross-section.

Doppler broadening arises because we see only the integrated radiation from atoms moving with different velocities along the *line-of-sight*. It is described by a Gaussian profile:

$$\psi(\nu - \nu_0) = \frac{1}{\Delta\nu_D \sqrt{\pi}} e^{-(\nu - \nu_0)/\Delta\nu_D]^2} \quad (2.19)$$

The Doppler width is due to the thermal and non-thermal (microturbulence) motions of atoms:

$$\Delta\nu_D \equiv \frac{\nu_0}{c} \sqrt{\frac{2kT}{m} + \xi_t^2} \quad (2.20)$$

with m the mass of the atom under consideration. The parameter ξ_t is the microturbulence velocity defined as random motions on scales *smaller* than the photon mean free path.

The momentary smearing of the excited atomic levels and motion of atoms results in slight alteration of the frequency of the scattered photon. If the altered frequency is correlated with the original frequency of the photon, one has to introduce redistribution functions, which describe the probability of scattering photons from one frequency to another. In *coherent scattering*, the scattered photon does not change frequency but only the direction. This applies for Thomson (on free electrons) and Rayleigh (on atoms and molecules) scattering in the continuum.

For line formation calculations, the assumption of *complete redistribution* is often adopted, where any process of de-excitation is thought to be independent of the preceding excitation process. The reason is that elastic collisions are very frequent at the depths of line formation and lead to random reshuffling of excited electrons over the substates of the upper level before de-excitation occurs. So the emission make take place anywhere in the line profile with a probability given by the absorption profile. The total emission ψ and absorption ϕ probability distributions are equal:

$$\psi(\nu - \nu_0) = \phi(\nu - \nu_0) = \frac{H(a, \nu)}{\sqrt{\pi} \Delta\nu_D} \quad \text{with} \quad a = \frac{\gamma_R + \gamma_3 + \gamma_4 + \gamma_6}{4\pi \Delta\nu_D} \quad \nu = \frac{\nu - \nu_0}{\Delta\nu_D} \quad (2.21)$$

The Voigt function $H(a, \nu)$ is a convolution of profiles due to different broadening processes. The line source function is then frequency-independent inside a line and is expressed as:

$$S_\nu^l = \frac{2h\nu^3}{c^2} \frac{1}{\frac{N_i g_j}{N_j g_i} - 1} \quad (2.22)$$

The monochromatic line extinction coefficient *per unit volume* under assumption of complete redistribution is:

$$\kappa_\nu^l = N_i \sigma_\nu^l \left[1 - \frac{N_j g_i}{N_i g_j} \right] \quad \text{with} \quad \sigma_\nu^l = \frac{h\nu}{4\pi} B_{ij} \psi(\nu - \nu_0) \quad (2.23)$$

Here we again assume that i is the lower and j the upper level of a transition. Then, N_i is the number density of absorbing atoms at the lower state i , σ_ν^l is the monochromatic line extinction coefficient per particle in a state i , and B_{ij} is the Einstein coefficient for radiative excitation. Integrating σ_ν^l over all frequencies along the line profile, we get an expression for the *oscillator strength* f_{ij} :

$$\sigma^l = \frac{h\nu_0}{4\pi} B_{ij} = \frac{\pi e^2}{m_e c} f_{ij} = 0.02654 f_{ij} \quad (2.24)$$

The oscillator strength is obtained from laboratory measurements or calculations. It is usually combined with the statistical weight for a lower level of a transition g_i . The $\log gf$ value is then defined as a *transition probability*.

With the source function specified in the equations 2.10 (LTE) or 2.22 (NLTE) and the optical depth scale from 2.15, the resulting emergent intensity at the stellar surface is derived from:

$$I_\nu(\tau_\nu = 0, \mu) = \int_0^\infty S_\nu(\tau_\nu) e^{-\tau_\nu/\mu} d\tau_\nu/\mu \quad (2.25)$$

The integrand in this equation determines how much radiation comes from each depth, a so-called *contribution function*. We will use this notion in the analysis of spectral line formation.

In analogy to the microturbulence defined above, random motions in the atmosphere on *large* scales relative to the photon mean free path are represented by macroturbulence. One usually separates turbulent motions along a stellar radius and tangential to the surface, adopting a so-called radial-tangential model where each component is assumed to occupy a certain fraction of the surface A . Then, the emergent intensity profile I_ν^0 from the equation 2.25 is convolved with the sum of Gaussian velocity distributions for both components ξ_R and ξ_T :

$$I_\nu = I_\nu^0 \star \left[\frac{A_R}{\xi_R \cos \theta \sqrt{\pi}} e^{-\Delta\lambda/\xi_R \cos \theta} + \frac{A_T}{\xi_T \sin \theta \sqrt{\pi}} e^{-\Delta\lambda/\xi_T \sin \theta} \right] \quad (2.26)$$

Micro- and macro-turbulence are only needed in 1D modeling. They were originally introduced to account for the deficiencies in plane-parallel models due to inhomogeneities and dynamical effects. Later, observations of the Sun and results of hydrodynamical modeling gave more information about the velocity fields. In fact, the studies confirmed the existence of random motions on scales associated with micro- and macro-turbulence (Nordlund & Stein 1995). Thus, it is no wonder that both parameters are successful in describing the observed spectral line characteristics, except that they produce symmetric line profiles. Yet, sometimes microturbulence masks the true problems linked to NLTE or pressure broadening.

The instrumental broadening is treated like macroturbulence, by a Gaussian with the full width at half maximum $c/2\sqrt{\ln 2} R_{\text{sp}}$. Here, $R_{\text{sp}} = \lambda/\delta\lambda$ is the resolution of a spectrograph.

2.1.4 Hyperfine structure

Lines of Mn and Co show pronounced hyperfine structure (HFS). That means, a single line is in reality a tiny multiplet represented by several closely-located weak lines. This phenomenon arises because the atoms have odd number of protons in the nucleus, and thus non-zero nuclear spins (5/2 and 7/2 for Mn and Co, respectively). Associated with the latter nuclear magnetic moments interact with magnetic fields produced by outer electrons leading to the splitting of atomic energy levels. Also, there is a small contribution due to electrostatic interaction between electric quadrupole moments of the nucleus and electrons.

The mathematical description of this phenomenon was given by Casimir (1963), so that the energy of the level characterized by a quantum number F is calculated as:

$$E_F = E_J + A \frac{C}{2} + B \frac{3C(C+1) - 4J(J+1)I(I+1)}{8J(2J-1)I(2I-1)}$$

$$C = F(F+1) - J(J+1) - I(I+1)$$

$$A = -\mu \frac{\langle \alpha I J F | H(0) | \alpha I J F \rangle}{\mathbf{I} \cdot \mathbf{J}}$$

$$B = eQ_I \langle \alpha I J F | V_{zz}(0) | \alpha I J F \rangle$$

Here μ_I and Q_I are the magnetic dipole and electric quadrupole moments of the nucleus. E_J is the energy of a fine structure level, $\langle H(0) \rangle$ is the magnetic field due to the electrons at the position of nucleus, I is the nuclear spin, J is the total electronic angular momentum, F is the total angular momentum of the atom in every HFS level $J+I$, $\langle V_{zz}(0) \rangle$ is the electric field gradient at the nucleus. A and B are the constants describing magnetic dipole and electric quadrupole interaction of electrons with the nucleus. The latter values usually come from laboratory measurements. The frequencies of the HFS components depend on the interaction constants for *both levels* involved in a transition.

The width of HFS patterns in Mn and Co overwhelms any other source of broadening. Fig. 2.1 shows a Mn I line in the solar spectrum broadened by hyperfine structure. The width of a line is 40 mÅ compared to the 28 mÅ of a single Doppler broadened line.

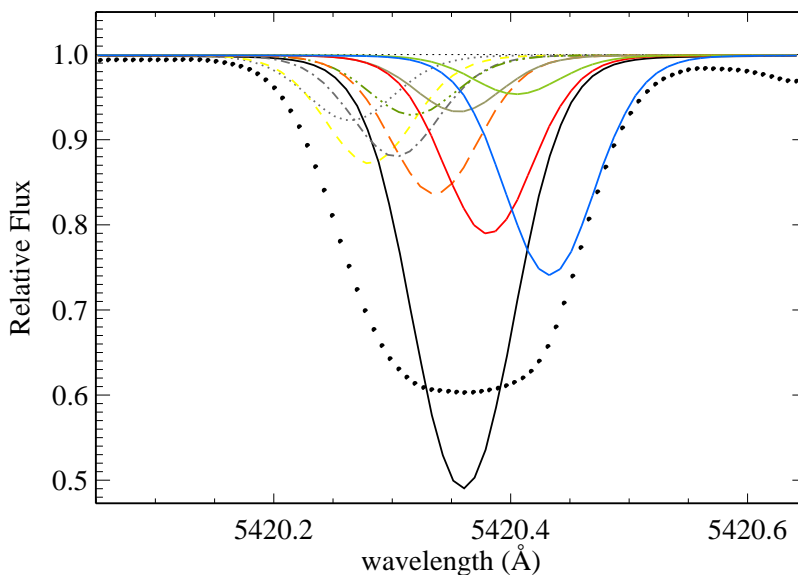


Figure 2.1: The Mn I line in the solar spectrum broadened by hyperfine structure. The profile computed under LTE assumption without HFS is shown with a solid black line. Profiles of 9 HFS components are shown in different colors. The observed spectrum from Kurucz et al. (1984) is marked with black dots.

The effect that HFS has on line profiles is very important. Neglect of hyperfine structure results in wavelength shifts, incorrectly determined damping parameters, and erroneous abundances. Although we may assume that the total absorption caused by weak lines is almost unaffected by HFS, this is not true for strong and saturated lines. In the latter case, HFS effectively de-saturates a line in a spectrum. Physically, the weak HFS components of a line are formed deeper in the photosphere (in the layers with higher temperature) compared with the same line, composed only of a single component. Hence, there is decreased absorption over the entire line profile. This has direct consequences on the abundances.

2.2 Physics translated to computer language

2.2.1 Calculation of level populations

To study NLTE line formation for a particular element, we need a method to solve the radiative transfer equation together with the statistical equilibrium equation. The most common and powerful is the method of lambda-iterations, where the procedure to derive J_ν from S_ν is defined as $\hat{\Lambda}_\tau$ operator. It can be visualized as follows. The equations of statistical equilibrium 2.11 are written in matrix form:

$$\hat{A}\hat{N} = \hat{B} \quad (2.27)$$

Assume that on the 1-st iteration step the level populations $N_1^{(0)} \dots N_{NK}^{(0)}$ are known (e.g. LTE). The superscript (0) in the quantities N , S , and J denotes the current iteration number, which can take n values. So the source function can be determined from:

$$S_\nu^{(0)} = \frac{2h\nu^3}{c^2} \frac{1}{\frac{N_i g_j}{N_j g_i} - 1} \quad (2.28)$$

With the source function one can obtain the formal solution of radiative transfer equation:

$$J_\nu^{(0)}(\tau_\nu) = \frac{1}{2} \int_0^\infty S_\nu^{(0)}(t_\nu) E_1(|\tau_\nu - t_\nu|) dt_\nu \quad (2.29)$$

Knowledge of the radiation field allows us to determine the radiative elements in the matrix of rates \hat{A} . So, we can solve the equations of statistical equilibrium 2.27 to derive the $N_1^{(1)} \dots N_{NK}^{(1)}$ level populations. The iterations can be repeated until the convergence is achieved. The *exact* lambda operator in this method is introduced as:

$$\hat{\Lambda}_\tau[f(t)] = \frac{1}{2} \int_0^\infty f(t) E_1(|t - \tau|) dt \quad (2.30)$$

So that the equation 2.29 can be written as:

$$J_\nu^{(n)} = \hat{\Lambda}_\nu[S_\nu^{(n)}] \quad (2.31)$$

The general scheme of the lambda-iteration is:

$$S_\nu^{(n+1)} - S_\nu^{(n)} = S_\nu^{FS} - S_\nu^{(n)} \quad (2.32)$$

Under *FS* we designate the formal solution, namely the "intermediate" source function obtained from the exact $\hat{\Lambda}_\nu$ operation on the known source function. The standard lambda iteration thus consists of three steps:

$$J_\nu^{(n)} = \hat{\Lambda}_\nu[S_\nu^{(n)}] \rightarrow N^{(n)} = f_1(J_\nu^{(n)}) \rightarrow S_\nu^{(n+1)} = f_2(N^{(n)}) \quad (2.33)$$

However, the usual lambda iteration performed with the exact operator has the property of slow convergence at large optical depth (Mihalas 1978). The successive corrections to the source function may become very small long before the correct solution is achieved.

A more efficient method to solve the statistical equilibrium and radiative transfer equations is the ALI method (accelerated lambda iteration). The basis of ALI method (see summary in Hubeny 2003) is to solve the radiative transfer equation approximately with a simplified operator. The exact operator is written as $\hat{\Lambda}_\nu = \hat{\Lambda}_\nu^* + (\hat{\Lambda}_\nu - \hat{\Lambda}_\nu^*)$, where $\hat{\Lambda}_\nu^*[S_\nu]$ is the *approximate* operator. The formula 2.31 used to perform the first step in the equation 2.33 is expanded to:

$$J_\nu^{(n)} = \hat{\Lambda}_\nu^*[S_\nu^{(n)}] + (\hat{\Lambda}_\nu - \hat{\Lambda}_\nu^*)[S_\nu^{(n-1)}] \quad (2.34)$$

where $S^{(n-1)}$ is the source function from the previous iteration. So the approximate operator acts on the new estimate of the source function, whereas the difference between the exact and approximate operator, $\hat{\Lambda}_\nu - \hat{\Lambda}_\nu^*$, operates on the previous known source function. The latter can be found from the formal solution. Then the new estimate is found from inverting the $\hat{\Lambda}_\nu^*$ only. This inverted approximate operator acts as an accelerating factor that ensures fast convergence.

Equation 2.34 must be solved for all frequencies ν that are related to the transitions in the atom under consideration and for all depth points τ_d in the model atmosphere. However, because the lambda-operator is integrated over all depths, the mean intensity for a certain depth point requires knowledge of source functions at all other depths. One could take into account the depth-dependency for both exact and approximate operators, but it is too costly in the computational sense. The solution is to choose the special form of the approximate operator $\hat{\Lambda}_\nu^*$, so that it is local for the first term in the right-handside of the equation 2.34. In this case, only the source function at one depth point τ_d is considered. This term can be written as $\hat{\Lambda}_\nu^*[S_{\tau_d}^{(n)}]$, whereas the dependency on other depth points $\tau_{d'}$ is taken into account only in the second term of the equation 2.34. This is called the diagonal operator, because the matrix Λ^* contains terms corresponding to the specified depth point d diagonally. Otherwise, one can take into account the interdependence of $S_\nu^{(n)}$ between several depth points, e.g. $d-1, d, d+1$ (a so-called tridiagonal operator). Then, instead of a fully local $\hat{\Lambda}_\nu^*[S_{\tau_d}^{(n)}]$ in the equation 2.34, one can use:

$$J_{\tau_d}^{(n)} = \hat{\Lambda}_{\tau_d, \tau_{d-1}}^*[S_{\tau_{d-1}}^{(n)}] + \hat{\Lambda}_{\tau_d, \tau_d}^*[S_{\tau_d}^{(n)}] + \hat{\Lambda}_{\tau_d, \tau_{d+1}}^*[S_{\tau_{d+1}}^{(n)}] + \Delta J_{\tau_d}^{(n-1)} \quad (2.35)$$

The solution in the form of 2.34 or 2.35 can be used in all equations where the mean intensity enters.

There is another method to solve the NLTE problem, complete linearization, where the radiative transfer and statistical equilibrium are solved simultaneously. However, the system is coupled over all depths (through radiative transfer) and all frequencies (statistical equilibrium). So the system is huge and only small atomic models can be considered at present. Complete linearization still can be used for numerical testing, because the method is very efficient and stable, and it can deal with very complicated multilevel cases on line formation problems.

Finally, we note that the *radiative transfer* in lines is calculated with a *fixed* atmospheric model, a so-called restricted NLTE problem. In this case, the equations of hydrostatic equilibrium (equation 2.3) and radiative equilibrium (equation 2.5) are excluded from the general solution, because pressure and $T(\tau)$ distribution are given in the model. Only the equations that specify the line formation are solved. This is only possible for elements, which have a negligible effect on the atmospheric structure. The elements that fit into this category are called *trace* elements. Both, Mn and Co make a negligible contribution to atmospheric opacity for the solar-type stars, hence they can be studied with restricted NLTE problem.

2.2.2 Calculation of spectral lines

”This technique stresses the computational strength of the analysis, and is basically a trial-and-error method in which the abundances, often the f -values and line-broadening parameters, and usually Doppler broadening are arbitrarily adjusted until the the shape of the observed spectrum is reproduced.” Gray (1992)

All methods to derive an element abundance are based on the analysis of lines in the observed stellar spectrum. That is why the derived abundances, although being model-dependent parameters, are often called “observed abundances”. The most accurate method is the *spectrum synthesis*, which is used in the present work. Below we describe the general procedure of spectrum synthesis, not going into details of numerical solution. Lets assume that we want to derive the abundance of a certain element and this element is represented by a number of lines in a stellar spectrum.

1. For a star we determine the fundamental parameters: T_{eff} , $\log g$, metallicity.
2. With these parameters the atmospheric model is calculated (e.g. using the algorithm described in section 2.1.1).

3. In the model, one has to specify a priori the abundances of different elements, which produce lines in a spectrum. Usually, a solar element distribution is taken as a starting estimate because for a majority of stars the *relative* abundances of different elements are similar to the Sun.
4. The observed spectrum is analyzed and the lines of the element suitable for abundance calculations are selected. The selection criteria is usually negligible blending and sufficient line strength.
5. Now, we calculate the number density of atoms for an element under investigation, which are excited to the lower level i of a transition, producing any of its lines. Either LTE level populations N_i^{LTE} are used, or NLTE populations N_i^{NLTE} derived from the solution of statistical equilibrium and radiative transfer equations. Hereafter, we will use the term *departure coefficient* for a level i defined as $b_i = N_i^{\text{NLTE}}/N_i^{\text{LTE}}$.
6. The selected spectral line is represented by a number of wavelength points λ_k^3 over the line profile (profile is discretised). This number is determined by the line broadening mechanisms. For each λ_k we calculate the volume line absorption coefficient κ_λ^l in analogy to the equation 2.23 but using the departure coefficients b_i :

$$\kappa_\lambda^l = \frac{\pi e^2}{m_e c} \lambda \frac{N_i^{\text{LTE}}}{N_{\text{El}}} N_{\text{H}} \log \varepsilon f_{ij} \frac{H(a, v)}{\Delta \lambda_D} \left(1 - \frac{b_j}{b_i} e^{-hc/\lambda kT} \right) \quad (2.36)$$

The *atmospheric abundance of the element* enters the equation as $\log \varepsilon$ and it is defined as:

$$\log \varepsilon = \log \frac{N_{\text{El}}}{N_{\text{H}}} + 12 \quad (2.37)$$

with N_{El} the total number density of atoms of the element under study and N_{H} the number density of hydrogen atoms. At this point, it is important to include the hyperfine broadening of the line (see section 2.1.4). The HFS components are calculated like blending lines. If I_F is the relative intensity of the component F with the wavelength λ_{0F} , the total absorption coefficient is:

$$\kappa_\lambda^l = \sigma^l N_l \sum_{F=1}^{NK} I_F \psi(\lambda - \lambda_{0F}) \left(1 - \frac{b_j}{b_i} e^{-hc/\lambda kT} \right) \quad (2.38)$$

The profile function $\psi(\lambda - \lambda_{0F})$ for each HFS component is the same as for a single line.

In the continuum, it is sufficient to calculate κ_λ^c only for a central wavelength λ_0 . The κ_λ^l due to blending lines of the other elements must be properly calculated and co-added. Calculating a line profile, one has to specify a value of the microturbulent velocity, which enters equation 2.36 under $\Delta \lambda_D$ (as long as 1D radiative transfer is calculated).

7. With $\kappa_\lambda = \kappa_\lambda^l + \kappa_\lambda^c$, the monochromatic optical depth is calculated from the equation 2.15.
8. The optical depth scale is then used in the equation 2.25 to derive the specific intensities $I_\lambda^l(\mu)$, or in the equation:

$$F_\lambda(0) = 2\pi \int_0^\infty S_\nu(\tau_\lambda) E_2(\tau_\lambda) d\tau_\lambda \quad (2.39)$$

to calculate the line fluxes F_λ^l for every wavelength point. The parameter E_2 is the second exponential integral. The instrumental broadening must be taken into account.

9. The same procedure (steps 7-8) is repeated for the line center continuum flux with F_λ^c calculated at λ_0 setting $\kappa_\lambda^l = 0$.
10. The derived fluxes are then visually compared with the observed fluxes. In case of discrepancies, the element abundance $\log \varepsilon$ is varied.

³Wavelengths λ of spectral lines in the visible region are traditionally expressed in Ångström

Chapter 3

Methods developed for Mn and Co

3.1 Stars and observations

The observed spectrum for the Sun is taken from the Kitt Peak Solar Atlas (Kurucz et al. 1984), which is based on observations of fluxes in the spectral region from 2 960 to 13 000 Å. The resolution is $R_{\text{sp}} = 522\,000$ in the red and infra-red spectral regions and 348 000 in the UV. The signal-to-noise ratio is $S/N = 2\,000 - 9\,000$.

The stellar sample consists of seventeen objects which were observed with the ESO UVES echelle spectrograph at the VLT UT2 on the Paranal, Chile, in 2001, and with the FOCES echelle spectrograph mounted at the 2.2m telescope of the CAHA observatory on Calar Alto, during 1999 and 2000. For four stars (HD 61421, HD 84937, HD 140283, and BD-4°3208) spectra obtained with both telescopes were available. The UVES spectra have a slit-determined resolution of $\lambda/\Delta\lambda \sim 50\,000$ and a signal-to-noise ratio better than $S/N \sim 300$ near 5 000 Å. The data cover a spectral range from 3 300 to 6 700 Å, with a beam-splitter gap between 4470 and 4620 Å.

For the other stars either only UVES spectra (HD 29907, HD 34328, HD 102200, HD 122196) or FOCES spectra (HD 19445, HD 25329, HD 103095, HD 200580, HD 134169, HD 148816, HD 184448) were available. The latter have a resolution of $\sim 60\,000$ but an S/N of only ~ 200 near 5 000 Å, with the exception of G20-8, which was observed with a resolution of only $\sim 40\,000$. The UVES observations of Procyon (HD 61421) and HD 84937 were taken from the UVESPOP survey (Bagnulo et al. 2003). All stars on our list were observed at least twice.

3.2 Stellar parameters

To calculate the statistical equilibrium of the elements, and to perform line synthesis, a set of parameters for each star (T_{eff} , $\log g$, metallicity, microturbulence) is required. For the analysis, we have adopted the data derived by Fuhrmann (2004), Gehren et al. (2004, 2006), and Mashonkina et al. (2008) using the methods described below.

The effective temperatures are determined from fitting under the LTE conditions of the observed H_{α} and H_{β} profiles. In table 3.2, the adopted T_{eff} are compared with data from the Alonso et al. (1996, 1999) determined by the method of Infrared Fluxes (IRFM). For all stars, the temperatures derived from Balmer lines are in agreement with the IRFM temperatures within the combined uncertainty of the two sets of values. The offset is ~ 40 K with RMS error 95 K. Generally, Balmer lines are considered to be ideal candidates for T_{eff} determination for stars with $T_{\text{eff}} < 8000$ K, as they are almost insensitive to stellar gravity and metallicity. However, fitting line

Table 3.1: *Stellar parameters and their estimated errors for the selected sample. Temperature and surface gravity errors are estimated, whereas π/σ_π represents the inverse fractional parallax error. In the last column, the sources of adopted stellar parameters are given.*

Object	HIP	T_{eff} [K]	$\log g$	ξ_t [km/s]	[Fe/H]	[Mg/Fe]	π/σ_π	Population	Ref. ^a
HD 19445	14594	5985 ± 80	4.39 ± 0.05	1.5	−1.96	0.38	22.7	Halo	1
HD 25329	18915	4800 ± 80	4.66 ± 0.08	0.6	−1.84	0.42	50.1	Thick Disk?	4
HD 29907	21609	5573 ± 100	4.59 ± 0.09	0.9	−1.60	0.43	17.3	Halo?	2
HD 34328	24316	5955 ± 70	4.47 ± 0.07	1.3	−1.66	0.42	14.4	Halo	2
HD 61421	37279	6510 ± 100	3.96 ± 0.05	1.8	−0.03	0.0	324.9	Thin Disk	5
HD 84937	48152	6346 ± 100	4.00 ± 0.08	1.8	−2.16	0.32	11.7	Halo	1
HD 102200	57360	6120 ± 90	4.17 ± 0.09	1.4	−1.28	0.34	10.5	Halo	2
HD 103095	57939	5110 ± 100	4.69 ± 0.10	1.0	−1.35	0.26	140.0	Halo	1
BD−4°3208	59109	6310 ± 60	3.98 ± 0.21	1.5	−2.23	0.34	3.7	Halo	2
HD 122196	68464	5957 ± 80	3.84 ± 0.11	1.7	−1.78	0.24	7.4	Halo	2
HD 122563	68594	4600 ± 120	1.50 ± 0.20	1.9	−2.51	0.45	5.2	Halo	3
HD 134169	74079	5930 ± 200	3.98 ± 0.1	1.8	−0.86	0.53	15.1	Thick disk	1
HD 148816	80837	5880 ± 200	4.07 ± 0.07	1.2	−0.78	0.36	27	Thick disk	2
HD 184448	96077	5765 ± 200	4.16 ± 0.07	1.2	−0.43	0.47	30.4	Thick disk	2
HD 140283	76976	5773 ± 60	3.66 ± 0.05	1.5	−2.38	0.43	18.0	Halo	2
G20-8	86443	6115 ± 80	4.20 ± 0.20	1.5	−2.19	0.4	5.1	Halo	1
HD 200580	103987	5940 ± 80	3.96 ± 0.06	1.4	−0.82	0.46	13.8	Thick Disk	2

^aReferences: (1) Gehren et al. (2006); (2) Gehren et al. (2004); (3) Mashonkina et al. (2008); (4) Fuhrmann (2004); (5) Korn et al. (2003)

profiles is a model-dependent method, and the uncertainties in the theory of model atmospheres (plane-parallel stratification, stationarity, convection), continuum placement, and line formation are reflected in the accuracy of T_{eff} . The shortcomings of model atmospheres will be discussed in section 3.3. Here, we will only mention some aspects of line formation calculations for hydrogen.

First of all, it remains to explore the validity of LTE in H I line formation for cool late-type stars. Our own preliminary studies for the Sun indicate that NLTE effects are small in the Balmer line wings but affect only the line cores (Khristorova 2005, Mashonkina et al. 2008). We find that the difference $T_{\text{eff}}^{\text{NLTE}} - T_{\text{eff}}^{\text{LTE}}$ is small for the selected solar-type stars, and is within the limits of errors (~ 80 K). Barklem (2007a) analyzed statistical equilibrium of hydrogen, concentrating on the influence of inelastic collisions with protons. The authors concluded that the NLTE effects in Balmer line wings, if present, are of the order of few percent. This would increase effective temperatures by ~ 100 K. Other authors (Barklem et al. 2002, Cowley & Castelli 2002, Przybilla & Butler 2004) report a satisfactory fitting of solar Balmer profiles with LTE.

Collisional broadening plays an important role in the formation of Balmer line wings, and in fact different theories, Ali & Griem (1965) and Barklem et al. (2000), lead to different results. In the theory of Ali & Griem the broadening by H I atoms is represented only by the resonance broadening, and it does not depend on the temperature. The Barklem et al. theory also includes van der Waals broadening. The difference in Balmer line profiles calculated with both theories is described in Barklem et al. (2000) in details. In brief, the Barklem et al. theory leads to stronger H_α wings and, thus, to lower effective temperatures. The difference can be as large as 150 – 250 K. However, for the solar H_α line we derive 5780 K with the Ali & Griem theory and 5720 K with Barklem et al. theory (Mashonkina et al. 2008). The former is in agreement with the actual value of $T_{\text{eff}} = 5777 \pm 10$ K, derived from the solar radius and the total flux. The best fitting of the solar H_β line with $T_{\text{eff}} = 5780$ K is also obtained using the Ali & Griem theory, whereas, the Barklem et al. theory does not reproduce the temperature of the Sun. As we perform the differential analysis of stars (see next section), it is necessary to adopt the same *type of models*

Table 3.2: *Stellar effective temperatures determined from Balmer lines and comparison with Alonso et al. (1996, 1999) IRFM data.*

Object	T_{eff}	
	Balmer lines	IRFM
HD 19445	5985 ± 80	6050 ± 109
HD 25329	4800 ± 80	4842 ± 97
HD 84937	6346 ± 100	6330 ± 83
HD 103095	5110 ± 100	5029 ± 65
HD 122563	4600 ± 120	4572 ± 61
HD 134169	5930 ± 100	5870 ± 84
HD 140283	5773 ± 60	5691 ± 69

for all program stars including the Sun. Hence, the stellar effective temperatures derived using the Ali & Griem (1965) theory are given a preference. For HD 122563, the effective temperature was derived with Barklem et al. (2000) theory and under NLTE assumption because it leads to consistent temperatures for H_α and H_β (Mashonkina et al. 2008). A relatively large error assigned to this T_{eff} actually reflects the difference between both broadening theories. In fact, HD 122563 is included in our stellar sample only for the purposes of a comparative analysis: a majority of Mn and Co abundance studies in the literature refer to giants.

The surface gravity for the program stars was calculated according to the formula:

$$[g] = [M] + 4[T_{\text{eff}}] + 0.4(\log \pi + m_{\text{vis}} + BC + 0.28) \quad (3.1)$$

The square brackets denote the logarithmic ratio of a parameter with respect to the Sun, m_{vis} is the apparent visual magnitude, M is the mass of a star. Parallaxes π were measured by *Hipparchos* (ESA 1997), and bolometric corrections BC from Alonso et al. (1995). Masses are determined from the tracks of Vandenberg et al. (2000) by interpolating in the $M_{\text{bol}} - T_{\text{eff}}$ diagram. The errors of surface gravities propagate as $\Delta[g] = \Delta[M] + 2\Delta[\pi] + 4\Delta[T_{\text{eff}}]$ with some minor additional error from interstellar extinction and bolometric correction. Since the individual errors in mass, parallax and effective temperature are largely independent, the errors of $\log g$ for turnoff stars are almost entirely due to the parallax errors, whereas errors in mass determination or temperature are usually at least a factor of 2 smaller. Two exceptions to this rule are the cool main sequence stars HD 29907 and HD 103095, for which the mass determination is most uncertain. The accuracy of parallaxes is $\sigma(\pi)/\pi < 0.2$ that translates to the uncertainties $\Delta \log g \sim 0.1$ dex (see Table 3.1). The worst parallax in our sample is that of the most distant star BD-4°3208 with $\sigma_\pi/\pi = 0.27$; this makes that particular surface gravity uncertain by more than ± 0.2 dex. Another method to determine surface gravity is to fit the Mg Ib lines, whose strong damping wings are excellent indicators of collision efficiency. Fuhrmann (2000) compared the surface gravities based on HIPPARCHOS parallaxes with those based on Mg Ib lines for ~ 100 stars. He found the discrepancy of only 0.02 ± 0.04 dex between two data sets that is the evidence of the high accuracy of both methods.

The iron abundances and microturbulent velocities were obtained from Fe II line profile fitting in LTE. This relies on the assumption that Fe II lines are free from NLTE effects. We will return to this issue in section 3.3. At the moment, we only note that calculations of 1D radiative transfer for iron in the Sun and metal-poor stars (Korn et al. 2003, Gehren, Butler, Mashonkina, Reetz & Shi 2001) confirm the nearly LTE populations of Fe II levels. Whereas, 3D calculations give evidence of significant NLTE effects in Fe II (Shchukina & Trujillo Bueno 2001, Collet et al. 2005). The idea of the method is to fix the microturbulence and find the Fe abundance with the minimum scatter between different lines of different strengths. Then the procedure is repeated for different values of ξ_t . The uncertainties in $[\text{Fe}/\text{H}]$ and ξ_t are 0.05 dex and 0.2 km/s, respectively.

Finally, the overall abundance of α -elements must be specified to calculate a model atmosphere. It is important for subgiant stars and stars on the tip of the giant branch because in cool atmospheres light elements with low ionization potential contribute significantly to the free electron pool. It is well-known that old metal-poor stars, which are formed in the period of SN II dominance in Galactic nucleosynthesis, have the excess of elements produced in α -process (Mg, Si, O) relative to Fe. Fuhrmann (1998) and Gehren et al. (2004, 2006) investigated abundances of Mg, Na, and Al in metal-poor stars and particularly for Mg found systematic enhancements of $\sim 0.2 - 0.4$ dex relative to Fe. Other authors also report that α -element overabundances can be as large as $0.4 - 0.5$ dex. Hence, for the thick disk and halo stars the abundances of α -elements are enhanced by 0.4 dex. The only exception is the giant HD 122563 for which the exact NLTE abundance ratio $[\text{Mg}/\text{Fe}] = [\alpha/\text{Fe}] = 0.45$ dex (Mashonkina et al. 2008) is adopted.

The population membership for each star is taken from analyses of Fuhrmann (2004) and Gehren et al. (2004, 2006). This parameter does not enter the calculations, but it is important for the interpretation of stellar abundances, which we undertake in Sect. 7. The population identification is based on stellar kinematic properties, ages, and abundance ratios $[\text{Al}/\text{Mg}]$. Stellar ages are derived interpolating according to the $[\text{Fe}/\text{H}]$ and $[\alpha/\text{Fe}]$ from evolutionary tracks calculated by Vandenberg et al. (2000). With the exception of Procyon, our sample contains only thick disk and halo stars. A few of the stars are not easy to interpret. HD 25329 is nitrogen-rich, and HD 29907 is a single-lined binary. Both have an $[\text{Al}/\text{Mg}]$ ratio that is typical for the thick disk rather than for the halo, but both have $[\text{Fe}/\text{H}]$ abundances more typical for the Galactic halo. The asymmetrical drift velocity of HD 29907 deviates significantly from the average thick disk velocity distribution, and its $[\text{Eu}/\text{Ba}]$ ratio is also typical for the halo (Mashonkina et al. 2008). The star HD 148816 has a retrograde Galactic orbit but due to its metallicity of -0.78 dex and light metal ratios atypical for halo stars (Gehren et al. 2004) we ascribe it to the thick disk. The last star is rather interesting, because Venn et al. (2004) noted that halo stars with strong retrograde motion ($V_{\text{rot}} < -200$ km/s) have *lower* α -element abundances than typical halo stars.

3.3 Model atmospheres

3.3.1 Reference models

For the NLTE calculations and analysis of the Sun and metal-poor stars, the theoretical models calculated with the MAFAGS code (Fuhrmann et al. 1997) are used. These are classical *static 1D plane-parallel models with line blanketing* using ODF's. The main assumptions used in construction of the models are described in section 2.1.1. They are valid only in the limited range of stellar parameters. LTE is not safe for evolved stars with low surface gravity, e.g. giants. Static atmospheric structure can be assumed as a first approximation only for slowly evolving stars on or near the main sequence. Also, models are calculated with the assumption that chemical composition does not change with depth. This is not true in evolved stars where deep mixing brings the material from the stellar core to the surface. The plane-parallel geometry is justified for stars with atmospheres on scales that are much smaller compared to stellar radius. This compels us to restrict our stellar sample to *turnoff stars*.

The line opacity is represented by all elements up to Ni, and diatomic molecules (e.g. H_2 , CH, CO, TiO, etc). This accounts for nearly 20 million atomic lines. In our reference models, line blanketing is treated with opacity distribution functions from Kurucz (1992). However, in the original ODFs the line opacity due to iron was calculated with the solar abundance $\log \varepsilon_{\text{Fe}, \odot} = 7.67$ dex. This value is too high compared to the meteoritic value of 7.48 ± 0.03 dex (Lodders 2003). Hence, in our model the overall metal abundance is scaled down by $[\text{Fe}/\text{H}] = -0.16$ dex to account for the high value used by Kurucz. The ODFs are correspondingly interpolated for the proper stellar metallicities.

The continuous extinction is represented by the free-free transitions in H I, He^- , H^- , and H_2^- , and by bound-free transitions in neutral metals (C, N, O, Al, Mg, Si, Ca, Fe), H^- , H I, He I, H_2^- and H_2^+ . Also included are the Rayleigh scattering for H, He, and H_2 , and Thomson scattering

on electrons. The solar chemical composition is taken from Holweger (1979); only the abundance of carbon is scaled down by 0.1 dex. For other stars these values are scaled by the stellar iron abundance.

The models also include convection, which is taken into account with the mixing-length theory described by Böhm-Vitense (1958). The mixing length parameter α is set equal to 0.5. This value was chosen by Fuhrmann et al. (1993) to provide simultaneously the best fitting of Balmer line profiles $H_\alpha \dots H_\delta$ in spectra of the Sun with $T_{\text{eff}} = 5780$ K. Barklem et al. (2002) also suggest that the best fit of Balmer line profile can be achieved with $\alpha = 0.5$. We note that the mixing-length approximation is one of the major shortcomings of our 1D models.

The problem of a stellar convection together with macro- and micro-turbulence is solved in 3D inhomogeneous atmospheric models (Asplund 2005). Furthermore, calculations of 3D spectral line formation show that hydrodynamics successfully describes line asymmetries and shifts, which can not be modeled with 1D atmospheres. The important question is to which extent do the results obtained with 1D models differ from those obtained with hydrodynamical models.

Let us consider iron, the only representative of iron-group elements treated with 3D. The 3D NLTE solar Fe abundance is 7.50 dex (Shchukina & Trujillo Bueno 2001). However, the same abundance 7.48...7.51 dex was obtained by Gehren, Korn & Shi (2001) from NLTE line formation calculations with MAFAGS-ODF plane-parallel models. Later, Shchukina et al. (2005) performed an analysis of the subgiant HD 140283 and found that NLTE abundances derived from Fe I lines in 3D and 1D are *equal*, $\log \varepsilon_{\text{Fe},*} = 5.77$ dex. The authors concluded that 1D NLTE analysis of Fe I lines in metal-poor stars can deliver reliable stellar parameters.

The 3D LTE analysis of Fe II lines in HD 140283 spectrum (Shchukina et al. 2005) produced the *same* Fe abundance as 1D analysis. However, large *positive* NLTE abundance corrections of $\sim +0.4$ dex were found for weak Fe II lines in 3D. NLTE effects are due to the pumping of highly-excited Fe II levels by a strong UV radiation field in granules where the temperature gradient is steeper than in the intergranular regions. This effect although less pronounced was demonstrated for 1D models by Cram et al. (1980) and Rutten (1988). Thus, stellar parameters derived from the LTE analysis of Fe II lines may not be reliable. However, it is hard to make conclusions based on one star. We also note that 3D models have not yet been subjected to the most important tests. Whether they can reproduce center-to-limb variation, absolute fluxes, and Balmer lines in the Sun and metal-poor stars is still questionable.

On the other side, Korn et al. (2003) calculated NLTE abundances from Fe I lines in four metal-poor stars, and succeeded to bring them *into agreement* with LTE abundances derived from Fe II lines. The authors used stellar parameters (T_{eff} , $\log g$, $[\text{Fe}/\text{H}]$, and ξ_t) consistent with our data to within 1%. So if Shchukina et al. (2005) claim the accuracy of NLTE 1D results obtained from Fe I lines, the same should be true for our stellar parameters obtained from LTE 1D calculations of Fe II lines.

Finally we note that MAFAGS-ODF models do not include chromospheres that is the case with all other line-blanketed atmospheric models so far. In reality, existence of chromospheres was claimed both for metal-poor subdwarfs (Smith & Churchill 1998) and giants (Dupree et al. 1990). The chromospheres are characterized by a temperature minimum at $\sim 0.75 T_{\text{eff}}$ and a steep rise further outwards to $T > 10\,000$ K (Kelch et al. 1978). Whereas, the outer layers in MAFAGS-ODF atmospheric models have low temperatures $\sim 0.6 T_{\text{eff}}$. This may affect the cores of some strongest low-excitation lines, which are formed in the outer layers.

3.3.2 Solar models

The analysis of element abundances in the solar spectrum is performed with two types of models: the MAFAGS-ODF model described in Sect. 3.3 and the semi-empirical solar model of Holweger & Müller (1974). The model of Holweger & Müller is based on the LTE interpretation of the observed Fe I lines of different strength. The line-center intensities were inverted to the brightness temperature according to $T_b = B_\nu^{-1}[I_\nu]$. The models are shown in Fig. 3.1. Differences in the temperature structure are small, the Holweger & Müller model is $\sim 100 - 150$ K warmer than the ODF model at $\log \tau_{5000} < -0.5$.

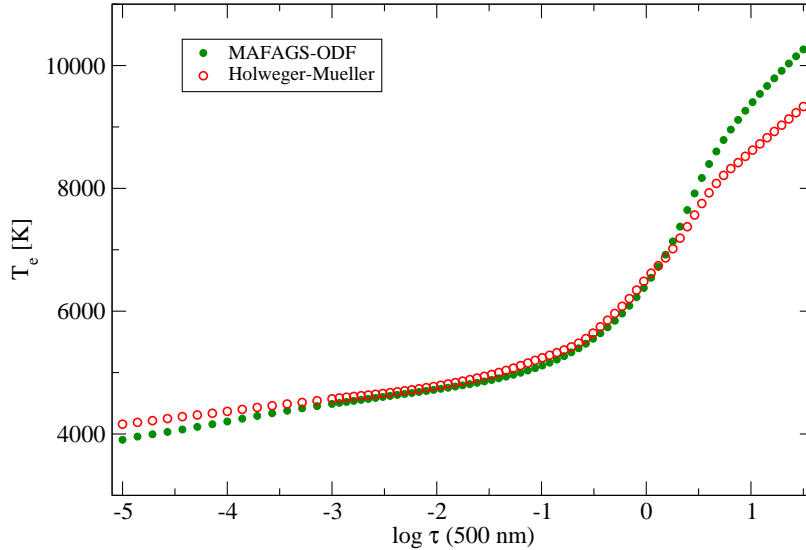


Figure 3.1: *The distribution of temperature with optical depth in the Holweger-Müller semi-empirical atmospheric model and in the theoretical line-blanketed MAFAGS-ODF model.*

The comparison of the MAFAGS-ODF with other theoretical and semi-empirical models can be found in Grupp (2004a). Unfortunately, the MAFAGS-ODF model does not reproduce observed absolute solar fluxes in the region $\sim 2000 - 4000 \text{ \AA}$, where we find few very strong Mn I lines, and all lines of Mn II and Co II. The calculated fluxes are too high (Grupp 2004a). In the more recent MAFAGS model with opacity sampling, the problem of missing UV opacity is solved with the new photoionization cross-sections for Fe I. The temperature and pressure distributions with depth are similar in ODF and OS models, but the latter is systematically warmer by $\sim 15 - 60 \text{ K}$ at $\log \tau_{5000} > -0.2$. Although, this indeed influences some general spectral characteristics, like flux distribution and Balmer line profiles (Grupp 2004b), we find that the effect on the near-UV lines of Mn and Co is minor. Moreover, the MAFAGS-ODF matches the absolute solar flux in the visible and near-IR, where the majority of weak and intermediate-strength lines of Mn and Co are located. Thus, in the atmospheric layers where these lines are formed the model has an approximately correct temperature gradient, and we do not expect significant abundance errors.

A careful reader would note that our reference MAFAGS-ODF models are calculated in LTE, whereas the line formation for Mn and Co will be calculated in NLTE. The results of different studies (Hauschildt et al. 1999, Anderson 1989) confirm that the difference between NLTE and LTE model atmospheres is small for stars with $T_{\text{eff}} < 10000 \text{ K}$. Deviations from LTE are important in the outermost optically-thin layers of the atmosphere. According to Hauschildt et al. (1999), deviations in the temperature structure occur only at $\log \tau_c < -3$, where τ_c refers to the optical depth in the continuum at 1.2μ . This is explained by the importance of collisional processes due to high density of free electrons in the atmospheres of solar-type stars.

3.4 NLTE calculations

The statistical equilibrium calculations are carried out with the code DETAIL, developed by Butler & Giddings (1985). The more recent version of the code is based on the ALI method described in section 2.2.1. Some modifications were implemented in the code that were necessary

for calculations of cross-sections and background opacities.

In the atomic models (see glossary) for Mn and Co, the following processes are taken into account: photon absorption in line transitions, photoionization, excitation and ionization by collisions with free electrons, and neutral hydrogen atoms. All processes include their reverse reactions; in particular, bound-bound radiative transitions (scattering processes) are assumed to follow complete frequency redistribution. It is known that under certain circumstances other interaction processes can also play a role, e.g. autoionization transitions, charge-transfer reactions or di-electronic recombination. No detailed information about these processes is available for manganese and cobalt in the literature, although, in particular, autoionization resonances could well contribute to the depopulation of some atomic levels.

3.4.1 Atomic structure and energy levels

Mn and Co belong to the group of transition elements which have fairly complicated, but interesting atomic structure (Johansson & Cowley 1988). Interesting properties result from the partly filled $3d$ subshell. Binding energies of electrons in the $4s$ subshell, which penetrates into the core of innershell electrons, are similar to those of the shielded $3d$ subshell. For neutrals, Mn I and Co I, the binding energy of $4s$ dominates, thus their ground configurations are $1s^2 2s^2 2p^6 3s^2 3p^6 3d^5 4s^2$ and $1s^2 2s^2 2p^6 3s^2 3p^6 3d^7 4s^2$, respectively. Also, the ground state¹ of Mn II a^7S_3 is occupied by $3d^5 4s$ configuration. However, $4d$ electrons are more bound in Co II leading to the ground configuration $3d^8$.

The term structure of Mn I and Co I is formed by different configurations of electrons. For Mn I, these are $3d^5 nl n'l'$, $3d^6 nl$, and $3d^7$ systems. For Co I, with two more electrons on the unfilled $3d$ subshell, $3d^7 nl n'l'$, $3d^8 nl$, and $3d^9$ electronic configurations determine the pattern of levels. As a result, laboratory studies alone give 364 levels and 2442 transitions for Co I (Pickering & Thorne 1996). The number of calculated levels and transitions in Co is even larger. For Mn, calculations give evidence for more than 500 levels and 2500 transitions (Kurucz & Bell 1995). Definite configurations can be assigned only to low-excited and ground states, thus LS coupling approximation holds for transitions to these levels. Whereas, many intermediate and high-lying levels are mixtures of different configurations. This results in a much larger number of observed transitions than expected from the pure LS coupling (Pickering & Thorne 1996, Blackwell-Whitehead, Xu, Pickering, Nave & Lundberg 2005). They significantly contribute to the radiative connection of levels.

Doubly excited configurations $3d^{(N-1)} 4s nl$ are numerous in both neutral atoms (N is 5 for Mn I and 7 for Co I). Together with singly excited configurations $3d^N nl$, doubly excited configurations create a system of low-lying levels with even and odd parity, which give rise to the majority of radiative transitions to the high excitation levels. All odd levels in Co I and Mn I with excitation energies below 4 and 5 eV, respectively, belong to the doubly excited configuration system. E.g. z^6G° is a representative of the doubly excited system in Co I. Correspondingly, the group of transitions $z^6G^\circ - e^6F$ produces lines of multiplet 158, which we use in the spectrum analysis. Multiplet 16 in Mn I, widely-used in stellar spectroscopy, results from transitions between the z^8P° and e^8S terms, which belong to the doubly excited electronic configuration.

The characteristic feature of Mn I is the presence of highly-excited singly excited and doubly excited levels² with similar energies, but strongly different main quantum numbers n . As we will show in Sect. 3.4.2, this requires a *modification* to the formula used to calculate photoionization cross-sections.

In statistical equilibrium calculations, we take into account doubly excited levels with total excitation energy below the first ionization limit (7.43 eV and 7.86 eV in Mn I and Co I, respectively) and treat them like "normal" singly excited levels. All levels with energies above the first ionization potential are neglected, that is, 180 levels of Mn I. This may not be a good approximation in our atomic models because these levels stipulate autoionization (see glossary) transitions,

¹The level designations are from Moore (1945) (see glossary).

²We use the notation singly excited or doubly excited levels as an abbreviation to levels, which result from either singly or doubly excited configuration system

thus creating strong resonances in photoionization cross-sections. In principle, this could affect excitation-ionization equilibria.

In the complete model, the Mn atom is constructed with 245 levels for Mn I and 213 levels for Mn II, respectively. The system is closed with the ground state of Mn III. The energies for these levels are taken from Sugar & Corliss (1985)³. We include all levels with $n < 15$ for Mn I, $n < 8$ for Mn II, and with energies of 0.03 and 1.11 eV below the respective ionization limits. Such a relatively complete model should provide a very close coupling of the upper atomic levels to the next ion ground state. The number of lines treated in NLTE is 1261 for Mn I and 1548 for Mn II.

The model of the Co atom is significantly larger: the number of levels and transitions is 246 and 6027 for Co I, and 165 and 2539 for Co II. The energy separation of the highest excited level from the continuum is 0.4 eV for Co I and ~ 1 eV for Co II. Energies and transitions used in the atomic model are taken from the online database of Kurucz, which is essentially a compilation from the large analyses of Pickering & Thorne (1996) and Pickering et al. (1998).

Hyperfine splitting of the levels was not included in the SE calculations. There is no reason to expect that the *relative* populations of HFS components deviate from thermal because radiative transitions between them are forbidden and collisions are very strong due to very small energy separations. Moreover, for the uppermost terms above 7 eV in Mn I and 6.3 eV in Co I the fine structure is not maintained. These terms are represented by a single level with a weighted mean of statistical weights and ionization frequencies of their fine structure levels. The transitions between two combined levels are also grouped, and the oscillator strength of a resulting line is the average of $\log gf$'s weighed according to the appropriate lower-level statistical weights. We made sure that none of the lines used in abundance analysis has either of its levels grouped.

Complete Grotrian diagrams for Mn and Co are shown in Fig. 3.3 and Fig. 3.2. In the Mn I atomic model, different multiplet systems from doublet to octet show up. In the case of the doublet system in Mn I, it seems that it can be completely ignored because it contains only a few levels and all of them are highly excited. Also, there are no useful doublet lines in the solar spectrum. This is different with the octet system, which is also only loosely coupled to quartets and sextets. However, a significant fraction of the Mn I atoms is found here, in addition to some interesting solar lines. Neutral cobalt is devoid of octet terms, whereas doublets, quartets, and sextets produce many important lines in the solar spectrum.

3.4.2 Radiative rates

Discrete transitions

For all lines of Mn and Co, wavelengths and oscillator strengths for radiative $b - b$ transitions are taken from Kurucz's database (Kurucz & Bell 1995) and Kurucz online database⁴. The largest part of the data is calculated semiempirically by using scaled Thomas-Fermi-Dirac radial wavefunctions (Stewart & Rotenberg 1965). The data for strong and intermediate-strength transitions in Mn I and Mn II were taken over from the compilation of experimental f -values of Martin et al. (1988). For Co I and Co II, the wavelengths are from Pickering & Thorne (1996) and Pickering et al. (1998). The transition probabilities are calculated or adopted from Fuhr et al. (1988). We note that more experimental results became available in the past 15 years. However, for the purposes of SE calculations most of the lines do not require data that are more precise than the values of Kurucz.

The oscillator strengths f_{ij} for all transitions in Mn I included in the SE calculations are shown in Fig. 3.4 (upper panel). The interesting feature of this plot is the presence of very strong transitions, $f_{ij} > 0.1$, with wavelengths in the UV, visible and near-IR spectral ranges. The strongest transitions occur between the ground state and the levels of the odd term y^6P° with 4.4 eV excitation energy. However, transitions from the z^8P° term with the excitation energy 2.3 eV, although being weaker, are more numerous. They dominate the excitation balance in Mn I.

³as delivered online by the large database of National Institute of Standards and Technology

⁴<http://kurucz.harvard.edu>

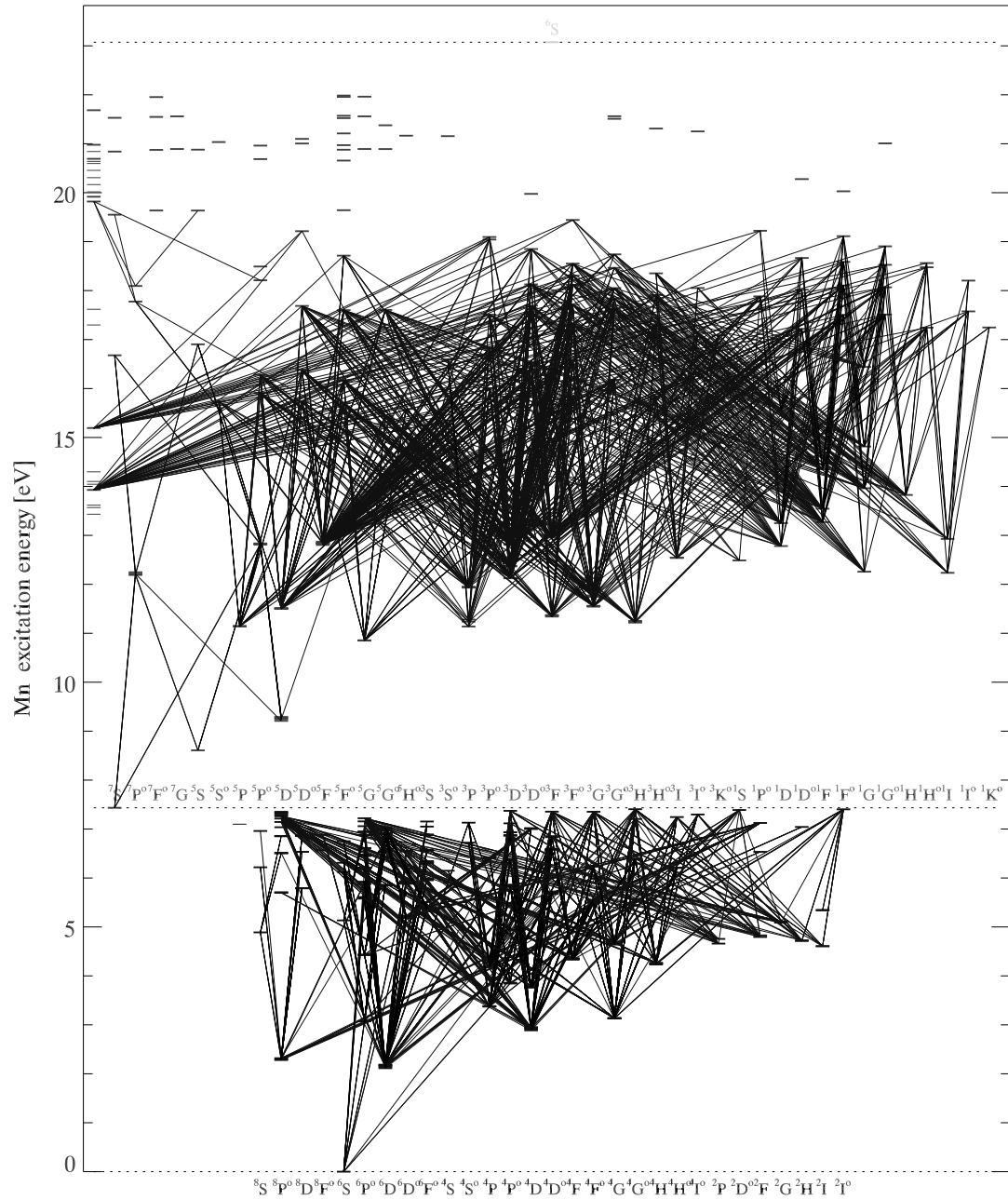


Figure 3.2: Grotrian diagram of the Mn model atom. Solid lines represent all allowed and forbidden transitions included in SE calculations.

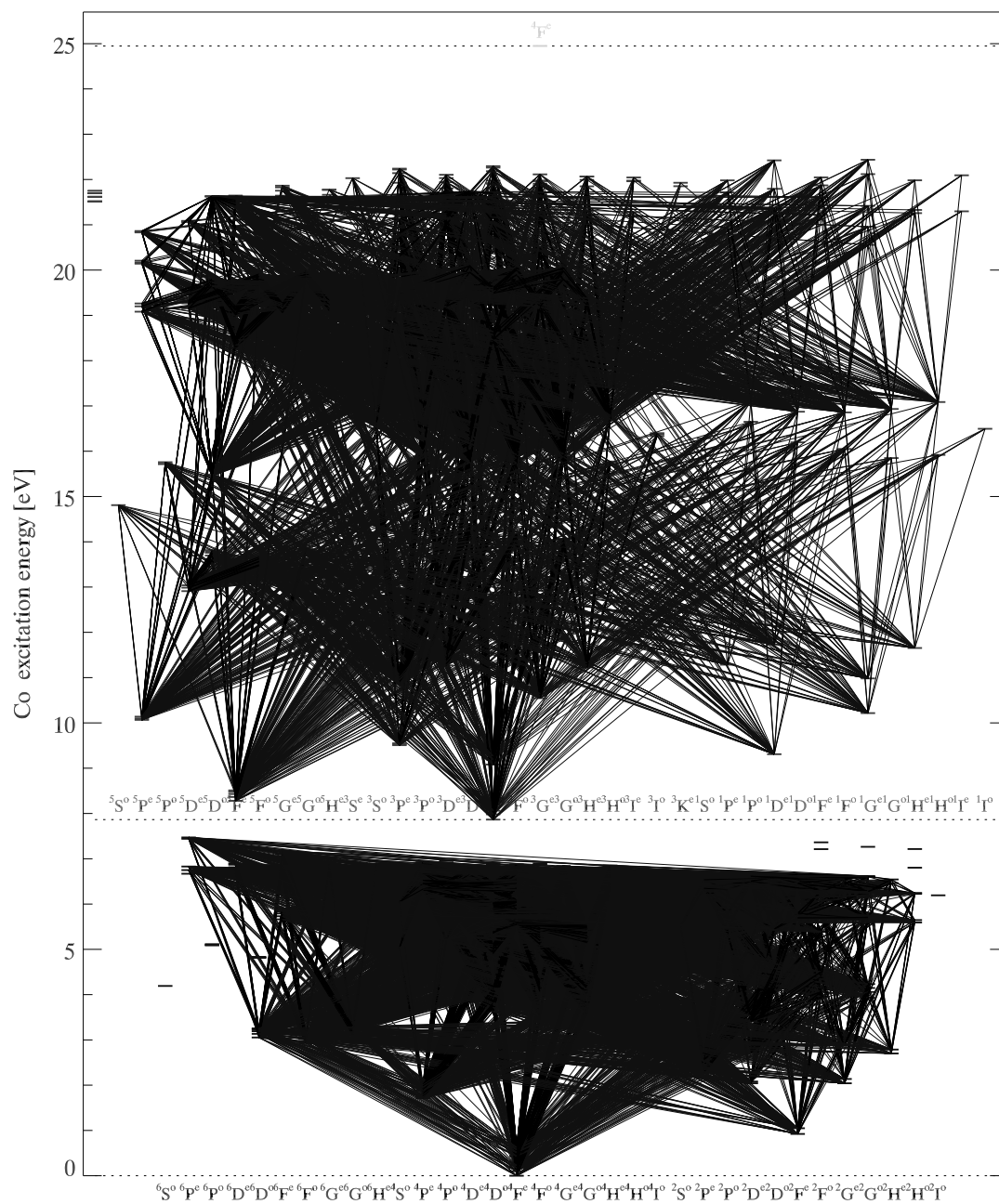


Figure 3.3: Grotrian diagram of the Co model atom. Solid lines represent all allowed and forbidden transitions included in SE calculations.

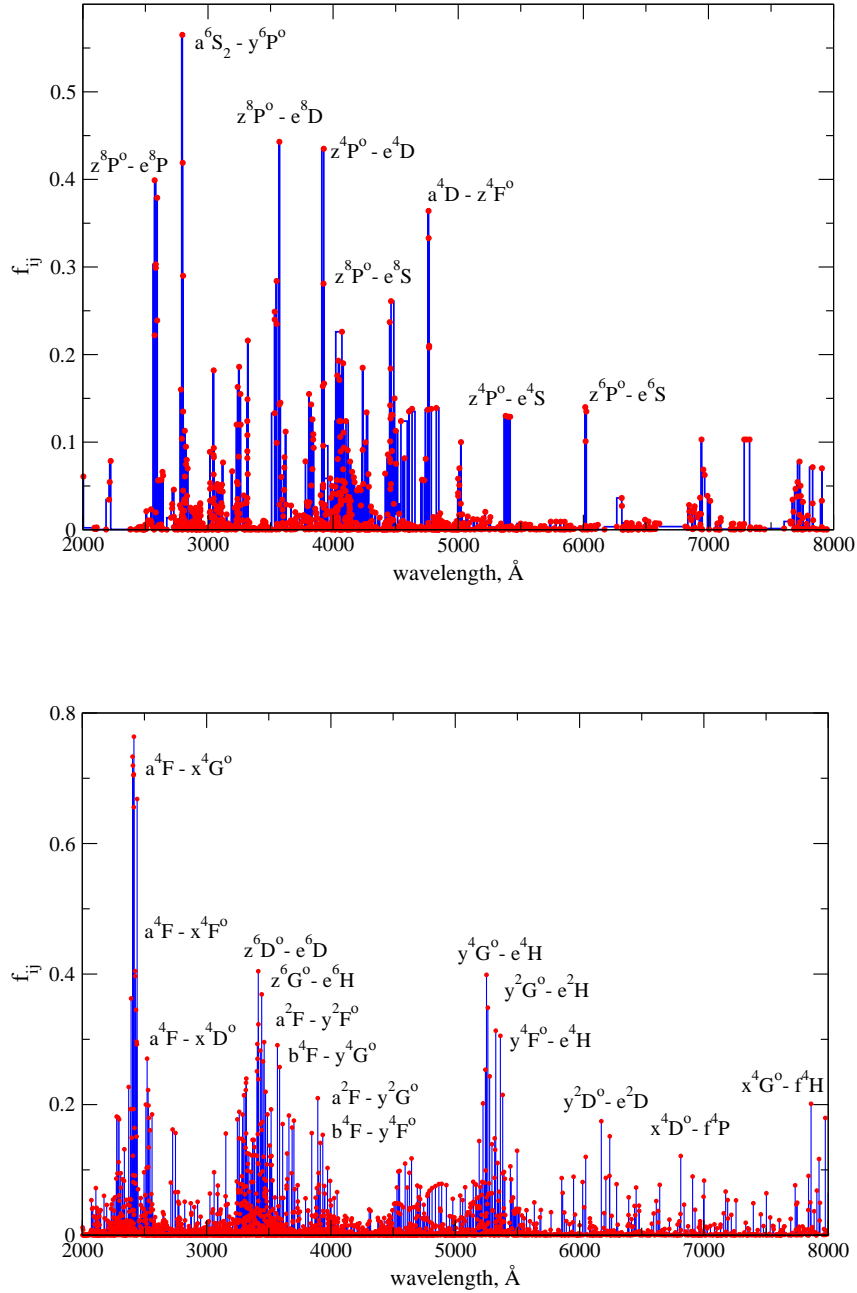


Figure 3.4: The oscillator strengths for transitions in Mn I (upper panel) and Co I (lower panel), which are used in statistical equilibrium calculations. Data are adopted from Kurucz & Bell (1995) and Kurucz online database (<http://kurucz.harvard.edu>).

There are also numerous strong transitions in Co I, which couple the Co I ground state, low metastable levels, and levels of 3 – 6 eV excitation energy (Fig. 3.4). They cover the spectral range from 2000 to 8000 Å. The total number of transitions is by a factor of four larger than that in Mn I. This maintains efficient radiative and collisional coupling between levels of different excitation energies that will be reflected on the distribution of atomic level populations.

Bound-free transitions

Photoionization cross-sections for Mn and Co are computed from Kramer’s formula (Rutten 2003):

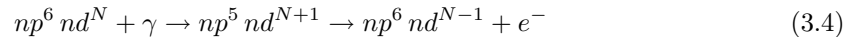
$$\sigma_{\nu}^{\text{bf}} = \frac{2.81510^{29} g_{\text{bf}}}{n^{*5} \nu^3} \quad (3.2)$$

where g_{bf} is the Gaunt factor. The necessary modification to the original Kramer’s formula mentioned in section 3.4.1 is the use of *effective* hydrogen-like main quantum number n^* :

$$n^* = \sqrt{R \frac{Z^2}{E_{\text{ion},i}}} \quad (3.3)$$

where R is the Rydberg constant, Z is the ionization stage (e.g. 1 for a neutral atom), and $E_{\text{ion},i}$ is the ionization energy from the level i . The effective main quantum numbers are introduced due to the presence of doubly excited configurations, which, opposite to those of single excitation, can not be simultaneously calculated with a simple hydrogenic approximation. The problem is that configurations of neighboring excitation energies but different main quantum numbers have strongly differing photoionization cross-sections if calculated with the *original* Kramers formula. Furthermore, the b-f collision cross-sections, calculated using the radiative b-f cross-sections, will differ for these neighboring levels by some orders of magnitude. The latter is important for the high excitation levels whose b-f collision rates compensate radiative b-f rates from the low-excitation levels and in this way establish the statistical equilibrium of the model atom.

In calculations, only bound-free interactions with the *ground state* of ionized species are included. This is also not adequate for atoms with doubly excited electronic configurations, where ionization to higher metastable levels of a next ion may occur. Information about such processes is very meager for Mn, and is not available at all for Co. It is known that there is a huge maximum in photoabsorption spectra of transition elements (West 2001), which is located above the ionization limit of the unfilled nd subshell. This maximum is interpreted (Amusia & Ivanov 1987) as a *giant autoionization resonance* related to the electronic transition from a inner closed np^6 subshell to the free states in nd , and further decay of this new state according to the scheme:



Such resonances have a huge width of 1 – 2 eV, that is a result of electron correlation in np and nd subshells. For Mn I, the $3p \rightarrow 3d$ autoionization resonance has a large effect on the $4s$ photoionization cross-section, thus affecting both Mn I and Mn II ions (Amusia & Ivanov 1987, Amusia et al. 1990). Bruhn et al. (1982) demonstrated that the transition with a largest contribution to the resonance cross-section is from the ground level ${}^6S_{5/2}$ in Mn I to the metastable 5D term of Mn II. It is also known that the $3p \rightarrow 3d$ autoionization resonance enhances the $4s {}^5S$ photoionization cross-section to the second ionization limit much stronger than $4s {}^7S$ cross-section to the first ionization limit (Amusia et al. 1988). These empirical and theoretical evidences indicate that photoionization processes in Mn and Co are very complicated. Thus, in the current analysis, the simple hydrogen-like photoionization cross-sections may be the most *uncertain* representation. One can also conclude this in analogy to the Fe I atom, for which it was found that the calculated photoionization cross-sections of Bautista (1997) are orders of magnitude *larger* than the hydrogenic approximation (Gehren, Butler, Mashonkina, Reetz & Shi 2001).

3.4.3 Collisional rates

Excitation and ionization by collisions with neutral hydrogen atoms

To derive the rates of transitions due to inelastic collisions with H I atoms, we use the Drawin's formula (Drawin 1968, Drawin 1969a, Drawin 1969b) in the version of Steenbock & Holweger (1984). Here, the Maxwell-averaged cross-section for excitation and ionization of particle species a by collisions with neutral hydrogen atoms is:

$$\langle \sigma_{ij} v \rangle = 16\pi a_0^2 \frac{2kT^{1/2}}{\pi\mu} Q \frac{m_a}{m_H} \frac{m_e}{m_H + m_e} \psi(W) \quad (3.5)$$

$$\mu = \frac{m_a m_H}{m_a + m_H} \quad \text{and} \quad \psi(W) = \left(1 + \frac{2}{W}\right) \frac{e^{-W}}{1 + \frac{2m_e}{W(m_H + m_e)}}$$

where m_e , m_H , and m_a are the masses of the electron, hydrogen atom and the atom under investigation.

In case of collisional excitation:

$$Q = \left(\frac{R}{E_j - E_i}\right)^2 f_{ij} \quad \text{and} \quad W = \frac{E_j - E_i}{kT} \quad (3.6)$$

where E_i , E_j denote the excitation energy of the lower i and upper j levels; f_{ij} is an oscillator strength of the corresponding transition from i to j . In the current analysis, only collisional transitions between radiatively coupled levels are included. In case of collisional ionization:

$$Q = \left(\frac{R}{E_{\text{ion},i}}\right)^2 f_i \xi_i \quad \text{and} \quad W = \frac{E_{\text{ion},i}}{kT} \quad (3.7)$$

where f_i is an effective oscillator strength for ionization, $E_{\text{ion},i}$ is the ionization energy of the level i , and ξ_i is the number of equivalent electrons in the outer electronic shell. For the ground states of Mn I and Co I $\xi_i = 2$. For all excited states $\xi_i = 1$ is used. The parameters f_i are calculated using the values given by Drawin (1969b).

There is much controversy about the validity of this formula, more exactly about the validity of its generalization to complex atoms. Originally, it was derived for collisions between equal atoms, such as H, or Ar (Drawin 1969a). Later, it was reformulated by Steenbock and Holweger for collisions between Li and H. Severino et al. (1993) argued that Drawin's cross-sections were *overestimated* by more than one order of magnitude. Their conclusion is based on the comparison of collision rates between the lowest levels of Na I in the solar atmosphere. Not only were the rates of H collisions in Drawin's version stronger than collisions with free electrons, but also they were significantly larger than H collision rates computed with the formula of Kaulakys (1985). This result was not very convincing because Kaulakys investigated highly excited transitions in Rydberg atoms. Subsequent experimental (Fleck et al. 1991) and theoretical (Belyaev & Barklem 2003) investigations gave evidence of the fact that Drawin's cross-sections are overestimated.

In stellar abundance calculations, it became a standard practice to determine the *scaling factor* S_H to the cross-sections calculated with the Drawin's formula empirically, i.e. from the analysis of lines of different excitation energies. Most of the studies confirmed the conclusions of Severino et al. (1993). They are based on the analysis Ba II, Na I, and Mg I in solar-type atmospheres (Mashonkina 1996) and Mg emission lines in the Sun and K giants (Sundqvist et al. 2008). These authors present convincing arguments in favor of very small ($\ll 1$) but non-zero values for S_H . There are no indications in the literature that S_H must be larger than unity, except for the Fe I work of Korn et al. (2003), who suggested $S_H = 3$. Gratton et al. (1999) also required a scaling factor larger than unity to bring Fe abundances from two ionization stages in RR Lyrae stars in agreement. However, for Mg, O, and Na they found $S_H \leq 0.5$.

The standard value of S_H used in the current work is 0.05. In the next chapter, we study the influence of inelastic collisions with H on populations of atomic levels in Mn and Co. However, it should be kept in mind that the *cross-sections are only an order-of-magnitude accuracy*.

Excitation and ionization by collisions with free electrons

The rates of allowed bound-bound transitions due to collisions with e^- are calculated using the formula of van Regemorter (1962):

$$\langle \sigma_{ij} v \rangle = 32 \star 10^{-8} f_{ij} \left(\frac{R}{\Delta E_{ij}} \right)^{\frac{3}{2}} \beta^{\frac{1}{2}} e^{-\beta} P(\beta) \quad (3.8)$$

Here, $\beta = \frac{\Delta E_{ij}}{kT}$, $\Delta E_{ij} = E_j - E_i$, and the function $P(\beta)$ was derived by approximation of theoretical and experimental data.

For cross-sections of collisional ionization, we use the formula of Seaton (Mihalas 1978):

$$\langle \sigma_{ik} v \rangle = 1.55 \star 10^{13} \sigma(\nu_{\text{thr}}) \frac{\bar{g}_i}{\sqrt{T}} \frac{e^{-\beta}}{\beta} \quad (3.9)$$

with ν_{thr} the threshold frequency, $\beta = h\nu_{\text{thr}}/kT$, $\sigma(\nu_{\text{thr}})$ the photoionization cross-section at threshold, \bar{g}_i takes the values 0.1, 0.2, 0.3 for $Z = 1, 2, > 2$, respectively.

The rates of forbidden transitions due to collisions with electrons are computed from the formula of Allen (1973):

$$\sigma_{ij} = \pi a_0^2 \frac{R}{E} \frac{\Omega_{ij}}{g_i} \quad (3.10)$$

Here E is the energy⁵ of a colliding electron, g_i a statistical weight, and Ω_{ij} is the collision strength, which is usually set to unity for neutral atoms.

3.4.4 Comparison of rates

To understand departures from LTE in selected ions, we find it useful to consider the rates of radiative and collisional processes, which produce transitions between various atomic levels. The rates are linked to the cross-sections of transitions: for collisions with free electrons $C_e = N_e \langle v_e \sigma_{ij}(e) \rangle$ and for collisions with neutral hydrogen atoms $C_H = N_H \langle v_H \sigma_{ij}(H) \rangle$. Here, $\langle v \sigma \rangle$ is the Maxwell-averaged cross-section, v_e and v_H are the velocities of free electrons and hydrogen particles, N_e and N_H their number density. The total collisional rates per particle are $C_{ij} = C_e + C_H$.

We emphasize that rates per unit particle R_{ij} and C_{ij} are examined, but not the integrated rates per cm^{-3} as in the next chapter. The former rates are derived directly from the formulas (3.5, 3.8, 3.9, 3.10), whereas the latter are obtained by multiplication with the particle densities, which are affected by *departures from LTE*. The discussion is based on calculations for Mn, the behavior of rates for Co is similar.

Fig. 3.5 (upper left panel) shows the *logarithmic* ratio of *bound-bound* rates due to collisions with H I atoms and free electrons C_H/C_e as calculated for transitions of Mn I with the solar model atmosphere. It is interesting that the collision rates between discrete levels depend on the term parity. Even terms have few times larger rates than odd terms. As expected from the formulas 3.5 and 3.8, the overall strength of collisions grows as energy separation between levels ΔE_{ij} decreases. Rates of collisional excitation by electrons are 0.5 – 1.5 orders of magnitudes *larger* than rates of excitation by H I atoms. The former dominate even at the smallest ΔE_{ij} .

The rates of collisional ionization are demonstrated in Fig. 3.5 (upper right panel). Calculations show that ionization rates due to collisions with H I atoms, C_H , increase much faster with increasing excitation energy E_i of a level when compared with rates of ionization by electrons, C_e . Moreover, C_H everywhere dominates over C_e , exceeding the latter by nearly three orders of magnitude for the uppermost levels. We conclude that collisional ionization in Mn I atom is fully controlled by neutral hydrogen. The role of inelastic collisions with neutral hydrogen is more important in atmospheres of metal-poor stars, where the number density of free electrons is smaller.

⁵ E refers to a reduced energy with respect to the heavy atom

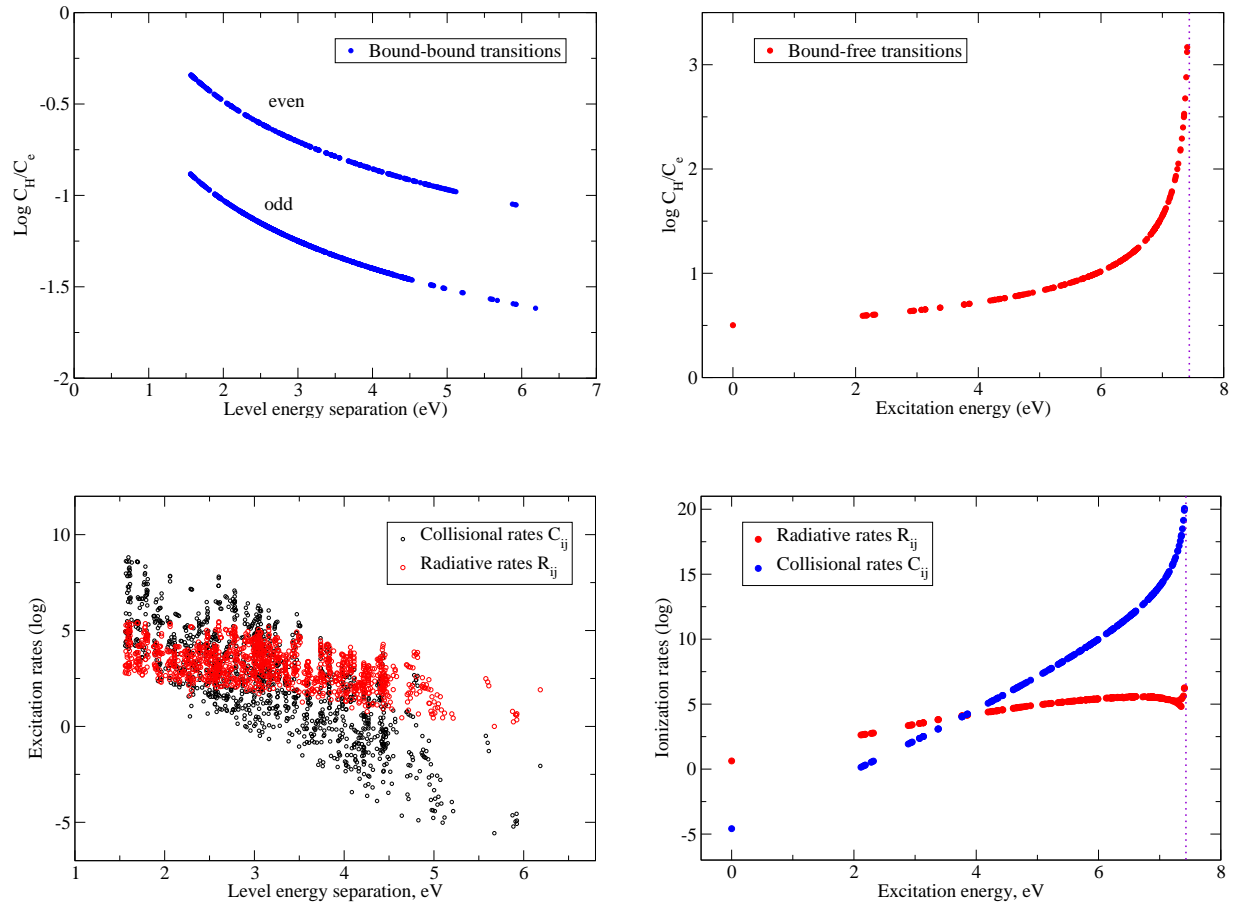


Figure 3.5: Collision rates with H I and e^- for bound-bound (upper left panel) and bound-free (upper right panel) transitions. Radiative and collision rates for bound-bound (lower left panel) and bound-free (lower right panel) transitions. All data are calculated for transitions in Mn I.

Now, we consider the ratio of radiative to collisional rates for discrete and continuous transitions. The lower left panel in Fig. 3.5 shows excitation rates R_{ij} and C_{ij} in logarithmic scale as a function of level energy separation ΔE_{ij} , where $C_{ij} = C_H + C_e$. At small ΔE_{ij} , collisional transitions dominate. This is to be expected because the average kinetic energy of electrons in the solar atmosphere is $\sim kT$. For $\Delta E_{ij} = 2 - 3$ eV, the rates R_{ij} and C_{ij} are comparable. But at $\Delta E_{ij} \sim 3$ eV, radiative rates take over. So especially transitions from low-excited levels, which typically have $\Delta E_{ij} > 3$ eV, are subject to NLTE effects due to the non-local radiation field.

The most interesting are bound-free transitions, which are responsible for ionization balance of an element. The rates of photoionization and collisional ionization from all levels of Mn I to the continuum are demonstrated in Fig. 3.5 (lower right panel). The overall increase of R_{ij} and C_{ij} , where j is now the ground state of Mn II, follows from the formulas 3.2 and 3.5. Rates of radiative b-f transitions grow smoothly and control ionization from levels with $E_i < 4$. For all higher levels, collisional ionization primarily due to H I atoms dominates. At this point, it is not possible to say whether the *ionization equilibrium* of the element is set by collisional or radiative ionization processes. For this, we must analyze the absolute rates, which are affected by NLTE effects (see below).

3.5 Spectrum synthesis and abundance analysis

Spectrum synthesis is carried out with the SIU code (Spectrum Investigation Utility) written by J. Reetz. NLTE line formation for Mn and Co is performed with departure coefficients b_i obtained from statistical equilibrium calculations. All other elements are treated in LTE. Abundances are calculated by fitting the observed line profiles to the computed lines. The analysis of stars is *differential* relative to the Sun, i.e. *any abundance estimate derived from a single line in a spectrum of a metal-poor star is referred to that from the corresponding solar line*. This excludes the use of absolute transition probabilities, but requires the knowledge of the $\log gf\varepsilon$ values for each line under investigation. The differential element abundance in a metal-poor star is given by:

$$[\text{El}/\text{H}] = \log(gf\varepsilon)_* - \log(gf\varepsilon)_\odot \quad (3.11)$$

This approach requires *a maximum similarity in the analysis of lines in the solar and stellar spectra*. Hence, $\log gf\varepsilon$ values for the Sun and metal-poor stars are calculated with the same type of theoretical atmospheric models, MAFAGS-ODF. The advantage of using the same type of model atmospheres is that the errors in abundances due to the model uncertainties are minimized. One of such shortcomings is the simple mixing length theory for convection.

Another requirement is a similar modeling of *microscale* non-thermal velocities in the Sun and stars. From observations of metal-poor stars, only a single depth-independent value of ξ_t can be recovered. So, the constant microturbulence $\xi_t = 0.9 \text{ km s}^{-1}$ is adopted for the Sun, although its anisotropy and depth dependence are now well established (Gray 1988).

In the solar analysis, the flux profiles are additionally broadened by the radial-tangential macro-turbulence velocity $\xi_{\text{RT}} = 2.5 \dots 4 \text{ km s}^{-1}$. Radial and tangential components of the velocity are assumed to be equal, and velocity distribution for each component is Gaussian. ξ_{RT} is allowed to vary with the line strength and depth of formation. The rotation of the Sun with $V_{\text{rot},\odot} = 1.8 \text{ km s}^{-1}$ (Gray 1992) is taken into account.

In spectra of metal-poor stars, all lines of selected elements are weak and spectral resolution is not sufficiently high, so that contribution of different external broadening mechanisms can not be easily separated. Hence, stellar line profiles are convolved only with the Gaussian of $\sim 3 - 6 \text{ km s}^{-1}$. The width of this broadening function was estimated from fitting the observed spectral lines. Rotational broadening and macro-turbulence are treated separately only for Procyon with $V \sin i = 2.6 \text{ km s}^{-1}$ (Fuhrmann 1998).

Broadening mechanisms taken into account in calculations of the line absorption coefficient are radiation damping, quadratic Stark and van der Waals broadening with constants γ_R , γ_4 and γ_6 , respectively. Natural broadening is calculated as $\gamma_R = \sum_{k < i} A_{ik} + \sum_{k < j} A_{jk}$. Einstein

coefficients A_{ik} are calculated from the oscillator strengths of transitions. Broadening constants due to quadratic Stark and van der Waals effects are derived from:

$$\gamma_4 = 39v_e^{1/3}C_4^{2/3}N_e \quad \text{and} \quad \gamma_6 = 17v_H^{3/5}C_6^{2/5}N_H \quad (3.12)$$

here v_e and v_H are the velocities of free electrons and hydrogen particles, N_e and N_H their number densities (Unsöld 1955).

Van der Waals broadening constants are calculated using Anstee & O'Mara (1995) theory which is based on the full interaction potential between an atom and a hydrogen particle, avoiding series expansion in $1/r$. Line broadening cross-sections $\sigma_6(v_0)$ for a relative collision speed $v_0 = 10 \text{ km s}^{-1}$ are tabulated as a function of effective principal quantum numbers for the upper and lower level of a transition. Damping constants are then calculated as:

$$\gamma_6 = N_H \left(\frac{4}{\pi}\right)^{\alpha/2} \Gamma\left(\frac{4-\alpha}{2}\right) \left(\frac{v}{v_0}\right)^{-\alpha} v \sigma_6(v_0) \quad (3.13)$$

with Γ the gamma function, v the relative velocity of an atom and perturber, and α the velocity exponent.

Another formalism to calculate broadening by neutral hydrogen was developed by Unsöld (1968). The author followed the assumption that broadening is dominated by collisions between atoms separated by a large distance r from each other. Thus, the interaction energy was approximated by the first term r^{-6} in the $1/r$ expansion, using the polarizability of a hydrogen particle α and mean square radius $\overline{R_k^2}$ of an excited state k of the atom:

$$C_6 = -\frac{\alpha \overline{R_k^2}}{r^6}$$

Setting $\alpha = 0.663 \times 10^{-24} \text{ cm}^3$ (Unsöld 1955), the interaction constant can be evaluated from:

$$C_6 = 64.4 \times 10^{-35} \frac{n^{*2}}{2} [5n^{*2} + 1] \quad (3.14)$$

with n^* the effective main quantum number (Sect. 3.4.2) of an excited state. We do not intend to present a detailed comparison of two theories, as this was carefully discussed in a number of papers (see e.g. Ryan 1998). The empirical analysis of strong solar lines showed that Unsöld's (1968) theory yields too small damping constants, thus line widths can not be reproduced. The reason for its failure was found in the assumption that *long-range* interactions dominate, whereas the interaction potential has a more complicated form than a simple r^{-6} dependence (Barklem 2007b).

Constants C_6 calculated for transitions in Mn I and Co I with Unsöld's (1968) and Anstee & O'Mara's (1995) theories are presented in Fig. 3.6. Damping for strong transitions in both neutral ions is systematically underestimated and for weak transitions overestimated with the former theory. The data shown in Fig. 3.6 are restricted to transitions with $n^* \leq 3$. Anstee & O'Mara noted that there is some evidence for numerical instability in cross-sections calculated for levels with larger main quantum numbers.

3.5.1 Oscillator strengths

There are several methods to determine f -values in the laboratory. In fact, all measurements nowadays are based on a combination of *level lifetimes* with *branching ratios* for different transitions. Branching ratios, or relative oscillator strengths, are obtained by emission or absorption techniques. In the former case, a source with a known number of atoms is used to produce an emission line spectrum. Otherwise, the continuum background radiation is shone through the source, and the absorption spectrum is analyzed. Absorption techniques make use of furnaces. Emission line sources are arcs and sparks. In the past 20 years, another emission technique, Fourier transform (FT) spectroscopy, has been extensively used to measure atomic data. There

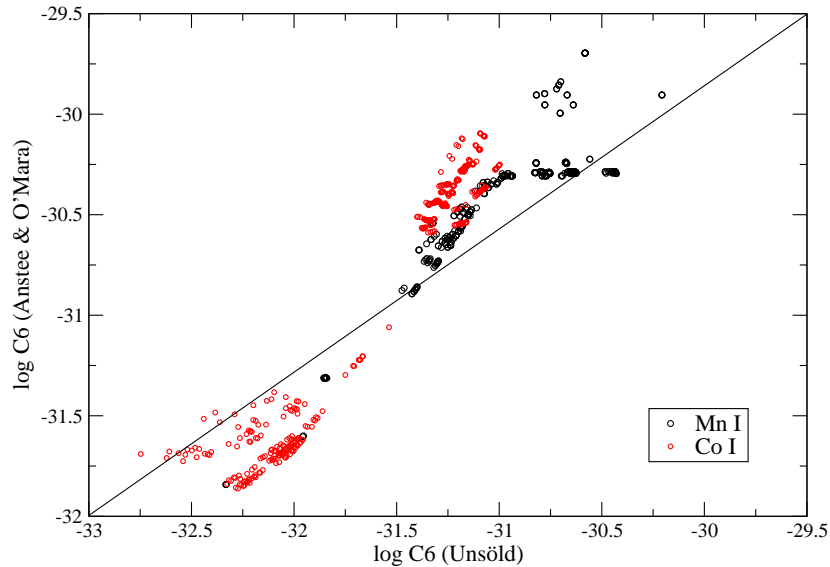


Figure 3.6: Interaction constants C_6 calculated for transitions in Mn I and Co I with Unsöld (1968) and Anstee & O'Mara (1995) theories.

are indeed some advantages of this method over the others, like wide wavelength coverage (UV to IR), accurate wavelengths, resolution of line profiles. All of these methods have deficiencies. In the FT spectroscopy, photon noise limits the accuracy with which weak lines can be measured (Thorne 1998). Boltzmann factors for upper levels of transitions are required in emission spectroscopy. For this, temperature of a source must be known precisely, which is the main problem. Due to non-uniform temperatures, self-absorption in spectral lines arises. Absorption instruments are limited in temperature, thus it is often not possible to measure highly-excited lines.

Moreover, relative oscillator strengths obtained with any of these methods must be finally put on the absolute scale. For this, either experiments with the strongest lines of the source aimed at a derivation of number densities of atoms, or measurements of upper level lifetimes are needed. The standard technique is to send a beam of atoms through a foil, where the atoms get excited, and then observe the beam at different distances to determine how the decay of excited atoms proceeds with time. Otherwise, a laser is used to populate the upper level.

Another option is to calculate transition probabilities. Two basic approaches are widely used: ab initio atomic structure calculations based on the self-consistent field method, and the semi-empirical method (Kurucz 1981), which makes use of available experimental data. Calculations deliver reliable data for simple atoms (H, He), but large deviations occur between theoretical and measured data for many-electron atomic systems where configuration interaction occurs (see e.g. Wiese & Fuhr 1990).

Oscillator strengths for Mn I lines are taken from three different sources (Table A.1 of the appendix). Most of the data are from Blackwell-Whitehead & Bergemann (2007), who measured branching ratios of transitions by FT spectroscopy. These were combined with lifetimes for upper levels from Schnabel et al. (1995), with the exception of the $e^6S_{2.5}$ level which was taken from Marek (1975). The accuracy of $\log gf$ values is 0.02–0.05 dex. Booth, Blackwell, Petford & Shallis (1984) performed absorption experiments with the Oxford furnace to derive relative f -values. The absolute oscillator strengths were calculated using the lifetimes of Becker et al. (1980), and Marek & Richter (1973). The accuracy of 3–7% claimed by the authors was later revised in the NIST⁶ atomic spectra database to be of the order of 10–20% (Martin et al. 1988). Finally, transition probabilities for several lines are from calculations of Kurucz (1988) for which no error estimate was given.

⁶National Institute of Standards and Technology, USA

A large number of f -values with the accuracy of $\sim 50\%$ (Martin et al. 1988) for Mn I and few lines of Mn II were determined by Woodgate (1966) from measurements of emission line intensities. Greenlee & Whaling (1979) used branching ratios from emission spectroscopy and level lifetimes from the beam-foil decay experiment to derive absolute oscillator strengths. Uncertainty in their data is of the order 25%. These data sources are not important for the calculations of the solar Mn abundance, but we use them for comparison with our *reference* set of transition probabilities taken from Blackwell-Whitehead & Bergemann (2007). The analysis of different experimental results is given in the NIST compilation of Martin et al. (1988).

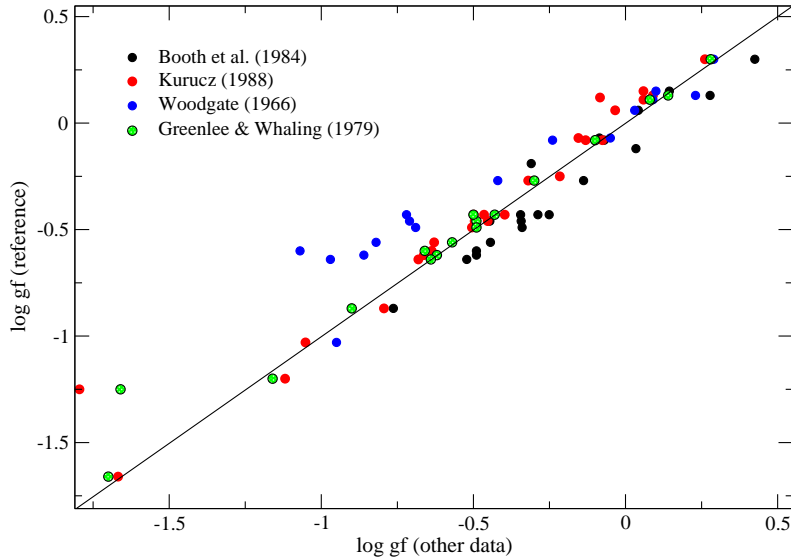


Figure 3.7: Oscillator strengths for Mn I lines from the literature. The reference set of transition probabilities is taken from Blackwell-Whitehead & Bergemann (2007).

A comparison between different datasets for common transitions is presented on the Fig. 3.7. Oscillator strengths published by Greenlee & Whaling show the best agreement with results of Blackwell-Whitehead & Bergemann, although the errors given for the former are nearly 4 times as large as the errors in latter measurements ($\sim 5 - 7\%$). Curiously enough, reliability of Greenlee & Whaling's (1979) data has been claimed independently by Martin et al. (1988). Large discrepancies are seen between the reference dataset and data of Woodgate, particularly $\log gf$ values for weak transitions from the latter source are strongly underestimated. The independent analysis of Woodgate's (1966) values performed by Martin et al. gave evidence for a systematic energy-level dependent error. Fig. 3.7 also suggests that the majority of transition probabilities measured by Booth, Blackwell, Petford & Shallis (1984) are systematically stronger. The average discrepancy is 20 – 30%. Booth, Blackwell, Petford & Shallis indicate that the 6013 and 6021 Å transitions from the $e^6S_{2.5}$ level are *twice* as strong as the measurements of Blackwell-Whitehead & Bergemann. This is an important finding because many analyses of Mn in the Sun and in metal-poor stars are based solely on Booth, Blackwell, Petford & Shallis's (1984) values. A relatively small spread is seen for the theoretical $\log gf$'s from Kurucz (1988).

Transition probabilities for Mn II lines are taken from Kling & Griesmann (2000). Branching ratios were measured with FT spectrometer and combined with lifetimes from laser-induced fluorescence experiment. The uncertainty of absolute oscillator strengths is $\sim 5\%$. In fact, *none* of the Mn II lines strong enough to be discerned in the *solar spectrum* are suitable for reliable abundance calculations. They are located in the near-UV and they are heavily blended, which makes the accurate continuum placement almost impossible. However, blending in the UV decreases in spectra of metal-poor stars, hence we use one line of Mn II to perform abundance calculations and, hence, to check the ionization equilibrium of manganese.

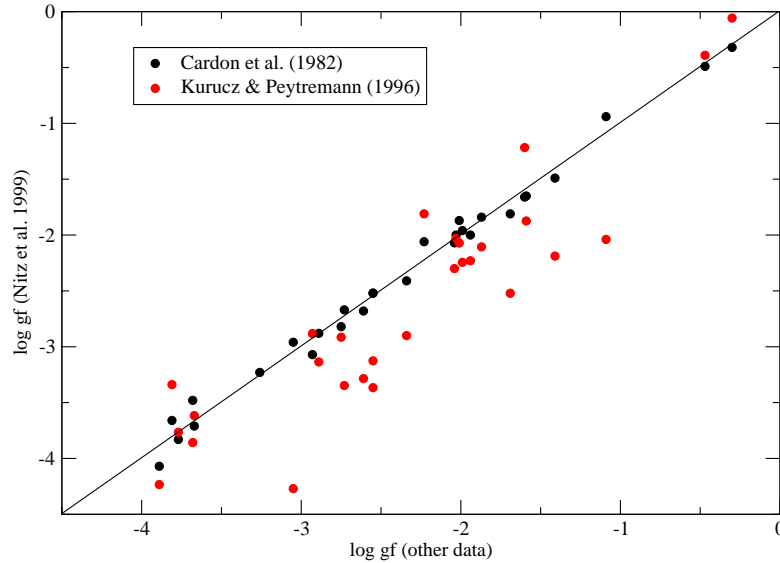


Figure 3.8: *Oscillator strengths for Co I lines from the literature.*

Our sample of Co I lines is small compared to Mn I (see Table A.2). Transition probabilities for the majority of the lines were taken from Cardon et al. (1982). Branching ratios were determined from the analysis of emission line spectra recorded by FT spectrometer at Kitt Peak National Observatory. The relative f -values were converted to absolute oscillator strengths using the lifetimes from laser-induced fluorescence measurements of Marek & Vogt (1977) and Figger et al. (1975). In addition, Cardon et al. employed the absorption hook technique to derive f -values for some transitions. The reported uncertainties of $\log gf$ values are $\sim 15 - 25\%$. Seven lines in our analysis were assigned transition probabilities from Nitz et al. (1999), which we consider the most reliable datasource. These authors used essentially the same technique and instrument as Cardon et al. However, uncertainties of transition probabilities are within $5 - 10\%$ that is by a factor of ~ 2.5 smaller than the uncertainties of Cardon et al. Otherwise, both datasets are consistent; this is seen in Fig. 3.8. For comparison, we also show calculated transition probabilities from Kurucz & Peytremann (1996)⁷. These are very discrepant and are not used in the analysis of the solar Co abundance.

The transition probabilities for Co II were calculated by Raassen et al. (1998) using the method of orthogonal-operators. This is a semi-empirical approach based on the adjustment of model Hamiltonian parameters to yield eigenvalues consistent with the experimental energies. No error estimates were given by the authors. However, Raassen et al. note slight discrepancies with experimental values of Salih et al. (1985) measured with FT spectroscopy. The errors of the latter values are different for weak and strong transitions; the authors estimate the standard error of measured values to be in the range of $10 - 50\%$. Also, Fuhr et al. (1988) estimated uncertainties of Salih et al. (1985) values as $\sim 10\%$ for strong transitions, and greater for weaker ones. We find typical differences of $0.1 - 0.2$ dex between both datasets, which are however not systematic. For the Co II line at 3501 \AA used in the solar abundance analysis, we adopt $\log gf = -1.22$ dex from Raassen et al. (1998). The solar Co abundance calculated with Salih et al. (1985) values will be also given for comparison.

3.5.2 Hyperfine structure

In spectrum calculations, the hyperfine structure of lines is taken into account by superposing individually synthesised HFS components (Sect. 2.2.2). This requires the knowledge of relative

⁷Note that this reference points to the online databank of Kurucz & Peytremann (1975) publication.

intensities and energy separations of the components. For the current work, wavelengths are computed using the laboratory data for magnetic dipole A and electric quadrupole B constants; HFS splittings are taken into account both for lower and upper levels of transitions under investigation. Relative intensities of the components are calculated according to the tables of White & Eliason (1933).

The hyperfine structure of Mn I has been a subject of a large number of experimental investigations, which started exactly 100 years ago with laboratory studies of Janicki (1909). White & Ritschl (1930) carried out a very detailed analysis of HFS patterns of Mn I lines using optical spectroscopy and computed interaction constants for a number of levels in different electron configurations. Luc & Gerstenkorn (1972) conducted experiments with a Fabry-Perot interferometer and a Fourier transform spectrometer to determine splittings of e^6D and y^6P° levels. Interference spectroscopy also formed the basis of Brodzinski et al.'s (1987) investigations. A very accurate measurement of the ground state $a^6S_{5/2}$ was reported by Davis et al. (1971), who used the technique of spin-exchange optical pumping. Dembczyński et al. (1979) and Johann et al. (1981) studied metastable Mn I levels of $3d^6 4s$ configurations with laser-induced resonance fluorescence method. Başar et al. (2003) used optogalvanic laser spectroscopy to measure HFS of 12 yellow and red lines. The technique of level crossing was applied by Handrich et al. (1969) to levels of $3d^5 4s4p$ electronic configurations. A relatively modern technique is the Fourier transform spectroscopy that allows to fully resolve the Doppler broadened line profiles of transitions. The magnetic dipole A and electric quadrupole B constants are computed from fitting the observed profiles. This method was used by Lefèbvre et al. (2003) and Blackwell-Whitehead, Pickering, Pearse & Nave (2005). To calculate splittings of Mn I levels, we use the data from all the above-mentioned literature sources (Table A.3). The errors of A values are typically between 0.05×10^{-3} and $0.5 \times 10^{-3} \text{ cm}^{-1}$. In most cases, B values were not available, but this is not critical because HFS is dominated by magnetic dipole interaction. Levels of Mn II are measured by Holt et al. (1999) with the collinear fast-ion-beam laser spectroscopy. We use their results.

Magnetic dipole and electric quadrupole constants for all Co I levels are taken from Pickering (1996), who analysed HFS patterns recorded with an FT spectrometer. The data are summarized in Table A.4. Recently, Juliet Pickering carried out analogous measurements for the a^5P and z^5D° levels of Co II, and kindly provided us with the data ahead of publication. These HFS constants are also listed in Table A.4.

Chapter 4

Statistical equilibrium of Mn and Co

In this section, the excitation-ionization equilibrium of Mn and Co in the atmospheres of the Sun and metal-poor stars is discussed. For this, we use the notation of the *departure coefficient* b_i for a level i :

$$b_i = N_i^{\text{NLTE}}/N_i^{\text{LTE}}$$

Under LTE, $b_i = 1$ and the level is said to be *thermalized*. Under NLTE, $b_i \neq 1$. If $b_i < 1$, than the level is *underpopulated*; if $b_i > 1$, the level is *overpopulated* relative to its value in local thermodynamic equilibrium.

It is convenient to compare and analyse departure coefficients for different levels as a function of the optical depth $\log \tau_{5000}$ in the continuum at 5000 Å. The relations of the form $\log \tau_{5000} - b_i$ are used throughout this chapter to explain the *processes which stipulate deviations of atomic level populations N_i from their LTE values*. The following mechanisms will be considered. Superthermal radiation field with mean intensity larger than the Planck function, $J_\nu > B_\nu(T_e)$, leads to the *overionization* and to enhanced excitation, the latter process is termed the *photon pumping*. If mean intensity falls below the Planck function, $J_\nu < B_\nu(T_e)$, a shortage of ionizations leads to the *overrecombination* to the upper levels. In the same conditions, the *photon suction* occurs, which implies a successive de-excitation of electrons through high-probability transitions to the lower levels if $J_\nu < B_\nu(T_e)$.

We also investigate how uncertain parameters, photoionization and collisions with neutral hydrogen, influence the results of NLTE calculations. Finally, we define the *reference* model atom, which will be used in calculations of metal-poor stars.

4.1 NLTE effects on Mn levels

Departure coefficients b_i for selected Mn I and Mn II levels calculated for the model atmosphere with solar parameters ($T_{\text{eff}} = 5780$ K, $\log g = 4.44$, $[\text{Fe}/\text{H}] = 0$, $\xi_t = 0.9$ km s⁻¹) are shown in Fig. 4.1. Each term is represented by one level because of the close coupling among the fine-structure levels. We are interested in those levels, which are *dominant* in establishing the statistical equilibrium of Mn, and in the levels that produce the lines used in the abundance analysis. Therefore, we have only entered a few levels which are typical for their depth dependence. As an example, the relative population of the ground state $a^6\text{S}_{5/2}$ is very similar to that of the low-lying metastable terms, $a^6\text{D}$, $a^4\text{D}$, and $a^4\text{G}$. Hence, the latter three terms are not shown in Fig. 4.1. The lowest odd levels of the terms $z^8\text{P}^\circ$ and $z^6\text{P}^\circ$ are also very similar. Another prominent group is represented by levels of intermediate energies 4 – 6 eV, e.g. $z^6\text{D}^\circ$ and $e^6\text{S}$, which neither couple to the ground state, nor to other lower or higher levels outside $\log \tau_{5000} \sim -1$.

Their behaviour is determined by non-equilibrium excitation processes. Finally, there is a number of highly-excited levels, which have thermal or even super-thermal populations. It is sufficient to consider only these three groups with low, intermediate, and high excitation energies to understand departures from LTE in manganese.

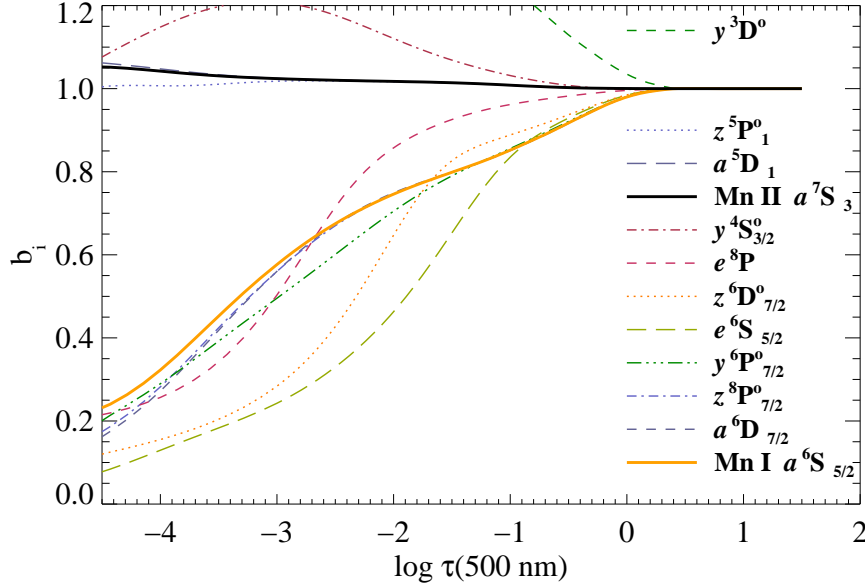


Figure 4.1: Departure coefficients b_i of selected Mn I and Mn II levels for the complete model atom with a total of 459 levels as a function of optical depth. The curves are labeled on the right. Hydrogen collision rates are scaled by $S_H = 0.05$. Photoionization cross-sections are calculated with the hydrogenic approximation. The ground state $a^6S_{5/2}$ is representative of most of the low metastable levels such as a^6D , a^4D , and a^4G all over the optical depth scale. The odd levels z^8P^0 and z^6P^0 are also very similar.

In the deepest layers, $b_i = 1$ for all levels. Deviations from LTE develop between $\log \tau_{5000} \approx 0.1 \dots 1$. At these depths, the atmosphere becomes *optically thin* (or *transparent*) for radiation with wavelengths below ionization thresholds of some low-lying levels, such as a^4D ($\lambda < 2729 \text{ \AA}$), z^6P^0 ($\lambda < 2844 \text{ \AA}$), y^6P^0 ($\lambda < 2884 \text{ \AA}$), and a^4H ($\lambda < 3876 \text{ \AA}$). The detailed balance is broken because processes of photoionization determined by the radiation temperature start dominating over recombinations, which depend on the local electronic temperature. Depopulation of the levels is followed by a depopulation of the Mn I ground state $a^6S_{5/2}$. The latter is depleted via optically thick transitions at $\sim 2800 \text{ \AA}$ ($a^6S_{5/2} - y^6P^0$) because collisions are not sufficiently strong to overcome the gap of 2 eV between the $a^6S_{5/2}$ and the first excited level. As a result, all low-lying levels are in *relative balance* out to $\log \tau_{5000} \approx -1.5$. Photoionization from the ground state is important only in the upper layers due to the low flux at $\lambda < 1620 \text{ \AA}$.

Radiation in strong lines significantly contributes to the redistribution in the atomic level populations. Here, two effects are important. The *photon pumping* powered by a superthermal radiation field with mean intensity $J_\nu > B_\nu(T_e)$ (Fig. 4.2, upper panel) increases the photoexcitation rates, which are not compensated by the inverse rates of de-excitation. This process takes action when the *optical depth drops below unity* in the wings of low- and intermediate-excitation lines, but their cores are still optically thick. Hence, at this depth, populations of the upper levels for the pumping transitions are amplified relative to their lower levels. As soon as the medium becomes optically thin at wavelengths of line cores, spontaneous transitions depopulate the upper levels and their departure coefficients display a sudden drop. The spectrum of Mn I is represented by a large number of lines in the wavelength region 280 – 600 nm, which are subject to these non-equilibrium excitation effects. Some of them belong to the multiplets 5 ($a^6D - z^6D^0$), 16 ($z^8P^0 - e^8S$) and 27 ($z^6P^0 - e^6S$) that we use in the abundance analysis. Also, many strong

lines connect the low-excitation levels, which are mainly metastable, with the uppermost levels with $E_i \geq 6.5$ eV (see Grotrian diagram for Mn in Fig. 3.2). For example, transitions $z^8P^\circ - e^8P$ with $\lambda \sim 2800$ Å and $a^4G - y^4G^\circ$ at $\lambda \sim 3000$ Å have f -values of the order of 0.5. In accord with the mechanism of optical pumping, the upper levels of these transitions, z^6D° , e^6S , and e^8P , are overpopulated relative to their lower levels in the layers with $\tau_\nu^{\text{core}} > 1$ and $\tau_\nu^{\text{wing}} < 1$ (Fig. 4.1). But at smaller depths, where $\tau_\nu^{\text{core}} < 1$, departure coefficients of these levels steeply decrease. Levels of the term e^6S display a drop at $\log \tau_{5000} \sim -0.9$, and for levels of the term z^6D° this drop shows at $\log \tau_{5000} \sim -1.5$. The cores of $z^8P^\circ - e^8P$ lines are formed even higher, at $\log \tau_{5000} \sim -2.3$.

The non-equilibrium excitation processes also affect the levels close to the continuum. First of all, due to photon pumping transitions, like those from low metastable z^8P° to highly-excited e^8P levels, other levels with the excitation energy $E_i \geq 7$ eV linked with e^8P by strong collisions are overpopulated. As low levels have very large relative populations due to the Boltzmann factor $N_i/N_j \sim \exp(h\nu/kT) \gg 1$, even a small low level decrease in b_i represents a huge increase in b_j . However, the high levels are also collisionally tied to the Mn II ground state, which is in LTE. Thus, uncompensated overpopulation of the highest levels is transferred to the continuum state, which results in a net collisional ionization from such levels.

Besides, a huge number of transitions with relatively small probability, $\log gf \sim -2$ couple the quartet term system, such as a^4G and a^4H , to the terms at 0.2 – 0.4 eV separation from the continuum, e.g. x^4G° , which enables an efficient transfer between intermediate- and highly-excited levels.

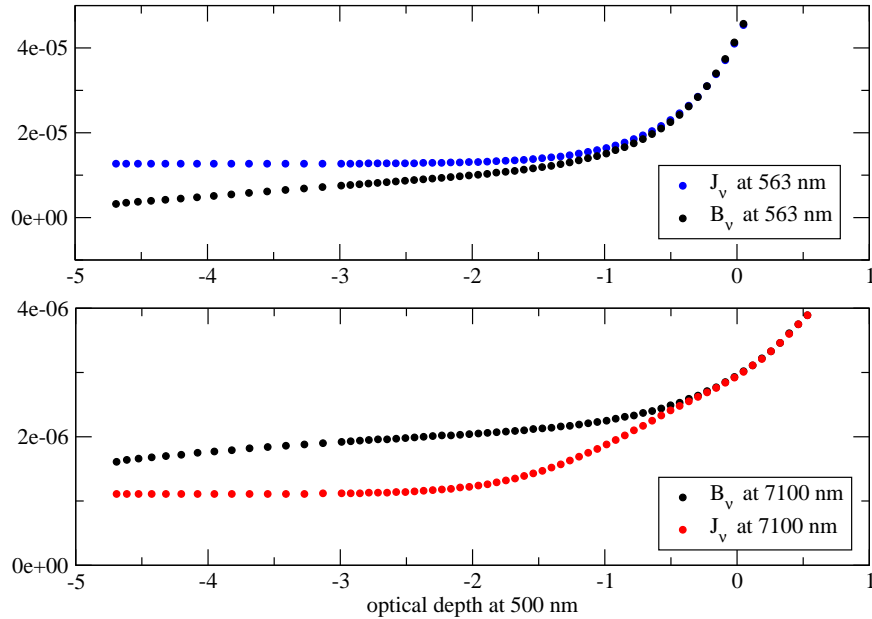


Figure 4.2: The run of the mean intensities at wavelengths 563 nm and 7100 nm compared to the run of the Planck functions at the same wavelengths with optical depth in the continuum at 500 nm.

Actually, the behaviour of the Mn I levels with an excitation energy above 6.5 eV is even more complex. A majority of them are slightly overpopulated or remain in detailed balance with the ground state of Mn II a^7S_3 . Photoionization from these levels is not efficient because the mean intensity J_ν at infra-red frequencies is smaller than the Planck function $B_\nu(T_e)$ already at large depths in the atmosphere (Fig. 4.2, lower panel). Lack of ionizing photons results in a *net recombination*. Nevertheless, overpopulations of highly-excited levels are partly canceled by the *photon suction* process. There is a number of high-probability transitions in Mn I, which couple the levels of 6 – 7 eV and 4 – 5 eV excitation energy, e.g. $z^6D^\circ - i^6D$ at ~ 7000 Å. Recombining

electrons de-excite through such transitions to the lower Mn I levels, and in this way even produce underpopulations of some highly-excited levels. At the same time, this mechanism reduces the effects of overionization and photon pumping on the lower levels.

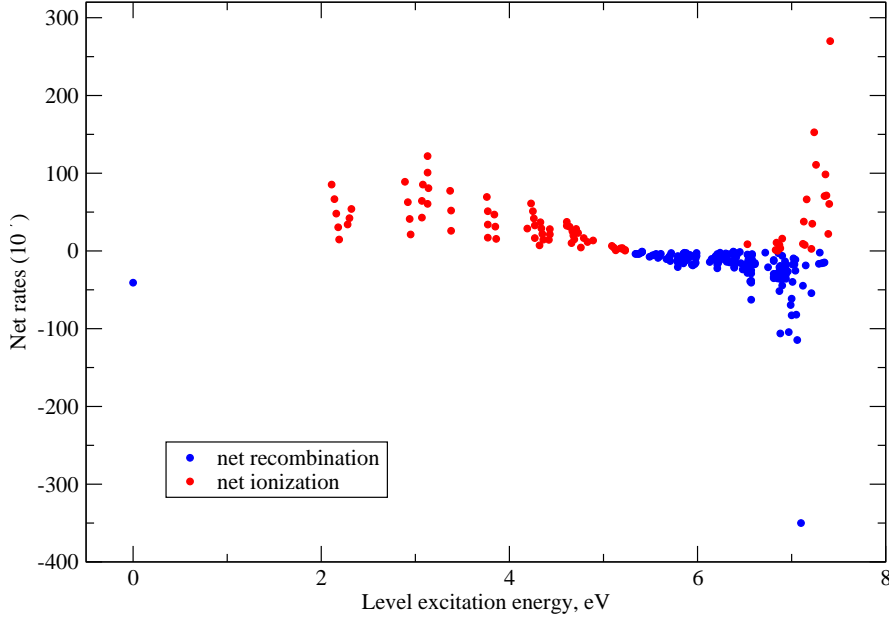


Figure 4.3: Net rates in Mn I. The net ionization and net recombination occur from/to the levels marked with red and blue circles, respectively. For clarity, upward rates are positive and downward rates are negative.

The considerations given above can be visualized with the help of the Fig. 4.3, where the *absolute* net ionization rates¹ per cm^{-3} for each level in Mn I at the optical depth $\log \tau_{5000} = -1.2$ are shown. The net rates are given by the balance between total rates (radiative and collisional) of transitions between discrete levels and the continuum. The net ionization and net recombination occur from/to the levels marked with red and blue circles, respectively. For clarity, upward rates are positive and downward rates are negative. All levels with low and intermediate excitation energies 2–5 eV are overionized by the superthermal radiation field. The net recombination occurs to the ground state of Mn I $a^6S_{5/2}$ because this level is already underpopulated, not because of a radiation imbalance. For levels with excitation energies $E_i \geq 5$ eV, recombination rates dominate. The overrecombination to the highly-excited levels is balanced by strong collisional ionization from the levels with $E_i > 7$ eV, i.e. the levels at negligible energy separations from the continuum.

A majority of Mn II levels with low and intermediate excitation energies share their populations in LTE with the ground state a^7S_3 . Only highly-excited levels above 9 eV with negligibly small absolute number densities, such as y^3D^o on Fig. 4.1, are overpopulated by photon pumping from the low metastable levels. The latter process does not change the population of the Mn II ground state, which keeps its thermodynamic equilibrium value. Neither is a^7S_3 affected by overionization from the levels of Mn I, because neutral atoms occupy less than 5% of the total element number density in an atmosphere with solar temperature.

The behaviour of departure coefficients in the atmospheres of metal-poor stars is qualitatively similar to that of the Sun. All Mn I levels are underpopulated above $\log \tau_{5000} \approx 0$, but more Mn II levels start to deviate from LTE. In general, the NLTE effects become more pronounced with increasing effective temperature and decreasing metallicity. In both cases the UV radiation field is amplified, and increases the rates of b-b and b-f transitions in the Mn I atom. Fig. 4.4a shows departure coefficients calculated for the model atmosphere with $T_{\text{eff}} = 6400$ K, $\log g = 4.20$,

¹The absolute rates per cm^{-3} used here are not to be mixed with the rates per particle defined in section 3.4.4

[Fe/H]= 0. In spite of a ~ 650 K higher effective temperature compared to the Sun, differences with the solar distribution of departure coefficients (Fig. 4.1) are relatively small. The reason is that with increasing temperature the collision rates also become larger due to an increased kinetic energy of the particles. This effect counteracts the NLTE influence of the radiation field.

Metallicity has a more pronounced effect on the population of the Mn levels. Decreased metallicity implies a lower number density of metals, which are the major suppliers of free electrons and important absorbers in the short-wave part of the spectrum. So, the reduced continuous opacity in the UV and decreased collision rates result in a depopulation of all Mn I levels. As an example, we consider a model with [Fe/H] = -2; the other parameters are approximately solar (Fig. 4.4b). The dominant NLTE process is overionization, which now efficiently depopulates all levels including the ground state $a^6S_{5/2}$ and the uppermost levels, e.g. y^4S° , thus leading to $b_i < 1$. Optical pumping is also amplified in the metal-poor atmosphere. However, it can not compete with photoionization anymore, thus lower levels of pumping transitions (e.g. $a^6D - z^6D^\circ$ and $z^6P^\circ - e^6S$) are either underpopulated relative to their upper levels or stay in equilibrium with them all over the optical depth scale. Note that the decoupling of the Mn I state from the other low-lying levels at $\log \tau_{5000} \sim -1.5$ is related to spontaneous transitions in the wings of strong resonance lines $a^6S_{5/2} - y^6P^\circ$. Another difference with the solar case is the presence of small deviations from LTE for intermediate-excitation Mn II levels. As seen on the Fig. 4.4b, the odd level $z^5P_1^\circ$ with excitation energy 5.4 eV is slightly overpopulated by optical pumping at $-1.5 < \log \tau_{5000} < 0$. But at smaller depths, photon losses in transitions of the multiplet $a^5D - z^5P^\circ$ result in a depopulation of the upper level.

Variation of gravity $\Delta \log g = \pm 1$ dex relative to the Sun has a marginal effect on the atomic level populations. For the whole range of stellar parameters considered here, the change in gravity from $\log g = 4.6$ to $\log g = 3.0$ results in a slightly weaker coupling of the levels with each other. This is a result of a decreased collision frequency that tends to destroy LTE population ratios between the levels.

4.2 Influence of uncertain parameters

NLTE calculations for Mn are very complex because a large number of processes enters the equations of statistical equilibrium. As emphasized in Sect. 3.4, the atomic data for certain processes, like inelastic collisions with H I atoms or photoionization, are uncertain. The sensitivity of the results to a variation of these parameters will be investigated in this section. Moreover, including all levels and transitions found in laboratory experiments and predicted by calculations is very expensive computationally. Thus, we will try to find a reduced atomic model, which gives similar results as the complete one. The test calculations are performed with the solar model atmosphere and a model atmosphere with the low metallicity ($T_{\text{eff}} = 6000$ K, $\log g = 4.00$, [Fe/H] = -2).

4.2.1 Completeness of the atomic model

The complete atomic model of Mn is represented by three ionization stages that results in a total of 459 levels and 2809 radiative transitions. This is a huge system. Hence, at first we check whether several ionization stages are necessary for a correct description of the excitation-ionization equilibrium of Mn.

The first reduced atomic model is closed by the ground state of Mn II. The departure coefficients calculated with this model and two model atmospheres corresponding to the Sun and a metal-poor star are shown in Figs. 4.5a and d. A comparison with Figs. 4.1 and 4.4b shows that the results derived with the reduced atomic model are *identical* all over the optical depth scale with those calculated with the complete model atom. That means, excited levels of Mn II do not play any role in the statistical equilibrium of Mn I. This is to be expected because Mn II is the dominant ionization stage at solar temperatures, and its ground state is the only one interacting with the Mn I system by photoionization. Therefore, it seems that *all* excited levels of ionized manganese can be completely ignored in statistical equilibrium calculations. Also, the only lines

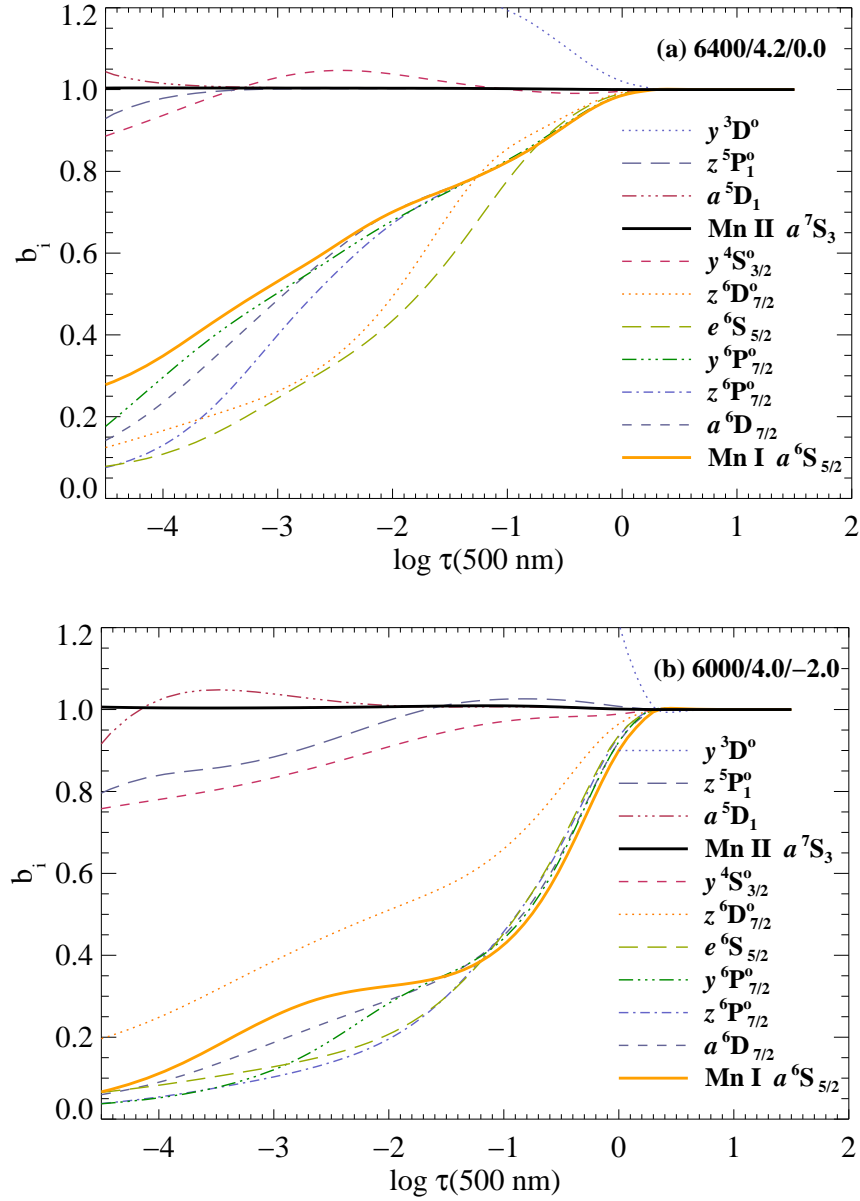


Figure 4.4: Departure coefficients b_i of selected levels calculated with the complete model of Mn atom and different model atmospheres (a): $T_{\text{eff}} = 6400$ K, $\log g = 4.20$, $[Fe/H] = 0$ (b): $T_{\text{eff}} = 6000$ K, $\log g = 4.00$, $[Fe/H] = -2$.

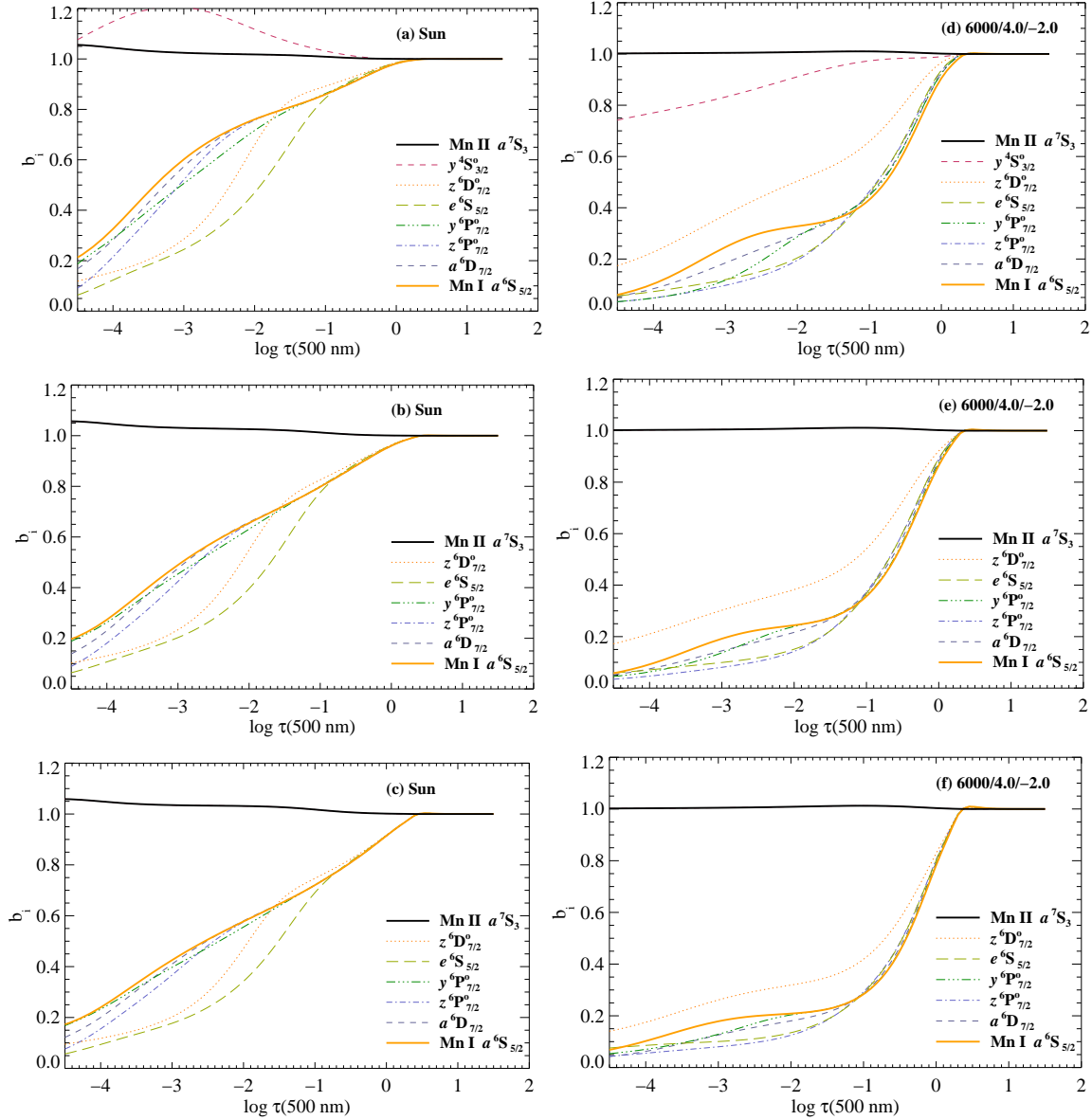


Figure 4.5: Departure coefficients b_i of selected Mn I levels calculated with atomic models of different size and two model atmospheres (see upper right corner in each figure). (a) and (d): The reduced model atom with a total of 246 levels. (b) and (e): The reduced model atom with a total of 146 levels. (c) and (f): The reduced model atom with a total of 66 levels. All models are closed by the Mn II ground state. Note that due to the model reduction some of the high-excitation levels in Fig. 4.1 are no longer present.

of Mn II sufficiently strong to be observed in a stellar spectrum are due to the transitions between the 2–5 eV levels, which have LTE populations all over the atmospheric depth in the solar model. In the metal-poor stars, populations of intermediate-excitation Mn II levels only slightly deviate from LTE (Fig. 4.4b). Thus, the whole ionized level system can be also neglected for stellar computations.

Further, it is interesting to what extent do highly-excited levels in Mn I affect its excitation equilibrium. The second reduced model of Mn I includes all 145 levels with the excitation energy below 6.42 eV ($E_{\text{ion}} = 7.43$ eV). The Mn I levels with $n = 6 \dots 15$ and all levels of Mn II, except the ground state, were excluded from the calculations. The results of calculations for the model atmospheres of the Sun and a metal-poor star are displayed in Figs. 4.5b and e. Note a *stronger* undepopulation of all low- and intermediate-excitation levels compared to the first reduced model, which includes the uppermost levels at $\sim 0.1 \dots 1$ eV separation from the continuum. This is a result of reduced collisional coupling to the ground state of Mn II that is in LTE. Overionization effects on the low-excited Mn I levels increase because less electrons recombine and de-excite to the lower levels via photon suction.

Even stronger overionization occurs, when the energy gap between both ions is increased to 2.2 eV. The trend is evident for both atmospheric models with the solar and low metallicity (Figs. 4.5c and f). The atomic model used here includes only 66 levels and the Mn II ground state, and it is not adequate for realistic statistical equilibrium calculations. However, it provides a clear insight on what process drives deviations from LTE in manganese (see next section).

In fact, any model of Mn I atom devoid of high-excited levels is not satisfactory because the system becomes sensitive to photoionization. Noticeable differences are seen for departure coefficients of all levels of interest in the layers $-2 < \log \tau_{5000} < 0$ that can affect the results of line formation calculations, and thus the abundances. However, the first reduced atomic model including all Mn I levels and the ground state of Mn II seems to satisfy our requirements. It produces a similar description of statistical equilibrium in Mn I as the complete model, but at the same time it is by a factor of two smaller than the latter. Thus, the time of computation is decreased significantly. We also demonstrated that all levels of interest in Mn II are in LTE irrespective of the number of ionization stages included in NLTE calculations. Therefore, the reduced atomic model closed by the Mn II state is our new reference model and the majority of calculations will be carried out with it.

4.2.2 Photoionization

The discussion presented in the previous section made it clear that radiative processes are very important in the excitation-ionization equilibrium of Mn. However, we also noted that hydrogenic photoionization cross-sections may be the most *uncertain* representation in our model. Now we carry out test calculations to check the effect of this assumption on the departure coefficients.

NLTE calculations were performed with the *reference* model atom for various scaling factors to the standard hydrogenic photoionization cross-sections from the formula 3.2, $S_{\text{p}} = 0$ and 300. The latter value is chosen because in the comparable atoms (Fe, Si) the cross-sections calculated within the Opacity project (Bautista 1997) are 100–1000 times larger than the hydrogenic approximation. Assumption of zero photoionization does not have any physical meaning, however this numerical experiment allows us to understand which process *induces* departures from LTE in Mn. In other words, which rates drive the others, and which are driven by others.

A plot of the resulting departure coefficients for the solar and stellar model atmospheres is presented in Fig. 4.6. A very interesting but *logical* result is that the absence of photoionization in the reference atomic model (Figs. 4.6a and d) does not restore LTE, as one would expect if the major and only NLTE mechanism were the overionization. Moreover, the results for zero photoionization cross-sections are similar to those of the reference model with $S_{\text{p}} = 1$ (Fig. 4.1 and 4.4b) that is characteristic of both atmospheric models. This result follows from the lengthy discussion in Sect. 4.1. Radiative transitions with strong optical pumping effects cause an overpopulation of the high-excitation levels with respect to the low-excitation levels. Due to the strong collisional coupling of the high-excitation levels with the Mn II ground state, which is in LTE, the

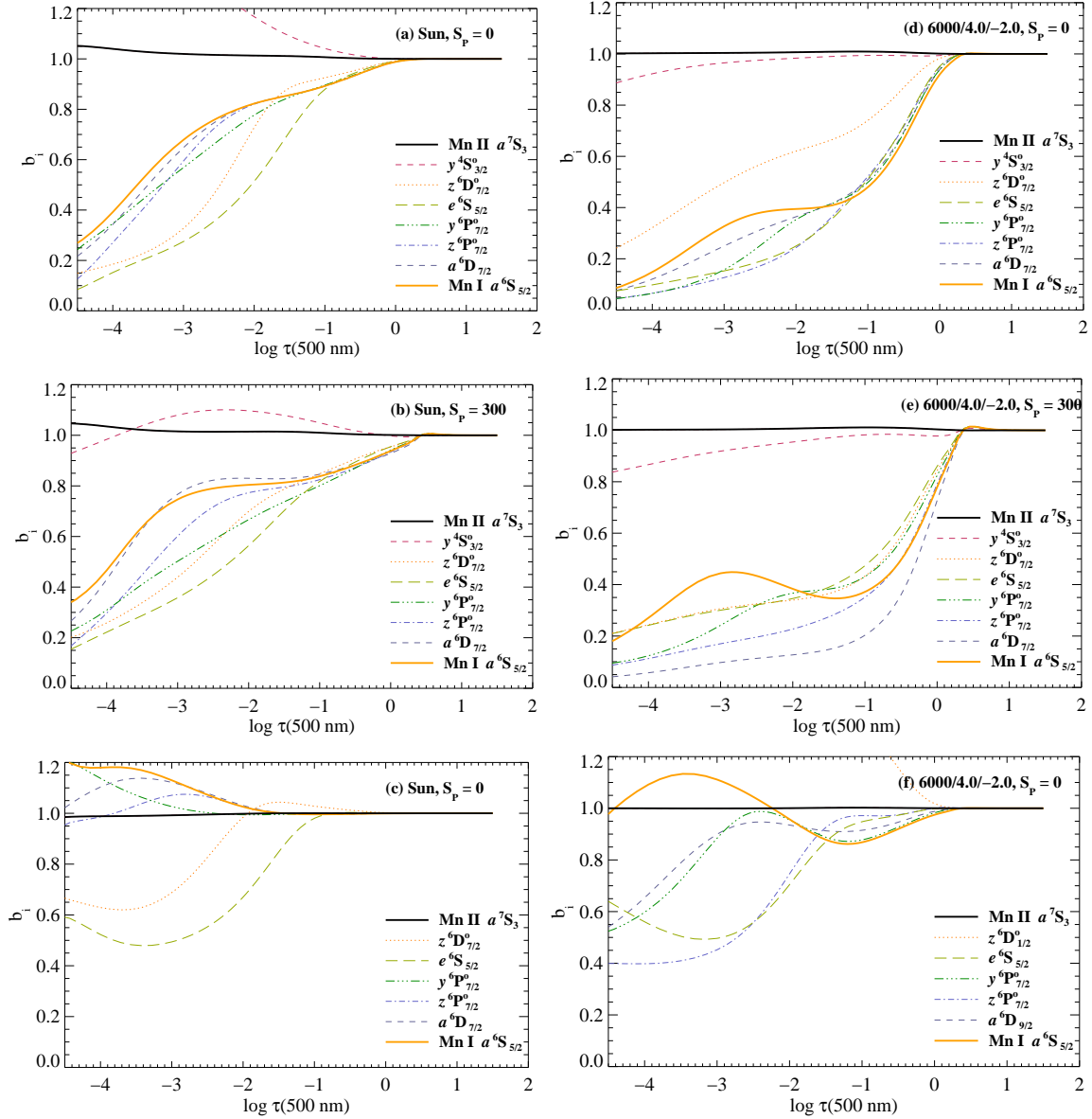


Figure 4.6: Departure coefficients b_i of selected Mn I levels calculated with different scaling factors to hydrogenic photoionization cross-sections, S_p , and two model atmospheres (see upper right corner in each figure). (a) and (d): $S_p = 0$, reference model atom with 245 levels of Mn I and closed by Mn II ground state. (b) and (e): The same as (a) and (d), but $S_p = 300$. (c) and (f): $S_p = 0$, reduced model atom with 65 levels of Mn I and closed by Mn II ground state.

departure coefficients of these levels are close to unity; consequently the departure coefficients of the low-excitation levels drop significantly below unity. Therefore, *it is not the photoionization that is underestimated, but the radiative b-b transitions are so strong and numerous, that they inevitably control the statistical equilibrium of the atom, especially so, when radiative b-f processes are excluded from calculations.* This conclusion is confirmed by an experiment, where the probabilities of all b-b transitions in the reference model are scaled by 10^{-2} . The SE calculations are then performed for $S_p = 1$ (standard hydrogenic approximation) and $S_p = 0$ (null photoionization) (Fig. 4.7). The corresponding diagrams supply the basic demonstration of the *overionization* phenomenon: the amplified photoionization results in large depopulations of all Mn I levels, whereas its absence completely thermalizes all atomic level populations.

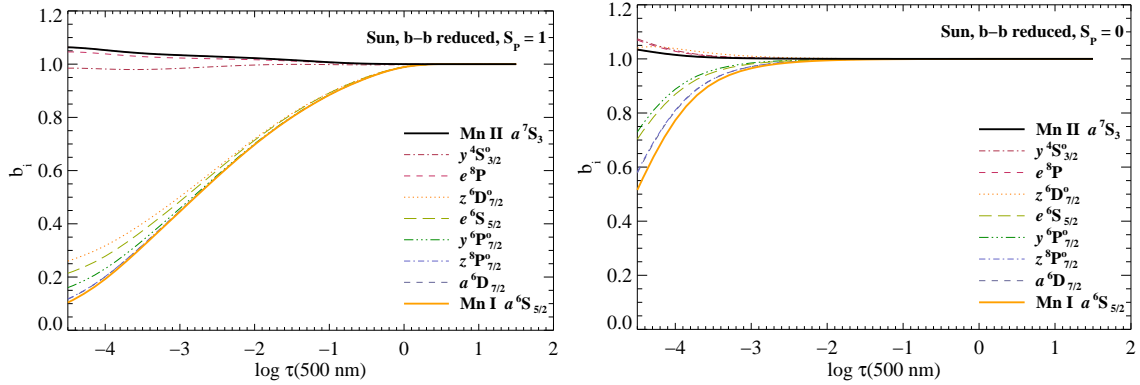


Figure 4.7: Departure coefficients b_i of selected Mn I levels calculated with transition probabilities decreased by a factor of 10^{-2} and different scaling factors to hydrogenic photoionization cross-sections: $S_p = 1$ (left panel), $S_p = 0$ (right panel).

The influence of increasing photoionization is demonstrated in Fig. 4.6b and e. In the model with $[\text{Fe}/\text{H}] = -2$, we clearly see *stronger deviations of b_i from unity for all levels* (Fig. 4.6e). Also, low metastable terms, like $a^6\text{D}$ decouple completely from the ground state. That confirms our conclusion in Sect. 4.1 that *overionization is a main NLTE process at low metallicity.* The effect of increased photoionization on the model with solar metallicity (Fig. 4.6b) can be understood if we recall how statistical equilibrium in Mn I is achieved. The ionization balance is dominated by the levels with $E_i \sim 2-3$ eV, which are simultaneously the lower levels of photon pumping transitions. At $-1 < \log \tau_{5000} < 0$, these levels are depopulated by overionization *and* by optical pumping. Hence, *increasing* the rates of radiative b-f transitions results in even stronger underpopulations at these depths. At $\log \tau_{5000} < -1$, photon pumping ceases since the lines become optically thin, and spontaneous de-excitations start to suppress the depopulation of the lower levels caused by overionization. At that depth, b_i of the upper levels steeply decrease. In the case of $S_H = 300$, the increased net ionization from the lower levels is balanced by an increased net recombination to the uppermost levels separated by ≤ 1 eV from the continuum. Recombined electrons cascade down and compensate the underpopulation of lower and intermediate-excitation levels ($z^6\text{P}^o$, $z^6\text{D}^o$, $e^6\text{S}$). Hence, instead of a sudden drop, their departure coefficients display a smooth decrease at $\log \tau_{5000} < -1$.

The absolute domination of photoionization in the statistical equilibrium of Mn at solar metallicity can be seen only for the 66 level model atom. Fig. 4.6c demonstrates the loss of the collision efficiency in coupling to the Mn II ground state. Here, removal of photoionization with $S_p = 0$ drives the lower level populations towards LTE in the line formation region. Above $\log \tau_{5000} \sim -1.5$, the photon suction along the lines now results in an *overpopulation* of low-excitation Mn I levels and *underpopulation* of high-excitation levels that is balanced by net collisional ionization. In the metal-poor model, Fig. 4.6f, all lower levels have $b_i < 1$, and the upper levels have $b_i > 1$ at $\log \tau_{5000} > -1.5$. In the higher layers, photon suction and spontaneous transitions in the wings of resonance lines, such as $a^6\text{S}_{5/2} - y^6\text{P}^o$ at ~ 2800 Å, lead to the

overpopulation of the Mn I ground state. The role of UV resonance transitions increases with decreasing metallicity.

4.2.3 Inelastic collisions with H I atoms

The reference atomic model of Mn I, as described above, was constructed with hydrogenic photoionization cross-sections and cross-sections for inelastic collisions with H I (both for b-b and b-f transitions) based on the Drawin's formula, but scaled by a factor $S_{\text{H}} = 0.05$. Comparison of the collision rates $C_{ij}(\text{H})$ and $C_{ij}(\text{e})$ shows that in the solar atmosphere the rates of discrete transitions due to collisions with electrons are on average greater by one order of magnitude (Sect. 3.4.4). However, collisional ionization in Mn I atom is fully controlled by neutral hydrogen. In order to test the influence of inelastic collisions with hydrogen, we carried out additional calculations for scaling factors from $S_{\text{H}} = 0$ to 1. The results for the solar model atmosphere are demonstrated in Fig. 4.8a and b. When inelastic collisions are ignored ($S_{\text{H}} = 0$), slightly larger deviations from LTE are seen for all Mn I levels. This is to be expected because collisions have a thermalizing nature. Also, with increasing rates of collisional excitations and ionizations by H I atoms departure coefficients get closer to unity, although perfect thermalization is not achieved. And even $S_{\text{H}} = 5$ (not shown here) does not lead to LTE atomic level populations.

A similar situation is seen for the metal-poor model (Fig. 4.8c and d). The absence of inelastic collisions leads to a different behavior of the highest levels, but it has nearly no effect on departure coefficients for all other Mn I levels. At $\log \tau_{5000} \sim 0$ there is a characteristic bump in b_i for the $y^4\text{S}_{3/2}^{\circ}$ level due to an overrecombination. Increasing the collision efficiency by a factor of 20, $S_{\text{H}} = 1$, also does not restore LTE (Fig. 4.8d). Departure coefficients at the depths of line formation $-1 < \log \tau_{5000} < 0$ change less steeply, but there are no qualitative differences. The effect of inelastic collisions on Mn abundances will be discussed in the next chapter, but even now we can predict that this effect will not be large.

4.3 NLTE effects on Co levels

The atomic level populations of Co I are affected by NLTE, although in a less complex way in comparison with Mn I. The spectra of both ions are characterized by the presence of strong transitions all over the UV - near-IR spectral range (see Fig. 3.4). However, the general number of transitions is by a factor of four larger than that in Mn I, which provides efficient coupling between levels of all excitation energies. The b -factors as a function of optical depth at 500 nm are presented in Fig. 4.9 for the *solar* model atmosphere. In order not to overload the figures, we show only some levels, which are sufficient to describe statistical equilibrium of Co. As in the case of Mn, these levels form three groups: the Co I ground state $a^4\text{F}$ and low levels of 1 - 3 eV excitation energy, the intermediate levels with $E_i \sim 4 \dots 5$ eV strongly coupled to the former by means of b-b transitions, and the upper levels close to the Co II ground state $a^3\text{F}$. In addition, two excited Co II levels $a^5\text{P}_3$ and $z^5\text{D}_4^{\circ}$ are indicated. A transition between these levels produces a spectral line at 3501 Å, which we use in the abundance analysis.

The upper left panel (Fig. 4.9a) shows the departure coefficients, calculated with the complete model of Co constructed with three ionization stages and a total of 458 levels. *The overall underpopulation of all Co I levels is due to the overionization.* Thus, distribution of departure coefficients up to $\log \tau_{5000} \sim -2$ has a very regular structure, with levels of ever decreasing energy gap from the continuum showing smaller deviations of b_i from unity. The Co I ground state is not subject to strong overionization. But its separation from the first metastable level $b^4\text{F}$ is only 0.4 eV, which favors a very efficient collisional interaction. Overionization is caused by radiative b-f processes from the levels of 2 - 3 eV excitation, e.g. $z^6\text{G}^{\circ}$, $z^4\text{F}^{\circ}$, and $z^2\text{G}^{\circ}$ with threshold wavelengths 2611, 2850, and 3151 Å, respectively. The underpopulation of these levels is transferred via b-b transitions to the lower metastable levels with $E_i \sim 0.5 - 2$ eV, such as $b^4\text{F}$.

In the higher layers, spontaneous transitions in strong lines of Co I slightly modify this simple pattern. At $\log \tau_{5000} \leq -2$, the medium becomes transparent to the radiation in transitions

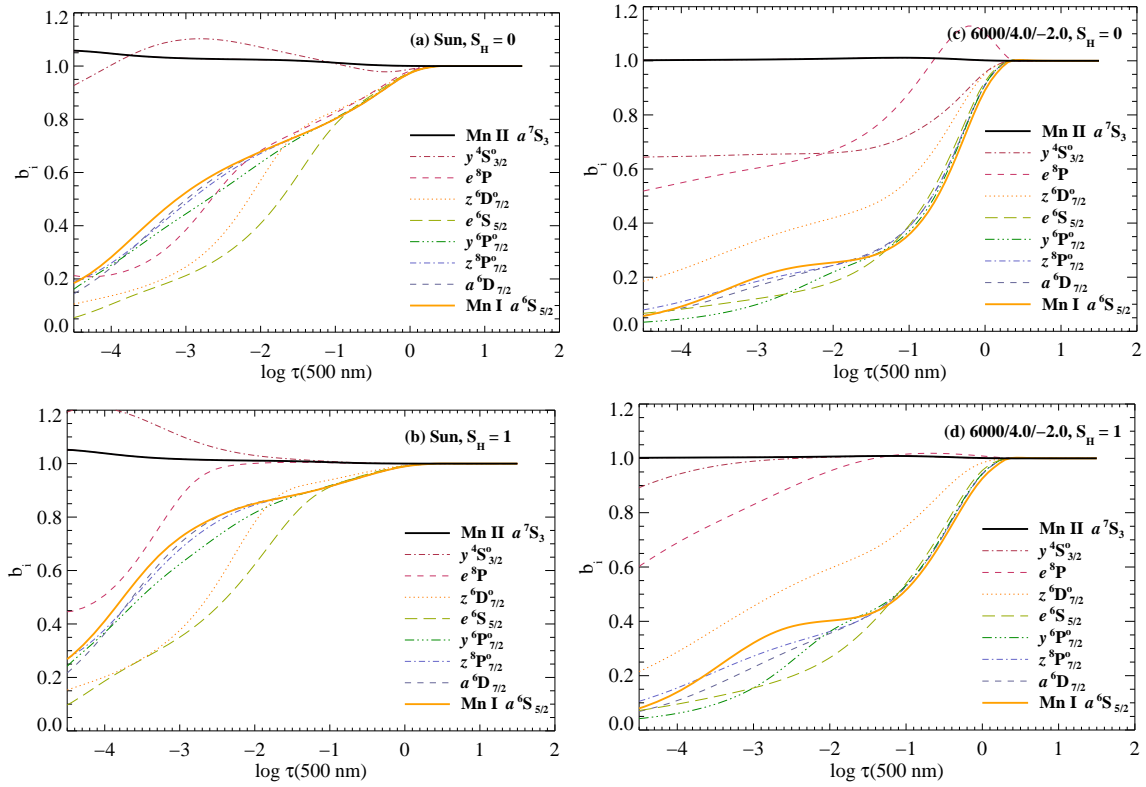


Figure 4.8: Departure coefficients b_i of selected Mn I levels calculated with different scaling factors to collision cross-sections S_H with H I atoms and two model atmospheres (see upper right corner in each figure). (a) and (c): $S_H = 0$. (b) and (d): $S_H = 1$.

between the low metastable levels and the levels of odd doublet and quartet term systems with ~ 4 eV excitation energy, $b^4F \rightarrow z^4F^\circ$ and $a^2F \rightarrow z^2G^\circ$. As a result, we see a sudden depletion of the upper levels. These two transitions are of a particular interest, because the corresponding spectral lines at 4020 and 4121 Å are the only observable in our spectra of metal-poor stars. Moreover, a large number of strong² transitions in Co I connect the low levels with $E_i \sim 0 - 3$ eV and the levels with 5 – 6 eV excitation energies (see Fig. 3.4), e.g. $a^4F \rightarrow x^4D^\circ$ ($\lambda \sim 2500$ Å), $b^4F \rightarrow w^4F^\circ$, and $z^6G^\circ \rightarrow e^6G$ ($\lambda \sim 3500$ Å). Hence, at depths with $-1 < \log \tau_{5000} < 0.2$ there is also *photon pumping* of the high-excitation levels. For example, the departure coefficient for the e^6G level even slightly increases at $-1 < \log \tau_{5000} < 0$. However, this process barely affects populations of the lower levels due to the large Boltzmann factor, and dominance of photoionization from these levels. A majority of the uppermost levels with $E_i > 6.5$ eV are underpopulated relative to the continuum. In fact, they interact much stronger *radiatively* with the low levels and with each other *by means of collisions* than with the Co II ground state. Only for a few highest levels with threshold ionization energies similar to the mean kinetic energy of the electrons in the solar atmosphere the collisional coupling to the a^3F level prevails. Thus, they are in thermal equilibrium with a^3F .

A notable difference with Mn is that the ground state of Co II is affected by NLTE, although departures in the line formation region are not large. This is a result of the higher ionization potential of Co I, which is 0.4 eV larger than that of Mn I. Hence, in the solar atmosphere, nearly 20 % of Co atoms are in the neutral ionization stage. The change of ionization rates from Co I perceptibly affects the atomic level populations of the next ionization stage, Co II. The excited levels of Co II are in thermal equilibrium with its ground state.

Now, we consider a reduced Co atomic model, which is constructed with 246 levels of Co I and closed by the Co II ground state (Figure 4.9b). It is clear that a^3F is more affected by overionization from Co I levels when the Co II excited levels are not taken into account. This confirms a well-known phenomenon: the NLTE effects in majority ions are due to line transitions rather than to bound-free transitions. Excluding all excited levels of Co II, we block the efficient spilling of electrons from the overpopulated ground state to the excited states in Co II. This process, defined above as photon pumping, would have diminished the excess population of a^3F as seen in Fig. 4.9a. Moreover, the influence of overionization on the Co I levels is decreased, which leads to *smaller* deviations of their atomic level population from LTE. Therefore, in contrast to Mn a reduction of the atomic model is not safe in Co. Hence, all NLTE calculations are carried out with the complete Co model including three ionization stages.

The influence of photoionization was studied by performing NLTE calculations for various scaling factors to the cross-sections, S_P . For the same reasons as in Mn I, we have chosen to scale the cobalt cross-sections σ_ν by factors 0 and 300 (Fig. 4.9c, d). Although the absence of photoionization leads to smaller deviations of departure coefficients from unity compared to the case of $S_P = 1$ (standard hydrogenic cross-sections), again we do not achieve LTE populations $b_i = 1$ for all levels. Qualitatively, the behavior of departure coefficients does not change, and even the *overpopulation* of the Co II levels persists. The phenomenon has already been elucidated for Mn: the non-zero *net radiative b-b rates* lead to non-zero collisional b-f rates, which also affect the excitation equilibrium of the ionized species. The results for Co confirm this conclusion. Fig. 4.9d demonstrates the effect of stronger photoionization ($S_P = 300$) on the atomic level populations. Noticeable differences with the reference model (Fig. 4.9a) occur in the deep layers $\log \tau_{5000} > -1.5$: depopulation of all levels is amplified, upper levels are now more closely coupled to the continuum in part due to increased recombinations, and the levels of intermediate energies, such as x^4D° , are less affected by non-equilibrium excitation processes. These processes force deviations of level departure coefficients from the bulk of *relatively* thermalized low levels in the reference Co model calculated with $S_P = 1$.

The influence of collisions with neutral hydrogen atoms is fully understood from Fig. 4.9e and f. When b-b and b-f transitions due to inelastic H I collisions are neglected, $S_H = 0$, the coupling of the uppermost levels in Co I to the continuum is weakened that is seen for the level

²Transitions with large probability.

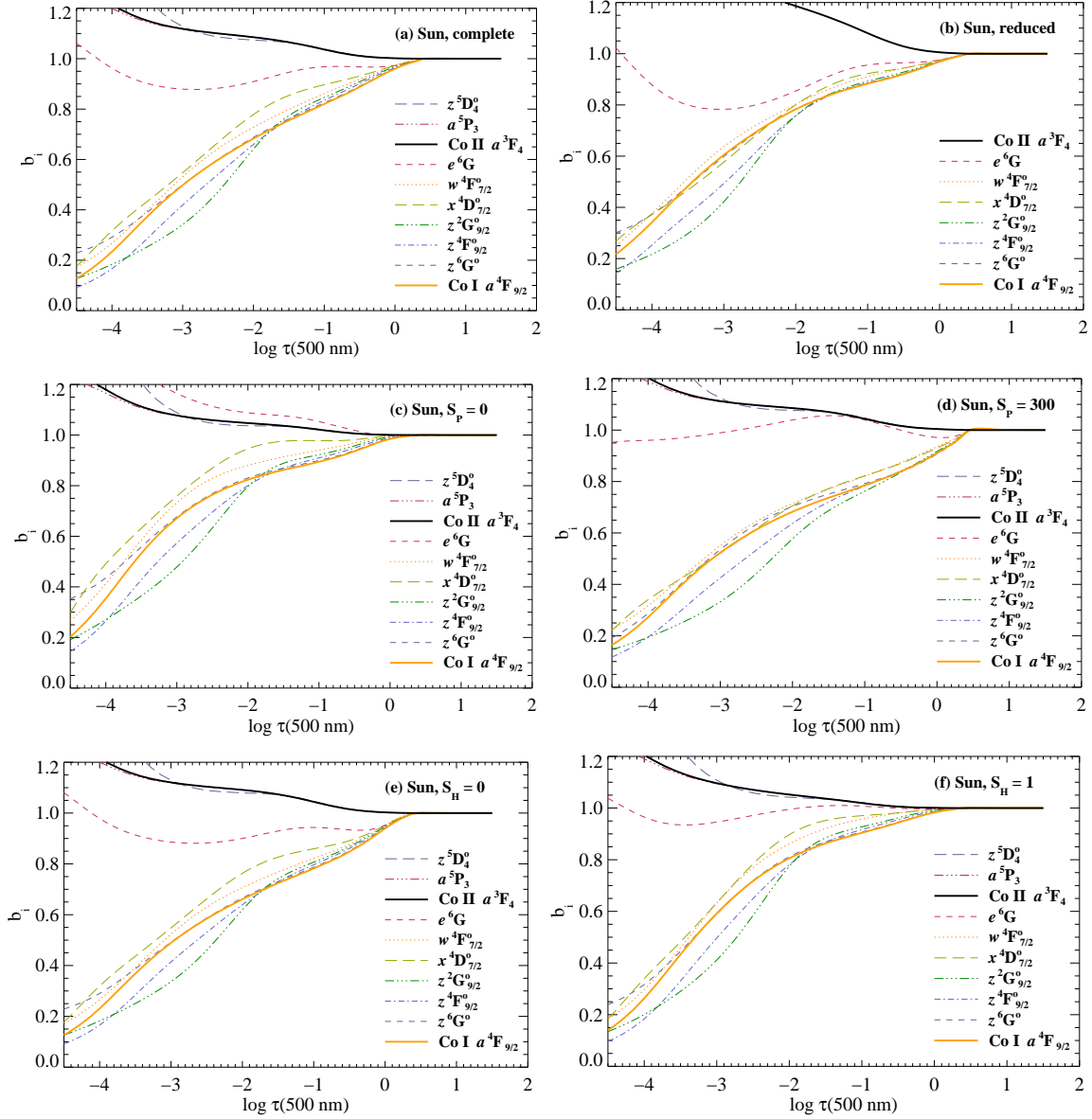


Figure 4.9: Departure coefficients b_i of selected Co I and Co II levels. (a) : The complete model with a total of 458 levels, represented by three ionization stages; the photoionization cross-sections are computed with the standard hydrogenic approximation $S_P = 1$, and cross-sections for inelastic collisions with H I atoms are calculated with Drawins formula, but scaled by $S_H = 0.05$. (b) : The reduced model atom with 246 levels of Co I and closed by the ground state of Co II a^3F_4 , $S_P = 1$ and $S_H = 0.05$. (c) The same as (a), but $S_P = 0$. (d) : The same as (a), but $S_P = 300$. (e) : The same as (a), but $S_H = 0$. (f) : The same as (a), but $S_H = 1$.

e^6G at $\log \tau_{5000} > -1$. However, there is negligible effect on the populations of the bulk of low and intermediate levels (compare with Fig. 4.9a where $S_H = 0.05$ is used), which interact with the Co II state only *via* photoionization. As emphasized in Sect. 3.4.4, the collisional excitation in the atoms is controlled by free electrons. Thus, it is only the b-f rates from the highest levels that are changed with variation of hydrogen collision strength. When the standard Drawins formula is used with the scaling factor $S_H = 1$ (Fig. 4.9f), all levels at line formation depths $-2 > \log \tau_{5000} > 0$ are affected, but this scaling factor is too small for LTE to be reached completely.

4.4 Statistical equilibrium of Co in metal-poor stars

The character of processes leading to NLTE effects in Co does not change for stellar atmospheres with parameters of cool turnoff stars, which form the basis of our abundance analysis. As emphasized in section 2.1.1, we are interested in the stars with effective temperatures $5000 < T_{\text{eff}} < 6500$ K, surface gravities from 3 to 5 dex, and metallicities from 0 to -3 dex.

Fig. 4.10a demonstrates the effect of increasing temperature on the departure coefficients of selected Co I and Co II levels. At $T_{\text{eff}} = 6400$ K, the ionization equilibrium Co I/Co II is different from that of the solar model. Nearly 97% of Co atoms are in a singly ionized stage, hence the ground state of Co II is not sensitive to overionization from the Co I levels. The level a^3F_4 keeps its thermodynamic equilibrium value, as well as a majority of excited Co II levels. However, departure coefficients in Co I show larger deviations from unity. The reason is that a stellar flux maximum is shifted to shorter wavelengths, thus overionization affects even the lowest metastable levels with excitation energies ~ 1 eV and $\lambda_{\text{thr}} \sim 1800$ Å, like a^2F . In contrast, in the solar model overionization is important only for the higher levels with excitation energies ~ 3 eV.

Decreasing metallicity has essentially the same effect on Co I levels as on Mn I but the influence of photoionization is more pronounced (Fig. 4.10b). The dramatic depopulation of all levels occurs at the depths of line formation, $-1 < \log \tau_{5000} < 0$. The overionization from the lowest levels is balanced by increased net recombination to the higher levels that results in a small overpopulation of the latter at $\log \tau_{5000} \sim 0$. In the higher layers, $\log \tau_{5000} \sim -1$ even an overpopulation of the Co II ground state develops. Also, we note an increasing importance of line pumping in Co II. The lower levels are thermalized with respect to the Co II ground state. As seen in Fig. 4.10b, $b_i(a^3F) = b_i(a^5P)$ up to $\log \tau_{5000} \sim -3$. But the departure coefficient for the level z^5D^o is much larger than unity already at $\log \tau_{5000} \sim -0.3$. This is characteristic of all Co II levels with $E_i > 5$ eV. Hence, we expect *substantial NLTE effects in the lines of both ions*.

A combination of low effective temperature, low gravity, and low metal content leads to a rather disorderly behavior of departure coefficients for different levels (Fig. 4.10c). Such stellar parameters are representative of giants where the collisional interaction is much weaker compared to dwarfs. Each level of Co I is not anymore coupled to the bulk of levels with similar energies, but displays *a distinct behavior that is determined by the competition of radiative b-f and b-b processes*. This is particularly true for the the higher levels, such as e^6G , w^4F^o , x^4D^o , for which a clear separation into component NLTE processes is not possible. The behavior of lower Co I levels is qualitatively similar to the model with high gravity and effective temperature (compare with Fig. 4.10b). As a result, line formation in NLTE can be different for transitions involving different levels. Nevertheless, it seems that *in atmospheres of giants deviations from LTE are not larger than in dwarfs, and the main stellar parameter that determines the magnitude of NLTE effects in cobalt is metallicity*.

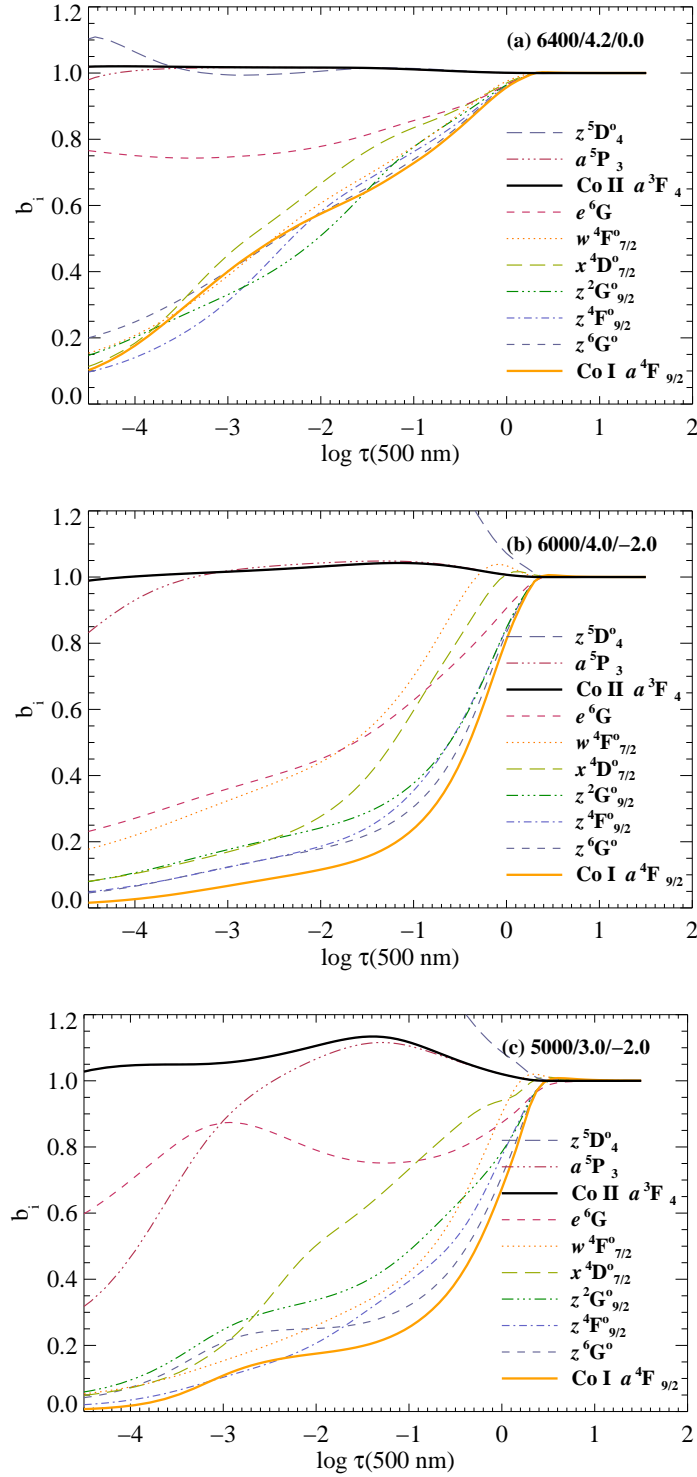


Figure 4.10: Departure coefficients b_i of selected levels calculated with the complete model of the Co atom and different model atmospheres (a): $T_{\text{eff}} = 6400 \text{ K}$, $\log g = 4.20$, $[\text{Fe}/\text{H}] = 0$ (b): $T_{\text{eff}} = 6000 \text{ K}$, $\log g = 4.00$, $[\text{Fe}/\text{H}] = -2$ (c): $T_{\text{eff}} = 5000 \text{ K}$, $\log g = 3.00$, $[\text{Fe}/\text{H}] = -2$.

Chapter 5

NLTE effects on spectral lines and abundances

The analysis of the statistical equilibrium of Mn and Co, presented in the last chapter, made it clear that NLTE effects on distribution of atomic level populations are significant. This chapter is devoted to the analysis of line formation for these elements. Only those lines are investigated, which are used in the abundance analysis of the Sun and/or metal-poor stars (Tables A.1 and A.2 in the appendix). Note that some lines with wavelengths in the UV part of a spectrum can not be used in studies of solar element abundances due to *severe blending*. This refers to the Mn I resonance triplet at 403 nm, and several Co I lines with $\lambda\lambda$ 3845, 3957 Å. Nevertheless, they will be discussed in this chapter and used in abundance calculations for the metal-poor stars. Also, we do not consider here the lines of Mn and Co with wavelengths below ~ 3500 Å and above ~ 8800 Å, although they are important in calculations of statistical equilibrium of the elements. This spectral range is not covered by our observational material.

As the emergent intensity depends on the source function and on the line optical depth according to the equation 2.25, we first consider the NLTE influence on S_ν^l and τ_ν^l . From the equation 2.23, the line extinction coefficient is:

$$\kappa_\nu^l \propto N_i \left(1 - \frac{N_j g_i}{N_i g_j} \right) = b_i \left(1 - \frac{b_j}{b_i} e^{-\frac{h\nu}{kT}} \right) \quad (5.1)$$

In the Wien's regime ($h\nu > kT$), the expression reduces to:

$$\kappa_\nu^l \approx b_i \quad (5.2)$$

When $b_i < 1$, the line opacity is decreased thus the line formation depth is increased. As the temperature in the deeper layers is higher, the final effect is the weakening of the absorption line. On the other side, $b_i > 1$ leads to an increased opacity in the line. The line is formed closer to the surface, where the temperature is lower, which leads to line strengthening with respect to the continuum. Hereafter, we will use κ_ν^l to designate line opacity under NLTE, and $\kappa_\nu^{l,LTE}$ for the line opacity under LTE.

The source function in a transition is an expression of the ratio of upper to lower level populations N_j/N_i . Under the assumption of complete redistribution (equation 2.22), the source function¹ can be written as:

$$S^l = \frac{2h\nu^3}{c^2} \frac{1}{\frac{N_i g_j}{N_j g_i} - 1} = \frac{2h\nu^3}{c^2} \frac{1}{\frac{b_i}{b_j} \left(e^{\frac{h\nu}{kT}} - \frac{b_j}{b_i} \right)} \quad (5.3)$$

¹For simplicity, we drop the subscript ν to designate a source function independent of frequency in the line S^l

When $h\nu > kT$, as is the case for all UV and visual spectral lines:

$$\frac{S^l}{B_\nu^l} \approx \frac{b_j}{b_i} \quad (5.4)$$

The line is weakened when $b_j > b_i$. Under such conditions, $S^l > B_\nu^l$. There are more atoms excited to the upper level of a transition j compared to those on the lower level i , than would be required by LTE. Hence, more emission occurs in the line in comparison to the emissivity given by Planck's law. On the other side, the absorption line becomes darker when $b_j < b_i$, $S^l < B_\nu^l$, because there are not enough atoms on the level j to produce the same emissivity as in LTE.

The physical basis for $b_i \neq b_j \neq 1$ *inequalities* for manganese and cobalt levels was the topic of the last chapter. The departures from thermal *level populations* are driven by splits between the mean intensity J_ν and the Planck function B_ν . These splits lead to the overionization and photon pumping when $J_\nu > B_\nu$, but overrecombinations and the photon suction occur when $J_\nu < B_\nu$.

The behavior of line profiles under NLTE can be understood from the analysis of level departure coefficients at the depths of line formation. For strong lines, it makes sense to consider the depths of formation of various parts of the line profiles, for example the layers where in the core or in the wing $\tau_\nu^l = 1$. We express the location of these layers using their optical depth at a standard wavelength 5000 Å. In fact, the notion $\log \tau_{5000}$ has already been used in the analysis of level departure coefficients.

Weak lines with small opacity relative to the continuum are formed in the deep layers. Their intensity profiles simply reflect the profile of κ_ν . However, radiation in strong lines comes from different depths. So even if κ_ν in the line center is large, $\tau_\nu^{\text{core}} > 1$, the wings are transparent with $\tau_\nu^{\text{wing}} < 1$. Here, the cross-talk between different frequencies within the line is important, and it largely determines the resulting NLTE effects in the profile. The frequency redistribution of photons over the line profile, as it occurs in scattering processes, may transfer photons from the optically thick core to optically thin wings, thus allowing the photons to escape from the photosphere. The process, termed as *photon loss in the wings*, drives the source function S^l away from the LTE value B_ν .

In this chapter, the NLTE effects on Mn and Co abundances are also described. Line profiles are computed under both LTE and NLTE assumptions; they are fitted to the observed profiles by means of element abundance variations. The logarithmic abundance differences of the fits with respect to the initial element abundance from the model atmosphere, $\Delta \log \varepsilon$, is referred to as the *abundance correction*. The difference in abundances required to fit LTE and NLTE profiles is referred to as the *NLTE (abundance) correction* $\Delta_{\text{NLTE}} = \log \varepsilon^{\text{NLTE}} - \log \varepsilon^{\text{LTE}}$.

5.1 NLTE and HFS effects on solar Mn line formation

The computed profiles for selected lines are given in Fig. 5.1 together with the solar spectrum. For comparison we show profiles under LTE and NLTE conditions, with and without HFS. The examples on the left and on the right panel are representatives of two groups of lines that we were able to distinguish in the analysis.

The first group contains those lines, mainly weak with $W_\lambda < 80$ mÅ that are formed deep in the photosphere, in the layers with $-1 < \log \tau_{5000} < 0$. At these depths, the gradient of the local temperature T_e is very strong (see Fig. 3.1), changing by ~ 1000 K between the layers with $\log \tau_{5000} \approx 0$ and $\log \tau_{5000} \approx -1$. The departure coefficients of the lower levels of the corresponding transitions are all below unity, which leads to an increase of the line formation depth according to the equation 5.2. Due to a large T_e gradient, even a small shift of the optical depth scale means that the formation of lines under NLTE takes place at significantly higher T_e when compared to the case of LTE. In addition, the lower levels are depopulated to a larger extent compared to the upper level, $b_i < b_j$ over the entire line formation depth. Hence, the line source function is larger than its LTE value, $S^l > B_\nu(T_e)$. The combined effect is that under NLTE *weak lines are even weaker*. NLTE abundance corrections Δ_{NLTE} are positive due to decreased absorption over the entire line profile. In this case, both LTE and NLTE profiles will fit the observed lines, provided

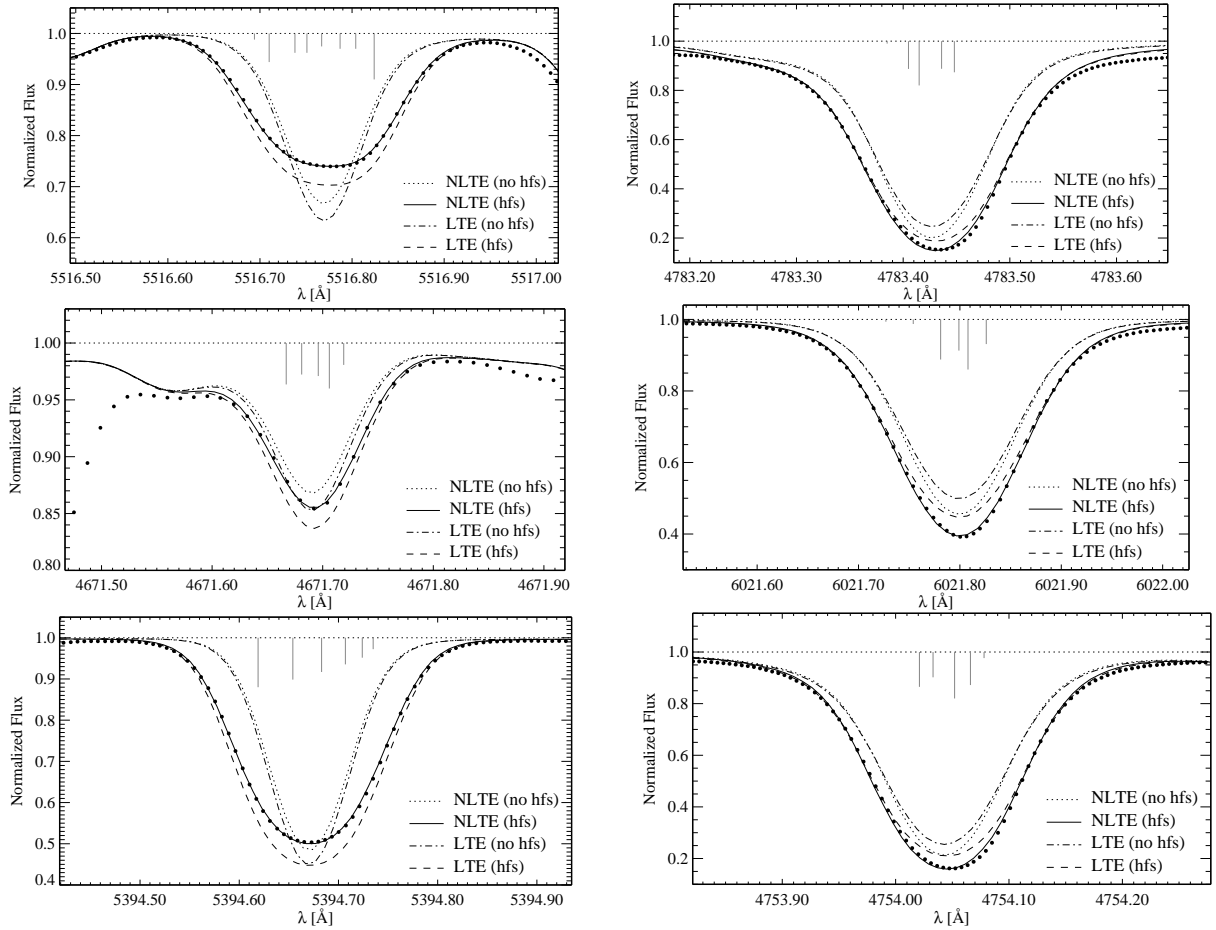


Figure 5.1: Selected observed solar Mn I profiles (filled circles). Synthetic NLTE and LTE profiles with and without HFS are labeled correspondingly. NLTE results are based on the reference atomic model. Wavelength positions and relative line strengths of the HFS components are indicated.

a certain abundance correction is performed. The good examples are two weak intercombination lines from the Mn I ground state, 5394 and 5432 Å.

Stronger lines are formed within larger depth ranges. At the depths of line core formation the upper levels are depopulated more efficiently than the lower ones, $b_i > b_j$. The source function drops below its LTE value, $S^l < B_\nu(T_e)$, which is driven by photon loss in the line wings. The departure coefficients of the lower levels are also below unity, $b_i < 1$. However, due to the small gradient of T_e at the depths of core formation, the change in opacity means small change in the local temperature. Thus, the dominant NLTE effect in the line core is the deviation of the source function from the Planck function. In the deeper layers with large gradient of T_e , where the wings are formed, overionization produces underpopulations of all levels $b_i < 1$. Accordingly, for the strongest lines (e.g. $\lambda\lambda$ 4783, 6021 Å in Fig. 5.1) the absorption in the core is amplified and the absorption in the wings is decreased relative to LTE. It is important that profiles computed under the LTE approach can not fit the observed lines due to their different profile shapes. NLTE abundance corrections are scattered around zero or negative.

The hyperfine splitting plays a crucial role in formation of Mn lines. Neither LTE, nor NLTE profiles in Fig. 5.1 computed without HFS fit the observed lines at all. The wings are too narrow, the cores are too deep for weak lines and too shallow for strong lines. The reason is that HFS is essentially a line broadening mechanism, which enters the line extinction coefficient (equation 2.38) and, thus, can alter the total energy absorbed in the line. Physically, the formation depth of individual weak HFS components is larger than for an unsplitted stronger line. Hence, HFS effectively de-saturates strong lines leading to a compound profile, where the strength of each component is more linearly proportional to the element abundance. The strong lines computed with HFS are deeper all over the profile. For the weak unsaturated lines, larger depth of formation means larger temperatures in the layers where $\tau_\nu^l < 1$. Thus, emission increases, and the line becomes shallower.

This can be visualized with the help of Table 5.1, where the depths of formation computed with and without HFS for a sample of lines with different W_λ and gf values are given. These are average depths of NLTE line formation calculated with the contribution function to the total emergent radiation according to Achmad et al. (1991). Both for strong and weak lines the depth of core formation decreases when hyperfine splitting is neglected in line synthesis. The corresponding shift in local temperatures ΔT_e is given in the last column. As expected, the formation of weaker lines takes place at significantly higher T_e . For instance, the resonance line at 5394.67 Å with 6 HFS components is formed in the layer with $T_e = 5340$ K, rather than in the layer with $T_e = 4920$ K (depth of formation for the same line with a single component).

Table 5.1: Average depths of Mn I NLTE line formation for a line with continuum according to Achmad et al. (1991).

λ [Å]	W_λ , [mÅ]	$\log \tau_{5000}$			ΔT_e , K
		HFS	no HFS	wing	
5394.67	78	-0.7	-1.4	-0.18	420
5432.51	48	-0.57	-0.86	-0.19	259
4055.54	136	-2.43	-2.68	0.05	57
4058.93	101	-1.88	-2.14	0.05	63
4070.28	70	-0.88	-1.10	0.05	135
6013.50	87	-1.03	-1.41	-0.26	190
6016.64	98	-1.18	-1.51	-0.26	137
6021.80	97	-1.68	-1.84	-0.26	46

The effect of hyperfine structure on Mn abundances derived from lines of different strength

is very large. The weak solar lines with $W_\lambda < 50 \text{ m}\text{\AA}$ (e.g. the intercombination line at 5432 \AA) computed as a single unsplitted component require the abundances ~ 0.15 larger than the same lines with included hyperfine splitting. For the strong solar lines, like 4783 and 4823 \AA , abundances calculated without HFS are overestimated by $0.3 - 0.35$ dex. Whereas, satisfactory fitting of the equivalent widths of intermediate-strength lines, like 5420 \AA with $W_\lambda \sim 85 \text{ m}\text{\AA}$, requires the abundance $0.5 - 0.6$ dex higher compared to the case when HFS is taken into account. These results confirm the significance of HFS effects, which *must be* treated correctly for lines of any strength. It is noteworthy that in many solar and stellar analyses of Mn hyperfine splitting is neglected on the basis that the abundances of *weak* lines are insensitive to the inclusion of HFS. We have just demonstrated that this assumption may be misleading.

5.2 NLTE effects on Mn lines in a wide range of stellar parameters

The NLTE effects on Mn lines in a wide range of stellar parameters can be understood by considering the NLTE corrections Δ_{NLTE} required to equalize the NLTE and LTE equivalent widths. These values are calculated with the reference model of the Mn atom, but with two different scaling factors for hydrogen collisions S_{H} . Tables A.5 and A.6 (see the appendix) show the NLTE abundance corrections calculated with $S_{\text{H}} = 0$ and $S_{\text{H}} = 0.05$, respectively. Hyphens in the tables refer to the lines with theoretical NLTE equivalent widths below $3 \text{ m}\text{\AA}$. The discussion below is based on the data from Table A.6 calculated with $S_{\text{H}} = 0.05$. The values derived for $S_{\text{H}} = 0$ only provide an upper limit on NLTE abundance corrections, when the thermalizing effect of collisions is minimized.

The NLTE mechanisms, responsible for the behavior of line profiles in models with different temperatures ($5000 \leq T_{\text{eff}} \leq 6200 \text{ K}$) and a solar metallicity, are essentially the same as for the Sun. The strong lines are characterized by an amplified absorption in the core and a decreased absorption in the wings relative to LTE. The physics behind is the overionization at the depth of the line wing formation, where $b_i < 1$ and $b_i < b_j$. At the depths of the core formation, photon losses in the line wings result in $b_i > b_j$, so the core in NLTE is deeper than in LTE. The net effect on the abundances is relatively small. As can be seen in Table A.6, for any model with $[\text{Fe}/\text{H}] = 0$ the NLTE abundance corrections Δ_{NLTE} vary from $+0.06$ to -0.1 dex. In particular, the triplet at 600 nm (Mult. 27) requires slightly smaller abundance in NLTE, whereas the lines of resonance triplet at 403 nm are systematically weaker in NLTE compared to LTE.

The near-UV resonance lines of multiplet 2 are strong at solar metallicity with $W_\lambda \geq 300 \text{ m}\text{\AA}$, and their wings dominate the profile. The lower and upper levels of the corresponding transitions are $a^6\text{S}$ and $z^6\text{P}^\circ$, respectively. At all depths above $\log \tau_{5000} \sim 0$, overionization leads to depopulation of the lower level $b_i < 1$, although $b_i \approx b_j$ up to $\log \tau_{5000} \sim -2$. Therefore, decreased absorption in the wings requires slightly larger abundances under NLTE. Above this optical depth, the upper level is depopulated to a larger extent than the lower level. Thus, the core is slightly darker compared to LTE.

The highly-excited near-IR lines of multiplet 27 do not have pronounced wings. A larger contribution to the line strengths comes from the cores. The cores are formed in the upper layers $\log \tau_{5000} \sim -2$, where spontaneous transitions efficiently depopulate upper levels, thus $b_i > b_j$ and $S^l < B_\nu(T_e)$. In addition, there is an interlocking with transitions of multiplet 2, which connect the Mn I ground state with lower levels of multiplet 27. Thus, photon pumping in the strong near-UV lines also increases populations of $z^6\text{P}^\circ$ levels. As a result, absorption in the cores of near-IR lines is amplified compared to LTE, and the Δ_{NLTE} are negative.

A third group that we are interested in contains three relatively strong lines with $\lambda\lambda 4754, 4783, 4823 \text{ \AA}$, which are formed in transitions from $z^8\text{P}^\circ$ to $e^8\text{S}$ levels. The NLTE abundance corrections for these lines (Mult. 16) are either positive for the models with lower temperatures, or slightly negative by ~ -0.02 dex for the models with $T_{\text{eff}} > 6000 \text{ K}$. Δ_{NLTE} reaches -0.1 dex when surface gravity decreases. NLTE corrections scattered around zero are due to the competing

influence of $S^l < B_\nu(T_e)$ at the depth of core formation and $S^l > B_\nu(T_e)$ at the depth of wing formation. At supersolar temperatures, photon pumping in transitions from the ground state ($a^6S - z^6P^\circ$) is amplified thus increasing the population of z^6P° which is collisionally bound with the z^8P° levels. As a result, departure coefficients for these levels increase, and in transitions of multiplet 16 S^l falls below $B_\nu(T_e)$.

With decreasing metallicity, line formation shifts to deeper layers, where photoionization is dominant in depopulating all Mn I levels. Hence, for $[\text{Fe}/\text{H}] \leq -1$ NLTE corrections for all lines are positive. In the models with $T_{\text{eff}} \leq 5500$ K and $[\text{Fe}/\text{H}] = -2$, the Δ_{NLTE} are larger for the excited lines than for the resonance lines. If T_{eff} also increases, the stellar flux maximum is shifted to the shorter wavelengths, and ionization from the ground state of Mn I becomes more important. So in the models with $T_{\text{eff}} \geq 6000$ K and $[\text{Fe}/\text{H}] \leq -2$, the NLTE abundance effect is more pronounced for the resonance triplet at 403 nm. However, as emphasized above, increasing T_{eff} also increases the rates of collisions, so *maximum* NLTE effects for the resonance lines are in fact found for the moderately warm models ($5500 \leq T_{\text{eff}} \leq 6000$) with lowest metallicity (smallest amount of free electrons).

The NLTE effects on the resonance Mn I line at 4033 Å for selected models from the grid are shown in Fig. 5.2. Three models with different metallicities 0, -1.2, -2.4 are selected for comparison. Other model parameters are equal: $T_{\text{eff}} = 6000$ K, and $\log g = 4$. This is a clear demonstration of the importance of deviations from LTE at decreased metallicity.

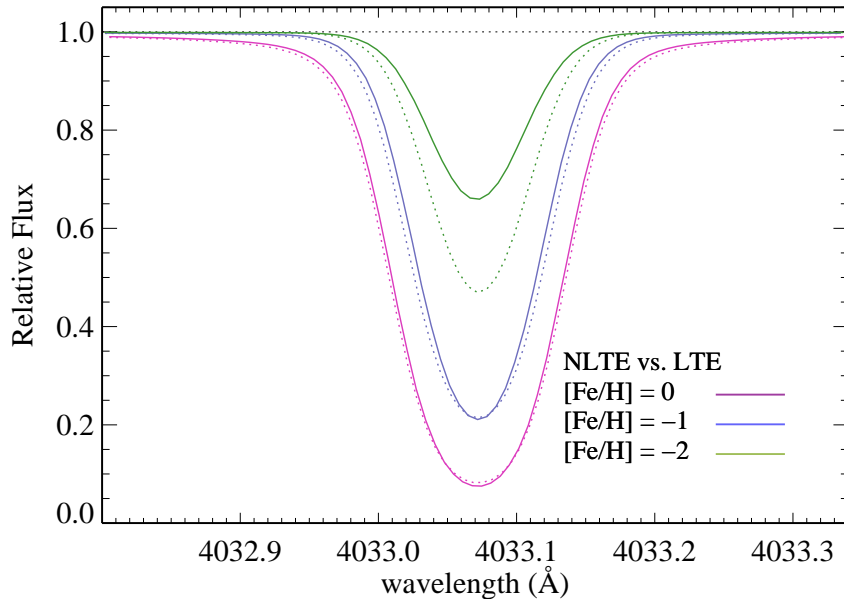


Figure 5.2: Synthetic profiles of the Mn I line at 4033 Å for models with constant effective temperature and gravity ($T_{\text{eff}} = 6000$, $\log g = 4$) and different metallicities ($[\text{Fe}/\text{H}] = 0, -1, -2$). NLTE and LTE profiles are marked with solid and dotted lines, respectively.

It is remarkable that for all models with $T_{\text{eff}} \geq 5500$ K and very low metal abundance, $[\text{Fe}/\text{H}] = -3$, we find a difference of 0.15 – 0.2 dex between the NLTE corrections for resonance and excited lines. For the models with low gravity, $\log g = 3.4$, resonance lines require 0.2 dex higher abundances compared to the excited lines with larger metallicity, $[\text{Fe}/\text{H}] = -2.4$. This difference is enhanced if collisions with neutral hydrogen atoms are neglected (Table A.5). Thus, NLTE can solve the discrepancy (see chapter 1) between the abundances derived from the Mn I resonance triplet at 403 nm and excited lines, which is found in analyses of metal-poor subdwarfs and subgiants (Gratton 1987, Gratton 1989, Lai et al. 2008). Test calculations for the cool giant model ($T_{\text{eff}} = 4800$ K, $\log g = 1.8$, $[\text{Fe}/\text{H}] = -3.3$, not shown in Tables A.5 and A.6) also indicate that the NLTE corrections for the resonance lines are by ~ 0.15 dex higher than those for excited

lines at 4783 and 4823 Å. This is the first evidence that *the discrepancies between two line sets found by Johnson (2002) and Cayrel et al. (2004) in their studies of giant stars are due to NLTE*. This issue will be in discussed in Sect. 7.1.2.

We have also checked the influence of HFS on Mn I line formation in metal-poor models. Fig. 5.3 shows NLTE profiles of Mn I line at 4033 Å calculated for three models with different metallicities ($[\text{Fe}/\text{H}] = 0, -1, -2$, $T_{\text{eff}} = 6000$ K, $\log g = 4$). The synthetic profiles computed with and without HFS are marked with solid and dotted lines, respectively. The line is splitted into six HFS components. In the solar metallicity model, the profile computed without HFS overestimates the abundance by 0.37 dex. In the models with $[\text{Fe}/\text{H}] = -1$ and -2 , the difference in profiles corresponds to an abundance correction of 0.33 dex and 0.06 dex, respectively. The resonance line at 4033 Å is still saturated at $[\text{Fe}/\text{H}] = -1$, hence a large discrepancy between profiles with and without HFS appears even at low metallicity. The abundance calculations performed for the weaker line at 4823 Å in the same models but with $T_{\text{eff}} = 5500$ K confirm the importance of HFS in the solar and mildly metal-poor atmospheres. In particular, the overestimate of Mn abundance at $[\text{Fe}/\text{H}] = 0$ is as large as 0.35 dex, and at $[\text{Fe}/\text{H}] = -1$ the error due to the neglect of HFS is still ~ 0.08 dex. This is significant, if one pretends at a high accuracy of calculated abundances in stars.

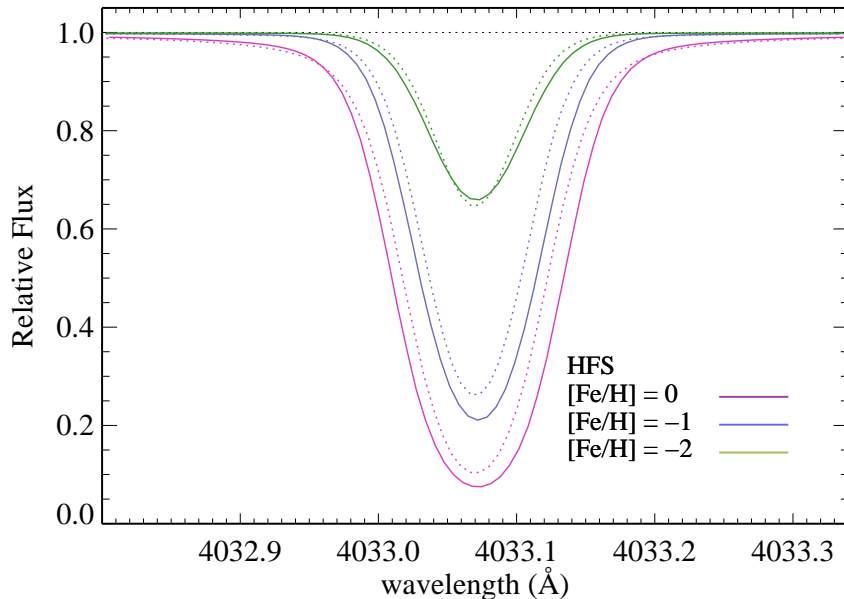


Figure 5.3: Synthetic profiles of the Mn I line at 4033 Å for models with constant effective temperature and gravity ($T_{\text{eff}} = 6000$, $\log g = 4$) and different metallicities ($[\text{Fe}/\text{H}] = 0, -1, -2$). NLTE profiles computed with HFS and without HFS are marked with solid and dotted lines, respectively.

We conclude that *the neglect of HFS alone in a differential analysis of a star with respect to the Sun leads to abundance errors of the order of 0.1 – 0.4 dex, depending on the line strength. If NLTE effects are also ignored, the combined error in abundances may exceed 1.0 dex.*

5.2.1 Collisions with H I atoms

It is useful to inspect the sensitivity of NLTE abundance corrections Δ_{NLTE} to the treatment of inelastic collisions with hydrogen. This is a factor that can produce systematic errors in NLTE calculations. In the following chapter, we will show how the *differential* $[\text{Mn}/\text{Fe}]$ ratios for the program stars react to changes of S_{H} . Here, we will rather concentrate on the change of NLTE abundance corrections derived for individual Mn I lines for several models from the grid.

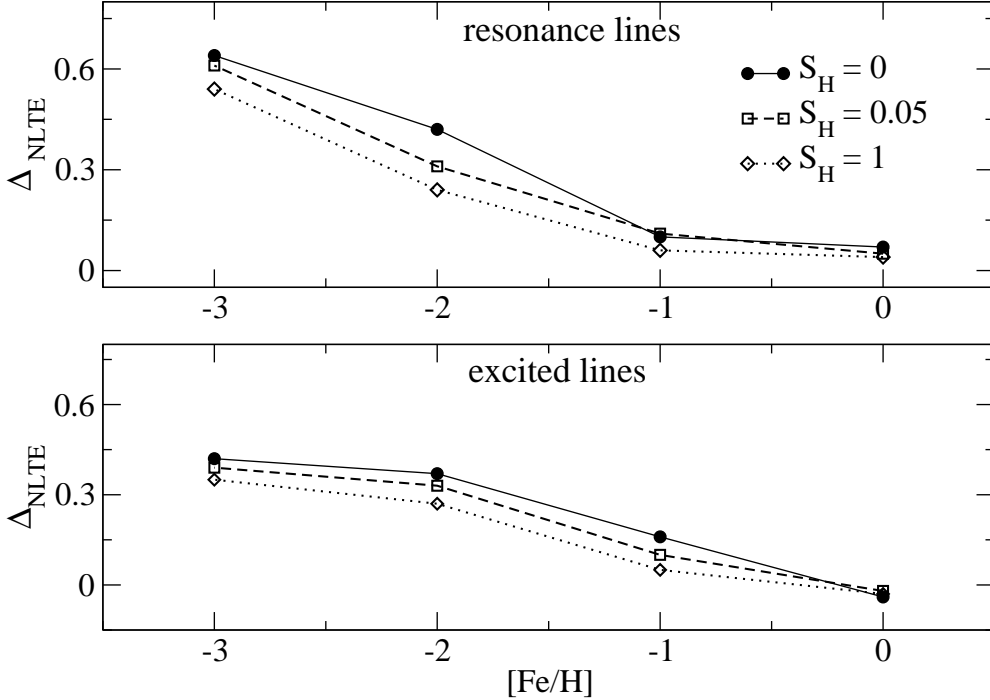


Figure 5.4: NLTE abundance corrections Δ_{NLTE} for Mn I lines calculated with three different values of a scaling factor to inelastic collisions with hydrogen $S_{\text{H}} = 0, 0.05, 1$: the average for the resonance triplet at 403 nm (top), the average for excited lines at 4783 and 4823 Å. Calculations are performed for four models with $T_{\text{eff}} = 6000$, $\log g = 4$, $[\text{Fe}/\text{H}] = 0, -1, -2, -3$.

Fig. 5.4 demonstrates the behaviour of Δ_{NLTE} calculated with three different scaling factors to the standard Drawin's formula 0, 0.05, 1 (solid, dashed, and dotted lines, respectively) as a function of a model metallicity ($T_{\text{eff}} = 6000$ K and $\log g = 4$). Here, the average Δ_{NLTE} derived for the resonance triplet at 403 nm are shown in the top panel, and that for the excited lines at 4783 and 4823 Å in the bottom panel. These five lines are traditionally used in the analyses of Mn in metal-poor stars. As expected, with increasing collision efficiency the NLTE abundance corrections decrease in magnitude. The resonance lines are weakly sensitive to H collisions at all metallicities, except for $[\text{Fe}/\text{H}] = -2$. But in the latter case, Δ_{NLTE} is already large enough. The excited lines steadily decrease in their sensitivity to H collisions for decreasing Fe abundance. This is not unexpected because the major overionization in Mn I is expected to occur from the low-excited levels, e.g. $z^8\text{P}^{\circ}$, but not from the ground state. In the metal-poor stars, overionization is strongly amplified as is obvious from the magnitude of NLTE corrections thus reducing the impact of collisions on level populations. The important result following from the Fig. 5.4 is that any collision scaling factor chosen within the reasonable range $0 \leq S_{\text{H}} \leq 1$ (see section 3.4.3) leads to a qualitatively similar behavior of NLTE abundance corrections. So, the error introduced by our bad knowledge of S_{H} is systematic much like the errors in stellar parameters and models. Having a free choice of S_{H} from 0 to 1, one would most likely choose the value that produces the NLTE abundance corrections lying in the middle of the upper and lower limits. In this respect, $S_{\text{H}} = 0.05$ (our reference value) seems to be a good choice. We will show in Sect. 7.1.3 that this value is also supported by the smallest fitted-abundance spread between different lines of selected stars.

5.3 NLTE and HFS effects on the formation of Co lines

The computed profiles for selected lines of Co I are compared with the solar spectrum in Fig. 5.5. The synthetic profiles were calculated under LTE and NLTE conditions, with and without HFS. In fact, all Co I lines selected for the abundance analysis in the Sun and metal-poor stars are relatively weak. The equivalent width of the strongest solar line at 4121 Å is 130 mÅ. Hence, the lines computed under NLTE behave similarly: they are uniformly weakened compared to the LTE profiles. The main effect is the shifting of the optical depth scale due to $b_i < 1$ at line formation depths. As a result, the NLTE abundance corrections are positive; for a majority of lines computed with the *solar* model atmosphere, $\Delta_{\text{NLTE}} \sim +0.15$ dex, which is larger than the NLTE corrections for Mn I lines. Some lines of Co I require an even larger abundance in NLTE: for the line at 4110 Å we derive $\Delta_{\text{NLTE}} = 0.2$ dex. This result is a direct consequence of the dominance of photoionization in the statistical equilibrium of Co I.

The errors in abundances introduced by neglecting HFS are of the same order of magnitude as for the Mn I lines. The abundances derived for saturated lines, like 4121 Å and 3501 Å are overestimated by 0.4 dex and 1 dex, respectively. The weak lines, like 5647 Å are less affected: the profile computed with all HFS components gives ~ 0.1 dex lower abundance. At low metallicity, $[\text{Fe}/\text{H}] = -2$, the abundances are almost insensitive to inclusion of HFS in spectrum synthesis; the errors for all investigated lines are not larger than 0.05 dex.

The NLTE abundance corrections calculated for atmospheric models with different parameters from the grid are given in Table 5.2. These values are computed only for five Co I lines, which can be detected in *our* spectra of stars with $[\text{Fe}/\text{H}] < -0.5$. Note that the line at 3501 Å, also present in the table, belongs to the Co II and it will be discussed below. Hyphens refer to the lines with computed NLTE equivalent widths below 1 mÅ. This limit is smaller than that for Mn I lines, 3 mÅ, because the Co I lines become very weak at metallicity $[\text{Fe}/\text{H}] = -1$. Only a near-UV line at $\lambda 3845$ Å (Mult. 34) and a blue line at 4121 Å (Mult. 28) can be studied down to the lowest metallicity $[\text{Fe}/\text{H}] = -3$. A line of multiplet 29 at 4110 Å is sufficiently strong at low temperatures $T_{\text{eff}} \leq 5500$, but as T_{eff} increases the line strength decreases rapidly. Hence at $T_{\text{eff}} > 6000$ K, the 4110 Å line disappears already at $[\text{Fe}/\text{H}] = -2$. The near-UV line at $\lambda 3957$ Å (Mult. 18) and a blue line at 4020 Å (Mult. 16) are relatively weak already at $[\text{Fe}/\text{H}] = 0$, and they almost disappear at $[\text{Fe}/\text{H}] < -1$. Although it is not our goal to investigate giant stars (Sect. 3.3.1), we have performed test calculations for the cool giant model ($T_{\text{eff}} = 4800$ K, $\log g = 1.8$, $[\text{Fe}/\text{H}] = -3.3$). This exception is made because nearly all analyses of Co abundances in metal-poor stars refer to bright cool giants. In spectra of these stars, a *larger* number of Co lines can be detected than in spectra of subdwarfs. Thus, having test NLTE corrections for a cool giant model, we can perform a rough comparison of our NLTE abundances of Co in metal-poor stars with the other data sources (see chapter 7).

Let us now examine how NLTE abundance corrections change with the variation of stellar parameters. In general, Δ_{NLTE} increase with decreasing metallicity from $\sim 0.1 - 0.2$ dex for $[\text{Fe}/\text{H}] = 0$ dex to $\sim 0.6 - 0.7$ dex for $[\text{Fe}/\text{H}] = -3$ dex. This is demonstrated in Fig. 5.6 (top panel) for the strongest solar Co I line at 4121 Å. Variation of the effective temperature by 1000 K leads to small changes in Δ_{NLTE} at solar metallicity and $[\text{Fe}/\text{H}] = -2$, but when the metal content is one tenth of the solar value the sensitivity of NLTE corrections to the effective temperature suddenly increases. For $T_{\text{eff}} = 5000$ K, we find $\Delta_{\text{NLTE}}(4121\text{Å}) = +0.15$ dex, and for $T_{\text{eff}} = 6000$ K $\Delta_{\text{NLTE}}(4121\text{Å}) = +0.47$ dex. The line at 3845 Å behaves similarly. Whereas, the NLTE abundance corrections increase rather uniformly for the warm and hot atmospheric models with $[\text{Fe}/\text{H}] < 0$, the pronounced change of Δ_{NLTE} is seen for the cool model with $T_{\text{eff}} = 5000$ K in the metallicity range $-2 \leq [\text{Fe}/\text{H}] \leq -1$. This behavior can be understood as follows. At subsolar temperatures and solar metallicities, the line 4121 Å is rather strong and its NLTE correction is determined by the *competition* of $S^l > B(\nu)^l$ in the wings and $S^l < B_\nu^l$ in the core. As discussed above, the condition $S^l/B_\nu^l < 1$ implies a strengthening of the line. At a decreased metallicity, $[\text{Fe}/\text{H}] = -2$, the line becomes weak and is formed in the deeper layers, where $S^l > B_\nu^l$ and $\kappa_\nu^l < \kappa_\nu^{l,\text{LTE}}$ over the entire line formation depth. The raised NLTE source function and decreased opacity cause significant weakening of the line, and, thus, large *positive* NLTE abundance corrections.

Table 5.2: NLTE abundance corrections for lines of Co I calculated with selected models of the grid. Hyphens refer to the lines with computed NLTE equivalent widths below 1 mÅ. Collisions with neutral hydrogen are included with the reference scaling factor $S_H = 0.05$. Note that Δ_{NLTE} for the Co II line at 3501 Å are also given for the cases when its equivalent width is below 1 mÅ.

$T_{\text{eff}}/\log g/$ [Fe/H]	Δ_{NLTE}					
	3501	3845	3957	4020	4110	4121
4800/1.8/-3.3	0.12	0.92	0.82	-	0.88	0.88
5000/4/ 0	-0.04	0.03	0.05	0.08	0.15	0.04
5000/4/-1	-0.04	0.13	0.17	0.18	0.28	0.15
5000/4/-2	-0.03	0.45	0.44	0.47	0.48	0.62
5000/4/-3	0.08	0.67	-	-	0.69	0.66
5500/4/ 0	-0.03	0.08	0.12	0.12	0.23	0.1
5500/4/-1	-0.01	0.27	0.3	0.32	0.36	0.35
5500/4/-2	0.02	0.66	-	0.63	0.63	0.67
5500/4/-3	0.17	0.75	-	-	-	0.74
5780/4.4/ 0	-0.02	0.11	0.14	0.12	0.23	0.1
6000/4/ 0	-0.02	0.1	0.15	0.18	0.22	0.13
6000/4/-1	0.01	0.4	0.39	0.39	0.4	0.47
6000/4/-2	0.06	0.64	-	-	0.63	0.63
6000/4/-3	0.31	0.69	-	-	-	0.7
6200/3.4/ 0	-0.02	0.15	0.17	0.18	0.23	0.16
6200/3.4/-1.2	0.01	0.5	0.47	0.46	0.47	0.52
6200/3.4/-2.4	0.11	0.65	-	-	-	0.64
6200/4.6/ 0	-0.01	0.1	0.13	0.13	0.17	0.12
6200/4.6/-1.2	0.01	0.43	0.42	0.41	0.42	0.46
6200/4.6/-2.4	0.11	0.61	-	-	-	0.59
6400/4.2/ 0	-0.01	0.15	0.17	0.18	0.2	0.15

On the other side, if a line is already weak in the solar atmosphere, then the NLTE abundance corrections display a very regular behavior at all temperatures and metallicities. As an example, we show Δ_{NLTE} for the 4020 Å line (Fig. 5.6, bottom panel) computed with different atmospheric models. The line becomes too weak at very low metallicity, hence Δ_{NLTE} is given only for the models with $[\text{Fe}/\text{H}] \geq -2$. The identical dependencies $\Delta_{\text{NLTE}} - T_{\text{eff}} - [\text{Fe}/\text{H}]$ are characteristic of the near-UV line at 3957 Å.

As expected, the response of NLTE corrections to the effective temperature is not uniform. For two strong lines at 3845 and 4121 Å, the NLTE corrections are maximal in the warm model $T_{\text{eff}} = 5500$ with the smallest metallicity. We have already encountered this phenomenon analyzing the Mn I lines: high temperatures increase the rates of collisions, hence deviations from LTE are slightly reduced. At low temperatures, NLTE abundance corrections are also smaller because the stellar flux maximum is shifted to longer wavelengths, away from ionization thresholds of the important Co I levels (see Sect. 4.3).

The NLTE corrections increase with decreasing surface gravity. However, for different metallicities and *supersolar* temperatures, reduction of $\log g$ from 4.6 to 3.4 changes the NLTE abundance corrections for all lines only by $\sim 0.03 - 0.05$ dex. We also performed test calculations for the models with $T_{\text{eff}} = 5000$, $\log g = 3$, $[\text{Fe}/\text{H}] = 0, -1, -2, -3$. The results are compared to the corresponding models with $\log g = 4$ in Fig. 5.6. For *cool* models, Δ_{NLTE} strongly depends on the stellar gravity. The reason is that due to the weakened UV radiation field, the rates of all transitions become more sensitive to collisions. In particular, when the surface gravity decreases by a factor of 10 ($\Delta \log g = 1$), the NLTE abundance corrections increase by 0.07 dex at $[\text{Fe}/\text{H}] = -1$ dex and by ~ 0.15 dex at $[\text{Fe}/\text{H}] = -2$ dex. The extreme values of Δ_{NLTE} are found for

the cool giant model with a subsolar temperature $T_{\text{eff}} = 4800$ K, $[\text{Fe}/\text{H}] = -3.3$, and a very low gravity $\log g = 1.8$. This is an expected result, because all collisional interactions become very weak due to the small metallicity and gravity, and the role of radiative processes increases in spite of the reduced temperature.

5.3.1 Lines of Co II in NLTE

In Sect. 4.4, we showed that many Co II levels with intermediate excitation energies 4 – 5 eV do not have LTE populations in the lower atmosphere, $b_j \neq 1$. Moreover, for many discrete transitions connecting these levels and the low-excitation levels of Co II, $b_i \neq b_j$. Non-equilibrium populations of the upper levels set deviations from LTE in the line source function. As a result, there are NLTE effects in line intensities.

Here, we investigate the formation of the Co II line at 3501 Å ($a^5\text{P}_{7/2} - z^5\text{D}_{9/2}$). It is relatively unblended in the solar spectrum and can be used to test the ionization equilibrium of Co even in the metal-poor stars. The profiles of this line computed under NLTE and LTE, with and without HFS are shown in Fig. 5.5. The NLTE abundance corrections calculated with different atmospheric models from the grid are presented in Table 5.2 and in Fig. 5.8. Already at solar metallicities, Δ_{NLTE} are *nonzero*. Low effective temperatures favor *negative* NLTE abundance corrections, down to -0.04 dex. But, even in the models with supersolar T_{eff} and solar metallicity, $\Delta_{\text{NLTE}} \sim -0.02$. The strengthening of the line profile under NLTE follows from the behavior of departure coefficients at the depths of line formation. Fig. 5.7 illustrates this for the model with $T_{\text{eff}} = 5000$ K, $\log g = 4.0$, $[\text{Fe}/\text{H}] = 0$. At $-1 < \log \tau_{5000} < 0$, departure coefficients of the lower and upper levels are in thermal equilibrium with the Co II ground state $a^3\text{F}$. The line source function is thermalized. However, the *absolute* populations of the levels are not in LTE, and the decisive factor is the opacity change. As $b_i > 1$ leads to the increased opacity, the wings that dominate the total equivalent width of the line are perceptibly stronger in NLTE.

At $[\text{Fe}/\text{H}] = -1$, there is a turning-point for all models: NLTE abundance corrections reach the minimum and then increase smoothly down to $[\text{Fe}/\text{H}] = -2$. In this metallicity range, several effects are important. The ionization equilibrium $N(\text{Co II})/N(\text{Co I})$ is different from the solar ionization equilibrium due to the smaller number of electrons. More than 90% of all Co atoms are singly-ionized. Hence, overionization from Co I only barely affects the populations of Co II levels. In particular, the ground state and low-excited levels have nearly LTE populations. Also, due to less ultraviolet opacity the radiation field is amplified producing overpopulation of the higher levels via the *photon pumping* mechanism. As seen in Fig. 4.10, the source function for the line 3501 Å becomes superthermal already at $\log \tau_{5000} \sim 0$, $b_j > b_i$, and the line is weakened compared to the LTE case. The same mechanism is responsible for the positive NLTE abundances corrections in the models with $[\text{Fe}/\text{H}] \leq -2$.

At very low metallicities and supersolar temperatures (Fig. 5.8), NLTE corrections are as large as $+0.3$ dex. This is a very interesting result and it could not be predicted from the analysis of NLTE effects on atomic level populations alone. But even with the subsolar effective temperature, $T_{\text{eff}} = 5500$ K, the calculated Δ_{NLTE} is as large as $\sim +0.2$ dex. Consequently, *the analysis of Co II lines in very metal-poor stars can lead to substantial errors in abundances, if NLTE effects are neglected.*

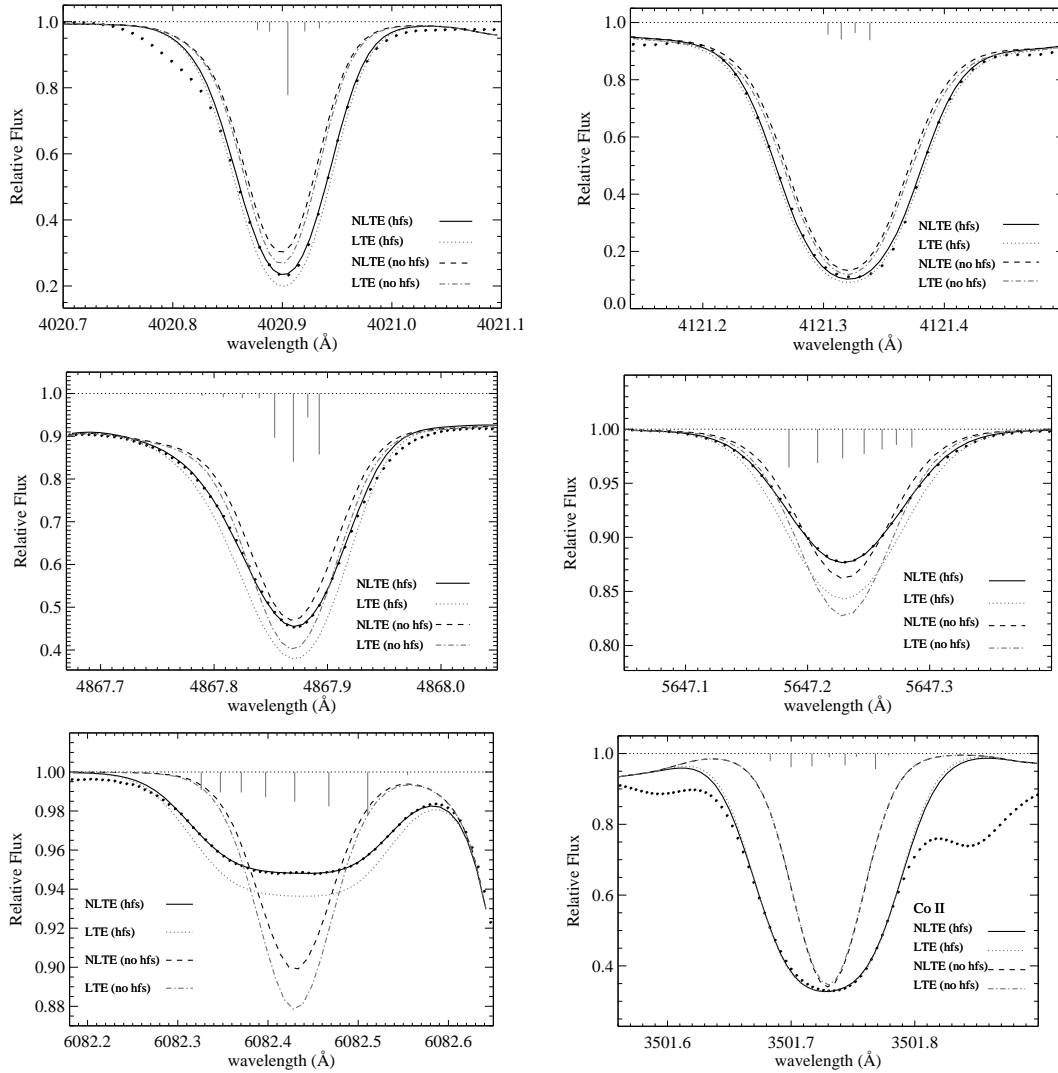


Figure 5.5: Selected observed solar Co I and Co II profiles (filled circles). Synthetic NLTE and LTE profiles with and without HFS are labeled correspondingly. NLTE results are based on the reference atomic model. Wavelength positions and relative line strengths of the HFS components are indicated. Note that the component strengths are not on the same scale in figures.

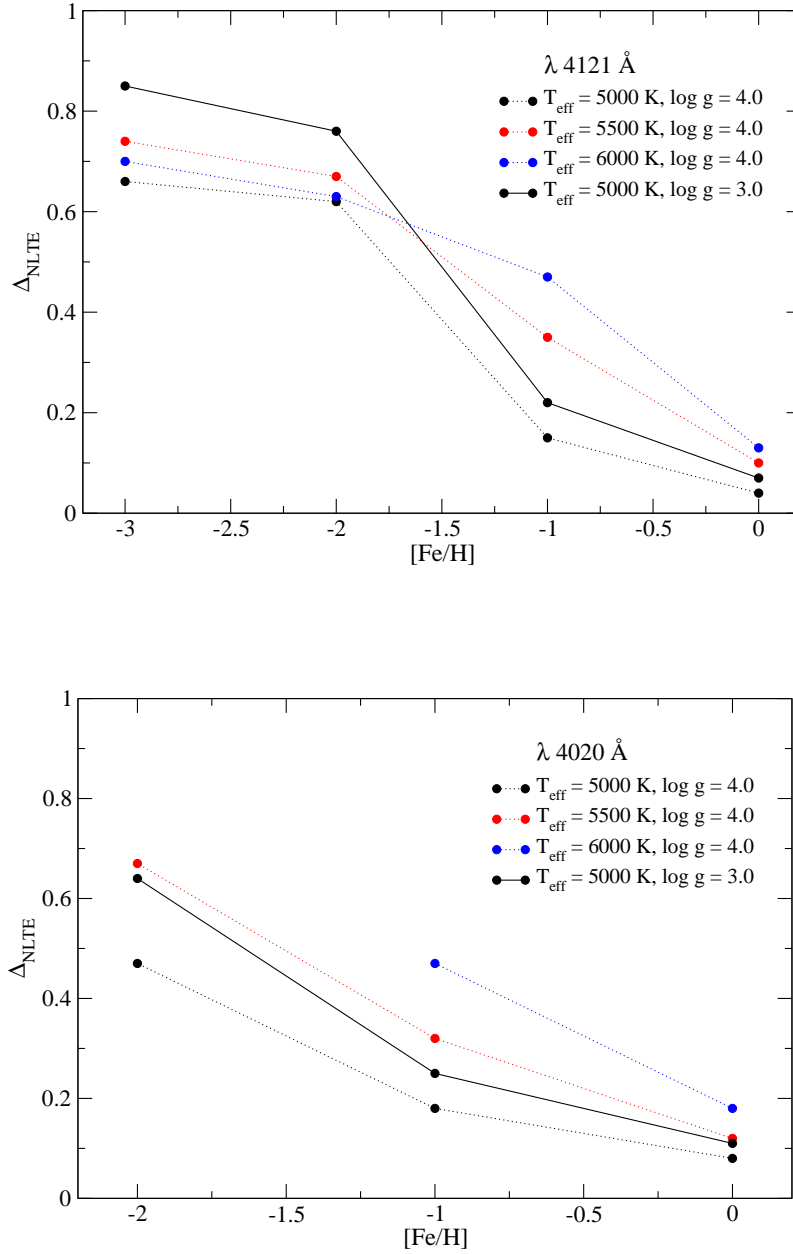


Figure 5.6: NLTE abundance corrections Δ_{NLTE} calculated for the Co I lines at 4121 (top) and 4020 (bottom) Å. Calculations are performed for sixteen models with $T_{\text{eff}} = 5000, 5500, 6000 \text{ K}$, $\log g = 3, 4$, $[\text{Fe}/\text{H}] = 0, -1, -2, -3$.

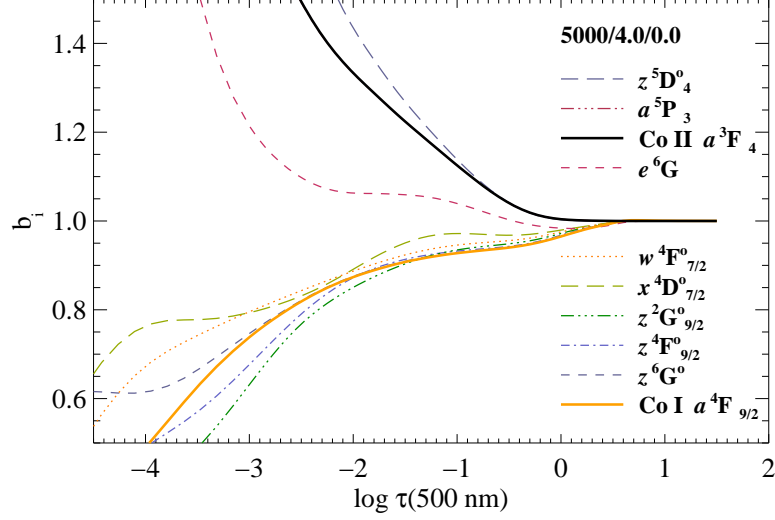


Figure 5.7: Departure coefficients b_i of selected Co I and Co II levels for the complete model of Co atom. The MAFAGS-ODF model atmosphere from the grid with the parameters $T_{\text{eff}} = 5000$ K, $\log g = 4.0$, $[\text{Fe}/\text{H}] = 0$ is used.

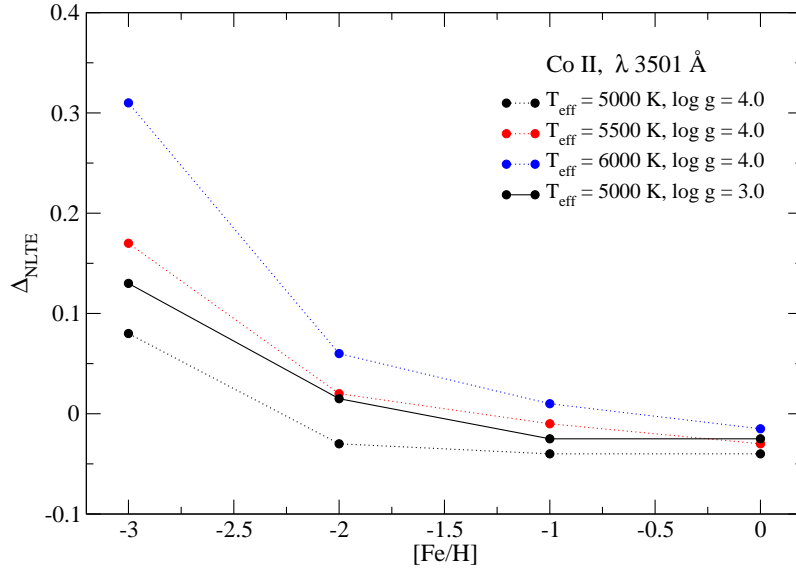


Figure 5.8: NLTE abundance corrections Δ_{NLTE} calculated for the Co II line at 3501 \AA . Calculations are performed for sixteen models with $T_{\text{eff}} = 5000, 5500, 6000$ K, $\log g = 3, 4$, $[\text{Fe}/\text{H}] = 0, -1, -2, -3$.

Chapter 6

Abundances in the Sun

One of the most important tasks associated with NLTE calculations is the analysis of *solar* photospheric element abundances. This is a very non-trivial problem: the uncertainties in oscillator strengths and in the line broadening, and the deficiencies of atmospheric models directly enter the calculated abundances. Exactly for this reason, *differential* abundances in stars can often be determined with a higher accuracy than absolute abundances in the solar photosphere. Still, the analysis of the solar chemical composition has some advantages. Many researchers maintain that the stringent test of the accuracy of spectroscopic abundances for a majority of elements is their agreement with that of chondritic meteorites. There are *no* analogous tests for the galactic stars.

The abundances of Mn and Co in the Sun and metal-poor stars are derived by the method of spectrum synthesis, which is in details described in Sect. 3.5. We note that this method yields the *product* of the oscillator strength for a transition and the abundance of the element, $\log gf\varepsilon$. This parameter is given in Tables A.1 and A.2 (see appendix) for Mn and Co lines, respectively. It is convenient to specify $\log(gf\varepsilon)_{\odot}$ for every line instead of an absolute abundance $\log \varepsilon$, because one does not have to undertake new calculations when more reliable *gf*-values are available. *Mean* abundances are obtained by taking an average over all lines. For all mean abundances, the standard deviations σ are quoted as errors. The calculations are performed with the theoretical MAFAGS-ODF model atmospheres. The solar abundances obtained using the Holweger-Müller semi-empirical model (see Sect. 3.3.2) are given for comparison.

6.1 Solar abundance of Mn

The visual inspection of the solar spectrum allowed us to select 37 lines of Mn I, which are good enough to determine the solar Mn abundance from fitting their profiles. They are listed in Table A.1 of the appendix. Note that three strong resonance lines at 403 nm (also given in the Table) do not enter our sample because they are heavily blended. Unfortunately, there is no single set of measured oscillator strengths for all selected lines, hence $\log gf$ values from different sources are used. These data are described and compared in Sect. 3.5.1. Figure 6.1 shows NLTE and LTE abundances for the 37 lines of Mn I as a function of their equivalent widths. There is no obvious trend in line-to-line abundances with W_{λ} , although their spread is fairly large. The absolute abundances determined assuming LTE are *lower* than those derived with NLTE level populations. However, the average difference is small. The mean NLTE and LTE abundances are $\log \varepsilon_{\text{Mn},\odot}^{\text{NLTE}} = 5.40$ dex and $\log \varepsilon_{\text{Mn},\odot}^{\text{LTE}} = 5.35$ dex, respectively. The standard deviations of both values are equal, 0.07 dex. This is the evidence that some common parameters used in spectrum synthesis, are erroneous (damping parameters, or oscillator strengths). First, we check whether the scatter of abundances reflects the input of inhomogeneous oscillator strengths from different sources.

The $\log \varepsilon_{\text{Mn},\odot}^{\text{NLTE}}$ values calculated for *each* set of *gf*-values are given in Table 6.1. The interesting result is that the spread of abundances is not very large. With four of six *gf* data sets,

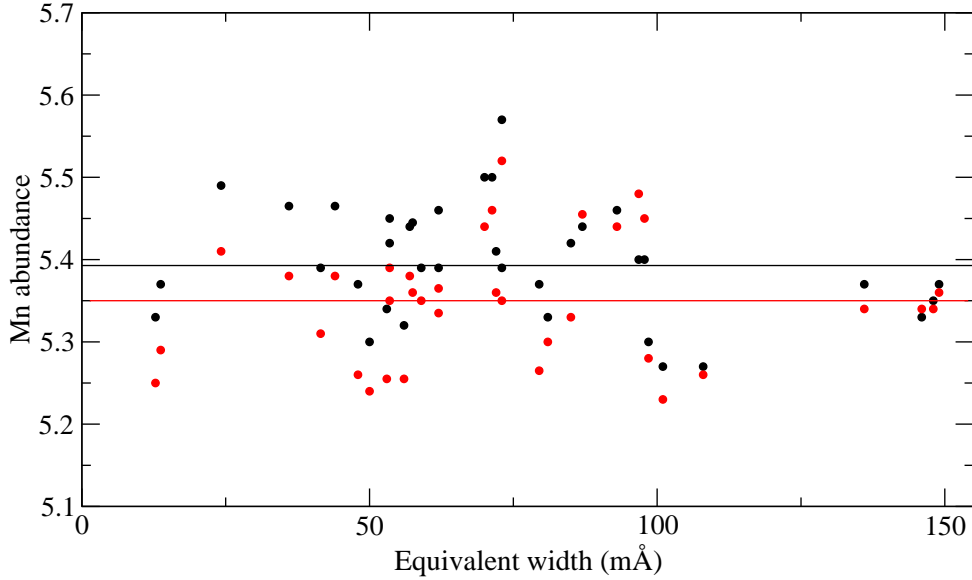


Figure 6.1: Abundances of the 37 solar Mn I lines. LTE abundances are marked with red circles, and NLTE abundances with black circles. The black and red lines indicate mean NLTE and LTE abundances, respectively.

we derive the mean NLTE abundance close to 5.4 dex. Obviously outstanding are the results obtained with the Woodgate’s (1966) and Booth, Blackwell, Petford & Shallis’s (1984) values. The former oscillator strengths seem to be too low, thus overestimating the Mn abundance. The standard deviation is also very large, 0.18 dex. The data measured by Booth, Blackwell, Petford & Shallis clearly underestimate the mean $\log \varepsilon_{\text{Mn},\odot}^{\text{NLTE}}$ value. As a matter of fact, these discrepancies are *not* unexpected. The statistical analysis of $\log gf$ values given in Sect. 3.5.1 showed that the transition probabilities measured by Booth, Blackwell, Petford & Shallis are systematically stronger compared to the data of Blackwell-Whitehead & Bergemann (2007). Also, $\log gf$ values for a majority of transitions measured by Woodgate (1966) were found to be underestimated. The oscillator strengths published by Greenlee & Whaling and Blackwell-Whitehead & Bergemann are consistent. Hence, it is not surprising that the $\log \varepsilon_{\text{Mn},\odot}^{\text{NLTE}}$ values calculated with the Blackwell-Whitehead & Bergemann’s (2007) and Greenlee & Whaling’s (1979) data are in agreement, with

Table 6.1: Mean NLTE abundances from Mn I lines based on oscillator strengths from different sources.

N_{lines}	Source of $\log gf^a$	Method	accuracy %	$\log \varepsilon_{\text{Mn},\odot}^{\text{NLTE}}$ [dex]	σ
17	1	beam foil	25	5.44	0.11
20	2	beam foil	50	5.52	0.18
19	3	laser excitation		5.40	0.11
25	4	total absorption	10	5.31	0.07
37	5	calculations		5.43	0.11
25	6	FT spectroscopy	10	5.39	0.07
37	7			5.40	0.07

^a References: (1) Greenlee & Whaling (1979); (2) Woodgate (1966); (3) Becker et al. (1980); (4) Booth, Blackwell, Petford & Shallis (1984); (5) Kurucz (1988); (6) Blackwell-Whitehead & Bergemann (2007); (7) All

the latter source leading to a slightly larger standard deviation. Only 25 lines in our list were measured by Blackwell-Whitehead & Bergemann (2007). When only those lines are used, we obtain $\log \varepsilon_{\text{Mn},\odot}^{\text{NLTE}} = 5.39 \pm 0.07$ dex and $\log \varepsilon_{\text{Mn},\odot}^{\text{NLTE}} = 5.36 \pm 0.07$ dex. The fact that these values are *consistent* with the NLTE and LTE abundances calculated with *all* lines from our sample is quite fortuitous.

Another useful approach is to analyze mean abundances and standard deviations for each *multiplet*. These values are presented in Table 6.2. There is a small difference between $\log \varepsilon_{\text{Mn},\odot}^{\text{NLTE}}$ for multiplets 1, 5...21 and all other lines. We have already encountered this curious feature in our previous study of the solar Mn abundance (Bergemann & Gehren 2007)(hereafter, Paper I) with the oscillator strengths of Booth, Blackwell, Petford & Shallis (1984). Lines with excitation energies 2.15 ... 2.9 eV gave the abundances lower by ~ 0.2 dex than lines with smaller or larger excitation energy. A similar irregularity was noted by Blackwell et al. (1982) and Simmons & Blackwell (1982) from the analysis of solar Fe I lines with $\log gf$'s measured with the Oxford furnace. Hence, in Paper I we suggested that that the discrepancy was related to the $\log gf$ values measured by the Oxford group. In fact, this conclusion was not wrong. The use of new values measured by means of Fourier transform spectroscopy (Blackwell-Whitehead & Bergemann 2007) significantly improves the situation: the *rms* scatter between multiplets is not anymore 0.15 dex, but only 0.05 dex (Table 6.2). For the weak lines of multiplets 1 and 20, there are no FTS oscillator strengths. Hence, we use the values of Booth, Blackwell, Petford & Shallis (1984); that is most likely responsible for the *low* Mn abundance derived from these lines. The remaining discrepancy in the stronger lines of multiplets 5, 16, and 21 can be due to the incorrectly chosen damping parameters.

Table 6.2: NLTE abundances $\log \varepsilon_{\text{Mn},\odot}^{\text{NLTE}}$ of Mn I multiplets. Values obtained with $\log gf$ -values from different sources are marked with an asterisk; $\Delta \log \varepsilon$ values are given relative to the mean NLTE abundance $\log \varepsilon_{\text{Mn},\odot}^{\text{NLTE}} = 5.40$ dex. For multiplets marked with an asterisk, van der Waals damping parameters $\log C_6$ were reduced by 0.1 – 0.2 dex relative to Anstee & O'Mara values to fit the wings of strong lines.

Mult.	N_{lines}	E_{low} [eV]	$\log C_6$	$\log \varepsilon_{\text{Mn},\odot}^{\text{NLTE}}$ [dex]	σ	$\Delta \log \varepsilon$
1	2	0.0	-31.4	5.37	0	-0.03
4*	5	2.14	-31.4	5.43*	0.05	0.03
5*	3	2.15	-31.0	5.38	0.12	-0.02
16	3	2.3	-30.7	5.35	0.02	-0.05
20	1	2.91	-30.8	5.37		-0.03
21*	7	2.9	-30.8	5.37	0.07	-0.03
22*	7	2.92	-30.7	5.41	0.06	0.01
23	1	2.94	-30.4	5.46		0.06
27*	3	3.06	-30.6	5.41	0.02	0.01
28	2	3.07	-30.7	5.43*	0.19	0.03
32	2	3.12	-30.7	5.45	0.06	0.05
49	3	4.42	-31.6	5.40	0.02	0

In order to test the influence of the Van der Waals damping we carried out spectrum synthesis calculations adjusting C_6 for each multiplet. The correction of this parameter was found from the requirement of obtaining equal abundances for weak and strong lines of a common multiplet. $\Delta \log C_6$ for the investigated multiplets varied from -0.6 to -0.8 dex relative to the Anstee & O'Mara (1995) data, which is close to values predicted by the Unsöld formula. Fig. 6.2 shows the influence of C_6 and $\log \varepsilon$ on the profile of the strong Mn I line at 4823 Å. Obviously, three combinations of both parameters, i.e. smaller abundance and larger damping, or larger abundance and smaller damping, lead to equally good fits. The difference between the profiles is visible only

in the blend on the blue line wing and in the outer red wing.

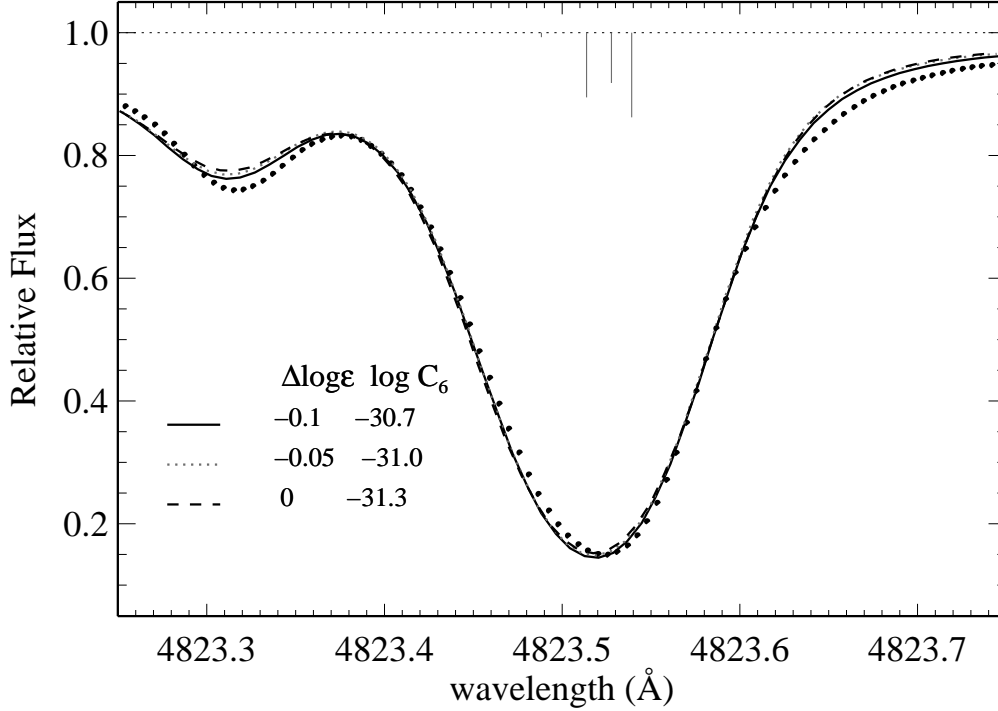


Figure 6.2: NLTE profiles of the Mn I line 4823 Å. Different combinations of damping parameters and resulting abundance deviations $\Delta \log \varepsilon$ from $\log \varepsilon_{\text{Mn},\odot} = 5.47$ dex are shown.

The lines of the following multiplet numbers demonstrated a sensitivity to the van der Waals damping: $\Delta \log \varepsilon(5) = +0.08$ dex, $\Delta \log \varepsilon(16) = +0.11$ dex, $\Delta \log \varepsilon(21) = +0.05$ dex, $\Delta \log \varepsilon(22) = +0.03$ dex, $\Delta \log \varepsilon(27) = +0.03$ dex. As a result, the mean NLTE and LTE abundances as calculated from all 41 lines increased to $\log \varepsilon_{\text{Mn},\odot}^{\text{NLTE}} = 5.43 \pm 0.05$ dex and $\log \varepsilon_{\text{Mn},\odot}^{\text{LTE}} = 5.38 \pm 0.07$ dex, respectively. If only 25 lines with the oscillator strengths from Blackwell-Whitehead & Bergemann's (2007) are used, we obtain $\log \varepsilon_{\text{Mn},\odot}^{\text{NLTE}} = 5.44 \pm 0.04$ dex and $\log \varepsilon_{\text{Mn},\odot}^{\text{LTE}} = 5.41 \pm 0.05$ dex. Note also a small reduction in the standard deviation of the abundances compared to the values calculated with the unadjusted $\log C_6$ from Table 6.2. Nevertheless, it is hard to believe that the errors in van der Waals damping are as large as 0.8 dex. The small reduction of line-to-line scatter requires significantly lower values of C_6 for all Mn I lines, which are sensitive to this parameter. Perhaps, the only vague evidence for somehow overestimated $\log C_6$ values is that a similar discrepancy between Mn I lines of different multiplets was obtained by Booth, Blackwell & Shallis (1984). They distinguished two groups of lines based on the lower excitation potential: the 0 eV intercombination lines, which show higher abundance, and those between 2 – 3 eV with lower abundances but sensitive to damping enhancement. However, another explanation was also suggested by Booth, Blackwell & Shallis, namely the uncertainties in lifetime measurements, which were used to put the oscillator strengths for the 0 eV and 2 – 3 eV lines on an absolute scale. The discrepancy between two line sets was found to be comparable to the errors claimed for the two lifetime measurements. The latter explanation seems to be more reasonable.

Using the NLTE approach and the recent measured $\log gf$ values we can solve the long-standing discrepancy between the solar photospheric abundance of Mn and the meteoritic value of 5.50 ± 0.03 dex (Lodders 2003). In particular, the NLTE abundance calculated with the adjusted $\log C_6$ values $\log \varepsilon_{\text{Mn},\odot}^{\text{NLTE}} = 5.44 \pm 0.04$ dex agrees with the latter to within the combined uncertainty of

the two values. This agreement does not automatically mean that the discrepancy was concealed in the overestimated damping constants. First, our NLTE abundance calculated with the Anstee & O'Mara damping parameters, $\log \varepsilon_{\text{Mn},\odot}^{\text{NLTE}} = 5.40 \pm 0.07$ dex, despite its larger uncertainty, *is in agreement with the meteoritic value as well*. Second, a solar Mn abundance consistent with that in type C I meteorites was reported by Greenlee & Whaling (1979) and Becker et al. (1980). However, it turned out that these high values resulted from the neglect of HFS, the LTE approach, and unaccounted blends. For instance, Greenlee & Whaling used only six Mn I lines with $W_\lambda < 14$ mÅ assuming that there are no unrecognized blends in the solar spectrum and neglecting HFS. Yet, we have found that four of these six lines contain blends, we therefore ignored them for our analysis.

The most recent and commonly used LTE abundance of Mn (5.39 ± 0.03 dex) is that of Booth, Blackwell & Shallis (1984). It is also very low compared to the abundance found in C I meteorites, hence the authors suggested that NLTE effects could be the cause of methodical errors. However, we have demonstrated that *the NLTE effects account for maximum 0.05 dex discrepancy in the solar Mn abundance derived from Mn I lines*. Instead, it became clear that the erroneous oscillator strengths are responsible for a large part of the discrepancy. Booth, Blackwell & Shallis (1984) used their own oscillator strengths reported in Booth, Blackwell, Petford & Shallis (1984). Our NLTE and LTE abundances derived with their oscillator strengths are 5.31 ± 0.07 dex (Table 6.1) and 5.26 ± 0.07 dex, respectively; both values are by ~ 0.1 dex lower than the result of Booth, Blackwell & Shallis (1984), because these authors used the semi-empirical Holweger-Müller model atmosphere. This model was calculated using the LTE assumption for formation of solar iron lines, and it is known to deliver higher abundances due to the slightly hotter temperature structure in the outer layers (see discussion in Rutten 2002).

Using the Holweger-Müller model, oscillator strengths from Blackwell-Whitehead & Bergemann (2007), and unadjusted $\log C_6$ values from the table 6.2, we obtain $\log \varepsilon_{\text{Mn},\odot}^{\text{NLTE}} = 5.51 \pm 0.07$ dex and $\log \varepsilon_{\text{Mn},\odot}^{\text{NLTE}} = 5.50 \pm 0.08$ dex. Both values are in agreement with the Mn abundance in the type C I meteorites. *What model should be given a preference in calculation of the solar Mn abundance, is thus not a critical issue*. However, the HM model atmosphere may also require adjustment of damping constants in order to eliminate the remaining line-to-line scatter of 0.07 dex. We refrain from using the HM model as the reference for the Sun because our analysis of the solar Mn I lines is mainly aimed at a derivation of atomic data to be used in metal-poor stars. Therefore, all line parameters are obtained from the spectrum synthesis under NLTE and with the MAFAGS-ODF atmospheric model. The Anstee and O'Mara damping parameters are adopted with small corrections to fit the wings of strong lines, as indicated in Table 6.2. Correspondingly, *the final estimate of solar Mn abundance is 5.40 ± 0.07 dex*.

6.1.1 Ionization equilibrium of Mn in the Sun

To investigate the ionization equilibrium of manganese, we have tried to determine the abundance from Mn II lines. Martinson et al. (1977) claim that Mn II lines can be used to obtain the same photospheric solar abundance as found from Mn I lines. From equivalent width measurements of 9 lines of ionized manganese these authors have calculated $\log \varepsilon_{\text{Mn},\odot} = 5.4 \pm 0.2$ dex. We have checked the solar spectrum of Mn II and found that no lines are suitable for any of the abundance determination methods. All lines strong enough to be discerned in the solar spectrum are located in the near-UV, and are heavily blended, which complicates the continuum placement. We have, nevertheless, synthesized these lines under the assumption of LTE: all lines of interest have saturated cores, i.e. the variation of the abundance within ± 0.2 dex affects only the strength of the wings. Due to the presence of strong blends in the line wings, *no conclusion can be made about the true abundance*. Thus, the comparison of abundances derived from two ionization stages of manganese turns out to be an unreliable technique.

For the line at $\lambda 3488$ Å, the effects of HFS and NLTE were investigated (see Fig. 6.3). The oscillator strength is adopted from Kling & Griesmann (2000) (Table A.1). HFS data for the levels involved in this transition were taken from Holt et al. (1999). Hyperfine structure broadens the profile and leads to a better fit of the inner wings provided the microturbulence is reduced

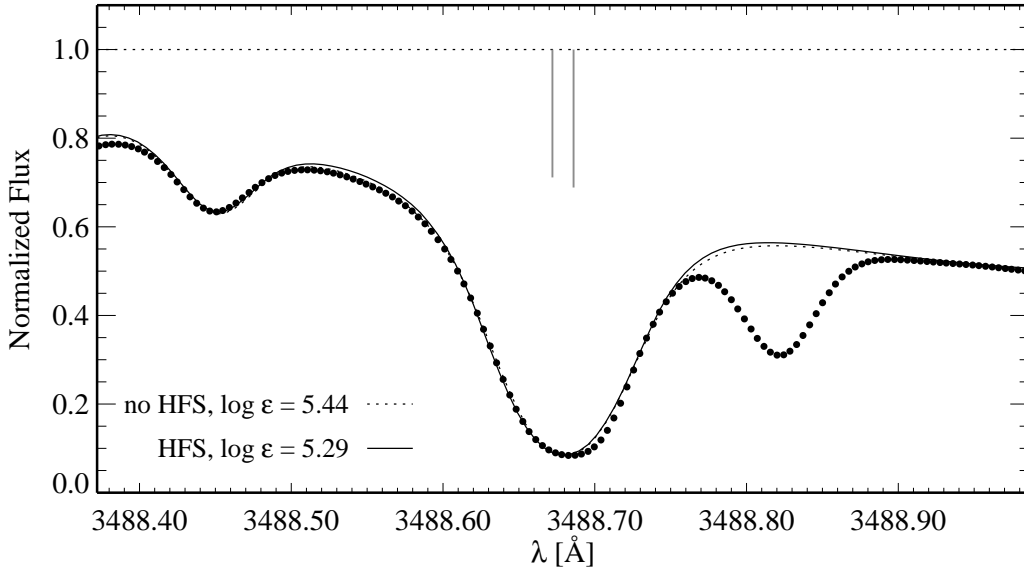


Figure 6.3: LTE line profiles of the Mn II line at 3488 Å. The strong line wings centered near 3489.05 Å are most likely due to an autoionization line, represented as an Fe I transition at 3.5 eV with an extremely large radiative damping constant.

to $\xi_t = 0.8 \text{ km s}^{-1}$. Its effect is very significant: a line profile calculated with no HFS and $\log \varepsilon_{\text{Mn},\odot}^{\text{LTE}} = 5.54$ dex is equal to a profile with 2 HFS components and $\log \varepsilon_{\text{Mn},\odot}^{\text{LTE}} = 5.39$ dex. Hence, abundances for the Mn II lines calculated without accounting for HFS can easily be overestimated by 0.15 dex. The NLTE abundance is only 0.005 dex lower than that determined under LTE. Hence, it seems that NLTE can be neglected in calculations. In fact, *the LTE Mn abundance as derived from the line at 3488 Å is in agreement with our solar NLTE abundance determined from a large number of Mn I lines* (see previous section). However, the uncertainty of the former value due to a very strong blending in the line is too large to claim the consistent solar ionization equilibrium of Mn.

6.2 Solar abundance of Co and related uncertainties

The number of Co I lines suitable for a reliable abundance analysis in the solar spectrum is very small (Table A.2). Out of the initially selected 20 lines, measured oscillator strengths are available for 17 lines. Two reference sources of experimental $\log gf$ values are Cardon et al. (1982) and Nitz et al. (1999). For three yellow lines of multiplet 158 we had to adopt the theoretical values of Kurucz & Peytremann (1996). However, the calculated data are very discrepant (see a discussion in Sect. 3.5.1), hence the lines of multiplet 158 are only used in the differential abundance analysis of metal-poor stars. Our final estimate of the solar Co abundance is based solely on the *experimental* $\log gf$ values.

Figure 6.4 shows NLTE and LTE abundances for 17 lines of Co I as a function of their equivalent widths. The relative abundance scatter is large for the lines with small W_λ . The line at 5369 Å shows very large abundance, 5.15 dex. As its gf -value seems to be reliable, it is likely that the line contains an unidentified blend. Also, four very weak lines ($\lambda\lambda 6189, 6814, 7417, 7712$ Å) have strongly deviating abundances both under LTE and NLTE assumption. We suggest that their oscillator strengths are erroneous because the errors (see Table A.2) are of the order of ~ 0.2 dex. Hence, we ignore them in the analysis, and our sample is further reduced to 12 lines. The

NLTE corrections to the abundances are significant. The average Δ_{NLTE}^1 is +0.14 dex, but for particular lines the abundances derived from LTE are ~ 0.2 dex smaller than those derived with NLTE departure coefficients. The corresponding NLTE $\log(gf\varepsilon)_\odot$ values for each line of Co I are given in Table A.2. The average NLTE abundance of Co in the solar atmosphere is $\log \varepsilon_{\text{Co},\odot}^{\text{NLTE}} = 4.94 \pm 0.04$ dex. The LTE abundance is much smaller, $\log \varepsilon_{\text{Co},\odot}^{\text{LTE}} = 4.81 \pm 0.04$ dex. The line-to-line scatter is of the same magnitude under NLTE and LTE that is most likely due to the errors in oscillator strengths. The errors are larger for the Cardon et al.'s (1982) gf -values, $\sim 15 - 25\%$. This shows up in the average NLTE abundance and its standard deviation, when calculated with the data from Cardon et al.: $\log \varepsilon_{\text{Co},\odot}^{\text{NLTE}} = 4.96 \pm 0.06$ dex. This value is nearly equal to the NLTE abundance calculated using 6 lines with oscillator strengths from Nitz et al. (1999) is $\log \varepsilon_{\text{Co},\odot}^{\text{NLTE}} = 4.95 \pm 0.03$. This confirms our conclusion from Sect. 3.5.1 about consistency of oscillator strengths from both experimental sources.

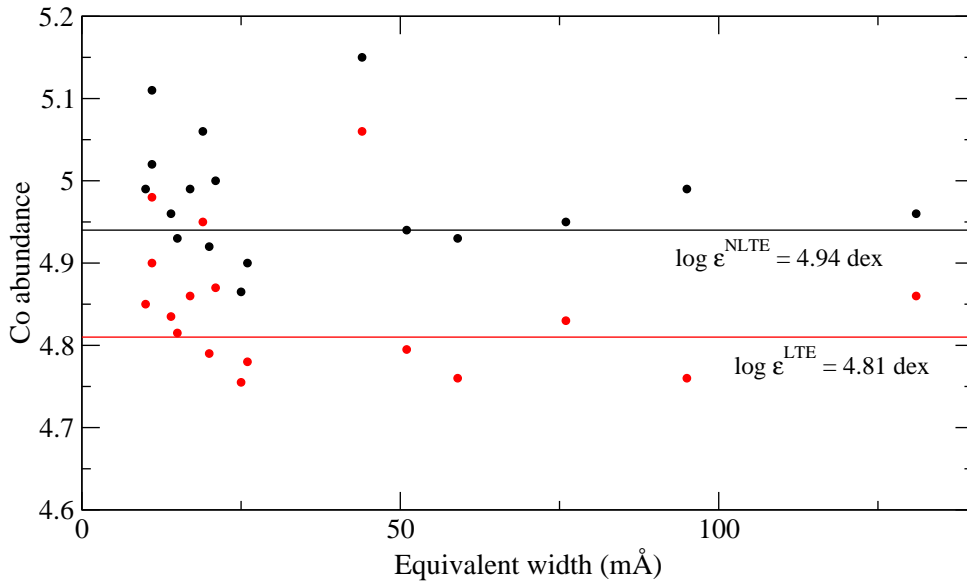


Figure 6.4: Abundances of the 17 solar Co I lines. LTE abundances are marked with red circles, and NLTE abundances with black circles. The mean NLTE and LTE abundances are indicated with black and red lines, respectively.

The majority of Co I lines are weak, and they are not sensitive to the van der Waals damping, neither are they affected by the microturbulence. We found only one strong line at 4121 Å, which gives different abundances with the variation of ξ_t or $\log C_6$. The corresponding variation of the NLTE line profile with both parameters is shown in Fig. 6.5. The difference in microturbulence velocity of ± 0.2 km s $^{-1}$ with respect to the reference value of 0.9 km s $^{-1}$ corresponds to an abundance correction of roughly ∓ 0.1 dex. If the van der Waals damping constant changes by ± 0.5 dex relative to the Anstee & O'Mara value, the Co abundance changes by ∓ 0.12 dex. With the exact Anstee & O'Mara's (1995) damping constant $\log C_6 = -31.7$ and $\xi_t = 0.9$ km s $^{-1}$, this line gives a NLTE abundance of 4.95 dex, which is consistent with abundances derived from the other Co I lines. Moreover, the standard deviation of the *average* Co NLTE and LTE abundances, 0.04 dex, is already smaller than the errors given for the oscillator strengths. Hence, we have not tried to adjust damping constants and microturbulence any further.

Whereas, damping and microturbulence are relatively unimportant in calculations of the solar Co abundance, thermalizing collisions with hydrogen atoms become the main source of $\log \varepsilon_{\text{Co},\odot}^{\text{NLTE}}$ uncertainty. This is stipulated by the large NLTE abundance corrections found for Co I lines. In order to check the influence of the inelastic H I collisions, we performed a series of NLTE

¹The NLTE correction was defined in Sect. 5 as: $\Delta_{\text{NLTE}} = \log \varepsilon^{\text{NLTE}} - \log \varepsilon^{\text{LTE}}$

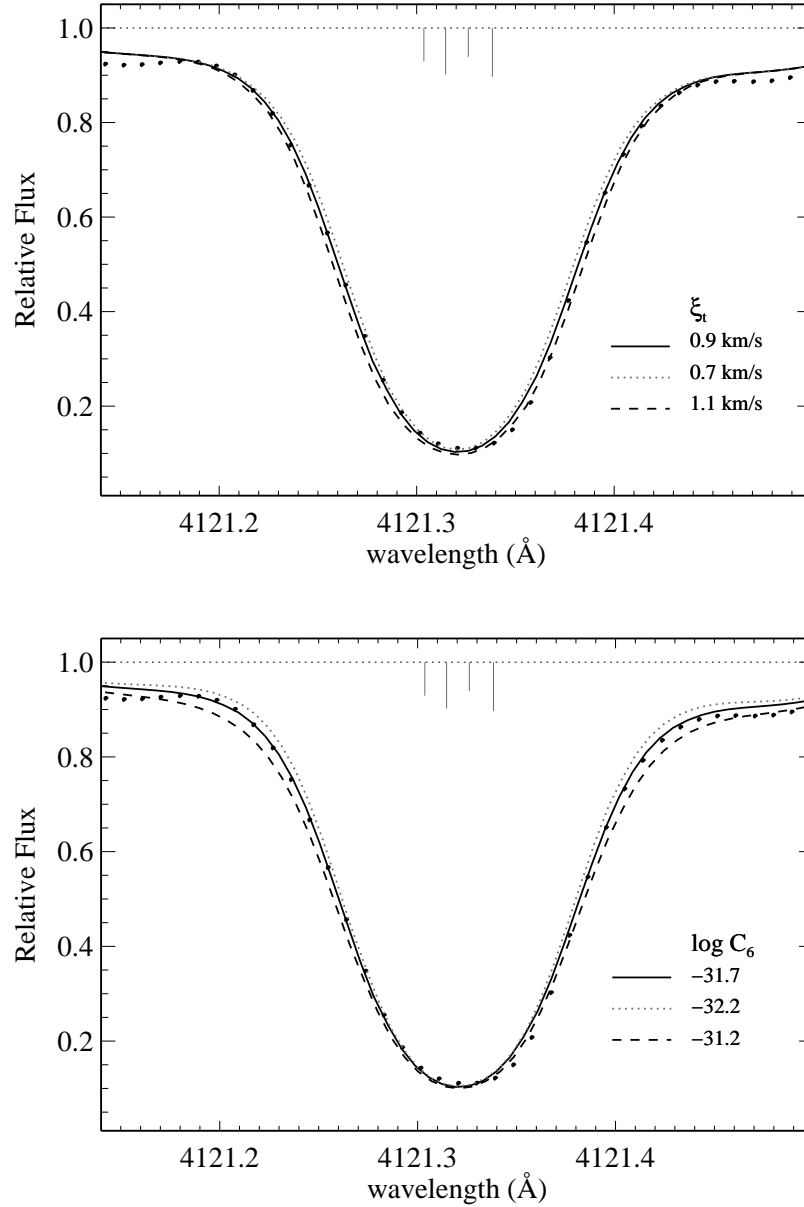


Figure 6.5: NLTE line profiles of the Co I line at 4121 Å compared to the solar spectrum. (top) Variation of the line profile with microturbulence velocity, $\xi_t = 0.7, 0.9, 1.1 \text{ km s}^{-1}$. (bottom) Variation of the line profile with van der Waals damping constant, $\log C_6 = -31.2, -31.7, -32.2$. All profiles are fitted with the Co abundance $\log \varepsilon_{\text{Co}, \odot} = 4.96 \text{ dex}$.

abundance calculations with different scaling factors to the b-b and b-f collision cross-sections computed from Drawin's formula. The NLTE results for $S_{\text{H}} = 0$, $\log \varepsilon_{\text{Co}, \odot}^{\text{NLTE}} = 4.96 \pm 0.04$, are almost identical to the case of $S_{\text{H}} = 0.05$. Also, with increasing scaling factor from 0.5 to 5, the abundance steadily decreases from 4.91 to 4.87 dex. For all values of S_{H} tested here, the line-to-line scatter is approximately constant, $\sigma \sim 0.04$ dex. Thus, *no conclusion can be drawn concerning the optimum value of the scaling factor to hydrogen collisions.*

6.2.1 Ionization equilibrium of Co in the Sun

In contrast to Mn, it is possible to check the *ionization equilibrium* of Co for the Sun, using the relatively unblended line of ionized cobalt Co II at 3501 Å (Fig. 5.5). The line is saturated and consists of 8 HFS components, which were calculated with the hyperfine splitting constants kindly provided to us by J. Pickering prior to publication (Table A.4). To produce a better fit to the observed profile, the magnetic dipole constant A for the upper level of a transition was decreased by 1 mK; this is within the errors of the measured HFS value. The oscillator strength is taken from Raassen et al. (1998), $\log gf = -1.22$ dex. With this value, we derive a NLTE abundance of cobalt $\log \varepsilon_{\text{Co}, \odot}^{\text{NLTE}} = 4.86$ dex that is by 0.08 dex lower compared to the NLTE abundance derived from Co I lines. Alternatively, we can use the oscillator strengths measured with FT spectroscopy by Salih et al. (1985). However, with the experimental value $\log gf = -1.18$, the solar Co abundance becomes even *lower*, $\log \varepsilon_{\text{Co}, \odot}^{\text{NLTE}} = 4.82$ dex. The discrepancy between the neutral and ionized Co lines is now 0.12 dex; that is too large to be explained by the measurement uncertainties, like continuum placement. Moreover, *unaccounted blends* in the UV Co II line would lead to a further reduction of the abundance. Even if the problem is concealed in hydrogen collisions, a very *large* scaling factor $S_{\text{H}} \geq 5$ is needed to bring two ionization stages in agreement. The uncertainty of the calculated oscillator strength provided by Raassen et al. (1998) is not known, whereas the accuracy of the Salih et al. (1985) gf -value for this line is not better than 50%, which translates to an abundance uncertainty of ~ 0.2 dex. In fact, the *problem also persists in the LTE analysis*. The abundance derived from the Co II line under LTE is 4.84 and 4.88 dex when calculated with the Salih et al. and Raassen et al. $\log gf$ value, respectively. The LTE abundance derived from 15 Co I lines is 4.81 ± 0.04 dex. In contrast to NLTE, the discrepancy between both ionization stages appears with the reverse sign. The influence of van der Waals damping is negligible: with variation of $\log C_6$ in the range $-31.0 \dots -33.0$, the abundance changes only by $-0.015 \dots +0.01$ dex. At present, *we can not determine what causes the failure to satisfy the excitation and ionization equilibrium of Co in the solar photosphere.* This issue will be further investigated in the next chapter devoted to the metal-poor stars.

The abundance of Co in C I meteorites is 4.89 ± 0.03 dex (Lodders 2003). It conforms to our NLTE abundance $\log \varepsilon_{\text{Co}, \odot}^{\text{NLTE}} = 4.94 \pm 0.04$ dex derived from Co I lines within the combined errors of both values. The LTE abundance calculated from Co I lines is too low, as well as the NLTE and LTE abundances calculated from the single Co II line with the $\log gf$ value from Salih et al. (1985). However, using the theoretical oscillator strength for that line from Raassen et al. (1998), we obtain *NLTE and LTE abundances consistent with the meteoritic one.* Previously, the photospheric abundance from the Co I lines was determined by Cardon et al. (1982), whose oscillator strengths we have used in the analysis. Using the LTE assumption, Cardon et al. calculated $\log \varepsilon_{\text{Co}, \odot} = 4.92 \pm 0.08$ dex. This value is ~ 0.1 dex higher than our LTE abundance, which is due to several reasons. First, the authors used the semi-empirical model atmosphere of Holweger (1967), which is essentially the same as the Holweger-Müller model (Holweger & Müller 1974). In Sect. 6.1, we showed for Mn that the latter model leads to higher abundances compared to the theoretical ODF model. Second, equivalent widths were used to measure the abundances. This method always gives only an *upper* limit on the abundance, because the contribution to a line strength from blending lines is neglected. In all other respects (oscillator strengths, microturbulence, line set), our study and the analysis of Cardon et al. are similar, hence the resulting abundances are consistent.

Chapter 7

Abundances in metal-poor stars

One of our principal goals is to perform a very careful analysis of Mn and Co abundances in a small sample of metal-poor stars in order to show how the NLTE effects and HFS influence the results. The plausibility of previous abundance estimates for the metal-poor stars, most of them performed ignoring HFS and NLTE, will be assessed. A sample of selected stars is given in Table 3.1; these are mainly subdwarfs in a wide range of metallicities.

The stellar abundances of Mn and Co are calculated according to the procedure described in Sect. 3.5. The *abundance ratio* relative to the Sun is:

$$[\text{El}/\text{H}] = \log(gf\varepsilon)_* - \log(gf\varepsilon)_\odot$$

The $\log(gf\varepsilon)_\odot$ values are taken from Tables A.1 and A.2. For Mn, we develop a slightly different approach to abundance calculations, which is in details described in the next section.

The discussion of results in this chapter is based on the ratios of Mn and Co abundances to iron, i.e. $[\text{Mn}/\text{Fe}]$ and $[\text{Co}/\text{Fe}]$. The reason is that when the ratios of *similar* elements are used, the systematic errors in abundances due to the wrong stellar parameters, e.g. microturbulence, and model structure largely cancel. Since the same atmospheric models were used to obtain iron abundances in the stars studied here (Sect. 3.2), we expect that the $[\text{Mn}/\text{Fe}]$ and $[\text{Co}/\text{Fe}]$ values are more accurate than the abundances of both elements relative to H.

7.1 Manganese

7.1.1 Some aspects of a differential stellar analysis

The number of Mn lines suitable for an abundance analysis in our stellar spectra varies from 20 for the thin disk star Procyon to 4 for the very metal-poor turnoff star BD−4°3208. In particular, in stars with $[\text{Fe}/\text{H}] < -2$ only five lines of multiplets 2 and 5, and three lines of multiplet 16 are detected. Unfortunately, the strong near-UV lines ($4018 \leq \lambda \leq 4041 \text{ \AA}$) of Mn I can not be used for abundance determinations in the *solar spectrum* due to a severe blending. Hence, we define another “reference” star, HD 102200, with $[\text{Fe}/\text{H}] = -1.28$ dex, whose $\log(gf\varepsilon)_{\text{ref}}$ values are used for the differential comparison with the more metal-poor stars. In this case, we calculate an average $[\text{Mn}/\text{H}]$ from all detected lines in spectrum of a metal-poor star relative to HD 102200, and then correct this value by an average $[\text{Mn}/\text{H}]$ derived from the visual and near-IR lines of HD 102200 relative to the Sun.

Obviously, our analysis relies on the assumption that the *relative* NLTE abundances $[\text{Mn}/\text{H}]$ deduced from near-UV lines of HD 102200 do not deviate from the abundances deduced from the other lines of this star. Usually, the large scatter results from the incorrectly treated line blends, which have different dependence on the T_{eff} and $\log g$. We have checked how blends contained in the near-UV Mn I lines affect the line profiles and Mn abundances derived from these lines in the Sun and in metal-poor stars. Fig. 7.1 shows the line at 4030 Å in the spectra of the Sun, HD

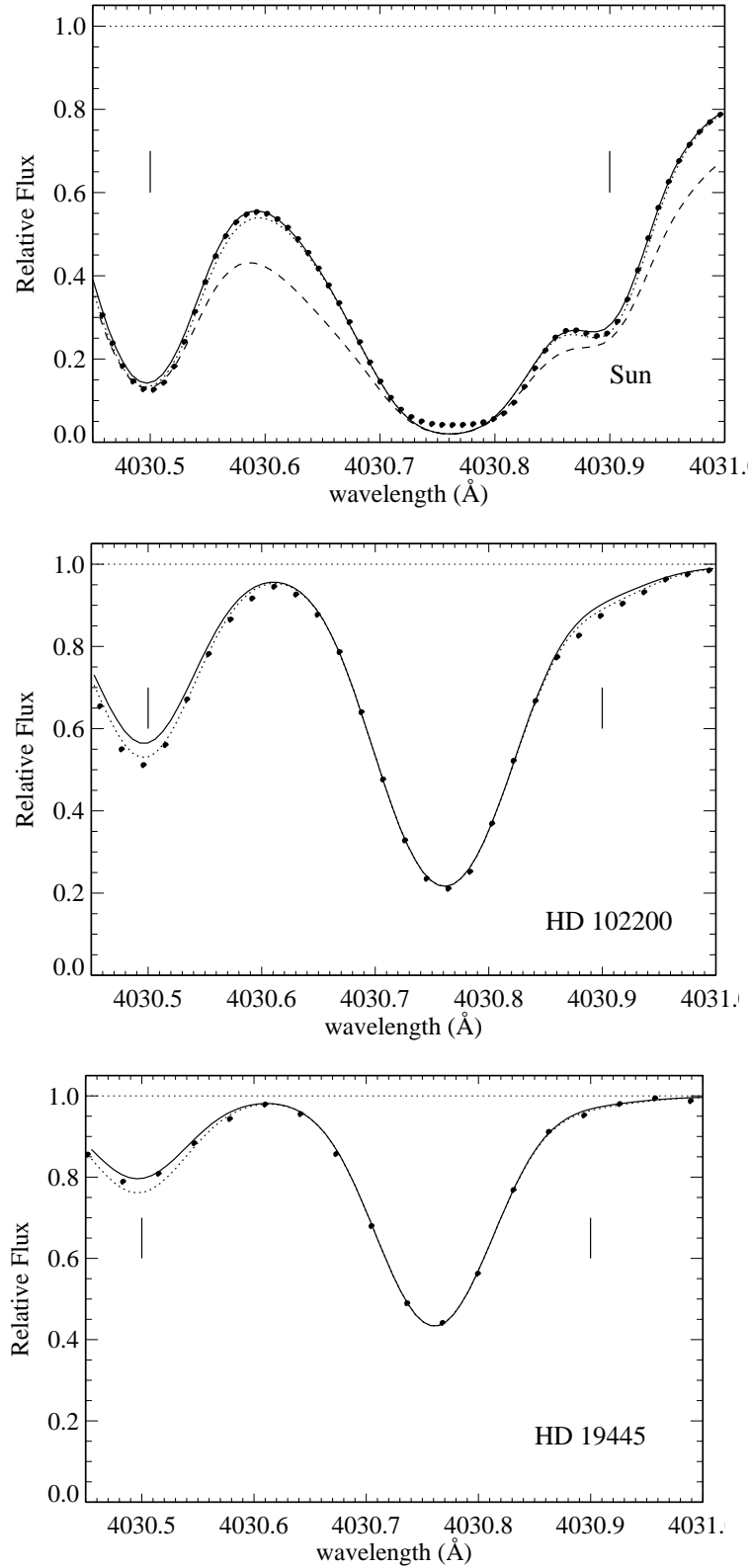


Figure 7.1: The Fe I blends in the blue and red wings of the Mn I line at 4030 Å in spectra of the Sun, HD 102200, and HD 19445 (from top to bottom). The best theoretical NLTE profile calculated with $\log C_6 = -31.2$ is marked with a solid line, the same profile with $\log gf$ for both Fe I blends increased by 0.1 dex is shown with a dotted line. The dashed line on the upper panel corresponds to the NLTE profile calculated with $\log C_6 = -30.5$.

102200, and HD 19445, respectively. Vertical lines mark the Fe I blends in the red and blue wing. A solid line represents the best theoretical NLTE profile, the dotted line shows the same profile with $\log gf$ for both Fe I blends increased by 0.1 dex. Even this small correction produces a poor fit of the Mn I line wings in the solar spectrum. Hence, we constrain the solar $\log gf$ values for the iron blends at 4030.5 and 4030.9 Å to -0.8 and -1.6 dex, respectively. The uncertainty of these values is 0.05 dex. The profile of the same Mn I line in a metal-poor star is practically insensitive to a variation of iron line strengths. We, thus, expect that the *relative* Mn abundances derived from the near-UV lines in metal-poor stars are reliable.

It is noteworthy that the *absolute LTE and NLTE abundances from the resonance triplet at 403 nm are lower than the abundances from the other lines on average by 0.07 – 0.3 dex*. This is characteristic for all stars in our sample. In the *differential LTE analysis* relative to HD 102200, this inconsistency also appears and increases with decreasing metallicity. For the metal-poor subgiant HD 140283 we infer the $\Delta[\text{Mn}/\text{H}]_{\text{LTE}}$ between the resonance and excited lines to be ~ 0.3 dex. It is interesting that a similar result was obtained by Cayrel et al. (2004). In their LTE analysis of Mn in metal-poor stars there is a systematic difference of ~ 0.4 dex between the near-UV (resonance triplet at 403 nm) and visual Mn I lines (4754 and 4823 Å). We will return to this issue in the next section.

The discrepancy is also present in a *differential NLTE analysis*, but even in the most metal-poor stars it does not exceed 0.05 dex. We have good reason to believe that the problem is concealed in the van der Waals damping, because strong and weak lines show different sensitivity to this parameter. A weak line in a metal-poor star is strong in the solar spectrum, so its $\log gf\varepsilon$ value depends on the adopted C_6 constant. When the resonance lines are calculated with $\log C_6 = -30.5$, the abundance differences between resonance and excited lines completely vanish for all stars in our sample. However, such a strong damping is unsuitable for fitting the solar resonance lines. There, the wings are too broad, and that discrepancy can not be removed by adjusting any other parameter in line synthesis (see upper panel in Fig. 7.1). Hence, we decided to adopt the $\log C_6 = -31.2$ for the resonance lines, keeping in mind the possible error of 0.05 dex introduced by the uncertain $\log C_6$ value.

The likely explanation for the discrepancy in *absolute* line abundances is that the oscillator strengths are erroneous. We use different sets of experimental gf -values for the near-UV and visual lines, that of Booth, Blackwell, Petford & Shallis (1984) and of Blackwell-Whitehead & Bergemann (2007), respectively. Cayrel et al. uses only the data of Booth, Blackwell, Petford & Shallis (1984). The comparison of Booth's values with the recent experiment of Blackwell-Whitehead & Bergemann (2007) revealed significant disagreement for several strong Mn I transitions. Unfortunately, the resonance triplet was not measured by Blackwell-Whitehead & Bergemann. To resolve the inconsistency we need new quality measurements of oscillator strengths.

7.1.2 Mn in metal-poor stars

The relative Mn abundance ratios $[\text{Mn}/\text{Fe}]$ and their standard deviations σ for all stars are listed in the Table 7.1. These values are calculated only from Mn I lines. Stars with metallicities larger than that of HD 102200 were analyzed directly relative to the Sun; in this case, the resonance triplet at 403 nm was not used for the reasons given above. The Mn abundances in stars more metal-poor than HD 102200 are calculated relative to this reference star, and corrected by an average Mn abundance derived for the HD 102200 relative to the Sun. These differential abundances are consistent within their σ with Mn abundances in the stars calculated from the excited lines strictly relative to the Sun. Figure 7.2 shows $[\text{Mn}/\text{Fe}]$ ratios for all stars as a function of metallicity. NLTE and LTE abundances are marked with filled and open circles, respectively. The most important result is that *the NLTE abundances of Mn in all stars are systematically higher than the LTE abundances*; as expected, the difference $[\text{Mn}/\text{Fe}]_{\text{NLTE}} - [\text{Mn}/\text{Fe}]_{\text{LTE}}$ increases with decreasing metallicity. There are no obvious differences between subgiants and subdwarfs, and the overall spread of abundances is relatively small at all metallicities with a standard deviation $\sigma = 0.11$ dex. For $-2.5 < [\text{Fe}/\text{H}] < -1$, the mean Mn underabundance is $\langle [\text{Mn}/\text{Fe}] \rangle = -0.07$, whereas for larger metallicities $\langle [\text{Mn}/\text{Fe}] \rangle = +0.01$. On these grounds, one could attribute a small deficiency

Table 7.1: The NLTE and LTE abundances of Mn and Co for the selected sample of stars. N is the number of Mn I and Co I lines used for individual stars. See text for further discussion of the data.

Object	[Fe/H]	[Mg/Fe]	Population	N_{Mn}	[Mn/Fe]		N_{Co}	[Co/Fe]	
					NLTE	LTE		NLTE	LTE
HD 19445	-1.96	0.38	Halo	10	-0.20 ± 0.03	-0.52 ± 0.06	1	0.63	0.07
HD 25329	-1.84	0.42	Thick Disk?	6	-0.06 ± 0.02	-0.23 ± 0.03	1	-0.01	-0.72
HD 29907	-1.60	0.43	Halo?	17	0.05 ± 0.03	-0.20 ± 0.03	1	0.69	0.14
HD 34328	-1.66	0.42	Halo	11	-0.10 ± 0.02	-0.37 ± 0.03	2	0.69 ± 0.02	0.17 ± 0.19
HD 61421	-0.03	0.0	Thin Disk	17	-0.06 ± 0.04	-0.08 ± 0.06	7	-0.1 ± 0.07	-0.14 ± 0.1
HD 84937	-2.16	0.32	Halo	7	-0.04 ± 0.02	-0.42 ± 0.08	2	0.66 ± 0.06	0.21 ± 0.13
HD 102200	-1.28	0.34	Halo	11	-0.04 ± 0.04	-0.26 ± 0.05	2	0.53 ± 0.03	0.08 ± 0.14
HD 103095	-1.35	0.26	Halo	10	-0.07 ± 0.02	-0.22 ± 0.03	1	-0.01	-0.11
BD-4°3208	-2.23	0.34	Halo	4	-0.12 ± 0.00	-0.56 ± 0.09	1	0.64	0.13
HD 122196	-1.78	0.24	Halo	12	-0.14 ± 0.03	-0.47 ± 0.07	1	0.49	-0.08
HD 122563	-2.51	0.45	Halo	7	-0.15 ± 0.05	-0.59 ± 0.10	3	0.59 ± 0.04	-0.05 ± 0.08
HD 134169	-0.86	0.53	Thick disk	7	0.05 ± 0.03	-0.11 ± 0.06	3	0.46 ± 0.04	0.20 ± 0.16
HD 148816	-0.78	0.36	Thick disk	6	-0.07 ± 0.05	-0.19 ± 0.03	6	0.39 ± 0.04	0.20 ± 0.07
HD 184448	-0.43	0.47	Thick disk	13	0.11 ± 0.04	0.08 ± 0.03	11	0.34 ± 0.04	0.28 ± 0.03
HD 140283	-2.38	0.43	Halo	7	0.02 ± 0.02	-0.45 ± 0.10	2	0.86 ± 0.01	0.21 ± 0.05
G20-8	-2.19	0.4	Halo	2	-0.02 ± 0.03	-0.48 ± 0.03	2	0.76 ± 0.06	0.28 ± 0.17
HD 200580	-0.82	0.46	Thick Disk	10	0.26 ± 0.07	0.14 ± 0.07	2	0.37 ± 0.03	0.13 ± 0.12

of Mn relative to iron to the halo stars, and nearly solar [Mn/Fe] ratios to the thick and thin disk stars. However, several stars stand out of this scheme. Two stars were identified as visual (HD 200580) or spectroscopic (HD 29907) binaries (Gehren et al. 2004); that could explain their high Mn abundances. The thick disk star HD 148816 has a slightly subsolar [Mn/Fe] ratio and a retrograde Galactic orbit. This may indicate that the star is a member of halo. It is interesting that Bai et al. (2004) derive *lower* [Mn/Fe] ratios for the *halo* stars with retrograde orbits compared to the other stars. A slightly supersolar [Mn/Fe] ratio is found for the subgiant HD 140283 with [Fe/H] = -2.38. Mashonkina et al. (1999) showed that this star has abnormally low [Ba/Fe] and [Sr/Fe] ratios that could indicate peculiar conditions in the ISM out of which this star formed. On the other side, we can interpret the nearly solar [Mn/Fe] ratios for HD 140283, HD 84937, and G20-8 as a manifestation of the *flat* [Mn/Fe] trend in the halo.

There are several stars, which are common in our analysis and analyses of the other authors: HD 140283, HD 122563, HD 200580, and HD 19445. In fact, for all of them the Mn abundances were found to be significantly *lower* than ours. As the main reason for overdeficiencies is the LTE assumption, there is no need to compare our NLTE abundances with results of earlier studies, where all calculations are performed in LTE and often neglecting HFS. Hence, the discussion below is restricted only to LTE abundances.

For the halo subgiant HD 140283, Gratton (1987) calculated [Mn/Fe] = -0.59 ± 0.06 . This is comparable with our LTE value [Mn/Fe] = -0.45 ± 0.1 . The difference of 0.15 dex stems either from the fact that Gratton used only the near-UV resonance triplet of Mn I, or from discrepant atmospheric parameters ($\Delta T_{\text{eff}} = 203$ K, $\Delta \log g = 0.36$, $\Delta[\text{Fe}/\text{H}] = 0.22$ between our and their stellar parameters). Ryan et al. (1996) performed an absolute LTE abundance analysis of HD 122563 and HD 140283 employing oscillator strengths from Booth, Blackwell, Petford & Shallis (1984). Their result for HD 140283 is *identical* to ours, [Mn/Fe] = -0.48 dex. However, the abundances strongly disagree for HD 122563; the difference in [Mn/Fe] is ~ 0.22 dex. The simple explanation is that Ryan et al. used [Fe/H] = -2.68 that is nearly 0.2 dex lower than our [Fe/H] value for this star. Clearly, using lower metallicity we would also arrive at a higher [Mn/Fe] value.

One outlier from our sample, HD 200580, was studied under LTE by Nissen et al. (2000). Three

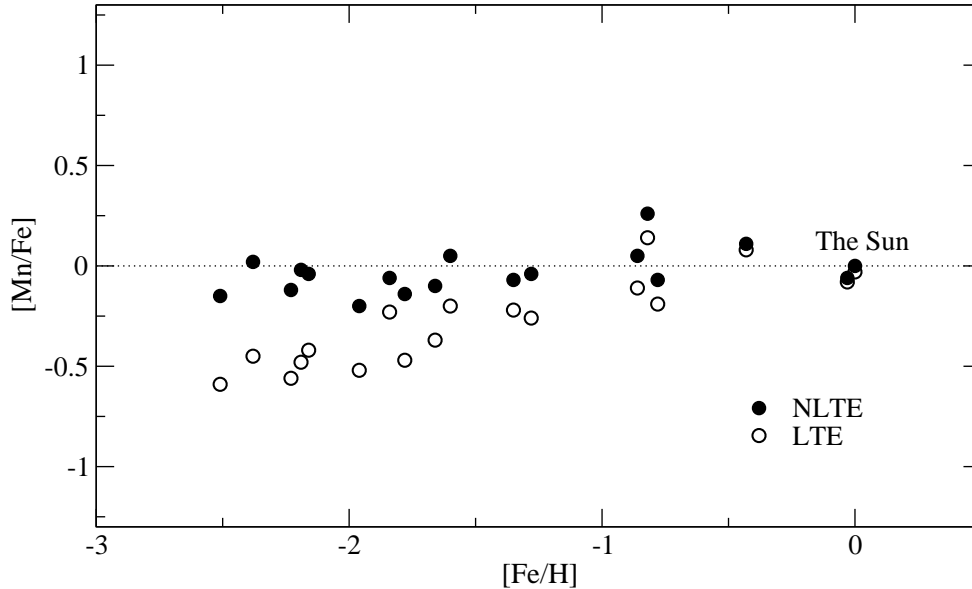


Figure 7.2: $[Mn/Fe]$ vs. $[Fe/H]$ in metal-poor stars. NLTE and LTE abundances are marked with filled and open circles, respectively.

near-IR lines of Mn I were used to calculate differential abundances with respect to the Sun. Their LTE $[Mn/Fe]$ ratio is by 0.27 dex lower than our value that is due to the 0.25 dex higher metallicity. However, the error estimate of our $[Fe/H]$ for this star is 0.1 dex. Unfortunately, Nissen et al. (2000) do not provide enough information for a discussion of the $[Fe/H]$ discrepancy. The $[Mn/Fe]$ ratio for another peculiar star HD 148816 was determined by Wallerstein (1962) using a curve-of-growth technique. The $[Mn/Fe]$ deficiency of -0.48 dex was reported, which is significantly lower than the value derived in the current LTE analysis. That is not surprising because stellar parameters are very discrepant, and also different methods of abundance calculations are applied. The Mn abundance for HD 148816 was also reported by Peterson (1981), and her $[Mn/Fe]$ ratio is in agreement with our result. Aller & Greenstein (1960) applied the curve-of-growth technique to calculate Mn abundances for the metal-poor stars HD 19445 and HD 140283. Instead of a deficiency, the overabundance of Mn relative to Fe was found. Perhaps, the main reason for this is the neglect of HFS in their analysis.

The investigations of Mn abundances in *giants* carried out by Johnson (2002) and Cayrel et al. (2004) deserve a special attention. These studies clearly reported *the failure to satisfy excitation-ionization equilibrium of Mn in metal-poor stars under LTE*. The large discrepancy was found between the abundances derived from the Mn I resonance triplet at 403 nm and excited lines, and also between lines of two ionization stages Mn I and Mn II. Johnson (2002) attributed the former to incorrect modeling of the upper layers in the model atmospheres and/or to the necessity of depth-dependent microturbulence. The problem of inconsistent ionization balance was left unexplained, although at low effective temperatures, $T_{\text{eff}} \leq 5000$ K, the discrepancy between Mn II and Mn I lines was as large as $0.3 \dots 0.5$ dex. Cayrel et al. (2004) did not analyze the lines of ionized manganese in their giants, but they confirmed the systematic underabundance of ~ -0.4 derived from the resonance Mn I lines when compared to the excited lines of multiplet 16. The erroneous oscillator strengths of Booth, Blackwell, Petford & Shallis (1984) or NLTE effects were suggested as the cause. Recently, the same problem was recognized for Galactic subdwarfs (Lai et al. 2008). Not going into the details of the problem, these authors preferred to neglect the whole Mn I stage and to use only abundances derived from Mn II lines under LTE. Whether the latter is a reliable assumption was not questioned. We have showed in Sect. 7.1.1 that the *absolute* abundances determined from the resonance and excited lines are indeed discrepant by

$\sim 0.1 \dots 0.3$ dex for all stars in our sample. For HD 122563, the only common star in our analysis and analyses of Johnson (2002) and Cayrel et al. (2004), we infer the difference of ~ 0.3 dex that is consistent with the results of both research groups. However, our LTE ratio $[\text{Mn}/\text{Fe}]$ for this cool giant is 0.28 dex lower than that of Johnson (2002), and 0.18 dex lower than that of Cayrel et al. (2004). Stellar parameters are very different between our and their studies: Cayrel et al. adopted $T_{\text{eff}} = 4600$, $\log g = 1.1$, $[\text{Fe}/\text{H}] = -2.8$, Johnson used $T_{\text{eff}} = 4450$, $\log g = 0.5$, $[\text{Fe}/\text{H}] = -2.65$, and our values are $T_{\text{eff}} = 4600$, $\log g = 1.5$, $[\text{Fe}/\text{H}] = -2.53$. This can explain the differences in LTE abundances.

In fact, NLTE offers a solution to the problem of inconsistent excitation equilibria. Test calculations in the wide range of stellar parameters (Sect. 5.2) show that the NLTE corrections for the triplet at 403 nm are especially high for models with $[\text{Fe}/\text{H}] \leq -2.5$ and supersolar effective temperatures (up to 0.6 dex). Whereas, NLTE abundance corrections for other lines do not exceed 0.2 – 0.4 dex. Also, there is ~ 0.15 dex difference in NLTE abundance corrections between the resonance and excited lines for the models with subsolar temperatures ($T_{\text{eff}} = 5500$ K) and $[\text{Fe}/\text{H}] \leq -3$. Hence, it is to be expected that LTE abundances of Mn in spectra of halo stars, where *only* the resonance near-UV lines can be detected, are significantly underestimated. Still, for HD 122563 even the *absolute* NLTE Mn abundances inferred from the resonance triplet and excited lines differ by 0.2 dex. This separation is further reduced to 0.1 dex in the *differential* NLTE analysis with respect to the Sun. As suggested in the previous section, erroneous damping constants for the resonance lines are likely responsible for the remaining discrepancy.

We have also checked the problem of *ionization equilibria* with NLTE. A single line of Mn II that can be used for a crude analysis of the Mn abundance in the Sun is located in the UV, at 3488 Å. Its LTE and NLTE abundances, as calculated with the solar model atmosphere, are nearly equal, $\log \varepsilon = 5.39$ dex (Sect. 6.1). Let us denote the Mn abundance as determined from the Mn I and Mn II lines as $[\text{Mn}/\text{Fe}]_{\text{I}}$ and $[\text{Mn}/\text{Fe}]_{\text{II}}$, respectively. These values were computed under NLTE and LTE assumption for selected stars with spectra extending to the UV. The results are given in Table 7.2.

Table 7.2: NLTE and LTE abundances for selected stars as calculated from Mn I and Mn II lines.

Object	$[\text{Mn}/\text{Fe}]_{\text{I}}$		$[\text{Mn}/\text{Fe}]_{\text{II}}$	
	NLTE	LTE	NLTE	LTE
HD 34328	-0.1	-0.37	-0.52	-0.51
HD 61421	-0.06	-0.08	-0.18	-0.17
HD 84937	-0.04	-0.42	-0.41	-0.42
HD 102200	-0.04	-0.26	-0.27	-0.25
HD 122196	-0.14	-0.47	-0.45	-0.44
HD 122563	-0.15	-0.59	-0.23	-0.17
HD 140283	0.02	-0.45	-0.33	-0.35

As seen from the Table, the NLTE correction to the abundances derived from the Mn II line is very small. A surprising result is that for three subdwarfs, HD 84937, HD 102200, and HD 122196, the LTE abundances determined from the lines of both ionization stages are consistent. The discrepancy reappears under NLTE: $[\text{Mn}/\text{Fe}]_{\text{II}}^{\text{NLTE}} - [\text{Mn}/\text{Fe}]_{\text{I}}^{\text{NLTE}} = +0.37$ dex for HD 84937, $+0.23$ dex for HD 102200, and $+0.31$ dex for HD 122196. The difference between ionized and neutral lines for a subgiant HD 140283 is only $+0.1$ dex under LTE, and -0.35 dex under NLTE. The only exception is HD 122563, for which the Mn II line gives 0.42 dex higher LTE abundance compared to the LTE abundance determined from Mn I lines. It is interesting that for this cool giant Johnson (2002) reported a similar difference in LTE abundances between two ionization stages, ~ 0.5 dex. Neutral and ionized lines for this star also disagree under NLTE, $[\text{Mn}/\text{Fe}]_{\text{I}}$

$= -0.15$ vs. $[\text{Mn}/\text{Fe}]_{\text{II}} = -0.23$ dex. For Procyon, abundances are inconsistent by the same order of magnitude ~ 0.1 dex under LTE and NLTE. HD 34328 is dramatically *deficient* in Mn if abundances from Mn II lines are considered, whereas the NLTE results for Mn I suggest a *nearly* solar $[\text{Mn}/\text{Fe}]$ ratio.

In general, the differences between two ionization stages are *not* systematic. Fig. 7.3 displays the $[\text{Mn}/\text{Fe}]$ ratios determined from the Mn I and Mn II lines as a function of effective temperature for the stars from Table 7.2. The mean differences between abundances computed under NLTE and LTE are shown on the upper and lower panels, respectively. Under NLTE the abundances are higher for neutral lines, in LTE there is no obvious trend. So it is not clear what parameter should be blamed for this strange behavior. As mentioned in Sect. 6.1.1, the Mn II line is strongly blended in the solar spectrum. Hence, a missing or incorrectly treated blend could be responsible for the underestimated differential abundance of Mn in the metal-poor stars. Otherwise, we have to conclude that *the NLTE analysis fails to achieve consistent ionization equilibria of Mn in metal-poor stars.*

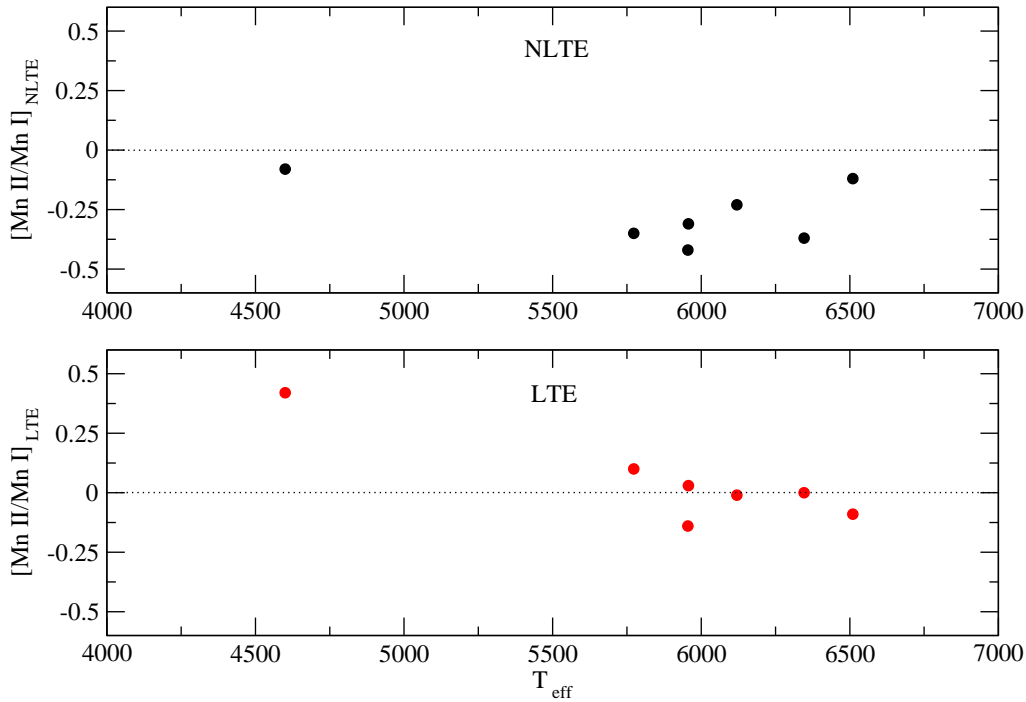


Figure 7.3: The $[\text{Mn}/\text{Fe}]$ ratios as derived from Mn I and Mn II lines under NLTE (upper panel) and under LTE (lower panel) as a function of effective temperature for selected stars.

7.1.3 Constraints on the accuracy of NLTE abundances

The most uncertain parameter in the NLTE calculations is S_{H} , the scaling factor to the cross-sections for inelastic H collisions, which are calculated with Drawin's (1968) formula. The exact value of S_{H} is not important for the Mn II lines because their abundances are anyway nearly *equal* under LTE and NLTE. The $[\text{Mn}/\text{Fe}]$ ratios as calculated from the Mn I lines are also not very sensitive to the choice of S_{H} , as long as very large scaling factors ($S_{\text{H}} \gg 1$) are not used. The test calculations for four metal-poor stars show (Fig. 7.4) that the change of a scaling factor $S_{\text{H}} = 0 \dots 1$ leads to a variation of the $[\text{Mn}/\text{Fe}]$ ratios ($\Delta[\text{Mn}/\text{Fe}]_{0\dots 1}$) in the range of $+0.05 \dots -0.1$ dex. For stars with $[\text{Fe}/\text{H}] > -1$, we derive $\Delta[\text{Mn}/\text{Fe}]_{0\dots 1} \sim +0.03 \dots -0.05$. The error bars on the Fig. 7.4 denote standard deviations σ of $[\text{Mn}/\text{Fe}]$ values. Obviously, small σ are achieved with $S_{\text{H}} \leq 0.5$. It is reasonable to suggest that $S_{\text{H}} = 0.05$ (our reference value) provides the

smallest scatter between different lines when all four stars are taken into account. This value is in agreement with the results derived for Ba and Eu by Mashonkina (1996) and for Mg emission lines by Sundqvist et al. (2008), who present convincing arguments in favor of very small ($\ll 1$) but non-zero values for S_H . Also, according to Belyaev & Barklem (2003) the standard Drawin's formula ($S_H = 1$) strongly *overestimates* the rate of transitions for Li. If these estimates are true for Mn as well, we can claim only *a slightly subsolar or even flat [Mn/Fe] trend with decreasing metallicity*. The variation of S_H within the range $0 \dots 1$ will not change the general trend in Fig. 7.2 given the large differences $[\text{Mn}/\text{Fe}]_{\text{NLTE}} - [\text{Mn}/\text{Fe}]_{\text{LTE}}$ in metal-poor stars.

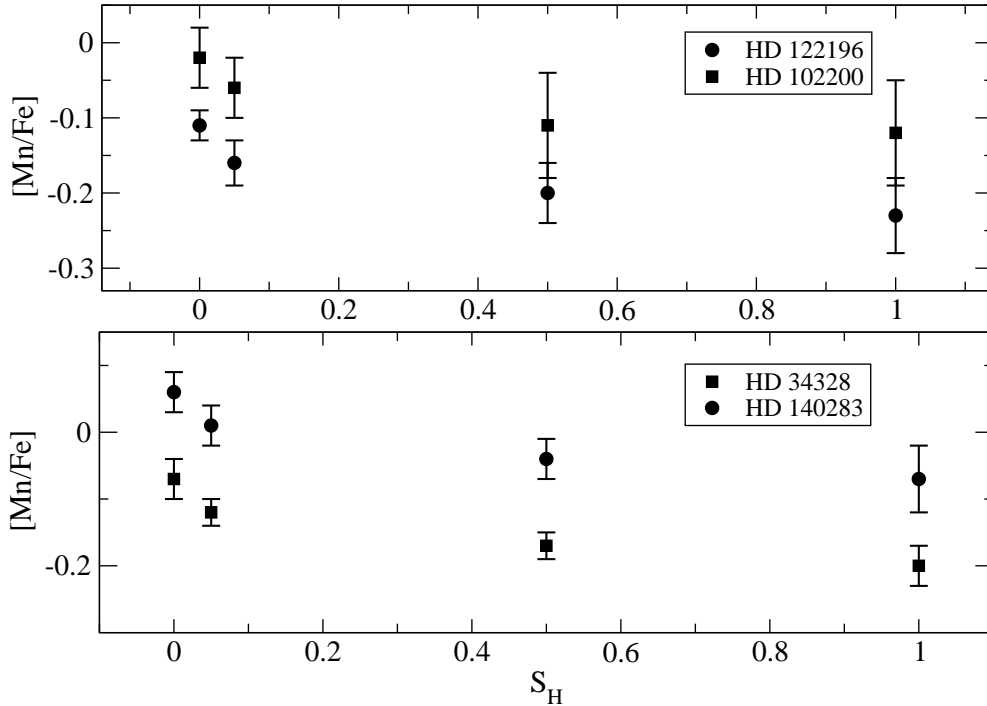


Figure 7.4: $[\text{Mn}/\text{Fe}]$ ratios for HD 34328, HD 102200, HD 140283, and HD 122196 calculated with $S_H = 0, 0.05, 0.5$, and 1.

We also expect that a thermalizing effect of H collisions in metal-poor stars would be compensated by enhanced photoionization rates. Given the sensitivity of Mn I level populations to the photoionization in metal-poor stars (Sect. 4.2.2), it is natural to expect that with the *proper* photoionization cross-sections the NLTE effects in Mn I will be amplified. This would raise the abundances determined from Mn I lines. We performed test NLTE calculations for the star HD 34328 with photoionization cross-sections for all levels increased by a factor of 300. The effect turned out to be significant: Mn abundances derived from the excited lines increased by 0.4 dex, on average. The abundances determined from the resonance lines at 403 nm change only by +0.05 dex. *Strongly different NLTE corrections required for the resonance and excited lines in the metal-poor star point at the inadequacy of a simple hydrogenic photoionization approximation. This may be also the reason for the apparent failure to yield a consistent ionization balance of Mn in metal-poor stars.*

Taking into account possible residual systematic errors due to underestimating photoionization in Mn I by the hydrogen-like approximation, we can conclude that $[\text{Mn}/\text{Fe}]$ follows the solar value throughout the range of metal abundances analyzed here.

7.2 Cobalt

The abundances from Co I lines in metal-poor stars are calculated strictly relative to the Sun. The results of calculations are given in Table 7.1. In Fig. 7.5, $[\text{Co}/\text{Fe}]$ ratios computed under NLTE and LTE are plotted as a function of the stellar iron abundance. Indeed, the effects of overionization on Co I atoms are significant in metal-poor atmospheres. The NLTE abundances of Co in the metal-poor stars are *higher* than the LTE abundances by 0.4–0.8 dex. The mean Co overabundance in stars with subsolar metallicity is $\langle [\text{Co}/\text{Fe}] \rangle = +0.53$ with the dispersion $\sigma = 0.15$ dex, if two metal-poor stars with very small $[\text{Co}/\text{Fe}]$ ratios are ignored.

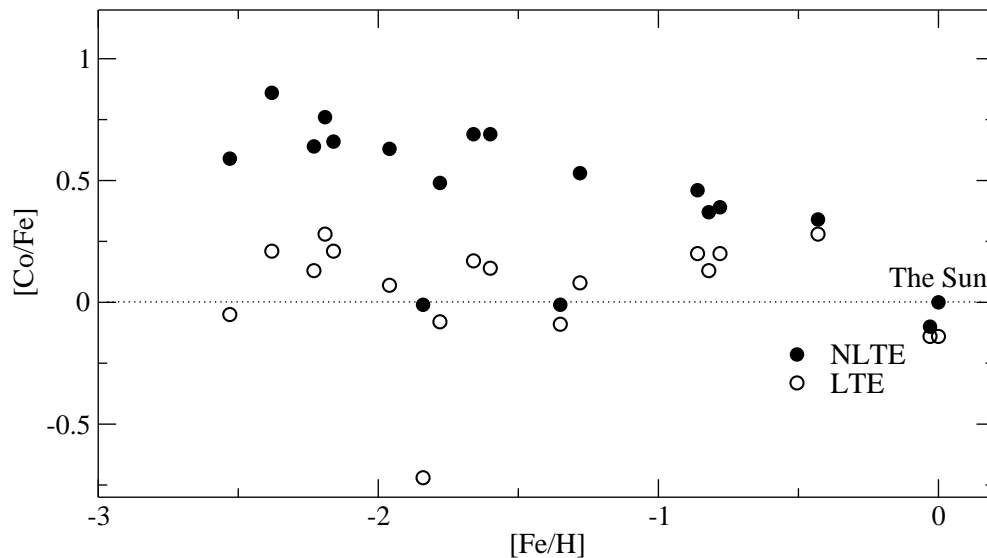


Figure 7.5: $[\text{Co}/\text{Fe}]$ vs. $[\text{Fe}/\text{H}]$ in metal-poor stars. The Co abundances are derived from Co I lines. NLTE and LTE abundances are marked with filled and open circles, respectively.

The Co abundances of thick disk stars with $-1 < [\text{Fe}/\text{H}] < -0$ are based on 6 to 10 lines, which have $W_\lambda > 20$ mÅ in the solar spectrum. In spectra of the halo stars, only three Co I lines are detected ($\lambda\lambda 4020, 4110, 4121$). Initially, we used all three lines. However, a more careful analysis revealed a systematic discrepancy between abundances derived from two lines located in the near and far red wing of H δ , 4110 and 4121 Å. Under NLTE, the difference amounts to 0.06 dex for the Sun, and increases to ~ 0.2 dex in the metal-poor stars. The LTE assumption makes the situation even worse: in the solar case, the abundance derived from the line at 4110 Å is 0.2 dex lower than that from the line at 4121 Å. In the metal-poor stars, the discrepancy is of the same magnitude but with reverse sign. After unsuccessful attempts to ascertain the reason for the discrepancy, we decided to use only the line at 4121 Å. In contrast to the line at 4110 Å, the line at 4121 Å is sufficiently strong even in the most metal-poor stars so that uncertainty due to continuum placement is small. No indications of this problem are found in the literature, mainly because there are only a few *accurate* studies of Co abundances in metal-poor stars, and neither of those includes the line at 4110 Å.

Two stars with very low NLTE $[\text{Co}/\text{Fe}]$ ratios are HD 25329 and HD 103095. Neither of those has anomalous Mn abundances. For HD 25329, Peterson (1981) calculated a much higher $[\text{Co}/\text{Fe}]$ ratio under LTE, +0.48 dex. As in the case of manganese, the discrepancy with our value probably stems from different model parameters and abundance analysis techniques. For HD 103095, Peterson derived a slightly lower LTE $[\text{Co}/\text{Fe}]$ ratio, 0.15 dex, compared to the other stars in her sample. Still, this value is higher than our NLTE abundance by 0.15 dex. Gratton & Sneden (1991) found the equal LTE abundance ratio $[\text{Co}/\text{Fe}] = -0.18$ for the giant HD 122563 and subgiant HD 140283. In comparison, our LTE abundance for HD 122563 is -0.05 , and the

huge NLTE correction further increases the abundance by 0.65 dex. For the same star, Ryan et al. (1996), Johnson (2002) and Cayrel et al. (2004) computed $[\text{Co}/\text{Fe}] = +0.33$, $[\text{Co}/\text{Fe}] = +0.25$, and $[\text{Co}/\text{Fe}] = +0.29$, respectively. All these values were derived under LTE assumption, and they systematically differ by $\sim +0.3$ dex from our LTE $[\text{Co}/\text{Fe}]$ ratio. As noted in the previous section, stellar parameters are very divergent in all three studies. So, the similarity of their $[\text{Co}/\text{Fe}]$ ratios is hard to explain.

As a final consistency check, we calculated Co abundances from the 3501 line of Co II. The values are also strictly differential with respect to the Sun. The results are given in Table 7.3 for the lines of neutral cobalt $[\text{Co}/\text{Fe}]_{\text{I}}$ and ionized cobalt $[\text{Co}/\text{Fe}]_{\text{II}}$. In contrast to ionized Mn, *the NLTE abundance corrections for ionized cobalt are not so small and have a positive sign*. For HD 84937 and HD 140283, $\Delta[\text{Co}/\text{Fe}]_{\text{II}}(\text{NLTE} - \text{LTE}) > 0.1$ dex. However, we encounter the same problem as for Mn: there is a significant discrepancy between abundances determined from the lines of Co I and Co II.

Table 7.3: NLTE and LTE abundance ratios $[\text{Co}/\text{Fe}]$ for selected stars as calculated from the Co I and Co II lines.

Object	$[\text{Co}/\text{Fe}]_{\text{I}}$		$[\text{Co}/\text{Fe}]_{\text{II}}$	
	NLTE	LTE	NLTE	LTE
HD 34328	0.69	0.17	0.21	0.17
HD 61421	-0.1	-0.14	-0.04	-0.05
HD 84937	0.66	0.21	0.09	-0.05
HD 102200	0.53	0.08	0.21	0.17
HD 122196	0.49	-0.08	-0.11	-0.15
HD 122563	0.59	-0.05	0.19	0.12
HD 140283	0.86	0.21	0.24	0.13

Fig. 7.6 displays the difference between $[\text{Co}/\text{Fe}]$ ratios computed from the lines of two ionization stages, $[\text{Co}_{\text{II}}/\text{Co}_{\text{I}}] = [\text{Co}/\text{Fe}]_{\text{II}} - [\text{Co}/\text{Fe}]_{\text{I}}$, as a function of stellar effective temperature. Obviously, *there is a systematic offset with the neutral Co giving higher NLTE abundances for all stars except the Procyon*. The offset between ionic and neutral lines under LTE seems to be random (Fig. 7.6, lower panel), and the magnitude of discrepancy is smaller than under NLTE. *Such a behavior is analogous to manganese* (compare with Fig. 7.3), and the reason is most likely the same. To get consistent ionization equilibria under NLTE, we need either significantly *lower* abundances from the neutral lines, and/or much higher abundances from the ionic lines. The former can be, at least partly, achieved with increasing a scaling factor to the H I collision cross-sections. We have demonstrated in Sect. 5.2.1 that increasing the collision efficiency leads to reduction of NLTE effects, and thus, *lowering* the abundances. Test calculations were performed for the halo subdwarf HD 34329 with $[\text{Co}/\text{Fe}]_{\text{I}}^{\text{NLTE}} = 0.69$ and $[\text{Co}/\text{Fe}]_{\text{I}}^{\text{LTE}} = 0.17$. The NLTE results for $S_{\text{H}} = 1$ are not very different from the case of $S_{\text{H}} = 0.05$ (our reference value): the abundance from the Co I lines decreased by 0.15 dex. It is only with $S_{\text{H}} = 10$ that the discrepancy is solved: $[\text{Co}/\text{Fe}]_{\text{I}}^{\text{NLTE}} = 0.26$ that is in agreement with $[\text{Co}/\text{Fe}]_{\text{I}}^{\text{NLTE}} = 0.21$. The abundances derived from Co II lines are not sensitive to variation of S_{H} . However, for HD 84937, assumption of $S_{\text{H}} = 10$ leads to $[\text{Co}/\text{Fe}]_{\text{I}} = 0.27$ that is still ≈ 0.2 dex higher than the NLTE abundance determined from Co II lines. Whether such a large scaling factor is justified is questionable. There are no indications in the literature that S_{H} must be larger than unity, except for the work of Korn et al. (2003), who suggested $S_{\text{H}} = 3$. Gratton et al. (1999) also required a scaling factor larger than unity to bring Fe abundances from two ionization stages in RR Lyrae stars in agreement. However, for Mg, O, and Na they found $S_{\text{H}} \leq 0.5$.

We also noted that increasing the abundances determined from ionic lines could solve the

problem. One of related possibilities is to vary the effective temperature. We have investigated the effect of temperature enhancement on the abundance analysis by repeating the calculations for the mildly metal-poor halo star HD 102200 with $\Delta T_{\text{eff}} = \pm 100$ K with respect to our originally adopted value $T_{\text{eff}} = 6120$ K. For both elements the effect turned out to be *negligible*. With the higher temperature, $T_{\text{eff}} = 6220$ K, abundances from Mn I and Co I lines *increased* respectively by 0.02 and 0.06 dex, and the abundances from the lines of ionized species *decreased* by ~ 0.02 dex. The abundance corrections of the same magnitude but with the reverse sign were derived for lower T_{eff} . Thus, to resolve the problem, one would have to assume *considerably lower effective temperatures* for all stars in our sample, by several hundred K. However, such low temperatures seem highly improbable. First, the uncertainties in our T_{eff} are ± 100 K or less, and this can give rise to 0.1 dex dispersion at most. Besides, the adopted values from the Table 3.1 are consistent with stellar parameters of Axer et al. (1995) for the common metal-poor stars. The latter authors showed that their effective temperatures for a majority of extreme halo stars with $[\text{Fe}/\text{H}] \leq -1.6$ lead to stellar ages exceeding 18 Gyr. The analogous problem was found for the Galactic disk stars, with ages > 10 Gyr. Thus, strongly decreasing effective temperatures, we might have to face the problem of inconsistency between ages of stars and of the universe.

To conclude, the problem of inconsistent ionization equilibria of Mn and Co is *not solved* with NLTE analysis. This failure could be due to the unrealistic atomic models used in SE calculations, because the important atomic data, cross-sections for photoionization and H I collisions, are missing. Alternatively, our atmospheric models are not satisfactory, and granulation inhomogeneities cause large effects on abundances in addition to NLTE.

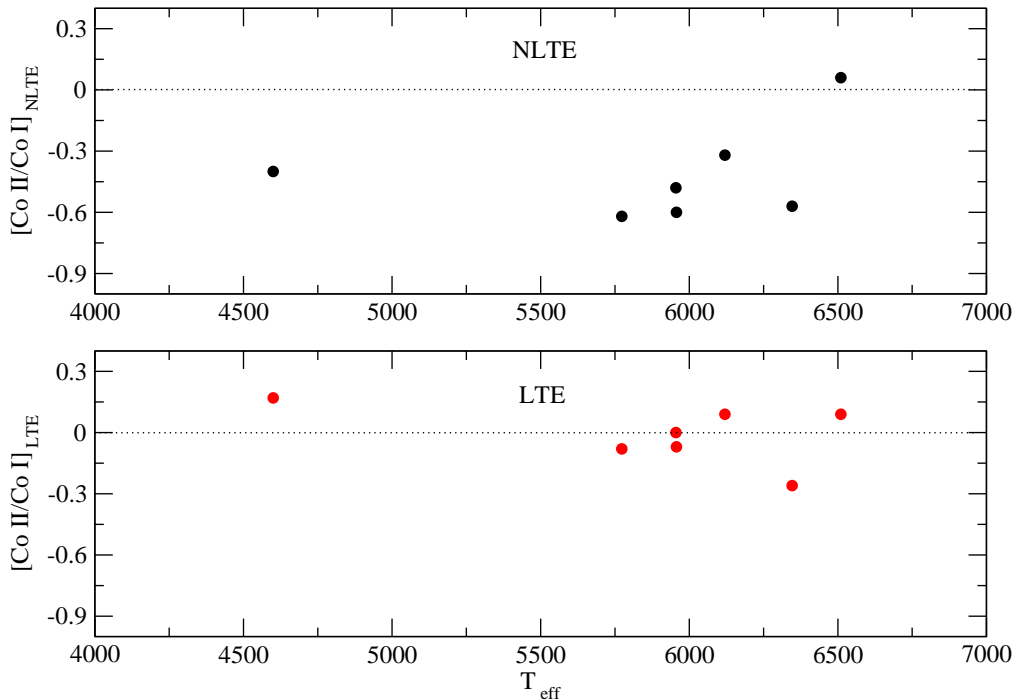


Figure 7.6: $[\text{Co}/\text{Fe}]$ ratios as determined from Co I and Co II lines under NLTE (upper panel) and under LTE (lower panel) as a function of effective temperature for selected stars.

7.3 The trend of $[\text{Mn}/\text{Fe}]$ with $[\text{Fe}/\text{H}]$

In the past 20 years, a large number of Mn and Co abundance analyses of metal-poor stars in different populations have appeared in the literature; *all studies refer to LTE*. We have mentioned some of them in the previous section, discussing our results for the individual stars. Here, we rather concentrate on the *average* trends of $[\text{Mn}/\text{Fe}]$ and $[\text{Co}/\text{Fe}]$ ratios with metallicity.

It is important to remember that *the direct combination of our abundances with the others is a complicated and sometimes a senseless task, even when NLTE corrections are applied*. Often, authors do not present sufficient information for a critical evaluation of their results using the term “differential analysis with respect to the Sun” as a self-explanatory expression. Whereas, in reality some of these studies have nothing in common with the *true differential analysis*, which requires that solar and stellar abundances are determined with the same type of model atmospheres, and only the $\log gf\varepsilon$ values are used to calculate the relative abundance ratios. In this section, we compare our trends with the data from the literature. But the reader should be aware that the agreement or disagreement of different trends may not be significant at all.

Fig. 7.7 shows the Mn abundances for stars of low metallicities from studies of Ryan et al. (1991), McWilliam et al. (1995), Nissen et al. (2000), Cayrel et al. (2004), Bai et al. (2004), Feltzing et al. (2007), Reddy et al. (2003), Reddy et al. (2006), and Sobeck et al. (2006) (see also Table 8.1). *Our NLTE abundances are systematically larger than the comparison studies*. The general offset of +0.2 to +0.4 dex is mainly due to the NLTE effects, as can be predicted from Table A.6. *In contrast, the Mn underabundance suggested by our LTE analysis is consistent with results of the others*.

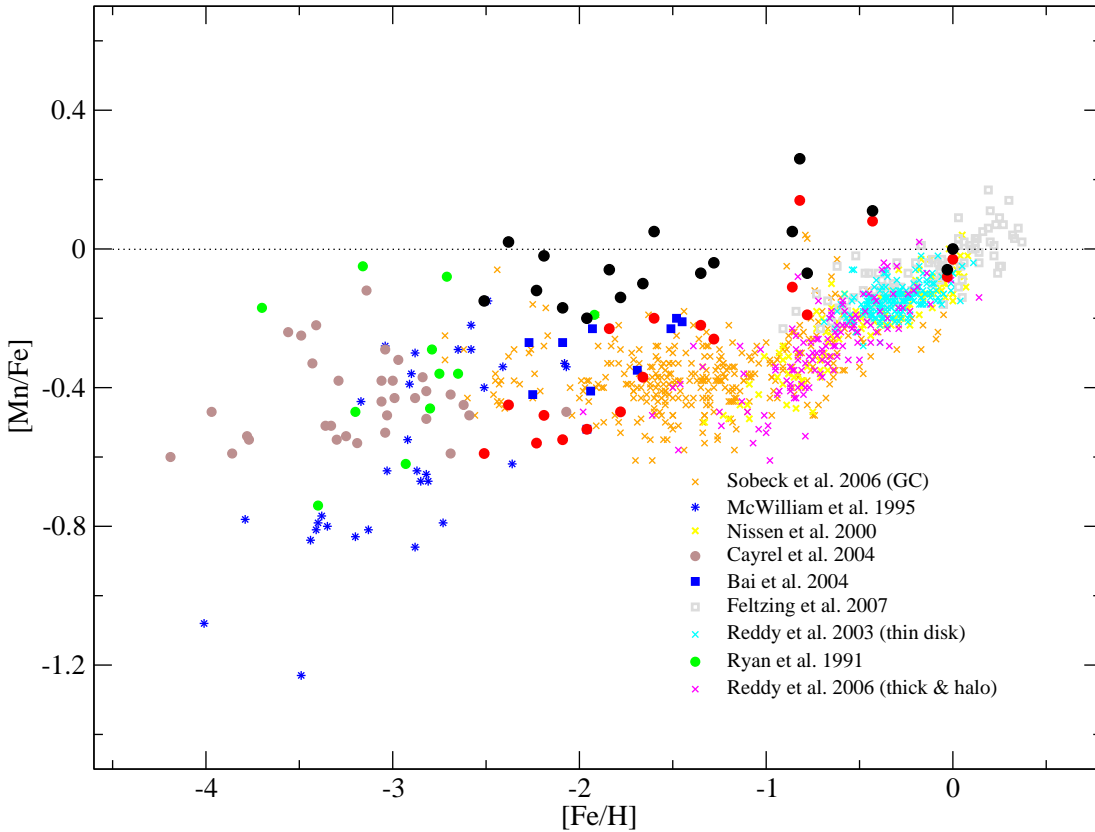


Figure 7.7: $[\text{Mn}/\text{Fe}]$ vs. $[\text{Fe}/\text{H}]$ in metal-poor stars. All Mn abundances are derived from Mn I lines. Our NLTE and LTE abundances are marked with filled black and red circles, respectively. The sources for other data are labeled in the plot.

The average Mn abundances for stars with metallicities $-1 \dots 0$ are in agreement between the compiled analyses as to slope and absolute values. This is seen for the data of Nissen et al. (2000), Reddy et al. (2003), and Feltzing et al. (2007). The similarity of trends is not surprising because the same abundance analysis techniques were employed. In particular, all three studies make use of near-IR Mn I lines at 600 nm and 1D LTE model atmospheres. Despite a general agreement of the trends, there is a disagreement in their interpretation. Nissen et al. (2000) performed an LTE analysis of 119 F-G stars representing three galactic populations and pointed at a [Mn/Fe] discontinuity at $[Fe/H] \approx -0.7$, which might indicate *a transition from the thick to thin disk*. Prochaska & McWilliam (2000) reanalyzed the Nissen et al. (2000) abundances on suspicion that the wrong hyperfine splitting data caused the curious [Mn/Fe] behavior. Indeed, their corrected Mn abundances were systematically higher by 0.15 dex compared to the Nissen et al.'s (2000) values. However, the trend and conclusions about the presence of a thin-to-thick disk transition remained the same. It is noteworthy that McWilliam et al. (2003) mentioned possible "systematic errors" in the analysis of Prochaska & McWilliam (2000); unfortunately, they did not specify the origin of these errors.

Reddy et al. (2003) also calculated a slightly negative trend for the thin disk stars, however in the subsequent analysis of the thick disk and halo stars (Reddy et al. 2006) no obvious differences in the [Mn/Fe] behavior between three stellar populations were found (see Fig. 7.7). Instead, [Mn/Fe] demonstrated a smooth decline to ~ -0.4 dex from the solar metallicity to $[Fe/H] \approx -1$, *independent of a stellar population* considered. In fact, the results of Reddy et al. (2006) for the thick disk are consistent with results of Nissen et al. (2000), although a different source of HFS was used. Feltzing et al. (2007) analyzed thick and thin disks only. They confirmed that *the thin disk stars have enhanced [Mn/Fe] ratios relative to the thick disk stars*. Nissen et al. (2000) discontinuity was dumped as a result of an incomplete sampling of two stellar populations. Taking only thick disk stars for $[Fe/H] < -0.7$ and thin disk stars for higher metallicities, Feltzing et al. arrived at the same result as Prochaska & McWilliam (2000), namely the *deficiency of Mn in the thick disk, and solar ratios in the thin disk*. They argued that the systematic offset of Reddy et al. (2006) data for the thick disk is a result of erroneous HFS used by the latter.

Our sample of the galactic disk stars is too small to test the above-mentioned findings. The NLTE abundance corrections are minimal for stars with $[Fe/H] > -0.5$, hence both *very mild underabundance* of Mn relative to Fe of ~ -0.05 dex (Prochaska & McWilliam 2000) or a *flat trend* (Feltzing et al. 2007) are plausible. At metallicities typical of the thick disk, $[Fe/H] \approx -0.8$ dex, the NLTE corrections are already large enough, $\Delta_{NLTE} \approx +0.15$ dex. Applying these NLTE corrections to the thick disk Mn abundances of Feltzing et al. (2007), we derive the mean $\langle [Mn/Fe] \rangle$ ratio of -0.05 dex that is equal to the $\langle [Mn/Fe] \rangle$ ratio found by Prochaska & McWilliam (2000) for the thin disk stars. *Consequently, the difference in [Mn/Fe] trends between the galactic thick and thin disks should be very small, if present at all*. This conclusion is also confirmed by the NLTE and LTE Mn abundances, which we find for the three thick disk stars. However, if the [Mn/Fe] trend of Reddy et al. (2006) is used, then the difference between two stellar populations is more evident, and it amounts to 0.15 dex on average.

For the halo stars with $[Fe/H] < -2$, we find a very large dispersion of [Mn/Fe] ratios with metallicity. The data for comparison in Fig. 7.7 are from Ryan et al. (1991), McWilliam et al. (1995), Cayrel et al. (2004), Bai et al. (2004). Unfortunately, most of the stars in the other studies are outside the range of metallicities covered by our stellar sample. McWilliam et al. (1995) provide Mn abundances for 33 giants with $-4 \leq [Fe/H] \leq -2.0$. Their data give a clear evidence of a rapid decline of [Mn/Fe] ratios for $[Fe/H] \leq -2.5$. Such a dramatic drop can be easily explained. McWilliam et al. used the problematic Mn I lines, the near-UV resonance triplet. The fact that these lines give *systematically lower* value for Mn is now firmly established (Sect. 7.1.2). Other authors tried to overcome this problem. For example, Cayrel et al. (2004) introduced a correction of +0.4 dex to their Mn abundances in giants derived from the resonance triplet. This is probably the reason why their abundances are on average larger than that of McWilliam et al. The remaining scatter between both studies is due to intrinsic uncertainties in the analyses. Approximately the same results are found by Ryan et al. (1991), again with a large spread of Mn abundances. The overdeficiency of Mn relative to Fe for four giants with $[Fe/H] < -2$ were

reported by François et al. (2003). Ryan et al. suggested a mean underabundance of Mn in halo of -0.32 dex that turned out to be consistent with the result of Gratton (1989). The latter author found $\langle [\text{Mn}/\text{Fe}] \rangle = -0.34$ for stars with $[\text{Fe}/\text{H}]$ between -2.5 and -1 dex, and a steady increase of $[\text{Mn}/\text{Fe}]$ up to solar metallicities. It is noteworthy that the Gratton (1989) is the first study that indicated that manganese mirrors the trend of α -elements with decreasing metallicity in that it is roughly constant in the halo stars and increases in disk stars. The same mean underabundance of Mn of -0.31 dex was obtained for 10 subdwarfs with $-2.3 < [\text{Fe}/\text{H}] < -1.4$ by Bai et al. (2004). It is seen in Fig. 7.7 that their data do not stand out of the average trend of $[\text{Mn}/\text{Fe}]$ with $[\text{Fe}/\text{H}]$, when all the above-mentioned studies are considered together. However, it does appear that the subdwarfs of Bai et al. (2004) lie on the same line as the subdwarfs of Ryan et al. (1991), whereas the subgiants studied by the latter authors show a positive shift in $[\text{Mn}/\text{Fe}]$ of ≈ 0.3 dex. Corrected for mean NLTE effects, the results of Bai et al. (2004) are in reasonable agreement with our NLTE abundances of Mn in metal-poor stars at an approximately constant level of $[\text{Mn}/\text{Fe}] \sim -0.1 \dots 0.0$.

The discussion presented above refers to the abundances derived from the Mn I lines only. A very important test is to compare these $[\text{Mn}/\text{Fe}]$ trends with those calculated using the Mn II lines. Fortunately, there is a number of publications (Johnson 2002, Lai et al. 2008), which provide LTE Mn abundances for both ionization stages. In Fig. 7.8, we present both Mn II (upper panel) and Mn I (lower panel) as a function of $[\text{Fe}/\text{H}]$; the data are our NLTE and LTE abundances, and also LTE abundances from Johnson (2002) and Lai et al. (2008). Addition of our LTE data to

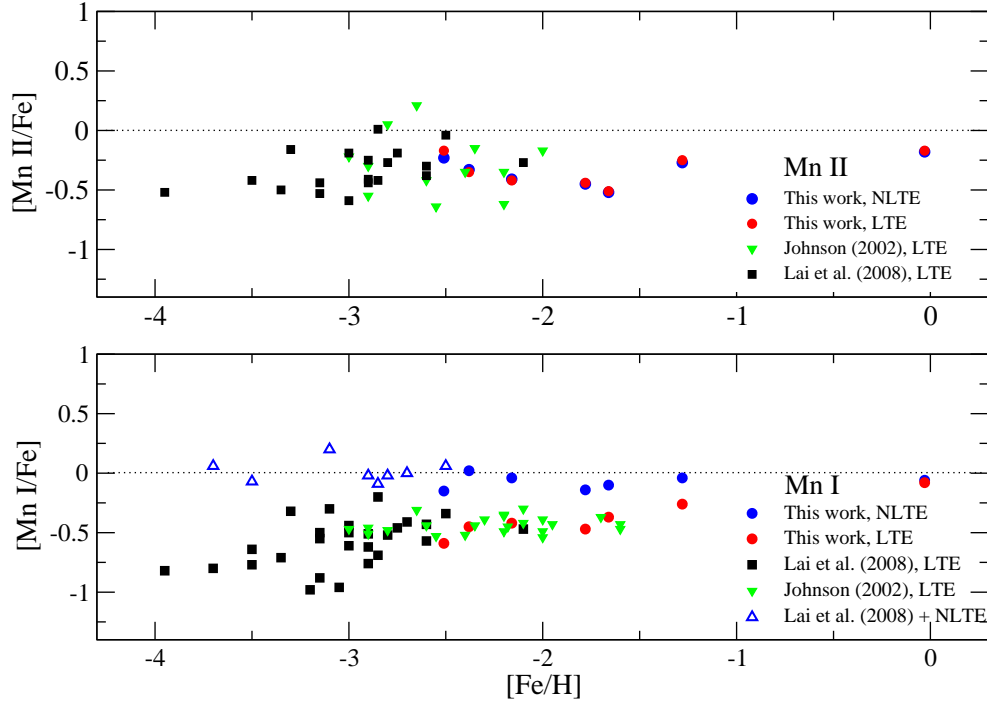


Figure 7.8: $[\text{Mn}/\text{Fe}]$ vs. $[\text{Fe}/\text{H}]$ in metal-poor stars. The Mn abundances derived from Mn II and Mn I lines are given on the top and bottom panels. NLTE and LTE abundances are marked with filled and open circles, respectively. The open blue triangles on the lower panel refer to the data of Lai et al. (2008) corrected for the NLTE effects from the present study.

the results of the other authors reveals a very interesting pattern: *[Mn II/Fe] appears to be flat, whereas a declining trend of [Mn I/Fe] with metallicity is clearly seen.* In studies of Johnson (2002) and Lai et al. (2008), we find a clear offset between neutral and ionized Mn, with Mn II giving larger abundances. Note, however, that our NLTE abundances are systematically lower for Mn II lines. A dispersion in star-to-star abundances derived from neutral lines is small, but it doubles if ionic lines are used. Whether this dispersion indicates real variations of Mn abundances in the halo stars or it simply reflects the deficiencies of abundance analysis techniques is still questionable. If we declare Mn II abundances reliable because they are almost *insensitive to NLTE effects in our analysis*, then it can be suggested that *[Mn/Fe] remains constant in the stars with [Fe/H] ≥ -1 and then rapidly increases up to 0 for solar metallicity.* This would confirm the conclusion of Gratton (1989). Otherwise, assuming that the NLTE approach predicts correct abundances from Mn I lines, and applying NLTE corrections to the data of Lai et al. (2008) (see Fig. 7.8, lower panel), we can claim that *Mn follows the depletion of Fe even in the most metal-poor stars. This conclusion contradicts all previously proposed trends of Mn in metal-poor stars.* We will revert to this important issue in the next chapter to check whether one of the two hypotheses is consistent with theory of nucleosynthesis.

Finally, we wish to note that Gratton (1988) found different runs of [Mn/Fe] with decreasing Fe for cluster and field stars of the Galactic halo. It was then suggested that two systems have different nucleosynthetic histories and the theory that field stars were debris of disrupted globular clusters does not hold. Ryan et al. (1991) also discussed this idea, but they did not draw any conclusion due to lacking observational data. Cohen et al. (2004) compared their Mn abundances for the field stars with the results for globular clusters from the literature and argued that there is a definite offset between both groups. We note, however, that inhomogeneous stellar samples, differences in the procedure of stellar parameter and abundance calculations lead to systematic offsets of different trends. Hence, Cohen et al. (2004) conclusions are not very convincing. Recently, Sobeck et al. (2006) carried out an accurate LTE analysis of Mn abundances in globular cluster, open cluster, and field stars. No evidence was found for the differentiation between three stellar groups. Their results for globular cluster stars (GC) are shown in Fig. 7.7. The field stars are not included in the plot, because they lie essentially on the same line as the GC stars. Sobeck et al.'s (2006) abundances appear to have a slight positive offset from our LTE abundances at $[\text{Fe}/\text{H}] \leq -1.7$ dex.

7.4 The trend of [Co/Fe] with [Fe/H]

Several investigations of Co abundances have been done under LTE in various metallicity regimes and stellar populations. All of them are based on Co I lines. The results of these studies, along with our NLTE and LTE abundances are presented in Fig. 7.9. We used the same symbols for the data taken from the same sources as those in Fig. 7.7 for [Mn/Fe]: Ryan et al. (1991), McWilliam et al. (1995), Cayrel et al. (2004), Reddy et al. (2003), and Reddy et al. (2006). Other sources include Johnson (2002), Lai et al. (2008), and Gratton & Sneden (1991). Similar to Mn, cobalt abundances show a large scatter within a given study and between studies. The general trend can be hardly defined, although a majority of studies indicate that *Co is increasing with respect to iron towards very low metallicities. At [Fe/H] ≈ -2.5 , the trend changes slope, so that for less metal-poor stars the [Co/Fe] ratio is relatively flat.* Such a behavior was originally identified by McWilliam et al. (1995), who explained the observed large scatter in star-to-star Co abundances by a very low signal-to-noise ratio of their spectra.

A decade later, Cayrel et al. (2004) carried out an analysis of giant stars with $-4 < [\text{Fe}/\text{H}] < -2$ and confirmed supersolar [Co/Fe] ratios with a scatter of 0.15 dex. These authors claim that the measurement errors are significantly lower, thus this scatter reflects the true variations of Co abundances between halo stars. Investigating extremely metal-poor giants and dwarfs in the same metallicity range as Cayrel et al., Lai et al. (2008) also found high Co abundances relative to Fe, which match the results of Cayrel et al. in general scatter and slope. A similar very inhomogeneous behavior of [Co/Fe] in the halo was reported by Ryan et al. (1991). Hence, it appears that *the*

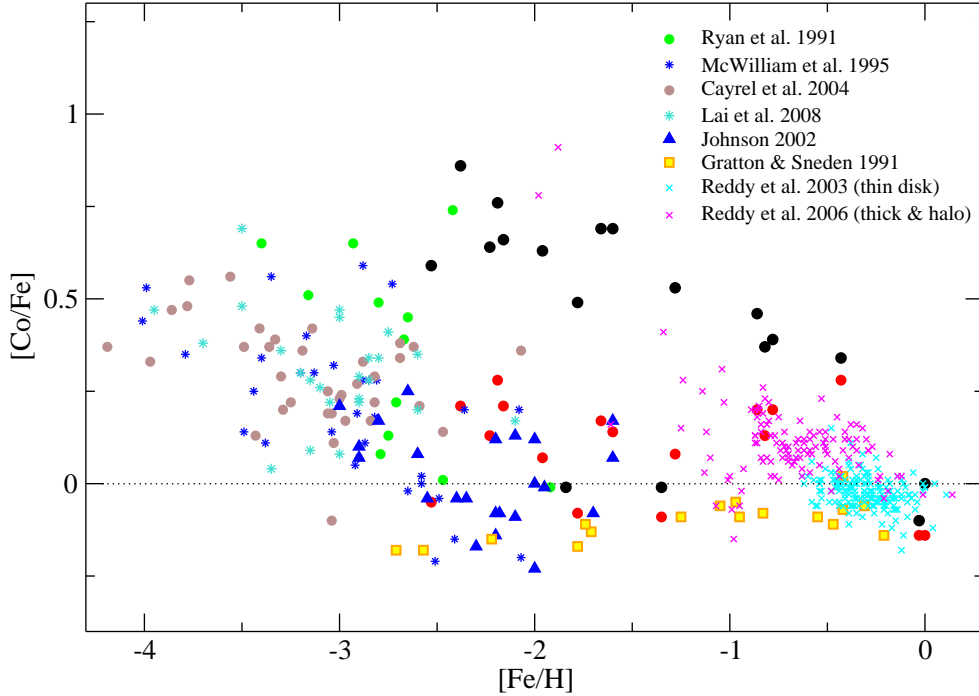


Figure 7.9: $[Co/Fe]$ vs. $[Fe/H]$ in metal-poor stars. All Co abundances are derived from Co I lines. Our NLTE and LTE abundances are marked with filled black and red circles, respectively. Other data sources are Ryan et al. (1991), McWilliam et al. (1995), Cayrel et al. (2004), Reddy et al. (2003), Reddy et al. (2006), Johnson (2002), Lai et al. (2008), and Gratton & Sneden (1991).

large dispersion of $[Co/Fe]$ ratios in the halo stars is not due to observational and interpretative errors, but it rather indicates inhomogeneous conditions at the time these stars formed.

The only study that suggests a radically different $[Co/Fe]$ trend with very small dispersion is Gratton & Sneden (1991). They found a *small deficiency of Co in metal-poor stars with the average of $\langle [Co/Fe] \rangle = -0.12$, and proposed even larger $[Co/Fe]$ depletion towards lower metallicities.* In fact, we can cast doubt on the latter conclusion. In the range of metallicities, where Gratton & Sneden's (1991) Co abundances overlap with those of McWilliam et al. (1995) and Johnson (2002), there is no significant difference between the datasets. Johnson's (2002) data are strongly scattered around zero, and for some stars $[Co/Fe]$ are even lower than that of Gratton & Sneden. McWilliam et al. also concluded that their $[Co/Fe]$ relations fit with the results of Gratton & Sneden. At higher metallicities, $-1 \leq [Fe/H] \leq 0$ the data of the latter are discrepant with calculations of Reddy et al. (2003) and Reddy et al. (2006). In particular, Reddy et al. (2006) find supersolar Co abundances for the thick disk stars. As seen in Fig. 7.9, there are two *halo stars* from Reddy et al. (2006) with extremely high $[Co/Fe]$ ratios. The one with $[Co/Fe] = +0.91$ dex is HD 19445, for which we derive an LTE abundance $[Co/Fe] = +0.07$ dex. We found no explanation for this discrepancy apart from the fact that Reddy et al. (2006) used 400 K lower effective temperature than we did. Reddy et al. (2006) also do not discuss why this star stands out of a general trend.

Our LTE abundances are in general consistent with the results of the other authors. For the thick disk stars, $[Co/Fe]$ is flat, in agreement with Reddy et al. (2006). Even the thin disk star, HD 61421, supports mild underabundance of Co in the thin disk as follows from the results of Reddy et al. (2003). Stars of the halo, $[Fe/H] < -1$ are on the same line as stars of Johnson's (2002), although that author analyzed only giants. However, our NLTE analysis offers a considerably

different picture from that of all other studies: *a strong overabundance of Co relative to Fe shows already in the thick disk stars and becomes even larger in halo stars.* It also appears that this behavior continues in extremely metal-poor stars. Applying the NLTE corrections from the Table 5.2 to the subdwarfs of Lai et al. (2008) with $[\text{Fe}/\text{H}] < -3.0$, we obtain the mean [Co/Fe] ratio of +1 dex that points at *further increasing [Co/Fe] ratios with decreasing Fe.* However, the difference of 1 dex with the solar abundance ratio seems to be too large. In the next chapter, we invoke the results of chemical evolution modeling to determine *whether the NLTE produces erroneous abundances, or the extreme excess of cobalt relative to iron in metal-poor stars is indeed required by the current theory of the Galactic chemical evolution.*

Chapter 8

Fe-peak elements and the Galactic evolution

The interpretation of the element abundance trends in Galactic metal-poor stars in terms of their nucleosynthetic origin is not a trivial task. It is not sufficient to compare the yields of SNe II and SNe Ia with the observations; the yields must be averaged over a reasonable initial mass function (IMF) and incorporated in a Galactic chemical evolution (GCE) model with a specified star formation rate (SFR). Most of the chemical evolution models in the literature are rather simple. The IMF is adopted in the time-independent power law form of Salpeter (1955) and the SFR is proportional to the surface gas density in the power 1 to 2 Schmidt (1959). More complex forms of the SFR take into account the dependence on the total mass density in the Galaxy, and the distance from the Galactic center. It is often assumed that stars produce elements instantaneously at the time of their birth. This assumption is justified only for very massive short-lived stars, and it is of little use for the interpretation of element abundances that are produced on different time scales, like α - and Fe-peak elements. Also, one usually assumes an instantaneous mixing of the elements into the ISM. This is not reasonable in studying the element abundances in stars, which belong to the old Galactic populations. Halo stars with very low metallicities may even reflect the yield pattern of a single supernova. In this case, stellar *abundance anomalies* give evidence for inhomogeneities during the halo formation. The models, which relax the instantaneous mixing approximation are referred to as inhomogeneous models. There are several other parameters that one has to take into account in *modeling* the GCE. For example, gas infall seems to be necessary to describe the formation and evolution of the Galactic thick and thin disks. It can be neglected for the halo, which formed relatively quickly. The most advanced are the chemo-dynamical models, which allow a consistent treatment of the GCE and dynamics of the Galactic components. Finally, it is important to note that all these models assume a simple monolithic collapse scenario for the formation of the Galaxy (Eggen et al. 1962). However, merging processes, such as suggested for the thick disk (Bekki & Chiba 2002), could significantly modify the formation history of the Galactic components, and hence their chemical evolution.

The discussion presented below is based on the different types of GCE models: simple, inhomogeneous, and chemo-dynamical. In fact, we will see that the last two types of models do not provide significantly different descriptions of Galactic abundance trends compared to the simple models.

8.1 Observational constraints

It has been generally acknowledged that a strong underabundance of Mn develops with decreasing metallicity: a plateau in $0 > [\text{Fe}/\text{H}] > -2.5$ and a rapid decline thereafter. For Co, a mirror trend was assumed, again characterized by a constant solar ratios down to $[\text{Fe}/\text{H}] \approx -2.5$ and an increase at lower metallicities. These trends were widely used to explain the *production sites* of

Mn and Co, and *the proportions, in which these element are produced in SNe II or SNe Ia*. This lead to several theories of Fe-group element production, which are summarized in Table 8.1 for Mn. We do not produce a separate table for Co due to a very limited number of specific studies, focussing on the nucleosynthetic origin of this element.

Table 8.1: *Earlier investigations of Mn abundance in the stars*

A.	What studied	What found	Notes	Theory of Mn production
1	119 F & G disk and halo stars on the main sequence	At $-1.4 < [\text{Fe}/\text{H}] < 0.0$: gradual increase $-0.5 < [\text{Mn}/\text{Fe}] < 0$ sharp increase at $[\text{Fe}/\text{H}] = -0.7$	Transition between thick and thin disk; [Mn/Fe] mirrors the trend of $[\alpha/\text{Fe}]$	Overproduction in SN Ia
2	200 stars in globular clusters; also field halo stars	Plateau at $-2.7 < [\text{Fe}/\text{H}] < -0.7$: glob. clusters: $\langle [\text{Mn}/\text{Fe}] \rangle = -0.37$ halo field stars: $\langle [\text{Mn}/\text{Fe}] \rangle = -0.36$ Increase of [Mn/Fe] above $[\text{Fe}/\text{H}] \sim -1$	In this [Fe/H] range, [Mn/Fe] is not metallicity-dependent	Contribution from SN II is uniform
3	33 halo giants $-4 < [\text{Fe}/\text{H}] < -1$	Plateau at $-2.5 < [\text{Fe}/\text{H}] < -1$: $\langle [\text{Mn}/\text{Fe}] \rangle \sim -0.4$ dex Decline to [Mn/Fe] ~ -0.9 dex at $[\text{Fe}/\text{H}] \sim -4$ dex		Overproduction in SN Ia (combined with Gratton 1989) SN II involved with metallicity-dependent yields
4	Stars of (1)	Bimodal value of [Mn/Fe]: at $[\text{Fe}/\text{H}] < -0.7$ [Mn/Fe] ~ -0.3 at $[\text{Fe}/\text{H}] > -0.7$ [Mn/Fe] ~ -0.05	At $[\text{Fe}/\text{H}] \sim -0.7$ transition from thin disk to the thick disk and halo population	Overproduction in SN Ia
5	25 dwarfs and giants $-2.4 < [\text{Fe}/\text{H}] < -0.1$	In $-2.5 < [\text{Fe}/\text{H}] < -1$: constant $\langle [\text{Mn}/\text{Fe}] \rangle \sim -0.34$ Increasing trend at $[\text{Fe}/\text{H}] > -1$	[Mn/Fe] mirrors the trend of $[\alpha/\text{Fe}]$	Overproduction in SN Ia Different values of neutron-excess or initial Fe abundance
6	95 dwarf stars of thin and thick disks	In $-1 < [\text{Fe}/\text{H}] < 0$: thin disk: constant [Mn/Fe] ~ 0 thick disk: increase $-0.2 \leq [\text{Mn}/\text{Fe}] \leq 0$	No thin disk - thick disk discontinuity	SN II involved with metallicity-dependent yields Thin disk: SN Ia contribution
7	Solar neighborhood stars Galactic bulge giants Sgr dSph giants	$-2.6 < [\text{Fe}/\text{H}] < 0.2$ $-1.3 < [\text{Fe}/\text{H}] < 0.4$ $-1.6 < [\text{Fe}/\text{H}] < 0.1$	Bulge: increasing [Mn/Fe] with [Fe/H] dSph Sgr galaxy: [Mn/Fe] deficiency	SN II with metallicity-dependent yields SN Ia with metallicity-dependent yields

^a References: (1) Nissen et al. (2000); (2) Sobeck et al. (2006); (3) McWilliam et al. (1995);

(4) Prochaska and McWilliam (2000); (5) Gratton (1989); (6) Feltzing et al. (2007); (7) McWilliam et al. (2003)

Some authors (Gratton 1989, McWilliam et al. 1995, Nissen et al. 2000) note that Mn mirrors the trend of α -elements. The abundances of the latter increase steadily to $[\alpha/\text{Fe}] \approx +0.4$ from the solar metallicity to $[\text{Fe}/\text{H}] \approx -1$, and then remain constant down to $[\text{Fe}/\text{H}] \approx -2.5$. If SNe Ia are responsible for the $[\alpha/\text{Fe}]$ decline with increasing metallicity (Tinsley 1979), then these objects are also responsible for the increase of the $[\text{Mn}/\text{Fe}]$ ratio. So manganese can be a good chemical tracer of SNe Ia. The theory of Mn *overproduction* with respect to Fe in SN Ia and underproduction in SN II is supported by the analyses Prochaska & McWilliam (2000), del Peloso et al. (2005), and Sobeck et al. (2006). However, there are other results, which either do not conform with or even contradict this theory. Feltzing et al. (2007) combined their Mn abundances for the thick and thin disk stars with results of the other authors for the halo and dwarf spheroidal (dSph) galaxies. However, the abundance comparison was made against oxygen rather than iron because oxygen is only produced in SN II. They found a flat trend of $[\text{Mn}/\text{O}]$ for the halo and thick disk stars with $[\text{O}/\text{H}] < -0.5$ and increasing $[\text{Mn}/\text{O}]$ for $[\text{O}/\text{H}] > -0.5$. This was interpreted as a manifestation of *metallicity-dependent yields from SN II*. For the RGB stars in dSph galaxies, Feltzing et al. obtained significantly higher $[\text{Mn}/\text{O}]$ ratios compared to the metal-poor giants in the Galaxy, which was attributed to the slower star formation in these galaxies. McWilliam et al. (2003) also suggest that it is *not overproduction of Mn in SN Ia* that determines the observed trends of $[\text{Mn}/\text{Fe}]$. Their analysis is based on the comparison of the solar neighborhood stars from the studies of Gratton (1989), Nissen et al. (2000), Prochaska & McWilliam (2000), Johnson (2002), and Reddy et al. (2003), with giants in the Galactic bulge and dSph Sagittarius (Sgr) galaxy. They pointed out that the increasing trend of $[\text{Mn}/\text{Fe}]$ with $[\text{Fe}/\text{H}]$ in the bulge stars is identical to that in the halo and thick disk. The bulge is thought to be formed rapidly, with nucleosynthesis dominated by SNe II. As *solar $[\text{Mn}/\text{Fe}]$ ratios are also observed for the bulge stars*, these should be entirely due to *SNe II with metallicity-dependent yields*. However, the observed $[\text{Mn}/\text{Fe}]$ deficiency in stars of the dSph Sagittarius galaxy was explained by the *metallicity-dependent yields from SN Ia*. The last argument was questioned by Carretta et al. (2004), who noted that if the dSph Sgr stars of Bonifacio et al. (2000) are also considered, the trend of $[\text{Mn}/\text{Fe}]$ with $[\text{Fe}/\text{H}]$ in dSph Sgr galaxy increases to solar metallicities. The primary goal of Carretta et al. was an analysis of the largest Galactic globular cluster, 47 Tuc. The only conclusion that they could draw from their abundances is that *Mn yields are metallicity-dependent* and SNe, which enriched the gas that formed this 47 Tuc had ≈ 1 dex lower metallicity than the SNe enriching the Galactic field stars.

For cobalt, there is *no* explanation of the observed trends as seen in Fig. 7.9. According to the results of Gratton & Sneden (1991), Co follows the depletion of Fe down to $[\text{Fe}/\text{H}] \approx -2.5$. At lower metallicities, McWilliam et al. (1995) observe a strong increase of cobalt with respect to iron. These authors found the change in slope at $[\text{Fe}/\text{H}] \approx -2.5$ also for the $[\text{Cr}/\text{Fe}]$ abundance ratios, which was attributed to the *nucleosynthesis connection of both elements*. For Mn, the reverse behavior was observed: a rapidly decreasing $[\text{Mn}/\text{Fe}]$ trend below $[\text{Fe}/\text{H}] \approx -2.5$. The only interpretation for the radically different trends for Mn and Co at very low metallicities was that the term "iron-peak" does not imply the products of a *single nuclear reaction*. del Peloso et al. (2005) obtained a different trend for $[\text{Co}/\text{Fe}]$, characterized by a steady increase towards supersolar ratios of $\sim +0.2$ from $[\text{Fe}/\text{H}] = 0$ to -0.8 . This was related to the *Co production in both SN II and SN Ia but with uncertain relative contributions*.

As our NLTE abundance trends for Co and Mn are considerably different from the results of the other authors, we can not proceed without first delving into the nuclear physics of Fe-peak elements production.

8.2 Explosive nucleosynthesis

Fe-peak elements are formed in the *explosive* burning of silicon, hence the physical conditions of their formation are similar except for the important fact that these elements are produced in separate regions. The regions are characterized by slightly different temperatures, so that the one with lower T undergoes *incomplete* Si burning, whereas *complete* Si burning occurs in the region

with higher T . In short, the explosive nucleosynthesis proceeds as follows. As the burning becomes more extreme, it approaches nuclear statistical equilibrium, where the rates of all nuclear reactions are nearly compensated by the inverse. During the subsequent expansion and cooling of matter, all rates converting free particles to nuclei become too slow. So the nuclear abundances “freeze out” at some temperature characteristic of each nuclei. The resulting abundances of *neutron-rich* nuclei depend critically on the neutron excess prior to the freeze-out (Truran & Arnett 1971) because explosive nucleosynthesis does not allow a sufficient number of β -decays to change the neutron-to-proton ratio of a star from its initial value. What is also important for the final abundance pattern, is whether some extra α -particles are left after freezing. This could be a result of the *too slow* triple- α reaction during the decreasing temperatures in a low-density environment. This mechanism leaves a large number of free α -particles, which are not in a complete equilibrium with the Fe-peak nuclei. The extra α -particles then recombine with other Fe-peak nuclei to form elements *heavier* than Fe. For example, Co, being a product of the ^{59}Cu decay, is mostly synthesized during such an *α -rich freeze-out* that takes place in the complete Si-burning region. On the other side, Cr formed as ^{52}Fe and Mn formed as ^{55}Co are typical elements of the incomplete Si-burning. Furthermore, *the relative amount of Mn, Cr, and Co ejected from a SN depends on the relative masses of regions, where they are produced.* For a SN II, the latter is a sensitive function of the mass cut between the ejected material and the remnant, the explosion energy, and the neutron excess (Umeda & Nomoto 2002). The former two are “free parameters” even in modern calculations of massive star nucleosynthesis. Assuming a delayed detonation model for SN Ia (Iwamoto et al. 1999), in which a C-O white dwarf experiences an initial central deflagration followed by a detonation, a deflagration-detonation transition determines the contribution of complete and incomplete Si-burning regions.

Mn and Co are both neutron-rich elements; as noted above, their abundances must be sensitive to the neutron excess η available to the progenitor star in the explosive Si-burning phase. Obviously, in environments with large η odd-Z nuclei are produced more readily than the even-Z nuclei resulting in the *odd-even effect*. The neutron enrichment is determined by the *initial metal content* of a star and by the previous hydrostatic burning stages. On the one side, creation of neutron-rich nuclei during the CNO cycle of H burning and subsequent He burning implies the dependency of the neutron excess on the initial stellar abundance of carbon, nitrogen, and oxygen, and hence, on the metallicity (Truran & Arnett 1971). For the solar metallicity star, this mechanism produces $\eta \approx 0.0022$. On the other side, neutron enrichment can result from the *hydrostatic carbon burning stage*, which occurs in stars with a mass $> 9M_{\odot}$. According to Arnett (1971), the neutron excess resulting from the complete C burning is $\geq 0.0009 - 0.002$. Thus, Arnett concludes that the difference in η between an extreme Population II and a typical Population I star is probably not larger than 3, although the total metal content changes by a factor of 1000. A very important consequence is that *the amount of heavy odd-Z elements produced in the Population II and I SNe would be nearly equal, and hence independent of metallicity at least for $[Fe/H] \leq -0.5$.* This was confirmed by Woosley & Weaver (1982), who studied nucleosynthesis yields of two $25M_{\odot}$ stars of different populations.

In the past 15 years, several research groups published the results of explosive nucleosynthesis calculations for massive and intermediate-mass stars. Perhaps, the most widely-used are the yields of Woosley & Weaver (1995) for stars with $12 \dots 40M_{\odot}$ and metallicities varying from 0 to solar. For SN Ia, a standard reference is the metallicity-independent W7 model of Nomoto et al. (1984) in the more recent version of Iwamoto et al. (1999). The dependence of the Fe-peak on the neutron excess requires that *metallicity-dependent yields* are used in chemical evolution calculations. This is not critical for the SN Ia model, because the neutron excess in the regions where Fe-peak nuclei are produced is primarily determined by electron captures on ^{56}Ni *in the explosion* (Thielemann et al. 2007). For the massive stars exploding as SN II, the neutron excess strongly depends on the β -decays in the pre-explosive hydrostatic burning stages.

8.3 Chemical evolution of Mn and Co in the Galaxy

There are several models in the literature, which provide the evolution of Fe-peak element abundances in the Galaxy. The most widely used is the homogeneous model of Timmes et al. (1995) with gas infall, which is based on the SN II yields of Woosley & Weaver (1995) and SN Ia yields of Nomoto et al. (1984). Other one-zone models with gas infall were presented by Kobayashi et al. (2006) and Goswami & Prantzos (2000); the latter authors also took into account gas outflows for the halo. Argast et al. (2000) computed an inhomogeneous model for the halo with metallicity-independent yields for SN II adopted from Thielemann et al. (1996) and Nomoto et al. (1997). François et al. (2004) combined a two-infall GCE model of Chiappini et al. (1997) with *metallicity-independent yields* of Iwamoto et al. (1999) and Woosley & Weaver (1995) to calculate the abundance trends for different elements in a large range of metallicities. The most complex is the chemodynamical model of Samland (1998), which includes metallicity-dependent Woosley & Weaver (1995) yields for SN II. Recently, Cescutti et al. (2008) investigated the [Mn/Fe] evolution in the solar neighborhood, the bulge, and the Sagittarius dSph galaxy. The chemical evolution models for three stellar systems were adopted from François et al. (2004), Ballero et al. (2007), and Lanfranchi et al. (2004, 2006).

The [Mn/Fe] and [Co/Fe] versus [Fe/H] relations as predicted by these models are shown in Fig. 8.1. The symbols for observed stars are the same as in Fig. 7.7 and 7.9. The spectroscopically determined [Mn/Fe] are taken from Nissen et al. (2000), Cayrel et al. (2004), and Feltzing et al. (2007). For Co, the data sources include Ryan et al. (1991), Cayrel et al. (2004), Reddy et al. (2003), Reddy et al. (2006), and Johnson (2002). Our LTE and NLTE abundances (Table 7.1) determined from the lines of *neutral species* are marked with red and black filled circles, respectively. Solid lines show the ratios predicted by the Galactic chemical evolution models, assuming reference sets of input parameters. Dashed lines indicate adjustment of stellar yields performed by some authors to get a better fit to the observations. In particular, Timmes et al. decreased iron yields from SN II by a factor of 2 to match to the data of Gratton (1989) for Mn and Gratton & Sneden (1991) for Co (black dashed line). Goswami & Prantzos (2000) provide calculations for two sets of SN II yields: Woosley & Weaver (1995) at constant solar metallicity (green dashed curve) and the metallicity-dependent Woosley & Weaver (1995) yields (green solid curve). We also superpose two curves from François et al. (2004). The solid red line gives their calculation with the original metallicity-independent (solar) Woosley & Weaver (1995) and Iwamoto et al. (1999) yields. The dashed red line gives their results for Mn, when the Woosley & Weaver (1995) SN II yields are increased by $\sim 70\%$ for $13 - 18M_{\odot}$ progenitors and decreased by $\sim 60\%$ for $30 - 40M_{\odot}$ progenitors. For Co, François et al. found that the lowered Woosley & Weaver (1995) yields for SN II with $11 - 22M_{\odot}$ progenitors and increased for more massive stars produce a better match to the observed data of Cayrel et al. (2004). They also required higher Co yields from SN Ia models of Iwamoto et al. (1999). The [Mn/Fe] trend from Kobayashi et al. (2006) is very similar to that given by Timmes et al. (1995), hence we avoid the former in order not to overload the figure; for [Co/Fe], Kobayashi et al. (2006) predict nearly solar ratios down to the lowest metallicities. The large yellow circles in Fig. 8.1 (upper panel) depict [Mn/Fe] ratios of SN II models of the given progenitor mass from Argast et al. (2000); very small black dots represent model low-mass stars from the same reference. We note that this model was designed to explain the *scatter* in halo star abundances, hence there is no *single averaged curve* as given for the other GCE models. However, the increasing homogeneity of the ISM as more and more SNe explode is seen on the decreasing dispersion of the model star abundances with increasing [Fe/H].

In general, all models predict the existence of a trend in [Mn/Fe] and [Co/Fe] ratios with iron abundance. However, the difference between theoretical trends is strikingly large. Although, GCE models suggest that Mn is depleted relative to Fe in metal-poor stars, the magnitude of predicted depletion at [Fe/H] < -1.5 varies by a factor of 6. The shape of the trends is similar, characterized by a plateau at low metallicities and a steady increase towards solar the [Mn/Fe] ratio *above* [Fe/H] ~ -1.5 . However, the change of the slope occurs at rather different metallicities, from [Fe/H] ≈ -0.5 dex in the Timmes et al. model to [Fe/H] ≈ -1.4 in the model of François et al.. As first SNe Ia explode approximately at this time (Tinsley 1979), the change and subsequent increase of

[Mn/Fe] is usually interpreted as due to the *larger contribution of SN Ia to the ISM enrichment in Mn compared to the SN II*. Samland (1998) find that 75% of the Galactic Mn is produced in SNe Ia. However, Timmes et al. obtain different results: the [Mn/Fe] trends calculated with contributions from both types II and Ia supernovae and with SNe II only are nearly identical (compare the solid black line and the dotted-dashed black line in Fig. 8.1). In their model, massive stars with solar metallicity have ~ 5 times larger Mn yields than metal-poor stars, and this leads to an increase of [Mn/Fe] at [Fe/H] > -1 up to the solar value. Hence, Timmes et al. conclude that *nucleosynthesis in massive stars with metallicity-dependent yields is sufficient to explain the observations provided that total iron yields are reduced by a factor of 2*. This is true, if we compare their suggested trend (dashed black line) with stellar abundances of Mn derived by Cayrel et al. (2004) (filled brown circles) and Feltzing et al. (2007) (open grey squares). However, the Timmes et al. model is incompatible with our LTE abundances (red filled circles) below [Fe/H] ≈ -1.8 , and it is *fully inadequate to represent our NLTE Mn abundances in stars* (black filled circles).

Quite unexpectedly, the observed trends for the Galactic thick and thin disks are *not* reproduced with the model of Samland (1998). It utilizes metallicity-independent yields for SN Ia that could be the case of discrepancies at $-1.5 \leq [\text{Fe}/\text{H}] \leq 0$. At very low metallicities, the calculated evolution of Mn is consistent with the Cayrel et al. (2004) data. Moreover, when compared to the predicted [Mn/Fe] ratios of Argast et al. (2000), it seems to give a correct *average* description of the halo Mn abundances. Also, the scatter in the [Mn/Fe] ratios of the model stars given by the Argast et al. model agrees well with the observed data points, even at lowest metallicities, [Fe/H] ≈ -4 . In fact, this scatter could explain the presence of extremely metal-poor stars with nearly solar [Mn/Fe] ratios in the Cayrel et al. (2004) investigation. Curiously, Argast et al. casted doubt on the reality of their predictions for Mn because those were inconsistent with the spectroscopic abundances of McWilliam et al. (1995). However, we showed that the extremely low [Mn/Fe] ratios found in metal-poor stars by McWilliam et al. (1995) could be due to the deficiencies of their abundance analysis method (Sect. 7.3).

The only model, which describes the LTE Mn trends in the solar neighborhood is that of François et al. (2004). It is compatible with the observed abundances derived for the thin and thick disk stars by Nissen et al. (2000) and Feltzing et al. (2007). As the model is based on the metallicity-independent SN Ia yields of Iwamoto et al. (1999) in the same treatment as all other GCE models described so far, it is not clear what stipulates the agreement. At low metallicities, this model predicts too low [Mn/Fe] ratios, which are not supported by observations. In fact, even their *adjusted model* (dashed red line) with increased SN II yields for $11 - 20 M_{\odot}$ progenitors is not much better.

Finally, we consider the GCE model of Goswami & Prantzos (2000), which differs from the other 1D models in that it uses the IMF from Kroupa et al. (1993) (multi-component power law), and assumes strong outflow in the halo phase and slow infall in the disk. The yields for SN II were taken from Woosley & Weaver (1995) and are reduced by a factor of 2 for the Fe-peak elements, in accord with the suggestion of Timmes et al. (1995) (see above). The SN Ia yields were taken from Iwamoto et al. (1999). Fig. 8.1 clearly shows that the cases of the metallicity-dependent and metallicity-independent SN II yields are radically different (compare the green solid and the dashed lines). In fact, *the Goswami & Prantzos model with metallicity-independent SN II and SN Ia yields provides excellent agreement with our NLTE Mn abundances in metal-poor stars*. This is a very unexpected result, especially because metallicity-independent yields in the same recipe were adopted by François et al. (2004), who could not achieve agreement with observations. This might mean that the treatment of the IMF has important consequences on the results of chemical evolution calculations. As shown by Wang & Silk (1993), the shape of the IMF introduces a factor of 2 uncertainties to the absolute yield value of an element. The fact that Mn remains constant down to low metallicities indicates that *Mn and Fe are produced in the same (solar) proportions in both types of supernovae*. Metallicity-independent yields are consistent with the original Arnett's (1971) suggestion that the neutron excess, which determines heavy odd-Z element production, may stem in almost equal amounts from the hydrostatic C burning in low-metallicity massive stars and from CNO burning alone in solar-metallicity stars (see Sect. 8.2). In Fig. 8.1 (top), we also present the chemical evolution calculations of Arnett (1971) for two cases: the hydrostatic

C burning is not included (solid orange line) and it is assumed to have occurred to completion (dashed orange line). Clearly, in the absence of hydrostatic C burning stage, the Mn abundances are roughly proportional to the initial metal content of a star. That means, Mn is clearly a secondary nucleus. In contrast, hydrostatic C burning dramatically increases the neutron excess, so that Mn production is predicted to be nearly independent of metallicity, as we indeed observe. Furthermore, this result does not require Mn *overproduction* in SN Ia relative to SN II, which anyway does not occur in all delayed detonation SN Ia models of Iwamoto et al. (1999). In fact, the latter was always claimed as a severe deficiency of the Iwamoto et al. (1999) models.

Let us examine whether the change of the neutron excess is still compatible with the observed Co abundances. Figure 8.1 (bottom) suggests that neither of the GCE models are able to describe our NLTE [Co/Fe] trend in metal-poor stars (black filled circles). The Goswami & Prantzos model with metallicity-independent SNe yields (dashed green line) now gives *only qualitatively* similar behavior, characterized by increase of [Co/Fe] ratios from the solar metallicity down to the lowest metallicities. This is compatible with our suggestion in Sect. 7.4 made on the basis of NLTE abundance corrections. However, this model gives a very good fit to the LTE Co abundances from the current work (red filled circles) and LTE results of Cayrel et al. (2004), Reddy et al. (2003), and Johnson (2002). Some discrepancies are seen with the thick disk stars from Reddy et al. (2006). More close to our NLTE results is the model of François et al. (2004) with *unadjusted metallicity-independent* SN yields (solid red line), but the offset between theoretical calculations and the data is still too large, ~ 0.25 dex. As for the rest, this model gives a good fit to the data of Reddy et al. (2006) but it is at variance with the spectroscopic abundances from the other sources. The chemical evolution models with metallicity-dependent SN yields (Timmes et al. 1995, Samland 1998, Goswami & Prantzos 2000) predict radically different [Co/Fe] trends, which are ruled out by observations. The same is true for the results of Arnett's (1971) Co evolution calculations, whether with or without hydrostatic carbon burning. This discrepancy was also noted by Arnett et al. (1971) and Arnett (1971), who proposed that [Co/Fe] ratio should be *strongly* correlated with the SN Ia progenitor metal content and the amount of mixing in the ISM. In particular, for the incomplete mixing they allow for a possibility that the presence of heavy elements suppresses efficient star formation, and, hence, nucleosynthesis. So every subsequent stellar generation is formed from the most metal-poor part of the system. What effect this would have on the abundances in metal-poor stars is not really clear; perhaps, following Arnett (1971), the calculated Co evolution would be more flat. But, if applied to lower metallicities [Fe/H] < -2 , the hypothesis contradicts the theory of a *supernova-induced star formation* (Tsujimoto et al. 1999), in which extremely metal-poor stars are formed following each SN event.

Otherwise, the conclusion is that *massive stars overproduce Co relative to Fe*. The observed fall of [Co/Fe] can be explained by an underproduction of Co in SN Ia, but the possibility that SN II and SN Ia Co yields are metallicity-dependent is also not excluded. However, we see that all chemical evolution models, which utilize metallicity-dependent yields, are inadequate to describe the [Co/Fe] (and [Mn/Fe]) trend suggesting that the problem is in the stellar yields themselves. In fact, this is not unexpected, given the sensitivity of supernova yields to the details of explosion. For SN Ia models, these are discussed in Iwamoto et al. (1999). Woosley & Weaver (1995) emphasized that their SN II iron yields could be in error by a factor of 2, ascribing even larger uncertainties to the elements produced in α -rich freeze-out due to the great sensitivity of those to the mass cut placement. Nakamura et al. (1999) showed that the position of the mass cut influences the ratio of abundances from alpha-rich freeze-out and incomplete Si-burning. For deeper mass cuts, more Co and less Mn is produced. But our results suggest that *Mn should not be underproduced relative to Fe*. Nakamura et al. also found that increasing neutron excess increases the Co and Mn production, but the Ni fraction becomes too large. Umeda & Nomoto (2003, 2005) showed that if a large-scale uniform mixing occurs in the inner layers of very massive stars, $M > 25M_{\odot}$, than Co is produced more efficiently and the effect is even enhanced for larger explosion energies. The latter generally assumes introduction of hypernova (Nomoto et al. 2004), where one can also avoid the overabundance of Ni. In connection, Nagataki et al. (1997) demonstrated that the axisymmetric explosion in SN II models also boosts α -rich freeze-out, and hence production of Co. Interestingly, the results of massive star nucleosynthesis calculations performed by Heger

& Woosley (2008) suggest that there is no need for hypernova to explain element abundance patterns in extremely metal-poor stars. The variety of mechanisms, which could affect the Fe-peak production, is overwhelming (Thielemann et al. 2007). Thus it is not hard to believe that the disagreement between observations and predictions of chemical evolution models is, at least in part, due to the deficiencies of the latter.

Several particular points deserve emphasis. We noted above that Mn and Co are both produced in the explosive Si-burning, hence it is to be expected that their abundances *are correlated*. This correlation is demonstrated in Fig. 8.2 (top panel). With increasing metallicity, the relative abundance of Mn increases with respect to Co, with a steep slope at $-1 \leq [\text{Fe}/\text{H}] \leq 0$ and nearly constant $[\text{Mn}/\text{Co}] \sim -0.4$ at lower metallicities. This means, the average contribution of different SNe II to the underproduction of Mn relative to Co in the halo is equal, however SN Ia should underproduce Co relative to Mn in the thick and thin disk phase. Otherwise, *if SNe Ia do not change the ratio $[\text{Mn}/\text{Co}]$ significantly, SNe II of later generations should do the work ejecting more manganese compared to a previous SNe II generation.*

A more instructive experiment is to investigate the relative ratios of Fe-peak and α -elements. For this, we select *magnesium as a typical representative of SN II*, although according to Timmes et al. (1995) a small contribution to Mg production from SN Ia can not be excluded. The results for $[\text{Mn}/\text{Mg}]$ and $[\text{Co}/\text{Mg}]$ as a function of a stellar $[\text{Mg}/\text{H}]$ ratio are given in Fig. 8.2 (middle and bottom panels). Mg abundances are taken from the NLTE analyses of Gehren et al. (2004, 2006), who find nearly constant $[\text{Mg}/\text{Fe}] \sim +0.4$ for $[\text{Fe}/\text{H}] < -1$ and a rapid $[\text{Mg}/\text{Fe}]$ decline toward the solar value above this metallicity. Fig. 8.2 suggests that the $[\text{Mn}/\text{Mg}]$ trend is nearly flat for $[\text{Mg}/\text{H}] \leq -0.5$, when the ISM enrichment with chemical elements is dominated by SNe II. That means, massive stars with *different metallicities* produce Mn and Mg on average in the same proportions. The increase of $[\text{Mn}/\text{Mg}]$ ratio above $[\text{Mg}/\text{H}] \approx -0.5$ can be due to metallicity-dependent SN II yields, or due to SNe Ia. A radically different picture is seen for $[\text{Co}/\text{Mg}]$ (Fig. 8.2, bottom panel): Co is overproduced relative to Mg by SNe II, which seem to contribute less and less cobalt as the overall metallicity increases. *At $[\text{Mg}/\text{H}] \geq -0.5$, Co tends to become increasingly overdeficient with respect to Mg.* The latter can not be explained, unless we assume that *SNe Ia produce very little amounts of cobalt and magnesium, and the yields of SN II are strongly metallicity-dependent.* In fact, this would solve the acute problem of *seemingly too small* Co yields in SN Ia models of Iwamoto et al. (1999).

Based upon the apparent constant $[\text{Mn}/\text{Fe}]$ trend and steadily increasing $[\text{Co}/\text{Fe}]$ trend toward low metallicities our results suggest few possibilities. The production of Mn can be associated with the primary (metallicity-independent) event in SNe II of high masses, possibly combined with a secondary event in lower-mass SNe II, which requires pre-existing metals. However, the latter process should be able to maintain *constant* $[\text{Mn}/\text{Fe}]$ ratios, which can be achieved if Mn produced by lower-mass SNe II is balanced by Fe produced by SN Ia. A second scenario assumes metallicity-independent Mn yields from all SNe II, and an overproduction of Mn relative to Co in SNe Ia. This scenario allows for the possibility that a larger fraction of Fe and Mn is produced in SNe Ia compared to the SNe II. For Co, we favor a secondary origin and suggest that the largest yield has to come from short-lived massive stars, exploding as SNe II. Whereas, contribution of SNe Ia to Co production is relatively small.

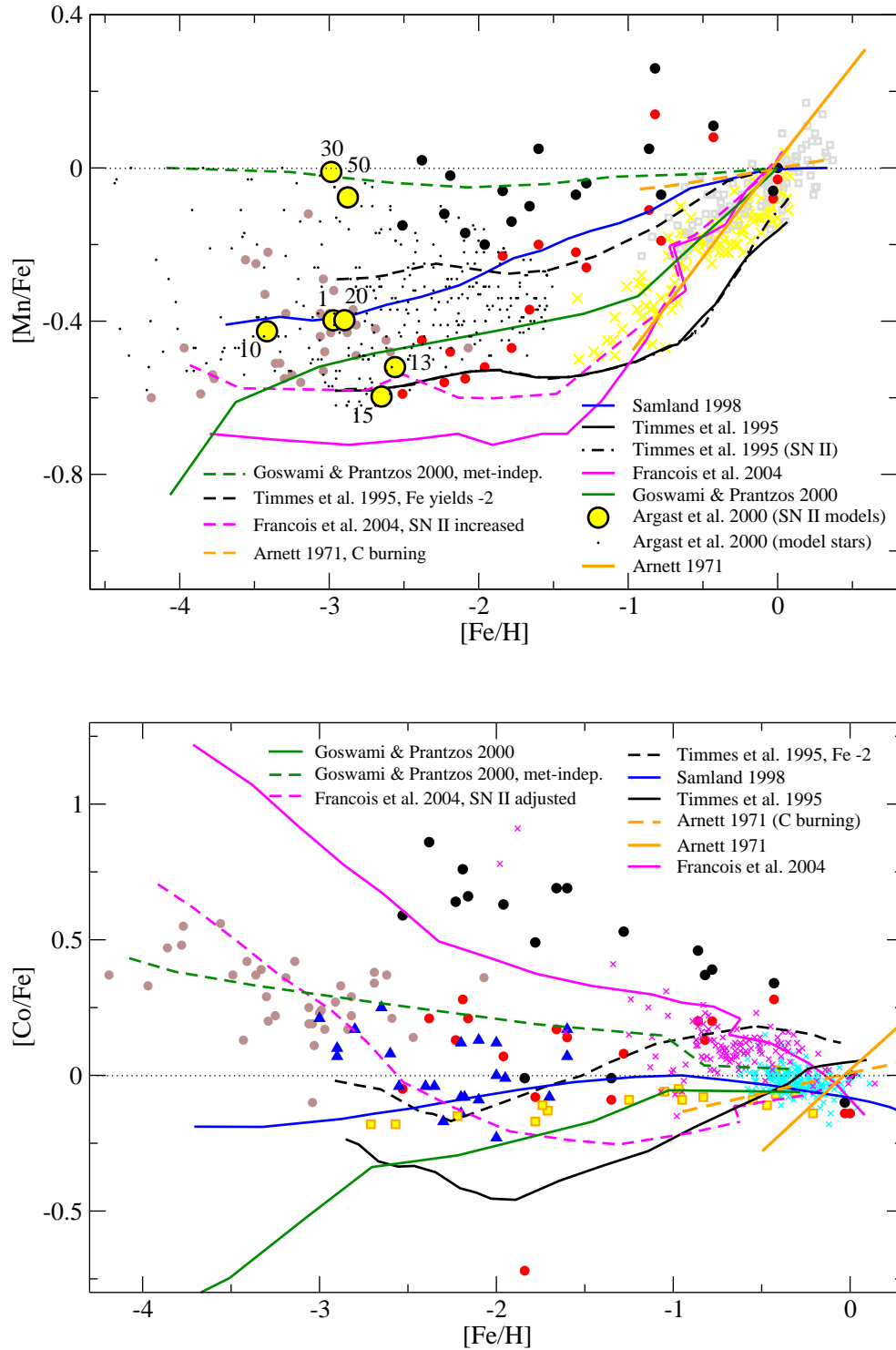


Figure 8.1: Evolution of $[Mn/Fe]$ and $[Co/Fe]$ ratios as a function of $[Fe/H]$. Solid lines show the ratios predicted by the Galactic chemical evolution models taken from the sources specified in the figures. Dashed lines of the same color indicate adjustment of stellar yields (Timmes et al. 1995, Goswami & Prantzos 2000, François et al. 2004). On the top panel, the large yellow circles depict $[Mn/Fe]$ ratios of SN II models of the given progenitor mass from Argast et al. (2000); very small black dots represent model stars from the same reference. Symbols for spectroscopically determined $[Mn/Fe]$ values are the same as in Fig. 7.7 and 7.9. See text.

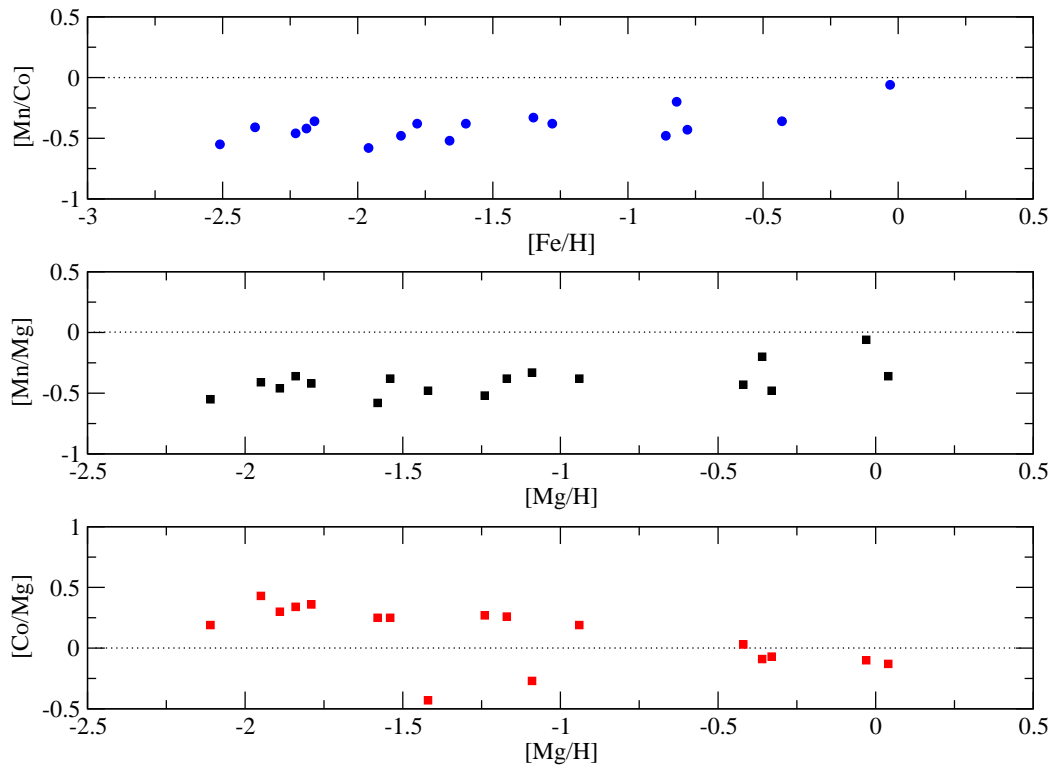


Figure 8.2: $[Mn/Co]$ versus $[Fe/H]$ (top panel). Evolution of $[Mn/Mg]$ and $[Co/Mg]$ ratios as a function of $[Mg/H]$ (middle and bottom panels).

Chapter 9

Conclusions

The distribution of manganese and cobalt atoms over excitation energies and ionization stages in stellar atmospheres is far from what local thermodynamic equilibrium prescribes. This finding has different implications in several astrophysical domains: stellar atmospheres, stellar evolution, and Galactic chemical evolution.

Statistical equilibrium of Mn and Co in the atmosphere of the Sun is established by several processes: photoionization and photorecombination, photon pumping and photon suction, ionization due to inelastic collisions with neutral hydrogen atoms. The role of these processes in the distribution of atomic level populations is different for Mn and Co, which is a reflection of the atomic properties of the elements, such as the separation of energy levels, number and strength of transitions, and the ionization potential.

Deviations from LTE for Co I are controlled by overionization from low levels due to a strong non-local UV radiation field below 3500 Å. At all atmospheric depths, number densities of neutral Co atoms with all excitation energies are smaller than those predicted by the Maxwell-Boltzmann distribution for a plasma in local thermodynamic equilibrium with physical conditions of the solar atmosphere. The depopulation of Co I affects the number densities of Co II levels because nearly 20% of the total Co atoms are neutral. Also, photon pumping from the Co II ground state leads to the overpopulation of the excited levels of Co II relative to LTE. As a result, NLTE effects on the line formation occur for lines of both ionization stages. For Co I, reduced line opacity stipulated by the overionization leads to general weakening of lines. In contrast, lines of Co II are affected by the deviation of line source functions from the Planck function. In the solar model atmosphere, deviations are small, and it is safe to adopt LTE in calculations of Co II line formation. However, LTE is inappropriate for calculations of Co I lines in the solar spectrum: depending on the line strength, NLTE leads to 0.1 – 0.2 dex larger abundances.

The average solar abundance of Co derived from the NLTE analysis of Co I lines is 4.94 ± 0.04 dex that is 0.13 dex higher than under the LTE assumption. The abundance calculated from the single relatively unblended Co II line in the solar spectrum is 4.86 dex. The discrepancy of 0.08 dex between lines of two ionization stages points either at a *failure of the NLTE approach to describe the ionization equilibrium of Co*, or to the possibility that the theoretical oscillator strengths for the Co II transition are of low accuracy. A better agreement between the abundances derived from both ionization stages is obtained with the cross-sections for transitions due to inelastic collisions with H I atoms increased by a factor of 5. In this case, $\log \varepsilon_{\text{Co},\odot}^{\text{NLTE}}(\text{Co I}) = 4.87 \pm 0.04$ dex and $\log \varepsilon_{\text{Co},\odot}^{\text{NLTE}}(\text{Co II}) = 4.84$ dex. However, there are no other evidences, which support such a large scaling factor. The NLTE abundances of Co calculated with $0.05 \leq S_{\text{H}} \leq 5$ are in agreement with that measured in C I meteorites, 4.89 ± 0.03 dex.

The NLTE effects on Mn I in the solar atmosphere are rather complex because several channels compete in establishing non-equilibrium level populations. However, neither of the processes can be regarded as a dominating type. The radiative discrete transitions are so strong and numerous, that they inevitably control the statistical equilibrium of the Mn I atom, especially so, when radiative bound-free processes are rather weak. This is the case in the adopted atomic model,

where cross-sections for photoionization are assumed to take a simple hydrogenic form. Also, a very small energetic separation of the highest Mn I levels from the Mn II ground state favors powerful collisional interaction between them. The final effect is *underpopulation of all Mn I levels*. In contrast, a majority of Mn II levels have LTE populations. Overionization from the levels of Mn I has a negligible effect on the Mn II ground state, because neutral atoms occupy less than 5% of the total element number density in an atmosphere with solar temperature.

We may conclude that the LTE assumption is appropriate for Mn II. But this statement is valid only within the framework of the *physical accuracy* of the model used in statistical equilibrium calculations. There is an evidence that ionization from levels of a neutral complex atom occurs directly to low-excited metastable states of the ionized atom, the process that we can not take into account due the lack of necessary data for both elements. What effect this process has on atomic level populations of ionization stages is unknown.

Deviations from LTE in the Mn I lines are determined by two mechanisms: reduced line opacity and deviation of the line source function from the Planck function. For the weak and intermediate strength lines ($W_\lambda < 80 \text{ m}\text{\AA}$), NLTE and LTE assumptions give a similarly good fit to the observations, provided a certain abundance correction is performed. The NLTE corrections for these lines are positive and amount to 0.1 dex. Formation of the stronger lines ($W_\lambda > 80 \text{ m}\text{\AA}$) is characterized by an amplified absorption in the core and a decreased absorption in the wings, compared to LTE. NLTE abundance corrections for strong lines are scattered around zero or negative.

Using the NLTE approach and the recently measured $\log gf$ values, we derive the solar Mn abundance 5.40 ± 0.07 dex. This estimate based on the Mn I lines agrees with the abundance in C I carbonaceous meteorites 5.50 ± 0.03 to within the combined uncertainty of the two values. A solar abundance of 5.39 dex is derived from the single Mn II line in the UV. However, the uncertainty of this value due to a very strong blending in the line is too large to claim a consistent solar ionization equilibrium of Mn.

In the environments where the radiation field is amplified, such as stars with low metallicities and/or supersolar effective temperatures, the overionization in Mn I and Co I is a dominant process. The *ground states* of singly ionized elements are almost unaffected by NLTE. However, we find an increasing importance of line pumping in Co II with decreasing $[\text{Fe}/\text{H}]$. As a result, the NLTE abundance corrections for the lines of *neutral* elements vary from +0.1 to +0.6 dex depending on the metallicity and the effective temperature. In contrast, line profiles of ionized elements computed under NLTE do not behave similarly. For Mn II lines, the NLTE abundance corrections amount to ± 0.03 dex, on average. However, NLTE corrections for Co II lines are as large as +0.3 dex in the models with very low metallicities and supersolar temperatures. Consequently, the analysis of Co II lines in very metal-poor stars can lead to substantial errors in abundances, if NLTE effects are neglected. Our results for the giant models with low effective temperature, low gravity, and low metal content suggest that in atmospheres of giants deviations from LTE are not larger than in dwarfs, and *the main stellar parameter that controls the magnitude of NLTE effects in Mn and Co is metallicity*.

For the *solar-metallicity* stars, the incorrect treatment of hyperfine structure leads to large errors in abundances. For the lines with saturated cores, the neglect of HFS leads to an abundance overestimate by 0.5 – 1 dex. Even the weak lines in the solar spectrum are not free from HFS effects, showing the difference of 0.05...0.15 dex. The influence of HFS on the line profiles and abundances is negligible in the metal-poor stars; it does not exceed 0.05 dex.

The differential abundance analysis of 17 stars with $-2.5 \leq [\text{Fe}/\text{H}] \leq 0$ demonstrated that the evolution of Mn and Co abundances in the Galaxy is radically different from all previously reported trends. Instead of a strong depletion of Mn relative to Fe in metal-poor stars as found in LTE studies, NLTE suggests *nearly solar* values of $[\text{Mn}/\text{Fe}]$ throughout the range of metallicities analyzed here. That means, *the stars of the thin disk, thick disk, and the halo have the same ratios of Mn to Fe*. Another striking result is the strong overabundance of Co relative to Fe that is seen for the thick disk stars and increases further towards the lowest metallicities. This behavior also differs from the typical trend of α -elements in metal-poor stars. In comparison, all LTE studies, carried out so far, indicate that $[\text{Co}/\text{Fe}]$ ratio is roughly solar down to $[\text{Fe}/\text{H}] \approx -2.5$

and rapidly increases thereafter. These results suggest several possibilities for the nucleosynthetic origin of both elements. The production of Mn can be associated with the *primary* event in SNe II of high masses, possibly combined with a secondary event in lower-mass SNe II. However, the latter process should be able to maintain *constant* [Mn/Fe] ratios, which can be achieved if Mn produced by lower-mass SNe II is balanced by Fe produced in SNe Ia. A second scenario assumes metallicity-independent Mn yields from all SNe II, and an overproduction of Mn relative to Co in SNe Ia. This scenario allows for the possibility that a larger fraction of Fe and Mn is produced in SNe Ia compared to the SNe II. For Co, we favor a *secondary* origin and suggest that the largest yield has to come from short-lived massive stars, exploding as SNe II. Whereas, contribution of SNe Ia to Co production is relatively small.

The models of Galactic chemical evolution reported in the literature are inadequate to represent the [Mn/Fe] and [Co/Fe] ratio in metal-poor stars, *if* they utilize metallicity-dependent yields for SNe II. We relate the discrepancy to the *deficiency in SN yields* themselves. The one-zone GCE model of Goswami & Prantzos (2000) with metallicity-independent yields from Woosley & Weaver (1995) gives an excellent description to the NLTE [Mn/Fe] trend, but it gives only a qualitatively similar behavior of the [Co/Fe] trend. As metallicity-dependent yields from SNe II are proposed to explain the observed overabundance of Co relative to Fe in metal-poor stars, it is not surprising that there is a quantitative disagreement with the model of Goswami & Prantzos (2000).

It is important to note that all conclusions given above are based on the Mn and Co abundances in metal-poor stars derived from the lines of neutral elements. The differential NLTE abundances determined from the UV lines of ionized elements are systematically lower by 0.3–0.6 dex. In fact, the discrepancy could be due to the unaccounted blends in the ionic lines of the solar spectrum. Otherwise, we have to acknowledge that the NLTE analysis in its present state fails to provide a correct description of the *ionization equilibrium* for Mn and Co in metal-poor stars.

Glossary

Abundance

The abundance of an element ϵ (including all ionization stages) is expressed through the ratio of its number density N_{EI} to the total hydrogen number density N_{H} :

$$\log \epsilon = \log \frac{N_{\text{EI}}}{N_{\text{H}}} + 12$$

Asymmetrical drift

The negative of the V component of space velocity (see *velocity dispersion*) of a stellar population. In general, it increases with random motion within the population, so that the older the population, the more negative the V velocity. For example, the young thin disk population has an asymmetric drift of 0 km/s, whereas the halo population has an asymmetric drift of about 200 km/s

Atomic model

A whole of intrinsic atomic parameters that enter equations of statistical equilibrium. These include excitation and ionization energies, level designations, lines, cross-sections for bound-bound (oscillator strengths) and bound-free transitions

Autoionization

The atomic transition from a neutral doubly-excited state to an ionized singly-excited state. The former is a result of a bound-bound excitation of two electrons simultaneously. Then the transfer of excitation energy of one of the two electrons to another allows the latter to leave the atom, and the atom becomes ionized

Bound-free resonances

Autoionization and dielectronic recombination result in resonances in photoionization cross-sections that form peaks in the cross-section frequency dependence. These lie above the threshold frequency. Theoretical studies give evidence for numerous resonances for many-electron systems, like Fe I and Fe II

Branching ratio

The branching ratio for a transition from an upper level j to the lower i is defined as a ratio of a transition probability A_{ji} to the sum of transition probabilities of all possible lines from the same upper level $\frac{A_{ji}}{\sum_{\text{trans}} A_{ji}}$

Brightness temperature

The temperature to be entered to the Planck function to obtain the observed specific intensity at some frequency:

$$I_\nu = B_\nu(T_b)$$

$T_b = T_e(\tau_\nu = \mu)$, if the observed intensity emerges from an optically thick plane-parallel LTE medium when the Eddington-Barbier approximation holds

Collinear fast-ion-beam laser spectroscopy

A method based on observations of laser-induced optical transitions in ionic beams. In essence, the beam of ions is accelerated in the external field and is probed by the monochromatic laser light in a collinear geometry with the beam. The laser frequency is scanned over the Doppler-shifted transition of interest, and fluorescent light, emitted in the decay of the upper level of the transition to its ground state, is observed

Damping parameter

Half-width at half-maximum of Lorentzian broadening in angular frequencies

Departure coefficient

The ratio of NLTE to LTE number densities of atoms excited to a certain level i :

$$b_i = n_i^{\text{NLTE}}/n_i^{\text{LTE}}$$

Differential analysis

The analysis of stellar parameters, e.g. abundances, relative to the solar values. For a particular element, the abundance is expressed as:

$$[\text{El}/\text{H}] = \log \left(\frac{N_{\text{El}}}{N_{\text{H}}} \right)_{\text{star}} - \log \left(\frac{N_{\text{El}}}{N_{\text{H}}} \right)_{\text{sun}}$$

Eddington-Barbier approximation

If the source function varies linearly with depth, the emergent intensity from the surface is:

$$I_\nu(\tau_\nu = 0, \mu) = S_\nu(\tau_\nu = \mu)$$

Effective temperature

The temperature of an equivalent black body that gives the same total power per unit area and is directly given by integrated stellar surface flux

Equivalent width

Width of a perfectly black line with the same area under continuum level as the line under study:

$$W_\lambda = \int_0^\infty \frac{F_c - F_\lambda}{F_c}$$

where F_c and F_λ are fluxes in the continuum and in the line

- First ionization limit** In complex atoms, this is the limit corresponding to ejection of the most weakly bound outer electron. For example, for Mn I with the ground electronic configuration $\dots 3d^5 \uparrow 4s \downarrow 4s \uparrow$, the ejection of the $4s \uparrow$ electron produces the $4s(^5S)$ final state and that of the $4s \downarrow$ electron the $4s(^7S)$. The latter has lower binding energy
- Fourier transform spectroscopy** A method to derive a spectrum based on measurements of temporal coherence of a *radiative source*. A signal from a scanning Michelson interferometer is recorded by a detector (an interferogram) and is sampled at equal intervals of path difference. The latter are determined from the fringes of He-Ne laser following the same path through the interferometer. The spectrum of the source is then calculated by performing the inverse Fourier transform of the interferogram (Thorne et al. 1987)
- Galactic rotation velocity** The motion of Galactic objects is characterized by a rotation velocity around the Galactic center $V_{\text{rot}} = \Omega R$, where Ω is the angular rotation velocity, and R is the distance from the center
- Infall**
Initial mass function (IMF) Gaseous matter accreted by galaxies
A number of stars with a given mass born in each generation of stars. It provides information about the *rate* at which different stars contribute chemical elements to the interstellar matter
- Intercombination lines** Transitions between levels of different multiplicities or with $\Delta L > 1$, i.e. lines that do not obey *LS* selection rules
- Laser rf double resonance technique** A method similar to atomic beam magnetic resonance of Rabi (1988), but inhomogeneous magnetic fields for state selection and signal detection are replaced by laser beams. Here, a laser creates a *population* difference between neighbouring hyperfine structure states by optical pumping. Then resonance fluorescence (rf) transitions between these states, which tend to equalize population numbers, can be detected by repeating the optical pumping experiment and looking for the laser induced fluorescent light. This allows determination of hyperfine level splittings with very high accuracy

Level crossing method

A technique to study fine and hyperfine structure of excited states of atoms and molecules. It is based on the phenomenon of spatial interference in the scattering of resonance radiation, which occurs if two levels are made degenerate that is usually achieved by application of a magnetic field

Level designations

The conventions for level designations are from Moore (1945). The lowest even-parity LS term of multiplicity M and orbital angular momentum L is labeled as $a^M L$, the next lowest as $b^M L$, and etc. In analogy, the label of the lowest odd-parity term is $z^M L$, the next lowest is $y^M L$, etc. The superscripts o are added at the righthand side to designate odd levels

Lifetime of a level

The lifetime t_j of an excited level is defined by its decay as

$$N_j(t) = N_j(0) \exp(-t/t_j)$$

As all transitions tend to reduce the lifetime of a level, in general t_j is expressed as inverse sum of transition probabilities from this level downwards to all other levels

$$t_j = \frac{1}{\sum_{\text{trans}} A_{ji}}$$

where A_{ji} is the Einstein coefficient for a spontaneous de-excitation from the upper level j to the lower level i

Local Standard of Rest

The motion of the Sun relative to a hypothetical circular orbit about the center of the Galaxy. The local standard of rest is approximately 16.5 km s^{-1} in the direction of the galactic coordinates $l = 53^\circ, b = 23^\circ$

Metallicity

The logarithmic ratio of the iron abundance in a star relative to the Sun:

$$[\text{Fe}/\text{H}] = \log \left(\frac{N_{\text{Fe}}}{N_{\text{H}}} \right)_{\text{star}} - \log \left(\frac{N_{\text{Fe}}}{N_{\text{H}}} \right)_{\text{sun}}$$

Mixing-length theory

The theory assumes that the convective energy is carried by elements with a certain size and fixed geometry, which dissolve after a mixing length l . A mixing length parameter α is defined as the mixing length relative to the pressure height of the homogeneous atmosphere $\alpha = l/H_p$, where $H_p = P/\rho g$

Neutron excess

The ratio:

$$\eta = \frac{N_n - N_p}{N_n + N_p}$$

where N_n and N_p are the total numbers of free and bound neutrons and protons, respectively

Optical depth

Integrated absorptivity of a gas layer with thickness D along the line-of-sight z at particular frequency ν (number of photon mean free paths):

$$\tau_\nu(D) = \int_0^D \kappa_\nu(z) dz$$

Optogalvanic laser spectroscopy

A method based on the change of the electric resistance of a gas as a result of resonance absorption of laser radiation. In practice, the current passing through a gas discharge is monitored. When the laser excites an atom from a low-lying state to a state of higher excitation, the probability that the atom will be ionized by discharge collisions increases. This contributes to an increase in the discharge current that can be measured with high sensitivity

Polarizability

The relative tendency of a charge distribution, like the electron cloud of an atom or molecule, to be distorted from its normal shape by an external electric field, which may be caused by the presence of a nearby ion or dipole

Rydberg atoms

An excited atom with one or more electrons which have a very high main quantum number. It is common to observe radiation from the interstellar medium that corresponds to the transition $n = 109$ to $n = 108$ in hydrogen

Solar-type stars

Solar-type (solar-like) stars are similar to the Sun in mass and evolutionary stage that implies a similar internal structure, e.g. presence of a convective envelope (Cayrel de Strobel 1996). The stars have $0.48 < (B - V) < 0.8$ (Cayrel de Strobel 1996), or even $0.5 < (B - V) < 1$ (Soderblom & King 1999) with the spectral types F8V to K2V¹

Space velocity

The space velocity of a star relative to the Local Standard of Rest is expressed as $\sqrt{U^2 + V^2 + W^2}$. Space velocities are calculated using observed radial velocities (from Doppler effects in spectra) and proper motions (requires accurate distances)

¹<http://www.lowell.edu/users/jch/workshop/drs/drs-p1.html>

Specific intensity

The specific intensity of radiation is defined as the energy emitted from a surface area dS into a direction $\vec{\Omega}$ per second:

$$I_\nu = I(\vec{r}, \vec{\Omega}, \nu, t)$$

with dimensions $[\frac{\text{erg}}{\text{cm}^2 \text{ s Hz sterad}}]$. The specific intensity averaged over all directions is the mean intensity J_ν . If I_ν is averaged over the apparent stellar disk, we get a radiative flux F_ν . For stars, which are unresolved point sources, only F_ν can be measured

Spectrum synthesis

Computation of a complete spectral interval in which all the observed lines are included

Spin exchange optical pumping method

When two spin-polarized atoms in their ground state experience a spin-exchange collision, the total spin of the atoms is conserved but the orientation of the individual spins may change, thus altering the hyperfine state of atoms. In practice, source atoms are polarized in a magnetic field by spin-exchange with optically pumped mediator atoms. Then, if a field is applied that induces resonance fluorescence in source atoms, the latter are depolarized and spin-exchange collisions depolarize mediator atoms. This leads to a change in intensity of the pumping light transmitted through the system

Star formation rate (SFR)

The parameter that determines how fast the gas is converted into stars

Stellar yield

The mass ejected in the form of a particular element i by a star of mass M

Subdwarfs

Dwarf stars of the Galactic halo. In comparison with main-sequence stars of the same mass, subdwarfs have higher effective temperatures and lower metallicities. These stars are thought to be old

Transition element

An element whose atom has an incomplete d subshell, or which can give rise to ionised species with an incomplete d subshell

Velocity dispersion

The peculiar velocities, or velocity dispersions, are designated as σ_U , σ_V , and σ_W , where U , V , and W are the components of *space velocity* along the radius of the Galaxy, along the direction of rotation, and along the axis of rotation, respectively

Nomenclature

A	magnetic dipole constant
A_{ij}	Einstein coefficient for spontaneous de-excitation
B	electric quadrupole constant
B_ν	Planck function
B_{ij}	Einstein coefficient for radiative excitation
C_{ij}	rate of an atomic transition due to collisions with particles
E_i	excitation energy of a level
$E_{\text{ion},c}$	ionization energy for a ground state of the ionization stage c
$E_{\text{ion},i}$	ionization energy for a level i
M_\odot	mass of the Sun
N	number density of particles
N_H	number density of hydrogen atoms
N_e	number density of free electrons
N_i	population of a level i
P_e	electron pressure
R	Rydberg constant
R_{sp}	resolution of a spectrograph
R_{ij}	rate of an atomic transition due to radiative
S^l	source function independent of frequency inside a line
S_ν	frequency-dependent source function
T_e	electron temperature
W_λ	equivalent width of a line
Δ_{NLTE}	NLTE abundance correction
Ω_{ij}	collision strength
S_H	scaling factor to hydrogen collisions calculated with Drawin's formula
S_P	scaling factor to photoionization cross-sections

T_{eff}	effective temperature
ξ_{RT}	macroturbulence velocity
ξ_t	microturbulence velocity
η_ν	emission coefficient
γ	damping constant
κ_ν	extinction coefficient
$\lambda\lambda$	wavelengths (e.g., when multiple lines are discussed)
$\log C_6$	interaction constant for van der Waals damping
$\log \varepsilon$	solar abundance of an element relative to H
$\log g$	surface gravity
$\log gf$	transition probability (see page 10)
$\log \varepsilon$	abundance of an element relative to H
$\log gf\varepsilon$	product of the oscillator strength for a transition and the abundance of the element
$\log(gf\varepsilon)_\odot$	$\log gf\varepsilon$ value calculated from the solar lines of Mn or Co under NLTE, if not otherwise indicated
$\log \tau_{5000}$	optical depth at wavelength 5 000 Å
σ	standard deviation of a value (usually, abundance)
σ_ν	atomic cross-section
τ_ν^l	optical depth at a frequency ν
v	particle velocity
$b - b$	bound-bound transition
$b - f$	bound-free transition
b_i	departure coefficient of a level i
e^-	electron
f -value or f_{ij}	oscillator strength
f_i	effective oscillator strength
g_i	statistical weight of a level
k	Boltzmann's constant
m	particle mass
n	main quantum number
n^*	effective main quantum number
[Fe/H]	metallicity
[Mn/Fe] _{II}	Mn abundance determined from Mn II lines

$[\text{Mn}/\text{Fe}]_{\text{I}}$	Mn abundance determined from Mn I lines
El II	ionized element
El I	neutral element
$\sigma_{ij}(\nu)$	cross-section of a transition from i to j
I_{ν}	specific intensity

Appendix A

Tables

Table A.1: Lines of Mn I and Mn II selected for solar and stellar abundance calculations. N_{H} denotes a number of HFS components for a line. E_{low} is the excitation energy of the lower level of a transition. The van der Waals damping constants $\log C_6$ are calculated according to Anstee & O'Mara (1995); an initial correction $\Delta \log C_6 \approx -0.1 \dots -0.2$ is applied to fit the wings of strong lines of multiplets 4, 5, 21, 22, 27. The error entry refers to an oscillator strength; no error estimate is given for Kurucz's $\log gf$ values. The parameters $\log(gf\varepsilon)_{\odot}$ are based on the NLTE abundances $\log \varepsilon$ derived for each line from the solar spectrum. An asterisk in the wavelength entry refers to the lines, for which solar $\log(gf\varepsilon)_{\odot}$ values can not reliably calculated due to the strong blending. These lines are not used in the determination of the solar Mn abundance.

No.	λ [Å]	Mult.	N_{H}	E_{low} [eV]	Lower level	Upper level	W_{λ} [mÅ]	$\log gf^a$	Error	$\log C_6$	$\log(gf\varepsilon)_{\odot}$
Mn I											
1	4018.10*	5	5	2.11	$a^6D_{9/2}$	$z^6D_{7/2}^{\circ}$	127.	-0.19 [1]	0.03	-31.0	-
2	4030.76*	2	5	0.00	$a^6S_{5/2}$	$z^6P_{7/2}^{\circ}$	329.	-0.47 [2]	0.1	-31.2	-
3	4033.07*	2	4	0.00	$a^6S_{5/2}$	$z^6P_{5/2}^{\circ}$	315.4	-0.62 [2]	0.1	-31.2	-
4	4034.49*	2	3	0.00	$a^6S_{5/2}$	$z^6P_{3/2}^{\circ}$	243.	-0.81 [2]	0.1	-31.2	-
5	4041.36*	5	5	2.11	$a^6D_{9/2}$	$z^6D_{9/2}^{\circ}$	160.3	0.29 [2]	0.1	-31.0	-
6	4055.513	5	4	2.13	$a^6D_{7/2}$	$z^6D_{7/2}^{\circ}$	136.	-0.08 [1]	0.03	-31.0	5.29
7	4058.911	5	3	2.17	$a^6D_{3/2}$	$z^6D_{1/2}^{\circ}$	101.	-0.46 [1]	0.02	-31.0	4.81
8	4070.264	5	3	2.19	$a^6D_{1/2}$	$z^6D_{1/2}^{\circ}$	70.	-1.03 [1]	0.02	-31.0	4.47
9	4436.342	22	3	2.91	$a^4D_{5/2}$	$z^4D_{3/2}^{\circ}$	71.3	-0.43 [1]	0.02	-30.7	5.07
10	4451.581	22	3	2.88	$a^4D_{7/2}$	$z^4D_{7/2}^{\circ}$	93.	0.13 [1]	0.02	-30.7	5.50
11	4453.001	22	2	2.93	$a^4D_{3/2}$	$z^4D_{1/2}^{\circ}$	53.5	-0.62 [1]	0.02	-30.7	4.83
12	4457.010	28	3	3.06	$z^6P_{5/2}^{\circ}$	$e^6D_{3/2}$	50.	-0.56 [2]	0.1	-30.6	4.75
13	4470.143	22	2	2.93	$a^4D_{3/2}$	$z^4D_{3/2}^{\circ}$	53.5	-0.44 [2]	0.04	-30.7	4.86
14	4490.067	22	2	2.94	$a^4D_{1/2}$	$z^4D_{3/2}^{\circ}$	56.	-0.52 [2]	0.04	-30.7	4.68
15	4498.901	22	2	2.93	$a^4D_{3/2}$	$z^4D_{5/2}^{\circ}$	57.	-0.46 [1]	0.02	-30.7	4.96
16	4502.220	22	2	2.91	$a^4D_{5/2}$	$z^4D_{7/2}^{\circ}$	59.	-0.43 [1]	0.02	-30.7	4.94
17	4671.667	21	5	2.88	$a^4D_{7/2}$	$z^4F_{5/2}^{\circ}$	12.8	-1.66 [1]	0.02	-30.8	3.83
18	4709.705	21	4	2.88	$a^4D_{7/2}$	$z^4F_{7/2}^{\circ}$	72.	-0.49 [1]	0.02	-30.8	4.92
19	4739.088	21	4	2.93	$a^4D_{3/2}$	$z^4F_{3/2}^{\circ}$	62.	-0.60 [1]	0.02	-30.8	4.79
20	4754.021	16	5	2.27	$z^8P_{5/2}^{\circ}$	$e^8S_{7/2}$	146.	-0.07 [1]	0.02	-30.7	5.26
21	4761.508	21	4	2.94	$a^4D_{1/2}$	$z^4F_{3/2}^{\circ}$	73.	-0.27 [1]	0.02	-30.8	5.12
22	4762.358	21	5	2.88	$a^4D_{7/2}$	$z^4F_{9/2}^{\circ}$	108.	0.30 [1]	0.02	-30.8	5.57
23	4765.851	21	3	2.93	$a^4D_{3/2}$	$z^4F_{5/2}^{\circ}$	81.	-0.08 [1]	0.02	-30.8	5.25

continued on next page

continued from previous page

No.	λ [Å]	Mult.	N_{H}	E_{low} [eV]	Lower level	Upper level	W_{λ} [mÅ]	$\log gf^a$	Error	$\log C_6$	$\log(gf\varepsilon)_{\odot}$
24	4766.413	21	4	2.91	$a^4D_{5/2}$	$z^4F_{7/2}^{\circ}$	98.5	0.11 [1]	0.02	-30.8	5.41
25	4783.389	16	5	2.29	$z^8P_{7/2}^{\circ}$	$e^8S_{7/2}$	148.	0.06 [1]	0.02	-30.7	5.41
26	4823.460	16	6	2.31	$z^8P_{9/2}^{\circ}$	$e^8S_{7/2}$	149.	0.15 [1]	0.02	-30.7	5.52
27	5004.894	20	4	2.91	$a^4D_{5/2}$	$z^6F_{7/2}^{\circ}$	13.7	-1.63 [3]	0.1	-30.8	4.12
28	5117.913	32	3	3.12	$a^4G_{5/2}$	$z^4F_{3/2}^{\circ}$	24.2	-1.20 [1]	0.02	-30.7	4.29
29	5255.287	32	6	3.12	$a^4G_{11/2}$	$z^4F_{9/2}^{\circ}$	41.5	-0.87 [1]	0.04	-30.7	4.54
30	5394.619	1	6	0	$a^6S_{5/2}$	$z^8P_{7/2}^{\circ}$	79.5	-3.50 [2]	0.1	-31.4	1.87
31	5407.331	4	10	2.13	$a^6D_{7/2}$	$y^6P_{7/2}^{\circ}$	53.	-1.74 [2]	0.1	-31.4	3.60
32	5420.265	4	9	2.13	$a^6D_{7/2}$	$y^6P_{5/2}^{\circ}$	85.	-1.46 [2]	0.1	-31.4	3.96
33	5432.512	1	5	0	$a^6S_{5/2}$	$z^8P_{5/2}^{\circ}$	48.	-3.80 [2]	0.1	-31.4	1.58
34	5470.560	4	8	2.15	$a^6D_{5/2}$	$y^6P_{5/2}^{\circ}$	57.5	-1.70 [4]	-	-31.4	3.74
35	5516.697	4	8	2.17	$a^6D_{3/2}$	$y^6P_{3/2}^{\circ}$	44.	-1.85 [2]	0.1	-31.4	3.62
36	5537.692	4	5	2.18	$a^6D_{1/2}$	$y^6P_{3/2}^{\circ}$	36.	-2.02 [4]	-	-31.4	3.45
37	6013.465	27	6	3.06	$z^6P_{3/2}^{\circ}$	$e^6S_{5/2}$	87.	-0.43 [1]	0.05	-30.6	5.01
38	6016.586	27	6	3.06	$z^6P_{5/2}^{\circ}$	$e^6S_{5/2}$	97.8	-0.25 [1]	0.05	-30.6	5.15
39	6021.727	27	6	3.06	$z^6P_{7/2}^{\circ}$	$e^6S_{5/2}$	96.8	-0.12 [1]	0.05	-30.6	5.28
40	8700.877	49	10	4.41	$y^6P_{5/2}^{\circ}$	$e^6D_{5/2}$	11.	-0.48 [4]	-	-31.6	4.94
41	8703.559	49	11	4.41	$y^6P_{5/2}^{\circ}$	$e^6D_{7/2}$	15.5	-0.33 [4]	-	-31.6	5.09
42	8740.705	49	13	4.42	$y^6P_{7/2}^{\circ}$	$e^6D_{9/2}$	26.	-0.06 [4]	-	-31.6	5.33
Mn II											
1	3488.675	3	2	1.84	a^5D_1	$a^5P_1^{\circ}$	160.7	-0.95 [5]	0.02	-32.3	4.42

^a References: (1) Blackwell-Whitehead & Bergemann (2007); (2) Booth, Blackwell, Petford & Shallis (1984); (3) Greenlee & Whaling (1979); (4) Kurucz (1988); (5) Kling & Griesmann (2000)

Table A.2: Lines of Co I and Co II selected for solar and stellar abundance calculations. Designations in the table are the same as used in Table A.1.

No.	λ [Å]	Mult.	N_H	E_{low} [eV]	Lower level	Upper level	W_λ [mÅ]	$\log gf^a$	Error	$\log C_6$	$\log(gf\varepsilon)_\odot$
Co I											
1	3845.470	34	4	0.92	$a^2F_{7/2}$	$y^2G_{9/2}^o$	120	0.01 [2]	0.14	-31.93	-
2	3957.930	18	3	0.58	$b^4F_{5/2}$	$z^4D_{5/2}^o$	60	-2.07 [2]	0.17	-31.97	-
3	4020.905	16	6	0.43	$b^4F_{9/2}$	$z^4F_{9/2}^o$	76	-2.04 [1]	0.05	-31.84	2.91
4	4066.360	30	3	0.92	$a^2F_{7/2}$	$y^4D_{7/2}^o$	59	-1.60 [1]	0.05	-31.70	3.33
5	4110.530	29	6	1.05	$a^2F_{5/2}$	$z^2F_{5/2}^o$	95	-1.08 [2]	0.26	-31.67	3.91
6	4121.320	28	4	0.92	$a^2F_{7/2}$	$z^2G_{9/2}^o$	131	-0.30 [1]	0.05	-31.71	4.66
7	4792.862*	158	6	3.25	$z^6G_{7/2}^o$	$e^6F_{5/2}$	34	-0.07 [3]	-	-30.28	4.92
8	4813.480*	158	7	3.22	$z^6G_{9/2}^o$	$e^6F_{7/2}$	44	0.05 [3]	-	-30.32	5.09
9	4867.870*	158	10	3.17	$z^6G_{11/2}^o$	$e^6F_{9/2}$	60	0.23 [3]	-	-30.45	5.25
10	5212.691	170	9	3.51	$z^4F_{9/2}^o$	$f^4F_{9/2}$	25	-0.11 [2]	0.08	-30.28	4.76
11	5280.631	172	8	3.63	$z^4G_{9/2}^o$	$f^4F_{7/2}$	20	-0.03 [2]	0.09	-30.25	4.89
12	5301.047	39	5	1.71	$a^4P_{5/2}$	$y^4D_{5/2}^o$	21	-1.94 [1]	0.05	-31.63	3.06
13	5331.460	39	5	1.78	$a^4P_{1/2}$	$y^4D_{3/2}^o$	17	-1.00 [1]	0.05	-31.61	3.99
14	5352.049	172	5	3.58	$z^4G_{11/2}^o$	$f^4F_{9/2}$	26	0.06 [2]	0.08	-30.28	4.96
15	5369.590*	39	4	1.74	$a^4P_{3/2}$	$y^4D_{5/2}^o$	44	-1.59 [1]	0.05	-31.63	3.56
16	5483.340	39	7	1.71	$a^4P_{5/2}$	$y^4D_{7/2}^o$	51	-1.41 [1]	0.05	-30.29	3.53
17	5647.234	112	6	2.28	$a^2P_{3/2}$	$y^2D_{5/2}^o$	14	-1.56 [2]	0.23	-31.46	3.4
18	6189.000*	37	5	1.71	$a^4P_{5/2}$	$z^4D_{5/2}^o$	11	-2.45 [2]	0.18	-31.97	2.66
19	6454.990	174	8	3.13	$z^4D_{7/2}^o$	$e^6F_{9/2}$	15	-0.25 [2]	0.09	-30.55	4.68
20	6814.950*	54	5	1.96	$b^4P_{3/2}$	$z^4D_{3/2}^o$	19	-1.90 [2]	0.19	-31.67	3.16
21	7417.380*	89	8	2.04	$a^2D_{3/2}$	$z^4D_{5/2}^o$	11	-2.07 [2]	0.20	-31.68	2.95
22	7712.661*	126	8	2.04	$b^2P_{3/2}$	$z^2D_{5/2}^o$	10	-1.57 [2]	0.23	-31.53	3.42
Co II											
1	3501.730	2	8	2.19	a^5P_3	$z^5D_4^o$	86	-1.22 [4]	-	-32.2	3.64

^a References: (1) Nitz et al. (1999); (2) Cardon et al. (1982); (3) Kurucz & Peytremann (1996); (4) Raassen et al. (1998)

Table A.3: HFS constants A and B (in units of 10^{-3} cm^{-1}) representing magnetic dipole and electric quadrupole interactions for Mn I and Mn II levels. Level energies E are given in eV.

No.	level	g	E	A	B	source	No.	level	g	E	A	B	source ^a	
1	$a^6S_{5/2}$	6	0.00	-2.4	0.0	1	34	$z^6F_{11/2}^o$	12	5.37	6.	0.0	8	
2	$a^6D_{9/2}$	10	2.11	17.	4.4	2	35	$z^6F_{9/2}^o$	10	5.38	5.2	0.0	8	
3	$a^6D_{7/2}$	8	2.14	15.3	0.7	2	36	$z^6F_{7/2}^o$	8	5.40	4.6	0.0	8	
4	$a^6D_{5/2}$	6	2.16	14.6	-1.5	2	37	$z^6F_{5/2}^o$	6	5.41	5.8	0.0	8	
5	$a^6D_{3/2}$	4	2.18	15.7	-2.2	2	38	$z^6F_{3/2}^o$	4	5.41	9.1	0.0	8	
6	$a^6D_{1/2}$	2	2.19	29.4	0.0	2	39	$z^4F_{9/2}^o$	10	5.49	4.4	0.0	4	
7	$z^8P_{5/2}^o$	6	2.28	19.1	0.9	3	40	$z^4F_{7/2}^o$	8	5.52	5.7	0.0	4	
8	$z^8P_{7/2}^o$	8	2.30	18.2	-3.4	3	41	$z^4F_{5/2}^o$	6	5.54	9.5	0.0	4	
9	$z^8P_{9/2}^o$	10	2.32	15.2	1.6	3	42	$z^4F_{3/2}^o$	4	5.56	22.3	0.0	4	
10	$a^4D_{7/2}$	8	2.89	-5.4	0.0	4	43	$x^6P_{7/2}^o$	8	5.58	9.4	0.0	4	
11	$a^4D_{5/2}$	6	2.92	-4.6	0.0	4	44	$x^6P_{5/2}^o$	6	5.60	9.7	0.0	4	
12	$a^4D_{3/2}$	4	2.94	1.7	0.0	4	45	$x^6P_{3/2}^o$	4	5.61	12.5	0.0	4	
13	$a^4D_{1/2}$	2	2.95	50.6	0.0	4	46	$z^4D_{7/2}^o$	8	5.67	1.3	0.0	9	
14	$z^6P_{3/2}^o$	4	3.07	19.1	0.4	5	47	$z^4D_{5/2}^o$	6	5.70	3.1	0.0	9	
15	$z^6P_{5/2}^o$	6	3.07	15.6	-2.5	5	48	$z^4D_{3/2}^o$	4	5.71	6.4	0.0	9	
16	$z^6P_{7/2}^o$	8	3.08	14.3	2.1	5	49	$z^4D_{1/2}^o$	2	5.73	35.	0.0	8	
17	$a^4G_{11/2}$	12	3.13	13.5	0.0	6	50	$e^8D_{3/2}$	4	5.79	38.4	0.0	4	
18	$a^4G_{9/2}$	10	3.14	13.2	0.0	6	51	$e^8D_{5/2}$	6	5.79	24.	0.0	4	
19	$a^4G_{7/2}$	8	3.14	14.6	0.0	6	52	$e^8D_{7/2}$	8	5.79	17.6	0.0	4	
20	$a^4G_{5/2}$	6	3.13	19.9	0.0	6	53	$e^8D_{9/2}$	10	5.79	15.7	0.0	4	
21	$z^4P_{5/2}^o$	6	3.84	-20.3	2.5	3	54	$e^8D_{11/2}$	12	5.79	14.5	0.0	4	
22	$z^4P_{3/2}^o$	4	3.85	-27.1	-1.3	3	55	$y^4P_{5/2}^o$	6	5.82	-1.	0.0	4	
23	$z^4P_{1/2}^o$	2	3.86	-71.1	0.0	3	56	$y^4P_{3/2}^o$	4	5.85	-10.	0.0	4	
24	$y^6P_{3/2}^o$	4	4.43	-32.4	0.6	7	57	$y^4P_{1/2}^o$	2	5.87	-32.5	0.0	4	
25	$y^6P_{5/2}^o$	6	4.43	-18.	-2.3	7	58	$e^6D_{9/2}$	10	5.85	15.5	0.0	7	
26	$y^6P_{7/2}^o$	8	4.44	-13.	-6.2	7	59	$e^6D_{7/2}$	8	5.85	15.8	0.0	7	
27	$e^8S_{7/2}$	8	4.89	24.6	1.6	3	60	$e^6D_{5/2}$	6	5.85	17.6	0.0	7	
28	$e^6S_{5/2}$	6	5.13	27.	0.0	3	61	$e^6D_{3/2}$	4	5.86	22.8	0.0	7	
29	$z^6D_{9/2}^o$	10	5.18	2.9	0.0	4	62	$e^6D_{1/2}$	2	5.86	61.6	0.0	7	
30	$z^6D_{7/2}^o$	8	5.20	1.3	0.0	4	63	$f^6S_{5/2}$	6	7.02	-20.6	0.0	8	
31	$z^6D_{5/2}^o$	6	5.21	-0.9	0.0	4	64	$e^4S_{3/2}$	4	7.12	-50.5	0.0	8	
32	$z^6D_{3/2}^o$	4	5.23	-5.	0.0	4	65	$g^6S_{5/2}$	6	6.31	23.2	0.0	8	
33	$z^6D_{1/2}^o$	2	5.23	-27.4	0.0	4								
Mn II														
1	a^5D_1	3	1.85	-1.95	-1.75	10	2	$z^5P_1^o$	3	5.4	-24.3	0.3	10	

^a References: (1) Davis et al. 1971; (2) Dembczyński et al. 1979; (3) Brodzinski et al. 1987; (4) Blackwell-Whitehead et al. 2005; (5) Handrich et al. 1969; (6) Johann et al. 1981; (7) Luc & Gerstenkorn 1972; (8) Lefèbvre et al. 2003; (9) Başar et al. 2003; (10) Holt et al. (1999)

Table A.4: HFS constants A and B (in units of 10^{-3} cm^{-1}) representing magnetic dipole and electric quadrupole interactions for Co I and Co II levels. Level energies E are given in eV. The interaction constants for all Co I levels are taken from Pickering (1996). For the Co II levels, the data provided by J. Pickering (private communication) are used.

No.	level	g	E	A	B	No.	level	g	E	A	B
1	$a^4F_{9/2}$	10	0.00	15.	4.6	51	$z^4F_{3/2}^o$	4	3.67	14.2	0.0
2	$a^4F_{7/2}$	8	0.10	16.4	3.2	52	$z^4G_{11/2}^o$	12	3.58	25.8	7.
3	$a^4F_{5/2}$	6	0.17	20.5	2.3	53	$z^4G_{9/2}^o$	10	3.63	17.3	6.
4	$a^4F_{3/2}$	4	0.22	34.8	2.3	54	$z^4G_{7/2}^o$	8	3.69	15.	5.
5	$b^4F_{9/2}$	10	0.43	27.7	-4.	55	$z^4G_{5/2}^o$	6	3.73	13.3	5.
6	$b^4F_{7/2}$	8	0.51	22.3	-2.6	56	$z^4D_{7/2}^o$	8	3.63	25.1	0.
7	$b^4F_{5/2}$	6	0.58	18.8	-1.8	57	$z^4D_{5/2}^o$	6	3.71	23.2	1.
8	$b^4F_{3/2}$	4	0.63	10.2	-2.	58	$z^4D_{3/2}^o$	4	3.78	23.5	1.
9	$a^2F_{7/2}$	8	0.92	13.	-5.	59	$z^4D_{1/2}^o$	2	3.81	27.5	0.
10	$a^2F_{5/2}$	6	1.05	37.1	-3.	60	$z^2G_{9/2}^o$	10	3.93	16.5	0.
11	$a^4P_{5/2}$	6	1.71	5.9	-8.	61	$z^2G_{7/2}^o$	8	4.06	30.7	5.
12	$a^4P_{3/2}$	4	1.74	10.6	4.	62	$z^2F_{7/2}^o$	8	3.95	15.	6.
13	$a^4P_{1/2}$	2	1.79	-23.6	0.0	63	$z^2F_{5/2}^o$	6	4.06	34.9	0.
14	$b^4P_{5/2}$	6	1.88	37.4	5.	64	$y^4D_{7/2}^o$	8	3.97	16.	5.
15	$b^4P_{3/2}$	4	1.96	15.4	-2.	65	$y^4D_{5/2}^o$	6	4.05	15.5	0.
16	$b^4P_{1/2}$	2	2.01	57.6	0.0	66	$y^4D_{3/2}^o$	4	4.11	19.7	0.
17	$a^2G_{9/2}$	10	2.04	20.5	2.	67	$y^4D_{1/2}^o$	2	4.15	58.9	0.
18	$a^2G_{7/2}$	8	2.14	28.	-3.2	68	$y^4F_{9/2}^o$	10	4.07	9.9	8.
19	$a^2D_{3/2}$	4	2.04	13.	0.0	69	$y^4F_{7/2}^o$	8	4.11	17.	0.
20	$a^2D_{5/2}$	6	2.08	46.3	4.	70	$y^4F_{5/2}^o$	6	4.21	20.1	0.
21	$a^2P_{3/2}$	4	2.28	11.2	4.	71	$y^4F_{3/2}^o$	4	4.24	39.7	-2.
22	$a^2P_{1/2}$	2	2.33	20.1	0.0	72	$y^2G_{9/2}^o$	10	4.15	14.7	0.
23	$b^2P_{3/2}$	4	2.54	5.5	2.	73	$z^2D_{5/2}^o$	6	4.15	15.4	0.
24	$b^2P_{1/2}$	2	2.63	17.2	0.0	74	$z^2D_{3/2}^o$	4	4.26	46.1	2.
25	$a^2H_{11/2}$	12	2.70	22.6	0.0	75	$y^2D_{5/2}^o$	6	4.48	16.4	0.
26	$a^2H_{9/2}$	10	2.79	26.4	0.0	76	$y^2D_{3/2}^o$	4	4.57	42.	0.
27	$b^2D_{5/2}$	6	2.72	18.5	15.	77	$y^2F_{7/2}^o$	8	4.40	13.9	0.
28	$b^2D_{3/2}$	4	2.87	30.8	4.	78	$y^2F_{5/2}^o$	6	4.50	30.4	0.
29	$b^2G_{9/2}$	10	2.87	36.9	0.0	79	$x^4D_{7/2}^o$	8	4.92	10.1	0.
30	$b^2G_{7/2}$	8	2.88	8.8	0.0	80	$x^4D_{5/2}^o$	6	5.00	11.9	1.
31	$z^6F_{11/2}^o$	12	2.93	28.5	-2.	81	$x^4D_{3/2}^o$	4	5.06	17.6	0.
32	$z^6F_{9/2}^o$	10	2.96	28.5	4.	82	$x^4D_{1/2}^o$	2	5.1	55.8	0.
33	$z^6F_{7/2}^o$	8	3.02	26.4	5.	83	$e^4F_{9/2}$	10	5.55	13.4	0.
34	$z^6F_{5/2}^o$	6	3.07	24.	2.	84	$e^4F_{7/2}$	8	5.59	11.1	1.
35	$z^6F_{3/2}^o$	4	3.11	20.1	0.0	85	$e^4F_{5/2}$	6	5.69	18.4	0.
36	$z^6F_{1/2}^o$	2	3.13	-2.1	0.0	86	$e^4F_{3/2}$	4	5.75	35.5	0.
37	$z^6D_{9/2}^o$	10	3.05	28.1	0.0	87	$e^6F_{11/2}$	12	5.66	33.5	5.
38	$z^6D_{7/2}^o$	8	3.13	27.2	-3.	88	$e^6F_{9/2}$	10	5.73	31.5	2.
39	$z^6D_{5/2}^o$	6	3.19	26.6	-6.	89	$e^6F_{7/2}$	8	5.79	28.7	-1.
40	$z^6D_{3/2}^o$	4	3.23	27.	0.0	90	$e^6F_{5/2}$	6	5.84	25.7	-1.
41	$z^6D_{1/2}^o$	2	3.26	33.4	0.0	91	$e^6F_{3/2}$	4	5.87	19.4	-1.
42	$z^6G_{13/2}^o$	14	3.12	25.3	8.	92	$e^6F_{1/2}$	2	5.89	-17.1	0.

continued on next page

<i>continued from previous page</i>											
No.	level	g	E	A	B	No.	level	g	E	A	B
43	$z^6G_{11/2}^o$	12	3.17	23.	7.	93	$f^4F_{9/2}$	10	5.89	36.	5.
44	$z^6G_{9/2}^o$	10	3.22	20.6	5.	94	$f^4F_{7/2}$	8	5.98	28.3	3.
45	$z^6G_{7/2}^o$	8	3.25	18.3	6.	95	$f^4F_{5/2}$	6	6.04	19.5	3.
46	$z^6G_{5/2}^o$	6	3.28	14.4	3.	96	$f^4F_{3/2}$	4	6.09	-1.5	0.
47	$z^6G_{3/2}^o$	4	3.30	4.9	4.	97	$g^4F_{9/2}$	10	6.34	9.2	0.
48	$z^4F_{9/2}^o$	10	3.51	27.	-2.	98	$g^4F_{7/2}$	8	6.35	11.2	0.
49	$z^4F_{7/2}^o$	8	3.57	21.9	1.	99	$g^4F_{5/2}$	6	6.46	13.9	0.
50	$z^4F_{5/2}^o$	6	3.62	18.7	1.	100	$g^4F_{3/2}$	4	6.53	14.	0.
Co II											
1	a^5P_3	7	2.20	40.0	-20.0	4	$z^5D_4^o$	9	5.74	8.0	10.0
2	a^5P_2	5	2.23	50.0	20.0	5	$z^5D_3^o$	7	5.83	8.0	0.
3	a^5P_1	3	2.27	60.0	2.0	6	$z^5D_2^o$	5	5.89	-30.0	12.0

Table A.5: NLTE abundance corrections to Mn I lines for selected models of the grid. Collisions with neutral hydrogen are neglected, $S_{\text{H}} = 0$.

$T_{\text{eff}}/\log g/[\text{Fe}/\text{H}]$	Δ_{NLTE}														
	4018	4030	4033	4034	4041	4055	4451	4754	4762	4766	4783	4823	6013	6016	6021
5000/4/ 0	0.03	0.05	0.05	0.05	0.04	0.04	0.03	0.02	0.03	0.03	0.03	0.04	-0.09	-0.1	-0.08
5000/4/-1	0.15	0.15	0.15	0.15	0.14	0.15	0.2	0.09	0.18	0.24	0.13	0.12	0.17	0.16	0.13
5000/4/-2	0.47	0.23	0.24	0.24	0.42	0.49	0.43	0.36	0.39	0.42	0.35	0.34	-	-	-
5000/4/-3	0.54	0.45	0.45	0.49	0.56	-	-	0.48	-	-	0.5	0.49	-	-	-
5500/4/ 0	0.05	0.08	0.08	0.08	0.05	0.02	0.05	0.05	0.05	0.06	-0.01	-0.01	0.05	0.04	0.01
5500/4/-1	0.28	0.1	0.15	0.15	0.26	0.25	0.26	0.15	0.22	0.29	0.14	0.14	0.24	0.24	0.22
5500/4/-2	0.42	0.28	0.31	0.35	0.48	0.43	0.39	0.38	0.38	0.38	0.4	0.4	-	-	-
5500/4/-3	0.51	0.69	0.7	0.72	0.51	-	-	0.5	-	-	0.52	0.52	-	-	-
5780/4.4/0						0.03	0.02	-0.01	0.01	0.02	0.01	0.01	0.1	0.1	0.09
6000/4/ 0	0.1	0.07	0.07	0.08	0.05	-0.02	0.05	-0.02	0.05	0.08	-0.03	-0.04	0.06	0.05	0.01
6000/4/-1	0.28	0.1	0.1	0.1	0.27	0.29	0.26	0.19	0.22	0.3	0.17	0.15	0.22	0.23	0.22
6000/4/-2	0.38	0.4	0.42	0.42	0.38	0.41	0.36	0.35	0.34	0.35	0.37	0.37	-	-	-
6000/4/-3	-	0.63	0.64	0.64	0.4	-	-	-	-	-	0.42	0.42	-	-	-
6200/3.4/ 0	0.03	0.06	0.07	0.07	0.01	0.02	0.01	-0.07	0	0.04	-0.07	-0.07	0	-0.03	-0.07
6200/3.4/-1.2	0.32	0.1	0.1	0.15	0.31	0.38	0.32	0.27	0.28	0.31	0.25	0.25	0.25	0.24	0.25
6200/3.4/-2.4	0.4	0.55	0.6	0.63	0.4	0.41	0.36	0.36	0.35	0.36	0.39	0.4	-	-	-
6200/4.6/ 0	0.05	0.08	0.08	0.07	0.02	0.03	0.03	-0.01	0.04	0.04	0.01	0.02	0.02	0	-0.03
6200/4.6/-1.2	0.28	0.15	0.15	0.15	0.26	0.31	0.28	0.24	0.25	0.28	0.23	0.22	0.23	0.23	0.23
6200/4.6/-2.4	0.38	0.43	0.47	0.51	0.39	0.39	0.35	0.35	0.34	0.34	0.36	0.36	-	-	-

Table A.6: NLTE abundance corrections to Mn I lines for selected models of the grid. Collisions with neutral hydrogen are included with a scaling factor $S_{\text{H}} = 0.05$ (our reference value).

$T_{\text{eff}}/\log g/[\text{Fe}/\text{H}]$	Δ_{NLTE}														
	4018	4030	4033	4034	4041	4055	4451	4754	4762	4766	4783	4823	6013	6016	6021
5000/4/ 0	0.03	0.04	0.04	0.05	0.03	0.03	0.03	0.02	0.02	0.02	0.02	0.02	-0.08	-0.09	-0.09
5000/4/-1	0.15	0.1	0.1	0.1	0.13	0.11	0.15	0.07	0.13	0.17	0.07	0.07	0.12	0.1	0.07
5000/4/-2	0.41	0.23	0.23	0.23	0.36	0.43	0.37	0.31	0.34	0.37	0.3	0.3	-	-	-
5000/4/-3	0.49	0.37	0.37	0.41	0.5	-	-	0.42	-	-	0.45	0.44	-	-	-
5500/4/ 0	0.02	0.05	0.04	0.04	0.02	0.03	0.01	0	0	0.01	0.01	0.01	-0.08	-0.12	-0.1
5500/4/-1	0.2	0.09	0.13	0.14	0.15	0.15	0.2	0.07	0.16	0.23	0.07	0.07	0.17	0.16	0.15
5500/4/-2	0.41	0.27	0.28	0.29	0.42	0.39	0.42	0.33	0.33	0.34	0.35	0.35	-	-	-
5500/4/-3	0.46	0.59	0.6	0.61	0.45	-	-	0.44	-	-	0.47	0.47	-	-	-
5780/4.4/0						0.03	0.02	-0.01	0.01	0.02	0.01	0.01	0.1	0.1	0.09
6000/4/ 0	0.02	0.05	0.05	0.05	0.01	0.01	0.01	-0.04	0.01	0.02	-0.02	-0.02	-0.02	-0.06	-0.08
6000/4/-1	0.21	0.11	0.1	0.11	0.18	0.21	0.2	0.13	0.17	0.22	0.1	0.1	0.16	0.16	0.17
6000/4/-2	0.35	0.3	0.3	0.33	0.34	0.37	0.31	0.3	0.3	0.31	0.33	0.33	-	-	-
6000/4/-3	-	0.6	0.61	0.61	0.38	-	-	-	-	-	0.38	0.39	-	-	-
6200/3.4/ 0	0.01	0.05	0.06	0.07	-0.03	0.01	0	-0.1	0	0.03	-0.08	-0.1	0	-0.03	-0.07
6200/3.4/-1.2	0.27	0.05	0.06	0.11	0.26	0.32	0.26	0.22	0.22	0.26	0.2	0.2	0.2	0.19	0.2
6200/3.4/-2.4	0.35	0.5	0.52	0.56	0.35	0.37	0.32	0.31	0.31	0.31	0.34	0.34	-	-	-
6200/4.6/ 0	0.01	0.04	0.05	0.05	0.05	0.01	0.01	-0.02	0.02	0.02	-0.01	-0.02	0	-0.02	-0.04
6200/4.6/-1.2	0.22	0.1	0.1	0.11	0.2	0.25	0.22	0.18	0.19	0.22	0.17	0.16	0.17	0.17	0.17
6200/4.6/-2.4	0.34	0.37	0.39	0.43	0.34	0.35	0.3	0.31	0.30	0.3	0.33	0.33	-	-	-

List of Figures

2.1	A Mn I line in the solar spectrum with hyperfine structure	11
3.1	Comparison of model atmospheres	20
3.2	Grotrian diagram of the Mn model atom	23
3.3	Grotrian diagram of the Co model atom	24
3.4	Oscillator strengths for transitions in Mn I and Co I	25
3.5	Comparison of rates for radiative and collisional transitions in Mn I	29
3.6	Interaction constants C_6 for transitions in Mn I and Co I	32
3.7	Spectrum synthesis: oscillator strengths for Mn I lines	33
3.8	Spectrum synthesis: oscillator strengths for Co I lines	34
4.1	Departure coefficients b_i of selected Mn I and Mn II levels	38
4.2	The mean intensities at wavelengths 563 nm and 7100 nm	39
4.3	Net rates in Mn I	40
4.4	Departure coefficients of Mn I levels for different model atmospheres	42
4.5	Departure coefficients of Mn I levels for different atomic models	43
4.6	Departure coefficients of Mn I levels for different photoionization cross-sections	45
4.7	Departure coefficients of Mn I levels for different transition probabilities	46
4.8	Departure coefficients of Mn I levels for different H I collision cross-sections	48
4.9	Departure coefficients of selected Co I and Co II levels	50
4.10	Departure coefficients of Co levels for different model atmospheres	52
5.1	Synthetic profiles of solar Mn I lines	55
5.2	Synthetic profiles of the Mn I line at 4033 Å	58
5.3	Synthetic profiles of the Mn I line at 4033 Å	59
5.4	NLTE abundance corrections for Mn I lines	60
5.5	Synthetic profiles of solar Co I and Co II lines	64
5.6	NLTE abundance corrections for Co I lines at 4121 and 4020 Å	65
5.7	Departure coefficients b_i of Co levels for the cool model from the grid	66
5.8	NLTE abundance corrections for the Co II line at 3501 Å	66
6.1	Solar Mn abundances	68
6.2	NLTE profiles of the Mn I line at 4823 Å	70
6.3	LTE profiles of the Mn II line at 3488 Å	72
6.4	Solar Co abundances	73
6.5	NLTE profiles of the Co I line at 4121 Å	74
7.1	The Mn I line at 4030 Å in spectra of the Sun, HD 102200, and HD 19445	78
7.2	[Mn/Fe] vs. [Fe/H] in metal-poor stars	81
7.3	[Mn/Fe] ratios as derived from Mn I and Mn II lines	83
7.4	[Mn/Fe] ratios calculated with $S_H = 0, 0.05, 0.5, \text{ and } 1$	84
7.5	[Co/Fe] vs. [Fe/H] in metal-poor stars	85
7.6	[Co/Fe] ratios as determined from Co I and Co II lines	87

7.7	[Mn/Fe] ratios in metal-poor stars compared with the data from the literature . . .	88
7.8	[Mn/Fe] vs. [Fe/H] in metal-poor stars derived from Mn II and Mn I lines	90
7.9	[Co/Fe] in metal-poor stars compared with the data from the literature	92
8.1	Evolution of [Mn/Fe] and [Co/Fe] ratios as a function of [Fe/H]	104
8.2	[Mn/Co] vs. [Fe/H], [Mn/Mg] and [Co/Mg] vs. [Mg/H]	105

List of Tables

3.1	Stellar parameters	16
3.2	Comparison of stellar effective temperatures	17
5.1	Average depths of formation for Mn I lines	56
5.2	NLTE abundance corrections for Co I lines for selected models of the grid	62
6.1	Solar NLTE abundances of Mn with different oscillator strengths	68
6.2	Solar NLTE abundances of Mn in multiplets	69
7.1	The NLTE and LTE abundances of Mn and Co for the program stars	80
7.2	Stellar NLTE and LTE abundances derived from Mn I and Mn II lines	82
7.3	Stellar NLTE and LTE abundances derived from Co I and Co II lines	86
8.1	Earlier investigations of Mn abundances in stars	97
A.1	Lines of Mn I and Mn II	121
A.2	Lines of Co I and Co II	123
A.3	HFS constants A and B for Mn I and Mn II levels	124
A.4	HFS constants A and B for Co I and Co II levels	125
A.5	NLTE Mn I abundance corrections for selected models, $S_{\text{H}} = 0$	127
A.6	NLTE Mn I abundance corrections for selected models, $S_{\text{H}} = 0.05$	127

Bibliography

- Abt A 1952 *AJ* **57**, 158.
- Ali A W & Griem H R 1965 *Physical Review* **140**, 1044–1049.
- Allen C W 1973 *Astrophysical quantities* London: University of London, Athlone Press, 1973, 3rd ed.
- Aller L H & Greenstein J L 1960 *ApJS* **5**, 139.
- Alonso A, Arribas S & Martínez-Roger C 1995 *A&A* **297**, 197–215.
- Alonso A, Arribas S & Martínez-Roger C 1996 *A&AS* **117**, 227–254.
- Alonso A, Arribas S & Martínez-Roger C 1999 *A&AS* **139**, 335–358.
- Amusia M I & Ivanov V K 1987 *Advances in Physical Sciences* .
- Amusia M Y, Dolmatov V K & Mansurov M M 1990 *Journal of Physics B Atomic Molecular Physics* **23**, L491–L494.
- Amusia M Y, Dolmatov V K & Romanenko V M 1988 *Journal of Physics B Atomic Molecular Physics* **21**, L151–L154.
- Anderson L S 1989 *ApJ* **339**, 558–578.
- Anstee S D & O'Mara B J 1995 *MNRAS* **276**, 859–866.
- Argast D, Samland M, Gerhard O E & Thielemann F K 2000 *A&A* **356**, 873–887.
- Arnett W D 1971 *ApJ* **166**, 153.
- Arnett W D, Truran J W & Woosley S E 1971 *ApJ* **165**, 87.
- Asplund M 2005 *ARAA* **43**, 481–530.
- Axer M, Fuhrmann K & Gehren T 1995 *A&A* **300**, 751.
- Başar G, Başar G, Acar G, Öztürk I K & Kröger S 2003 *Physica Scripta* **67**, 476.
- Bagnulo S, Jehin E, Ledoux C, Cabanac R, Melo C, Gilmozzi R & The ESO Paranal Science Operations Team 2003 *The Messenger* **114**, 10–14.
- Bai G S, Zhao G, Chen Y Q, Shi J R, Klochkova V G, Panchuk V E, Qiu H M & Zhang H W 2004 *A&A* **425**, 671–681.
- Ballero S K, Matteucci F, Origlia L & Rich R M 2007 *A&A* **467**, 123–136.
- Barklem P S 2007a *A&A* **466**, 327–337.
- Barklem P S 2007b in L. C Popovic & M. S Dimitrijevic, eds, 'Spectral Line Shapes in Astrophysics' Vol. 938 of *American Institute of Physics Conference Series* pp. 111–118.

- Barklem P S, Piskunov N & O'Mara B J 2000 *A&A* **363**, 1091–1105.
- Barklem P S, Stempels H C, Allende Prieto C, Kochukhov O P, Piskunov N & O'Mara B J 2002 *A&A* **385**, 951–967.
- Bautista M A 1997 *A&AS* **122**, 167–176.
- Becker U, Kwiatkowski M, Teppner U & Zimmermann P 1980 *Journal of Physics B Atomic Molecular Physics* **13**, 2505–2516.
- Bekki K & Chiba M 2002 *ApJ* **566**, 245–251.
- Belyaev A K & Barklem P S 2003 *Phys. Rev. A* **68**(6).
- Bergemann M & Gehren T 2007 *A&A* **473**, 291–302.
- Bergemann M & Gehren T 2008 *A&A*, *accepted*, *Paper I*.
- Blackwell D E, Shallis M J & Simmons G J 1982 *MNRAS* **199**, 33–36.
- Blackwell-Whitehead R & Bergemann M 2007 *A&A* **472**, L43–L46.
- Blackwell-Whitehead R J, Pickering J C, Pearse O & Nave G 2005 *ApJS* **157**, 402–409.
- Blackwell-Whitehead R J, Xu H L, Pickering J C, Nave G & Lundberg H 2005 *MNRAS* **361**, 1281–1286.
- Böhm-Vitense E 1958 *Zeitschrift fur Astrophysik* **46**, 108.
- Booth A J, Blackwell D E, Petford A D & Shallis M J 1984 *MNRAS* **208**, 147–159.
- Booth A J, Blackwell D E & Shallis M J 1984 *MNRAS* **209**, 77–81.
- Brodzinski T, Kronfeldt H D, Kropp J R & Winkler R 1987 *Zeitschrift fur Physik D Atoms Molecules Clusters* **7**, 161–164.
- Bruhn R, Schmidt E, Schröder H & Sonntag B 1982 *Physics Letters A* **90**, 41–44.
- Burbidge E M, Burbidge G R, Fowler W A & Hoyle F 1957 *Reviews of Modern Physics* **29**, 547–650.
- Butler K & Giddings J 1985 *Newsletter on Analysis of Astronomical Spectra, University of London* **9**.
- Cardon B L, Smith P L, Scalo J M & Testerman L 1982 *ApJ* **260**, 395–412.
- Carretta E, Gratton R G, Bragaglia A, Bonifacio P & Pasquini L 2004 *A&A* **416**, 925–940.
- Casimir H B G 1963 *On the interaction between atomic nuclei and electrons* San Francisco: Freeman.
- Cayrel de Strobel G 1996 *The Astronomy and Astrophysics Review* **7**, 243–288.
- Cayrel R, Depagne E, Spite M, Hill V, Spite F, François P, Plez B, Beers T, Primas F, Andersen J, Barbuy B, Bonifacio P, Molaro P & Nordström B 2004 *A&A* **416**, 1117–1138.
- Cescutti G, Matteucci F, Lanfranchi G A & McWilliam A 2008 *ArXiv e-prints*.
- Cohen J G, Christlieb N, McWilliam A, Sheckman S, Thompson I, Wasserburg G J, Ivans I, Dehn M, Karlsson T & Melendez J 2004 *ApJ* **612**, 1107–1135.
- Collet R, Asplund M & Thévenin F 2005 *A&A* **442**, 643–650.

- Cowley C R & Castelli F 2002 *A&A* **387**, 595–604.
- Cram L E, Lites B W & Rutten R J 1980 *ApJ* **241**, 374–384.
- Davis S J, Wright J J & Balling L C 1971 *Phys. Rev. A* **3**, 1220–1223.
- del Peloso E F, Cunha K, da Silva L & Porto de Mello G F 2005 *A&A* **441**, 1149–1156.
- Dembczyński J, Ertmer W, Johann U, Penselin S & Stinner P 1979 *Zeitschrift fur Physik* **291**, 207–218.
- Drawin H W 1968 *Zeitschrift fur Physik* **211**, 404–417.
- Drawin H W 1969a *Zeitschrift fur Physik* **225**, 470–482.
- Drawin H W 1969b *Zeitschrift fur Physik* **225**, 483–493.
- Dupree A K, Hartmann L & Smith G H 1990 *ApJ* **353**, 623–635.
- Eggen O J, Lynden-Bell D & Sandage A R 1962 *ApJ* **136**, 748.
- ESA 1997 *VizieR Online Data Catalog* **1239**, 0.
- Feltzing S, Fohlman M & Bensby T 2007 *A&A* **467**, 665–677.
- Figger H, Siomos K, Walther H & Heldt J 1975 *A&A* **43**, 389–394.
- Fleck I, Grosser J, Schnecke A, Steen W & Voigt H 1991 *Journal of Physics B Atomic Molecular Physics* **24**, 4017–4023.
- François P, Depagne E, Hill V, Spite M, Spite F, Plez B, Beers T C, Barbuy B, Cayrel R, Andersen J, Bonifacio P, Molaro P, Nordström B & Primas F 2003 *A&A* **403**, 1105–1114.
- François P, Matteucci F, Cayrel R, Spite M, Spite F & Chiappini C 2004 *A&A* **421**, 613–621.
- Fuhr J R, Martin G A & Wiese W L 1988 *Atomic transition probabilities. Iron through Nickel*. New York: American Institute of Physics (AIP) and American Chemical Society, 1988.
- Fuhrmann K 1998 *A&A* **338**, 161–183.
- Fuhrmann K 2004 *Astronomische Nachrichten* **325**, 3–80.
- Fuhrmann K, Axer M & Gehren T 1993 *A&A* **271**, 451.
- Fuhrmann K, Pfeiffer M, Frank C, Reetz J & Gehren T 1997 *A&A* **323**, 909–922.
- Gehren T, Butler K, Mashonkina L, Reetz J & Shi J 2001 *A&A* **366**, 981–1002.
- Gehren T, Korn A J & Shi J 2001 *A&A* **380**, 645–664.
- Gehren T, Liang Y C, Shi J R & Zhang, H. W. and Zhao G 2004 *A&A* **413**, 1045–1063.
- Gehren T, Shi J R, Zhang H W, Zhao G & Korn A J 2006 *A&A* **451**, 1065–1079.
- Goswami A & Prantzos N 2000 *A&A* **359**, 191–212.
- Gratton R G 1987 in ‘European Southern Observatory Astrophysics Symposia’ Vol. 27 of *European Southern Observatory Astrophysics Symposia* pp. 153–158.
- Gratton R G 1988 *The Messenger* **53**, 45–47.
- Gratton R G 1989 *A&A* **208**, 171–178.
- Gratton R G, Carretta E, Eriksson K & Gustafsson B 1999 *A&A* **350**, 955–969.

- Gratton R G & Sneden C 1991 *A&A* **241**, 501–525.
- Gray D F 1988 *Lectures on spectral-line analysis: F, G, and K stars* Arva: Ontario Gray, 1988.
- Gray D F 1992 *The Observation and Analysis of Stellar Photospheres* The Observation and Analysis of Stellar Photospheres, by David F. Gray, pp. 470. ISBN 0521408687. Cambridge, UK: Cambridge University Press, June 1992.
- Greenlee T R & Whaling W 1979 *Journal of Quantitative Spectroscopy and Radiative Transfer* **21**, 55–63.
- Grupp F 2004a *A&A* **420**, 289–305.
- Grupp F 2004b *A&A* **426**, 309–322.
- Handrich E, Steudel A & Walther H 1969 *Physics Letters A* **29**, 486–488.
- Hauschildt P H, Allard F & Baron E 1999 *ApJ* **512**, 377–385.
- Heger A & Woosley S E 2008 *ArXiv e-prints* .
- Holt R A, Scholl T J & Rosner S D 1999 *MNRAS* **306**, 107–111.
- Holweger H 1967 *Zeitschrift fur Astrophysik* **65**, 365.
- Holweger H 1979 in ‘Liege International Astrophysical Colloquia’ Vol. 22 of *Liege International Astrophysical Colloquia* pp. 117–138.
- Holweger H & Müller E A 1974 *Sol. Phys.* **39**, 19–30.
- Hubeny I 2003 in I Hubeny, D Mihalas & K Werner, eds, ‘Stellar Atmosphere Modeling’ Vol. 288 of *Astronomical Society of the Pacific Conference Series* p. 17.
- Iwamoto K, Brachwitz F, Nomoto K, Kishimoto N, Umeda H, Hix W R & Thielemann F K 1999 *ApJS* **125**, 439–462.
- Janicki L 1909 *Annalen der Physik* **334**, 833–868.
- Johann U, Dembczyński J & Ertmer W 1981 *Zeitschrift fur Physik* **303**, 7–12.
- Johansson S & Cowley C R 1988 *Journal of the Optical Society of America B Optical Physics* **5**, 2264–2279.
- Johnson J A 2002 *ApJS* **139**, 219–247.
- Kaulakys B 1985 *Journal of Physics B Atomic Molecular Physics* **18**, L167–L170.
- Kelch W L, Chang S H, Furenlid I, Linsky J L, Basri G S, Chiu H Y & Maran S P 1978 *ApJ* **220**, 962–979.
- Khristoforova M 2005 *Kinetic equilibrium of hydrogen in atmospheres of A-F stars*.
- Kling R & Griesmann U 2000 *ApJ* **531**, 1173–1178.
- Kobayashi C, Umeda H, Nomoto K, Tominaga N & Ohkubo T 2006 *ApJ* **653**, 1145–1171.
- Korn A J, Shi J & Gehren T 2003 *A&A* **407**, 691–703.
- Kurucz R & Bell B 1995 *Atomic Line Data (R.L. Kurucz and B. Bell) Kurucz CD-ROM No. 23. Cambridge, Mass.: Smithsonian Astrophysical Observatory, 1995.* **23**.
- Kurucz R L 1981 *SAO Special Report* **390**.

- Kurucz R L 1988 *Trans. IAU, XXB*, M. McNally, ed., Dordrecht: Kluwer pp. 168–172.
- Kurucz R L, Furenlid I, Brault J & Testerman L 1984 *Solar flux atlas from 296 to 1300 nm*
National Solar Observatory Atlas, Sunspot, New Mexico: National Solar Observatory, 1984.
- Kurucz R L & Peytremann E 1975 *SAO Special Report* **362**.
- Kurucz R L & Peytremann E 1996 *VizieR Online Data Catalog* **6010**, 0.
- Lai D K, Bolte M, Johnson J A, Lucatello S, Heger A & Woosley S E 2008 *ApJ* **681**, 1524–1556.
- Lanfranchi G A & Matteucci F 2004 *MNRAS* **351**, 1338–1348.
- Lanfranchi G A, Matteucci F & Cescutti G 2006 *MNRAS* **365**, 477–488.
- Lefèbvre P H, Garnir H P & Biémont E 2003 *A&A* **404**, 1153–1158.
- Lodders K 2003 *ApJ* **591**, 1220–1247.
- Luc P & Gerstenkorn S 1972 *A&A* **18**, 209.
- Marek J 1975 *A&A* **44**, 69–71.
- Marek J & Richter J 1973 *A&A* **26**, 155.
- Marek J & Vogt K 1977 *Zeitschrift fur Physik* **280**, 235–237.
- Martin G A, Fuhr J R & Wiese W L 1988 *Atomic transition probabilities. Scandium through Manganese* New York: American Institute of Physics (AIP) and American Chemical Society, 1988.
- Martinson I, Curtis L J, Smith P L & Biemont E 1977 *Physica Scripta* **16**, 35–38.
- Mashonkina L, Gehren T & Bikmaev I 1999 *A&A* **343**, 519–530.
- Mashonkina L J 1996 in S. J. Adelman, F. Kupka & W. W. Weiss, eds, ‘M.A.S.S., Model Atmospheres and Spectrum Synthesis’ Vol. 108 of *Astronomical Society of the Pacific Conference Series* p. 140.
- Mashonkina L, Zhao G, Gehren T, Aoki W, Bergemann M, Noguchi K, Shi J R, Takada-Hidai M & Zhang H W 2008 *A&A* **478**, 529–541.
- McWilliam A, Preston G W, Sneden C & Searle L 1995 *AJ* **109**, 2757.
- McWilliam A, Rich R M & Smecker-Hane T A 2003 *ApJL* **592**, L21–L24.
- Mihalas D 1978 *Stellar atmospheres /2nd edition/* San Francisco, W. H. Freeman and Co., 1978. 650 p.
- Moore C E 1945 *Contributions from the Princeton University Observatory* **20**, D16+.
- Nagataki S, Hashimoto M A, Sato K & Yamada S 1997 *ApJ* **486**, 1026.
- Nakamura T, Umeda H, Nomoto K, Thielemann F K & Burrows A 1999 *ApJ* **517**, 193–208.
- Nissen P E, Chen Y Q, Schuster W J & Zhao G 2000 *A&A* **353**, 722–728.
- Nitz D E, Kunau A E, Wilson K L & Lentz L R 1999 *ApJS* **122**, 557–561.
- Nomoto K, Hashimoto M, Tsujimoto T, Thielemann F K, Kishimoto N, Kubo Y & Nakasato N 1997 *Nuclear Physics A* **616**, 79–90.
- Nomoto K, Maeda K, Tominaga N, Ohkubo T, Umeda H, Deng J & Mazzali P A 2004 *Progress of Theoretical Physics Supplement* **155**, 299–302.

- Nomoto K, Thielemann F K & Yokoi K 1984 *ApJ* **286**, 644–658.
- Nordlund A & Stein R F 1995 in A Noels, D Fraipont-Caro, M Gabriel, N Grevesse & P Demarque, eds, ‘Liege International Astrophysical Colloquia’ Vol. 32 of *Liege International Astrophysical Colloquia* p. 75.
- Peterson R C 1981 *ApJ* **244**, 989–1000.
- Pickering J C 1996 *ApJS* **107**, 811.
- Pickering J C, Raassen A J J, Uylings P H M & Johansson S 1998 *ApJS* **117**, 261.
- Pickering J C & Thorne A P 1996 *ApJS* **107**, 761.
- Prochaska J X & McWilliam A 2000 *ApJL* **537**, L57–L60.
- Przybilla N & Butler K 2004 *ApJL* **610**, L61–L64.
- Raassen A J J, Pickering J C & Uylings P H M 1998 *A&AS* **130**, 541–549.
- Reddy B E, Lambert D L & Allende Prieto C 2006 *MNRAS* **367**, 1329–1366.
- Reddy B E, Tomkin J, Lambert D L & Allende Prieto C 2003 *MNRAS* **340**, 304–340.
- Rutten R J 1988 in R Viotti, A Vittone & M Friedjung, eds, ‘IAU Colloq. 94: Physics of Formation of FE II Lines Outside LTE’ Vol. 138 of *Astrophysics and Space Science Library* pp. 185–210.
- Rutten R J 2002 *Journal of Astronomical Data* **8**, 8.
- Rutten R J 2003 in I Hubeny, D Mihalas & K Werner, eds, ‘Stellar Atmosphere Modeling’ Vol. 288 of *Astronomical Society of the Pacific Conference Series* p. 99.
- Ryan S G 1998 *A&A* **331**, 1051–1058.
- Ryan S G, Norris J E & Beers T C 1996 *ApJ* **471**, 254.
- Ryan S G, Norris J E & Bessell M S 1991 *AJ* **102**, 303–322.
- Salih S, Lawler J E & Whaling W 1985 *Phys. Rev. A* **31**, 744–749.
- Salpeter E E 1955 *ApJ* **121**, 161.
- Samland M 1998 *ApJ* **496**, 155.
- Schmidt M 1959 *ApJ* **129**, 243.
- Schnabel R, Bard A & Kock M 1995 *Zeitschrift fur Physik D Atoms Molecules Clusters* **34**, 223–226.
- Severino G, Caccin B & Gomez M T 1993 *Memorie della Societa Astronomica Italiana* **64**, 565.
- Shchukina N G, Trujillo Bueno J & Asplund M 2005 *ApJ* **618**, 939–952.
- Shchukina N & Trujillo Bueno J 2001 *ApJ* **550**, 970–990.
- Simmons G J & Blackwell D E 1982 *A&A* **112**, 209–214.
- Smith G H & Churchill C W 1998 *MNRAS* **297**, 388–398.
- Sobeck J S, Ivans I I, Simmerer J A, Sneden C, Hoefflich P, Fulbright J P & Kraft R P 2006 *AJ* **131**, 2949–2958.

- Soderblom D R & King J R 1999 *in* J. B Hearnshaw & C. D Scarfe, eds, 'IAU Colloq. 170: Precise Stellar Radial Velocities' Vol. 185 of *Astronomical Society of the Pacific Conference Series* p. 102.
- Steenbock W & Holweger H 1984 *A&A* **130**, 319–323.
- Stewart J C & Rotenberg M 1965 *Physical Review* **140**, 1508–1519.
- Sugar J & Corliss C 1985 *Atomic energy levels of the iron-period elements: Potassium through Nickel* Vol. 14 Washington: American Chemical Society, 1985.
- Sundqvist J O, Ryde N, Harper G M, Kruger A & Richter M J 2008 *A&A* **486**, 985–993.
- Thielemann F K, Fröhlich C, Hirschi R, Liebendörfer M, Dillmann I, Mocalj D, Rauscher T, Martinez-Pinedo G, Langanke K, Farouqi K, Kratz K L, Pfeiffer B, Panov I, Nadyozhin D K, Blinnikov S, Bravo E, Hix W R, Höflich P & Zinner N T 2007 *Progress in Particle and Nuclear Physics* **59**, 74–93.
- Thielemann F K, Nomoto K & Hashimoto M A 1996 *ApJ* **460**, 408.
- Thorne A P 1998 *J. Anal. Atomic Spectrosc.* **13**, 407–411.
- Timmes F X, Woosley S E & Weaver T A 1995 *ApJS* **98**, 617–658.
- Tinsley B M 1979 *ApJ* **229**, 1046–1056.
- Truran J W & Arnett W D 1971 *Astrophysics and Space Science* **11**, 430–442.
- Tsujimoto T, Shigeyama T & Yoshii Y 1999 *ApJL* **519**, L63–L67.
- Umeda H & Nomoto K 2002 *ApJ* **565**, 385–404.
- Umeda H & Nomoto K 2003 *Nature* **422**, 871–873.
- Umeda H & Nomoto K 2005 *ApJ* **619**, 427–445.
- Unsöld A 1955 *Physik der Sternatmosphären, MIT besonderer Berücksichtigung der Sonne*. Berlin, Springer, 1955. 2. Aufl.
- Unsöld A 1968 *Physik der Sternatmosphären MIT besonderer Berücksichtigung der Sonne* Heidelberger Taschenbuecher, Berlin: J. Springer, —c1968, 2. Auflage.
- van Regemorter H 1962 *ApJ* **136**, 906.
- VandenBerg D A, Swenson F J, Rogers F J, Iglesias C A & Alexander D R 2000 *ApJ* **532**, 430–452.
- Venn K A, Irwin M, Shetrone M D, Tout C A, Hill V & Tolstoy E 2004 *AJ* **128**, 1177–1195.
- Wallerstein G 1962 *ApJS* **6**, 407.
- West J B 2001 *Journal of Physics B Atomic Molecular Physics* **34**, 45.
- White H E & Eliason A Y 1933 *Physical Review* **44**, 753–756.
- White H E & Ritschl R 1930 *Physical Review* **35**, 1146–1160.
- Wiese W L & Fuhr J R 1990 *in* R Wehrse, ed., 'Accuracy of Element Abundances from Stellar Atmospheres' Vol. 356 of *Lecture Notes in Physics, Berlin Springer Verlag* pp. 7–18.
- Woodgate B 1966 *MNRAS* **134**, 287.
- Woosley S E & Weaver T A 1982 *in* 'Essays in Nuclear Astrophysics' p. 377.
- Woosley S E & Weaver T A 1995 *ApJS* **101**, 181, WW95.

Acknowledgements

I would like to thank Prof. Thomas Gehren for the excellent guidance of my PhD project, Dr. Frank Grupp for help with the data, and my Diploma thesis supervisor Dr. Lyudmila Mashonkina for very useful advices and explanations.

I am indebtedely grateful to my mother Natalia Khristoforova. This PhD thesis was possible due to the all-round support of my husband Timo Bergemann.

Curriculum Vitae

Name: Maria Bergemann (born Khristoforova)

Born on: 26.05.1983

In: Kazan, Russia

Family status: married, 1 child

Citizenship: Russian

Education:

2005 - 2008 PhD study of Astronomy, Ludwig-Maximillan University, Germany

2000 - 2005 Diploma Astronomy, Kazan State University, Russia

June 2004 B.Sc. Physics, Kazan State University, Russia

1991 - 2000 Secondary School N18 for Advanced studies of English, Russia